ABSTRACT

Quantization of Black Holes and Singularity Resolution in Loop Quantum Gravity

Wen-Cong Gan, Ph.D.

Advisor: Anzhong Wang, Ph.D.

In this dissertation, we study the properties of quantum black holes in the framework of loop quantum gravity. Loop quantum gravity is based on the canonical quantization of holonomies and fluxes of densitized triads. In loop quantum cosmology (LQC), the effective Hamiltonian can be obtained from the classical Hamiltonian by polymerization. The interior of Schwarzschild black hole is isometric to Kantowski-Sachs cosmological model with symmetry group $\mathbb{R} \times SO(3)$. Thus loop quantization techniques of LQC can be used in loop quantization of black holes. On the other hand, different choices of quantum parameters δ_b, δ_c correspond to different quantization schemes and will lead to different loop quantum black hole solutions. In particular, we investigate global and local properties of Bodendorfer, Mele, and Münch (BMM) model, Alesci, Bahrami and Pranzetti (ABP) model and Böhmer-Vandersloot (BV) model. We find that different choice of parameters will lead to different asymptotic behaviors. Specifically, for appropriate parameters, BMM model has black hole/white hole structure, ABP model has asymptotic de Sitter solution, while in BV model, black hole/white hole horizon never forms due to large quantum effects.

Quantization of Black Holes and Singularity Resolution in Loop Quantum Gravity

by

Wen-Cong Gan, B.S., M.A.

A Dissertation

Approved by the Department of Physics

____

Lorin S. Matthews, Ph.D., Chairperson

Submitted to the Graduate Faculty of
Baylor University in Partial Fulfillment of the
Requirements for the Degree
of

Doctor of Philosophy

Approved by the Dissertation Committee

____

Anzhong Wang, Ph.D., Chairperson

____

Truell Hyde, Ph.D.

____

Gerald B. Cleaver, Ph.D.

____

Lorin S. Matthews, Ph.D.

____

Qin (Tim) Sheng, Ph.D.

Accepted by the Graduate School
May 2023

____

J. Larry Lyon, Ph.D., Dean

Page bearing signatures is kept on file in the Graduate School.

TABLE OF CONTENTS

LIST OF FIGURES

LIST OF TABLES

ACKNOWLEDGMENTS

I would like to thank Dr. Anzhong Wang for teaching me the physics of the general relativity and supporting my research interests. His attitude towards science always sets an example for me. I am really grateful for everything he has done for me.

I would like to acknowledge my committee members, Dr. Truell Hyde, Dr. Gerald B. Cleaver, Dr. Lorin S. Matthews and Dr. Qin (Tim) Sheng for their advice and guidance.

Special thanks to Chao Zhang, Bowen Li and Xiang Zhao for their friendly support on my life in Baylor University, and they also teach me a lot in physics.

Many thanks to Zhibo Rao, Tianwei Yan and Jia-Yue Yang being the best friends in my life.

I would also like to thank the Physics Department of Baylor University and our staff members Mrs. Chava Baker, Mrs. Marian Nunn-Graves and our former and current GPDs Dr. Gerald Cleaver and Dr. David Hilton for the support during my graduate studies at Baylor.

ATTRIBUTIONS

Chapter Three is published in [1]: W. C. Gan, N. O. Santos, F. W. Shu and A. Wang, Properties of the spherically symmetric polymer black holes, Phys. Rev. D **102**, 124030 (2020). All authors contributed equally. Copyright©2023 American Physical Society.

Chapter Four is published in [2]: W. C. Gan, G. Ongole, E. Alesci, Y. An, F. W. Shu and A. Wang, Understanding quantum black holes from quantum reduced loop gravity, Phys. Rev. D **106**, no.12, 126013 (2022). All authors contributed equally. Copyright©2023 American Physical Society.

Chapter Five has been submitted as [3]: W. C. Gan, X. M. Kuang, Z. H. Yang, Y. Gong, A. Wang and B. Wang, Non-existence of quantum black hole horizons in the improved dynamics approach, [arXiv:2212.14535 [gr-qc]]. All authors contributed equally.

To my parents Dong-Feng Gan and Ping Li

CHAPTER ONE

Introduction to Loop Quantum Gravity

1.1 3+1 decomposition and Hamiltonian formulation

Loop quantum gravity (LQG) is based on the canonical quantization of general relativity [4] which is based on the Hamiltonian formulation. Thus, we need to split four-dimensional (4D) spacetime into 1D "time" and 3D "space", i.e. $3+1$ decomposition of spacetime. To do this, we need to introduce a one-parameter family of 3D spacelike hypersufaces $\{\Sigma_t\}$ to foliate the 4D spacetime manifold $\mathcal{M}$. The induced metric on Σ reads

$$q_{\mu\nu} = g_{\mu\nu} + n_\mu n_\nu, \tag{1.1}$$

where $g_{\mu\nu}$ is metric on $\mathcal{M}$, and n_μ is the unit normal vector of Σ.

Further, we also need to associate points on different Σ_t to each other, in order to describe the field's evolution with respect to "time" parameter t. This can be done by introducing the timelike vector t^μ, which satisfies $t^\mu \nabla_\mu t = 1$. Its integral curves specify space coordinates x^a on each Σ_t. Then for each t, we have embedding $X_t : \Sigma_t \to \mathcal{M}$ such that $X_t(x) = X(t,x)$, where X^μ is spacetime coordinates. Then

$$t^\mu(X) = \left(\frac{\partial X^\mu(t,x)}{\partial t}\right)\bigg|_{X=X(t,x)}. \tag{1.2}$$

We can decompose t^μ in the following form

$$t^\mu(X) = N(X) n^\mu(X) + N^\mu(X), \tag{1.3}$$

where N and N^μ are called the *lapse* function and the *shift* vector, respectively. The freedom to use arbitrary spacetime coordinates corresponds to the freedom to use an arbitrary lapse function and shift vector.

We have $n^\mu = (t^\mu - N^\mu)/N$, then

$$g^{\mu\nu} = q^{\mu\nu} - n^\mu n^\nu = q^{\mu\nu} - \frac{1}{N^2}(t^\mu - N^\mu)(t^\nu - N^\nu). \tag{1.4}$$

In coordinates (t, x^a), we have $t^\mu = (1, 0),\ N^\mu = (0, N^a)$, then $n^\mu = (\frac{1}{N}, \frac{-N^a}{N})$,

$$q^{\mu\nu} = \begin{pmatrix} 0 & 0 \\ 0 & q^{ab} \end{pmatrix}, \tag{1.5}$$

and

$$g^{\mu\nu} = \begin{pmatrix} -\frac{1}{N^2} & \frac{N^a}{N^2} \\ \frac{N^b}{N^2} & q^{ab} - \frac{N^a N^b}{N^2} \end{pmatrix}, \tag{1.6}$$

thus

$$g_{\mu\nu} = \begin{pmatrix} -N^2 + N^a N_a & N_b \\ N_a & q_{ab} \end{pmatrix}, \tag{1.7}$$

which leads to

$$ds^2 = g_{\mu\nu} dx^\mu dx^\nu = -N^2 dt^2 + q_{ab}(dx^a + N^a dt)(dx^b + N^b dt). \tag{1.8}$$

Denote D_a as the spatial covariant derivative compatible with metric q_{ab}, i.e. $D_a q_{bc} = 0$, then the spatial curvature tensor is defind by

$$(D_a D_b - D_b D_a) v^c = {}^{(3)}R^c{}_{dab} v^d. \tag{1.9}$$

The extrinsic-curvature tensor is defined by

$$K_{ab} := D_a n_b = q_a{}^c q_b{}^d \nabla_c n_d. \tag{1.10}$$

The Ricci scalar is given by

$$R = {}^{(3)}R + K_{ab}K^{ab} - K^2 - 2\nabla_a v^a, \tag{1.11}$$

where $v^a = n^c\nabla_c n^a - n^a\nabla_c n^c,\ K = K^a{}_a$. We also have $g = -N^2 q$, where $g = \det g_{\mu\nu}$ and $q = \det q_{ab}$. Then up to a boundary term, we have

$$S_{\rm EH} = \int dt L = \frac{1}{16\pi G}\int d^3x N\sqrt{q}\left({}^{(3)}R + K_{ab}K^{ab} - K^2\right). \tag{1.12}$$

The conjugate momentum of q_{ab} reads

$$p^{ab} = \frac{\delta L}{\delta \dot{q}_{ab}} = \frac{1}{2N}\frac{\delta L}{\delta K_{ab}} = \frac{1}{16\pi G}\sqrt{q}\left(K^{ab} - Kq^{ab}\right). \tag{1.13}$$

Then the gravitational Hamiltonian is given by

$$H_{\rm grav} = \int d^3x\, p^{ab}\dot{q}_{ab} - L, \tag{1.14}$$

and can be written in the form

$$H_{\rm grav} = \int d^3x \left[16\pi G\frac{N}{\sqrt{q}}\Big(p_{ab}p^{ab} - \frac{1}{2}p^2\Big) - \frac{1}{16\pi G}N\sqrt{q}{}^{(3)}R + 2p^{ab}D_a N_b\right], \tag{1.15}$$

where $p = p^a{}_a$. The Lagrangian in Eq.(1.12) does not contain $\dot{N}$ and $\dot{N}^a$, thus we have primary constraints

$$p_N = \frac{\delta L}{\delta \dot{N}} \simeq 0, \quad p_a = \frac{\delta L}{\delta \dot{N}^a} \simeq 0, \tag{1.16}$$

where $\simeq$ means equal on the constraint surface. Primary constraints imply secondary constraints

$$0 \simeq H_a = -\{p_a, H_{\rm grav}\} = -2D_b p_a{}^b = -2\sqrt{q}D^b\left(q^{-1/2}p_{ab}\right), \tag{1.17}$$

called the diffeomorphism constraint (or vector constraint), and

$$0 \simeq H = -\{p_N, H_{\rm grav}\} = 16\pi G\frac{1}{\sqrt{q}}\Big(p_{ab}p^{ab} - \frac{1}{2}p^2\Big) - \frac{1}{16\pi G}\sqrt{q}{}^{(3)}R, \tag{1.18}$$

called the Hamiltonian constraint (or scalar constraint). Then

$$H_{\rm grav} = \int d^3x\ (NH + N^a H_a), \tag{1.19}$$

where integration by parts has been used and the boundary term $2\int d^3x\sqrt{q}D_a(p^{ab}\frac{N_b}{\sqrt{q}})$ has been ignored.

1.2 Ashtekar's variables

Orthonormal triads $e_i^a(x)$ for the spatial metric q_{ab} are introduced,

$$q_{ab}e_i^a e_j^b = \delta_{ij}, \tag{1.20}$$

and densitized triads are defined by

$$E_i^a = \sqrt{q}e_i^a, \tag{1.21}$$

which will be treated as the new canonical variables. The triads expand the internal space, and the covariant derivative for vectors in internal space reads

$$D_a v^i = \partial_a v^i + \Gamma_a{}^i{}_j v^j, \tag{1.22}$$

where the connection $\Gamma_a{}^i{}_j$ is determined by the compatibility condition,

$$D_a e_b^i = \partial_a e_b^i - \Gamma^c{}_{ab} e_c^i + \Gamma_a{}^i{}_j e_b^j = 0. \tag{1.23}$$

Spin connections are defined as

$$\Gamma_a^i = -\frac{1}{2}\epsilon^{ijk}\Gamma_{ajk}. \tag{1.24}$$

The Ashtekar-Barbero connection is defined by

$$A_a^i = \Gamma_a^i + \gamma K_a^i, \tag{1.25}$$

where

$$K_a^i = K_{ab}q^{bc}e_c^i, \tag{1.26}$$

and γ is called the Barbero-Immirzi parameter. Ashtekar found that

$$\{A_a^i(x), E_j^b(y)\} = 8\pi G\gamma\delta_a^b\delta_j^i\delta^{(3)}(x,y). \tag{1.27}$$

Introducing the covariant derivative with the Ashtekar connection as

$$\mathcal{D}_a v^i = \partial_a v^i + \epsilon^i{}_{jk}A_a^j v^k, \tag{1.28}$$

then there is a new constraint called the Gauss constraint

$$0 \simeq G_i = \frac{1}{8\pi\gamma G}\mathcal{D}_a E^a_i, \tag{1.29}$$

which generates the $SO(3)$ gauge transformation. In terms of Ashtekar's new variables, the diffeomorphism constraint reads

$$H_a = \frac{1}{8\pi\gamma G} F^i_{ab} E^b_i, \tag{1.30}$$

where

$$F^i_{ab} = \partial_a A^i_b - \partial_b A^i_a + \epsilon^i{}_{jk} A^j_a A^k_b. \tag{1.31}$$

The Hamiltonian constraint reads

$$H = \frac{1}{16\pi G}\frac{E^a_i E^b_j}{\sqrt{\det E}}\Big(\epsilon^{ij}{}_k F^k_{ab} - (1+\gamma^2)\big(K^i_a K^j_b - K^j_a K^i_b\big)\Big). \tag{1.32}$$

1.3 Holonomy and flux

The holonomy is defined by

$$h_e[A] = \mathcal{P}\exp\Big(\int_e A\Big), \tag{1.33}$$

where $\mathcal{P}\exp$ denotes the path-ordered exponential, and e is the curve parametrized by $s \in [0,1]$. The holonomy can be explicitly expressed as

$$h_e[A] = \mathbf{1}_{2\times 2} + \sum_{n=1}^{\infty}\int_0^1 ds_1 \int_{s_1}^1 ds_2 \cdots \int_{s_{n-1}}^1 ds_n\, \dot{e}^{a_1}(s_1) A_{a_1}\big(e(s_1)\big)\cdots \dot{e}^{a_n}(s_n) A_{a_n}\big(e(s_n)\big), \tag{1.34}$$

where $h_{e(0)} = 1$, and $A_a = A^i_a \tau_i$, with $\tau_i = -\frac{1}{2}\sigma^i$ the generators of $SU(2)$ (σ^i is the Pauli matrix). Then $h_e[A] \in SU(2)$. The conjugate momentum of the holonomy is given by the flux of densitized triads and is defined by

$$E_i(S) = \int_S d^2\sigma\, n_a(\sigma) E^a_i\big(x(\sigma)\big), \tag{1.35}$$

where S is a two-dimensional surface, σ is a coordinate on it, and

$$n_a(\sigma) = \epsilon_{abc}(\partial x^b/\partial\sigma^1), (\partial x^c/\partial\sigma^2) \tag{1.36}$$

is the normal one-form on S.

Suppose curve e intersects surface S at point P with parameter s_0, then the Poisson brackets are given by [5,6]

$$\big\{h_e[A], E_i(S)\big\} = -8\pi\gamma G\nu(S,e)h_{e(1,s_0)}\tau_i h_{e(s_0,0)}, \tag{1.37}$$

where the factor $\nu(S,e)$ is defined as

$$\nu(S,e) = \begin{cases} +1 & \text{if } S \text{ and } e \text{ have same orientation} \\ -1 & \text{if } S \text{ and } e \text{ have opposite orientation} \\ 0 & \text{if } e \text{ does not intersect } S \text{ or intersects } S \text{ tangentially} \end{cases} \tag{1.38}$$

If there are more than one intersection points between S and e, then each intersection point has contribution in the form (1.37).

1.4 Quantization

Wave functions are functions of all holonomies on Γ

$$\Psi_\Gamma[A] = \psi\big(h_{e_1}[A], \ldots, h_{e_N}[A]\big), \tag{1.39}$$

where Γ represent the graph. $\Psi_\Gamma[A]$ are called cylindrical functions on Γ. The kinematical Hilbert space is constructed by square-integrable complex-valued functions on $SU(2)^N$, i.e.

$$\mathcal{H}_{\rm kin} = L^2\left(SU(2), dg\right)^N, \tag{1.40}$$

where N is the number of oriented edges in graph Γ and dg is the Haar measure of $SU(2)$. If we parametrize

$$h = e^{\alpha_1 \tau_3/2} e^{\alpha_2 \tau_2/2} e^{\alpha_3 \tau_3/2}, \tag{1.41}$$

with $\alpha_1, \alpha_2, \alpha_3$ Euler angles, then for any function $f(h) \equiv f(\alpha_1, \alpha_2, \alpha_3)$, dg is defined by

$$\int dg(h) f(h) \equiv \frac{1}{8\pi^3} \int_0^{2\pi} d\alpha_1 \int_0^{\pi} \sin\alpha_2 d\alpha_2 \int_0^{2\pi} d\alpha_3 f(\alpha_1, \alpha_2, \alpha_3). \tag{1.42}$$

Then scalar product is defined as

$$\langle \Psi_\Gamma | \Phi_\Gamma \rangle = \int dg_1 \ldots dg_N \, \overline{\psi(g_1, \ldots, g_N)} \phi(g_1, \ldots, g_N). \tag{1.43}$$

Physical Hilbert space $\mathcal{H}_{\text{phys}}$ is obtained by imposing constraints

$$\mathcal{H}_{\text{kin}} \xrightarrow{\hat{G}_i \psi = 0} \mathcal{H}_G \xrightarrow{\hat{H}_a \psi = 0} \mathcal{H}_{\text{diff}} \xrightarrow{\hat{H} \psi = 0} \mathcal{H}_{\text{phys}}.$$

1.5 Conventions

The following conventions are used in this dissertation. The signature of metrics is $g_{\mu\nu} = \{-1, +1, +1, +1\}$. The Christoffel symbol is

$$\Gamma^\lambda_{\mu\nu} = \frac{1}{2} g^{\lambda\sigma} (\partial_\mu g_{\nu\sigma} + \partial_\nu g_{\sigma\mu} - \partial_\sigma g_{\mu\nu}).$$

The Riemann tensor is [7]

$$R^\rho{}_{\sigma\mu\nu} = \partial_\mu \Gamma^\rho_{\nu\sigma} - \partial_\nu \Gamma^\rho_{\mu\sigma} + \Gamma^\rho_{\mu\lambda} \Gamma^\lambda_{\nu\sigma} - \Gamma^\rho_{\nu\lambda} \Gamma^\lambda_{\mu\sigma}.$$

The Ricci tensor is

$$R_{\mu\nu} = R^\rho{}_{\mu\rho\nu}.$$

The Ricci scalar is

$$R = g^{\mu\nu} R_{\mu\nu}.$$

The Einstein tensor is

$$G_{\mu\nu} = R_{\mu\nu} - \frac{1}{2}Rg_{\mu\nu}.$$

The Weyl tensor in n dimensions is

$$C_{\rho\sigma\mu\nu} = C_{\rho\sigma\mu\nu} - \frac{2}{(n-2)}(g_{\rho[\mu}R_{\nu]\sigma} - g_{\sigma[\mu}R_{\nu]\rho}) + \frac{2}{(n-1)(n-2)}g_{\rho[\mu}R_{\nu]\sigma}R.$$

Einstein's equations are

$$G_{\mu\nu} = 8\pi G T_{\mu\nu}.$$

CHAPTER TWO

Introduction to Loop Quantum Black holes

2.1 *Symmetry reduction*

The interior of the Schwarzschild black hole is isometric to the Kantowski-Sachs (KS) cosmological model with symmetry group $\mathbb{R} \times SO(3)$. Introducing the fiducial metric ds_o^2 on homogeneous Cauchy slices of the KS model [8,9]

$$ds_o^2 := dx^2 + r_o^2(d\theta^2 + \sin^2\theta\, d\phi^2), \tag{2.1}$$

by imposing the symmetry and Gauss constraint, we find that the connection and triad are given by

$$A_a^i\,\tau_i\,dx^a \;=\; \bar{c}\,\tau_3\,dx + \bar{b}\,r_o\,\tau_2 d\theta - \bar{b}\,r_o\,\tau_1 \sin\theta\, d\phi + \tau_3\cos\theta\, d\phi, \tag{2.2}$$

and

$$E_i^a\,\tau^i \frac{\partial}{\partial x^a} \;=\; \bar{p}_c\, r_o^2\,\tau_3\,\sin\theta\,\frac{\partial}{\partial x} + \bar{p}_b\, r_o\,\tau_2\,\sin\theta\,\frac{\partial}{\partial\theta} - \bar{p}_b\, r_o\,\tau_1\,\frac{\partial}{\partial\phi}. \tag{2.3}$$

Then the metric is given by

$$ds^2 = -N^2 dt^2 + \frac{\bar{p}_b^2}{|\bar{p}_c|}\,dx^2 + |\bar{p}_c|\,r_o^2\,(d\theta^2 + \sin^2\theta\, d\phi^2), \tag{2.4}$$

and the symplectic structure

$$\bar{\Omega} = \frac{L_o r_o^2}{2G\gamma}\left(2d\bar{b}\wedge d\bar{p}_b + d\bar{c}\wedge d\bar{p}_c\right), \tag{2.5}$$

depends on L_o and r_o explicitly. We can absorb L_o and r_o by introducing

$$c = L_o\,\bar{c}, \quad p_c = r_o^2\,\bar{p}_c, \quad b = r_o\,\bar{b}, \quad p_b = r_o\,L_o\,\bar{p}_b, \tag{2.6}$$

which satisfy

$$\{c, p_c\} \;=\; 2G\gamma, \qquad \{b, p_b\} \;=\; G\gamma\;. \tag{2.7}$$

The Ashtekar connection and spatial triads now can be written as:

$$A^i_a\,\tau_i\,dx^a \;=\; \frac{c}{L_o}\,\tau_3\,dx + b\,\tau_2 d\theta - b\,\tau_1\sin\theta\,d\phi + \tau_3\cos\theta\,d\phi, \tag{2.8}$$

and

$$E^a_i\,\tau^i\partial_a \;=\; p_c\,\tau_3\,\sin\theta\,\partial_x + \frac{p_b}{L_o}\,\tau_2\,\sin\theta\,\partial_\theta - \frac{p_b}{L_o}\,\tau_1\,\partial_\phi. \tag{2.9}$$

And the metric now reads

$$ds^2 = -N^2dt^2 + \frac{p_b^2}{|p_c|L_o^2}dx^2 + |p_c|(d\theta^2 + \sin^2\theta d\phi^2), \tag{2.10}$$

which is invariant under rescaling $r_o \to \lambda_1 r_o$ and $L_o \to \lambda_2 L_o$, where λ_1, λ_2 are constants.

The volume of the fiducial cell is

$$V \;=\; \int d^3x\sqrt{\det q} \;=\; 4\pi\,L_o r_o^2|\bar{p}_b||\bar{p}_c|^{1/2} = 4\pi\,|p_b||p_c|^{1/2}\;. \tag{2.11}$$

2.2 Classical solution

The smeared Hamiltonian constraint in full theory [10]

$$H[N] \equiv \frac{1}{16\pi G}\int d^3x N H = \frac{1}{16\pi G}\int d^3x N\frac{E^a_i E^b_j}{\sqrt{\det E}}\Big(\epsilon^{ij}{}_k F^k_{ab} - (1+\gamma^2)\big(K^i_a K^j_b - K^j_a K^i_b\big)\Big) \tag{2.12}$$

reduces to the following form in terms of phase space variables in the reduced phase space

$$H^{\rm GR}[N^{\rm GR}] = -\frac{1}{2G\gamma}\left(2c\,p_c + \left(b + \frac{\gamma^2}{b}\right)p_b\right), \tag{2.13}$$

with the lapse function

$$N^{\rm GR} = \gamma\,b^{-1}{\rm sgn}(p_c)\,|p_c|^{1/2}. \tag{2.14}$$

The equations of motions (EoMs) of the system can be obtained from the Hamiltonian equations,

$$\frac{dA}{dT} = \{A, H\}\,, \tag{2.15}$$

for any physical variable A of the system. Then we find,

$$\begin{aligned}
\dot{b} &= \{b, H^{\rm GR}\} = G\gamma\frac{\partial H^{\rm GR}}{\partial p_b} = -\frac{1}{2b}\left(b^2+\gamma^2\right), && (2.16)\\
\dot{c} &= \{c, H^{\rm GR}\} = 2G\gamma\frac{\partial H^{\rm GR}}{\partial p_c} = -2c, && (2.17)\\
\dot{p}_b &= \{p_b, H^{\rm GR}\} = -G\gamma\frac{\partial H^{\rm GR}}{\partial b} = \frac{p_b}{2b^2}\left(b^2-\gamma^2\right), && (2.18)\\
\dot{p}_c &= \{p_c, H^{\rm GR}\} = -2G\gamma\frac{\partial H^{\rm GR}}{\partial c} = 2p_c, && (2.19)
\end{aligned}$$

where an overdot denotes the derivative with respect to T. Then, the integrations of Eqs.(2.16), (2.17) and (2.19) yield, respectively,

$$\begin{aligned}
b^{\rm GR}(T) &= \pm\gamma\sqrt{e^{T_o-T}-1}, && (2.20)\\
c^{\rm GR}(T) &= c_o e^{-2T}, && (2.21)\\
p_c^{\rm GR}(T) &= p_c^o e^{2T}, && (2.22)
\end{aligned}$$

where T_o, c_o and p_c^o are three integration constants with T_o and c_o being dimensionless and p_c^o of L^2. To find p_b, we can first substitute the above solutions to Eq.(2.18) and then integrate it to find p_b, which will contain an integration constant, say, p_b^o. But, this constant is not arbitrary and must be chosen so that the classical Hamiltonian given by Eq.(2.13) vanishes identically. A more straightforward way is to submit the above solutions into the classical Hamiltonian Eq.(2.13) and directly find p_b. In doing so, we find that [3]

$$p_b^{\rm GR}(T) = \mp\frac{2c_o p_c^o}{\gamma}e^{T-T_o}\sqrt{e^{T_o-T}-1}. \tag{2.23}$$

Hence, we find

$$N^{\rm GR} = \pm \frac{\mathrm{sgn}(p_c)\,|p_c^o|^{1/2}}{\sqrt{e^{T_o - T} - 1}} e^T, \tag{2.24}$$

and

$$\begin{aligned} ds^2 &= p_c^o \Bigg\{ - \frac{\mathrm{sgn}\,(p_c^o)\, e^{2T}}{e^{T_o - T} - 1} dT^2 \\ &\quad + \frac{4c_o^2 e^{-2T_o}}{\gamma^2 L_o^2} (e^{T_o - T} - 1) dx^2 + e^{2T} d\Omega^2 \Bigg\}. \end{aligned} \tag{2.25}$$

Clearly, to have the proper signature, we assume $p_c^o > 0$. Then, setting $r = \sqrt{p_c^o} e^T$ and rescaling x by

$$x \to t \equiv - \frac{2c_o \sqrt{p_c^o} e^{-T_o}}{\gamma L_o} x, \tag{2.26}$$

the above metric takes the form of the classical Schwarzschild solution in the internal region of the black hole

$$ds^2 = - \frac{1}{\frac{2m}{r} - 1} dr^2 + \left(\frac{2m}{r} - 1\right) dt^2 + r^2 d\Omega^2, \tag{2.27}$$

with $m \equiv \sqrt{p_c^o} e^{T_o}/2$, related to the mass of the black hole via the relation $M = m/G$.

From the above analysis, we can see that, without loss of the generality, the rescaling (2.26) simply allows us to set

$$\frac{2c_o \sqrt{p_c^o} e^{-T_o}}{\gamma L_o} = -1. \tag{2.28}$$

On the other hand, using the gauge residual $T \to \hat{T} = T + C_o$, we can always set $p_c^0 = 1$, where $C_o \equiv (1/2) \ln p_c^o$. Certainly, this rescaling will lead to $T - T_o = \hat{T} - \hat{T}_o$ and $m \equiv \sqrt{p_c^o} e^{T_o}/2 = e^{\hat{T}_o}/2$, where $\hat{T}_o \equiv T_o + C_o$. In addition, L_o does not appear in the dynamical equations (2.16) - (2.19). Therefore, without loss of the generality, we can always set $L_o = 1$. In summary, the constants p_c^o, c_o and L_o can be chosen as

$$p_c^o = 1, \quad L_o = 1, \quad c_o = - \frac{\gamma L_o e^{T_o}}{2\sqrt{p_c^o}} = -\gamma m, \tag{2.29}$$

without affecting the physics of the spacetimes of the corresponding dynamical equations. Hence, we obtain

$$\begin{aligned}
b^{\mathrm{GR}}(T) &= \pm\gamma\sqrt{2me^{-T}-1}, \\
p_b^{\mathrm{GR}}(T) &= \pm e^{T}\sqrt{2me^{-T}-1}, \\
c^{\mathrm{GR}}(T) &= -\gamma m e^{-2T}, \quad p_c^{\mathrm{GR}}(T) = e^{2T}.
\end{aligned} \tag{2.30}$$

In the rest of this dissertation, without loss of the generality, we shall choose the "+" signs for both $b^{\mathrm{GR}}(T)$ and $p_b^{\mathrm{GR}}(T)$.

It is interesting to note that there is essentially only one physical parameter m that determines the properties of the classical spacetime, while the parameter γ affects only the dynamical equations through Eqs.(2.16) - (2.19), but has no effect on the spacetime. This is true only classically, and quantum mechanically γ does affect the properties of quantum spacetimes. In particular, the considerations of black hole thermodynamics in LQG requires $\gamma \simeq 0.2375$ [11].

2.3 Loop Quantization

The connection c is considered over edges labelled by τ in the x-direction and b is considered over edges labelled by μ in the θ- and ϕ-directions. Then the holonomies are given by [8, 10]

$$h_x^{(\tau)} = \cos(\tau c/2) + 2\,\tau_3\,\sin(\tau c/2)\ , \tag{2.31}$$

$$h_\theta^{(\mu)} = \cos(\mu b/2) + 2\,\tau_2\,\sin(\mu b/2)\ , \tag{2.32}$$

and

$$h_\phi^{(\mu)} = \cos(\mu b/2) - 2\,\tau_1\,\sin(\mu b/2)\ . \tag{2.33}$$

The Kinematical Hilbert space is spanned by eigenstates of $\hat{p}_b$ and $\hat{p}_c$:

$$\hat{p}_b\,|\mu,\tau\rangle = \frac{\gamma\ell_{pl}^2}{2}\,\mu\,|\mu,\tau\rangle, \quad \hat{p}_c\,|\mu,\tau\rangle = \gamma\ell_{pl}^2\,\tau\,|\mu,\tau\rangle\ , \tag{2.34}$$

which satisfy orthonormal condition $\langle\mu',\tau'|\mu,\tau\rangle = \delta_{\mu\mu'}\delta_{\tau\tau'}$. Then

$$V_{\mu\tau} = 2\pi\gamma^{3/2}\ell_{pl}^3|\mu||\tau|^{1/2}. \tag{2.35}$$

The Hamiltonian constraint of the full theory can be written in the form [8]

$$H[N] = -\frac{N}{16\pi G}\int d^3x\, e^{-1}\varepsilon_{ijk}E^{ai}E^{bj}(\gamma^{-2}\,{}^oF_{ab}^k - \Omega_{ab}^k)\ , \tag{2.36}$$

where $\Omega = -\sin\theta\tau_3 d\theta\wedge d\phi$ is the curvature of the spin connection $\Gamma = \cos\theta\, d\phi$, and ${}^oF_{ab}^k$ is the curvature of extrinsic curvature

$$K_a^i = \gamma^{-1}(A_a^i - \Gamma_a^i). \tag{2.37}$$

To quantize the theory, we need to write the Hamiltonian constraint in terms of holonomies. We need to consider loops in $x-\theta$, $x-\phi$ an $\theta-\phi$ planes to define holonomies. The length of the edge along the x-direction is $\delta_c L_o$ and the length of each edge along longitudes and the equator of $\mathbb{S}^2$ is $\delta_b r_o$. Then [8]

$$\varepsilon_{ijk}e^{-1}E^{aj}E^{bk} = \sum_k \frac{{}^o\varepsilon^{abc}\,{}^o\omega_c^k}{2\pi\gamma G\delta_{(k)}\ell_{(k)}}\,\mathrm{Tr}\left(h_k^{(\delta_{(k)})}\{(h_k^{(\delta_{(k)})})^{-1}, V\}\tau_i\right), \tag{2.38}$$

where $\delta_{(k)}$ represents δ_b or δ_c, and $\ell_{(k)}$ represents L_o or r_o. And

$${}^oF_{ab}^k = -2\lim_{Ar_\Box\to 0}\ \mathrm{Tr}\left(\frac{h_{\Box_{ij}}^{(\delta_{(i)},\delta_{(j)})} - 1}{\delta_{(i)}\delta_{(j)}\ell_{(i)}\ell_{(j)}}\right)\ \tau^k\,{}^o\omega_a^i\ {}^o\omega_b^j, \tag{2.39}$$

where

$$h_{\Box_{ij}}^{(\delta_{(i)},\delta_{(j)})} = h_i^{(\delta_{(i)})}h_j^{(\delta_{(j)})}(h_i^{(\delta_{(i)})})^{-1}(h_j^{(\delta_{(j)})})^{-1}\ . \tag{2.40}$$

Plugging Eqs.(2.38) and (2.39) into the Hamiltonian constraint (2.36), we have [8]

$$
\begin{aligned}
H^{(\delta_b,\delta_c)}[N] = & - \frac{N}{16\pi G}\frac{2}{\gamma^3 G\delta_b^2\delta_c}\Bigg[2\,\gamma^2\delta_b^2 \mathrm{Tr}\left(\tau_3 h_x^{(\delta_c)}\left\{(h_x^{(\delta_c)})^{-1}, V\right\}\right) \\
& + \sum_{ijk}\varepsilon^{ijk}\mathrm{Tr}\left(h_{\Box_{ij}}^{(\delta_{(i)},\delta_{(j)})} h_k^{(\delta_{(k)})}\left\{(h_k^{(\delta_{(k)})})^{-1}, V\right\}\right)\Bigg], \qquad (2.41)
\end{aligned}
$$

which can be written as [12]

$$
N^{\mathrm{eff}} = \frac{\gamma\delta_b\sqrt{p_c}}{\sin(\delta_b b)}, \qquad (2.42)
$$

$$
H^{\mathrm{eff}}[N^{\mathrm{eff}}] = -\frac{1}{2\gamma G}\left[2\frac{\sin(\delta_c c)}{\delta_c}p_c + \left(\frac{\sin(\delta_b b)}{\delta_b} + \frac{\gamma^2\delta_b}{\sin(\delta_b b)}\right)p_b\right], \qquad (2.43)
$$

in terms of phase space variables (p_b, p_c, b, c). Because of Eq.(2.39), the classical expression is recovered under limit $\delta_b \to 0$, $\delta_c \to 0$, i.e. $H^{\mathrm{GR}}[N^{\mathrm{GR}}] = \lim_{\delta_b,\delta_c\to 0} H^{\mathrm{eff}}[N^{\mathrm{eff}}]$. Effective expressions can be obtained by the substitutions

$$
b \to \frac{\sin(\delta_b b)}{\delta_b}, \quad c \to \frac{\sin(\delta_c c)}{\delta_c}, \qquad (2.44)
$$

which is called “polymerization”.

Utilizing Eq.(2.43), we can obtain the effective Hamiltonian EoMs

$$
\begin{aligned}
\dot{b} = & \; G\gamma\frac{\partial H^{\mathrm{eff}}}{\partial p_b} = -\frac{1}{2}\Bigg\{2\left(\frac{c\cos(\delta_c c)}{\delta_c} - \frac{\sin(\delta_c c)}{\delta_c^2}\right)\frac{\partial \delta_c}{\partial p_b}p_c + \left[\frac{\gamma^2\delta_b}{\sin(\delta_b b)} + \frac{\sin(\delta_b b)}{\delta_b}\right] \\
& + p_b\frac{\partial}{\partial p_b}\left[\frac{\gamma^2\delta_b}{\sin(\delta_b b)} + \frac{\sin(\delta_b b)}{\delta_b}\right]\Bigg\}, \qquad (2.45)
\end{aligned}
$$

$$
\begin{aligned}
\dot{c} = & \; 2G\gamma\frac{\partial H^{\mathrm{eff}}}{\partial p_c} = -\Bigg\{2\left(\frac{c\cos(\delta_c c)}{\delta_c} - \frac{\sin(\delta_c c)}{\delta_c^2}\right)\frac{\partial \delta_c}{\partial p_c}p_c + 2\frac{\sin(\delta_c c)}{\delta_c} \\
& + p_b\frac{\partial}{\partial p_c}\left[\frac{\gamma^2\delta_b}{\sin(\delta_b b)} + \frac{\sin(\delta_b b)}{\delta_b}\right]\Bigg\}, \qquad (2.46)
\end{aligned}
$$

$$
\dot{p}_c = -2G\gamma\frac{\partial H^{\mathrm{eff}}}{\partial c} = 2p_c\cos(\delta_c c), \qquad (2.47)
$$

$$
\dot{p}_b = -G\gamma\frac{\partial H^{\mathrm{eff}}}{\partial b} = \frac{p_b}{2}\cos(\delta_b b)\left[1 - \frac{\gamma^2\delta_b^2}{\sin^2(\delta_b b)}\right], \qquad (2.48)
$$

where we have assumed that δ_b and δ_c depend only on p_b and p_c.

Different choices of δ_b and δ_c correspond to different quantization schemes and will lead to different effective dynamics.

2.3.1 μ_0 scheme

In the μ_0 scheme [10, 12, 13], δ_b and δ_c are set to be constants,

$$\delta_b = 2\sqrt{3}, \quad \delta_c = 2\sqrt{3}. \tag{2.49}$$

When δ_b and δ_c do not depend on phase space variables, Hamiltonian equations reduce to

$$\begin{aligned}
\dot{b} &= G\gamma\frac{\partial H^{\text{eff}}}{\partial p_b} = -\frac{1}{2}\left(\frac{\sin(\delta_b b)}{\delta_b} + \frac{\gamma^2\delta_b}{\sin(\delta_b b)}\right), && (2.50)\\
\dot{c} &= 2G\gamma\frac{\partial H^{\text{eff}}}{\partial p_c} = -2\frac{\sin(\delta_c c)}{\delta_c}, && (2.51)\\
\dot{p}_b &= -G\gamma\frac{\partial H^{\text{eff}}}{\partial b} = \frac{p_b}{2}\cos(\delta_b b)\left(1 - \frac{\gamma^2\delta_b^2}{\sin^2(\delta_b b)}\right), && (2.52)\\
\dot{p}_c &= -2G\gamma\frac{\partial H^{\text{eff}}}{\partial c} = 2p_c\cos(\delta_c c), && (2.53)
\end{aligned}$$

and has the general solution [9]

$$\begin{aligned}
\tan\left(\frac{\delta_c\, c(T)}{2}\right) &= \mp\frac{\gamma L_o\delta_c}{8m}e^{-2T}, && (2.54)\\
p_c(T) &= 4m^2\Big(e^{2T} + \frac{\gamma^2 L_o^2\delta_c^2}{64m^2}e^{-2T}\Big), && (2.55)
\end{aligned}$$

$$\cos\big(\delta_b\, b(T)\big) = b_o\tanh\left(\frac{1}{2}\Big(b_o T + 2\tanh^{-1}\big(\frac{1}{b_o}\big)\Big)\right), \tag{2.56}$$

where

$$b_o = (1+\gamma^2\delta_b^2)^{1/2}, \tag{2.57}$$

and

$$p_b(T) = -2\frac{\sin(\delta_c\, c(T))}{\delta_c}\frac{\sin(\delta_b\, b(T))}{\delta_b}\frac{p_c(T)}{\frac{\sin^2(\delta_b\, b(T))}{\delta_b^2} + \gamma^2}. \tag{2.58}$$

2.3.2 $\bar{\mu}$-scheme

In LQC, the consistent prescription for the polymerization parameters were obtained by requiring that the physical area $A_{x\theta}$ $(= \delta_b\delta_c p_b)$ [14] [1] of the closed holonomy loop in the (x,θ)-plane be equal to the minimum area gap predicted by loop quantum gravity, $\Delta \equiv 2\sqrt{3}\pi\gamma l_{pl}^2$, so that

$$\delta_b\delta_c p_b = \Delta. \tag{2.59}$$

However, for the holonomies on the two-sphere, the loop does not close, and BV required that $A_{\theta\phi}$ $(= \delta_b^2 p_c)$ be equal to the minimum area, i.e.

$$\delta_b^2 p_c = \Delta. \tag{2.60}$$

Then, from the above equations, we find

$$\delta_b = \sqrt{\frac{\Delta}{p_c}}, \quad \delta_c = \frac{\sqrt{\Delta p_c}}{p_b}, \tag{2.61}$$

which are all dimensionless and often referred to as the $\bar{\mu}$-scheme for the spherically symmetric spacetimes [15]. Hence, we have

$$\frac{\partial \delta_b}{\partial p_b} = 0,\ \frac{\partial \delta_b}{\partial p_c} = -\frac{\delta_b}{2p_c}, \tag{2.62}$$

$$\frac{\partial \delta_c}{\partial p_b} = -\frac{\delta_c}{p_b},\ \frac{\partial \delta_c}{\partial p_c} = \frac{\delta_c}{2p_c}. \tag{2.63}$$

[1] In the homogeneous isotropic universe, we have $\delta_b = \delta_c$. As a result, the condition (2.59) uniquely determines them. But, in the Kantowski-Sachs spacetime, this is no longer the case. So, in general we have $\delta_b \neq \delta_c$, and now one more condition is needed in order to determines them uniquely.

Inserting them into Eqs.(2.45) and (2.46), we obtain [3]

$$\dot{b} = -\frac{c\mathcal{F}}{2\frac{\sin(\delta_c c)}{\delta_c}}\cos(\delta_c c), \tag{2.64}$$

$$\begin{aligned}\dot{c} = & -\frac{\frac{\sin(\delta_c c)}{\delta_c}}{\mathcal{F}}\Bigg\{b\cos(\delta_b b) - b\cos(\delta_b b)\frac{\gamma^2\delta_b^2}{\sin^2(\delta_b b)} \\ & +2\frac{\gamma^2\delta_b}{\sin(\delta_b b)} \\ & +\delta_c c\cot(\delta_c c)\left[\frac{\gamma^2\delta_b}{\sin(\delta_b b)} + \frac{\sin(\delta_b b)}{\delta_b}\right]\Bigg\},\end{aligned} \tag{2.65}$$

$$\dot{p}_c = 2p_c\cos(\delta_c c), \tag{2.66}$$

$$\dot{p}_b = \frac{p_b}{2}\cos(\delta_b b)\left[1 - \frac{\gamma^2\delta_b^2}{\sin^2(\delta_b b)}\right], \tag{2.67}$$

where

$$\mathcal{F} \equiv \frac{\gamma^2\delta_b}{\sin(\delta_b b)} + \frac{\sin(\delta_b b)}{\delta_b}. \tag{2.68}$$

After taking the following identity into account

$$\frac{p_c}{p_b} = \frac{\delta_c}{\delta_b} = -\frac{\mathcal{F}}{2\frac{\sin(\delta_c c)}{\delta_c}}, \tag{2.69}$$

it can be shown that Eqs.(2.64)-(2.67) reduces to Eqs.(58)-(61) given in [15]. In particular, now the effective Hamiltonian (2.43) takes the form

$$H^{\text{eff}}[N^{\text{eff}}] = -\frac{p_c}{2\gamma G\sin(\delta_b b)\delta_c}C_{\text{BV}}, \tag{2.70}$$

$$C_{\text{BV}} \equiv 2\sin(\delta_b b)\sin(\delta_c c) + \sin(\delta_b b)^2 + \gamma^2\delta_b^2. \tag{2.71}$$

Therefore, the Hamiltonian constraint $H^{\text{eff}}[N^{\text{eff}}] \simeq 0$ can be written as $C_{\text{BV}} \simeq 0$.

CHAPTER THREE

Properties of the spherically symmetric polymer black holes

This chapter is published in [1]: W. C. Gan, N. O. Santos, F. W. Shu and A. Wang, Properties of the spherically symmetric polymer black holes, Phys. Rev. D **102**, 124030 (2020).

3.1 Abstract

In this chapter we systematically study a recently proposed model of spherically symmetric polymer black/white holes by Bodendorfer, Mele, and Münch (BMM), which generically possesses five free parameters. However, we find that, out of these five parameters, only three independent combinations of them are physical and uniquely determine the local and global properties of the spacetimes. After exploring the whole 3-dimensional (3D) parameter space, we show that the model has very rich physics, and depending on the choice of these parameters, various possibilities exist, including: (i) spacetimes that have the standard black/white hole structures, that is, spacetimes that are free of spacetime curvature singularities and possess two asymptotically flat regions, which are connected by a transition surface (throat) with a finite and nonzero geometric radius. The black/white hole masses measured by observers in the two asymptotically flat regions are all positive, and the surface gravity of the black (white) hole is positive (negative). In this case, there also exist possibilities in which the two horizons coincide, and the corresponding surface gravity vanishes identically. (ii) Spacetimes that have wormholelike structures, in which the two masses measured in the two asymptotically flat regions are all positive, but no horizons exist, neither a trapped (black hole) horizon nor an anti-trapped (white hole) horizon. (iii)

Spacetimes that still possess curvature singularities, which can be either hidden inside trapped regions or naked. However, such spacetimes correspond to only some limit cases. In particular, the necessary (but not sufficient) condition is that at least one of the two "polymerization" parameters vanishes. These results are not in conflict to the Hawking-Penrose singularity theorems, as the effective energy-momentum tensor, purely geometric and resulted from the "polymerization" quantization, satisfies none of the three (weak, strong or dominant) energy conditions in any of the two asymptotically flat regions for any choice of the three independent free parameters, although they can hold at the throat and/or at the two horizons for some particular choices of them. In addition, it is true that quantum gravitational effects are mainly concentrated in the region near the throat, however, in this model even for solar mass black/white holes, such effects can be still very large at the black/white hole horizons, again depending on the choice of the parameters. Moreover, in principle the ratio of the two masses (for both of the black/white hole and wormhole spacetimes) can be arbitrarily large.

3.2 Introduction

In classical Hamiltonian mechanics, a canonical transformation

$$(q_i,\ p_i) \to (Q_i,\ P_i), \tag{3.1}$$

is always allowed, and does not change the physics of the system, where $Q_i = Q_i(q_k, p_k; t)$, $P_i = P_i(q_k, p_k; t)$, $q_i = (b, c)$, and $p_i = (p_b, p_c)$ [16]. However, the polymerization (2.44) depends on the choice of the canonical variables, and different canonical variables in general lead to different effective theories. It was exactly along this vein, Bodendorfer, Mele, and Münch (BMM) considered the following transformation [17,18],

$$v_1 \equiv \frac{1}{24}\left|p_c\right|^{3/2}, \quad v_2 \equiv -\frac{1}{8}p_b^2, \tag{3.2}$$

for which the corresponding conjugate momenta are denoted by P_1 and P_2, respectively. Then, instead of Eq.(2.44), now the polymerizations are carried out via the replacements [17],

$$P_1 \to \frac{\sin(\lambda_1 P_1)}{\lambda_1}, \quad P_2 \to \frac{\sin(\lambda_2 P_2)}{\lambda_2}, \tag{3.3}$$

where λ_1 and λ_2 play the same role as δ_b and δ_c. In this approach, the polymerization scales (λ_1, λ_2) are taken as constants, but as pointed out in [18], this choice of polymerization scales does not correspond to μ_0-scheme in terms of the variables $(b,\ c)$, instead, when translated back to $(b,\ c)$, they correspond to a specific $\bar{\mu}$-scheme.

It must be noted that the BMM model is based on a set of new canonical variables (v_i, P_i). Although the canonical transformation (3.1) is always allowed classically, the corresponding loop quantization has not been carried out yet in terms of these new variables. As a result, it is not clear what are relations of such effective theory [obtained by simply the replacement of Eq.(3.3)] to LQG. Therefore, to be distinguished with the effective theory obtained from LQG by taking only the leading order of quantum corrections into account, we refer such black holes as polymer black holes. Additional questions related to this issue can be found from [10,19].

With the above caveat in mind, in this chapter, we shall systematically study the local and global properties of the model proposed in [17]. In particular, we find that, out of the five parameters appearing in the model, only three independent combinations of them are physically relevant, and uniquely determine the properties of the spacetimes. In this 3D phase space, there exist regions, in which the solutions can represent two asymptotically flat regions connected by a throat with a finite and nonzero geometric radius, and the masses read off in these two asymptotically flat regions are all positive. In such case, a black/white horizon exists or not also depending on the choice of the three free parameters. When they do exist, the surface gravity at the black (white) hole horizon can be positive (negative). When they do not exist, the spacetimes have wormhole structures. In all these solutions, spacetime curvature singularities are absent, which does not contradict to the Hawking-Penrose singularity theorems [20], as now the effective energy-momentum tensor does not satisfy any of the three energy conditions in the two asymptotically flat regions, despite the fact that the masses measured by observers in these two asymptotical regions are all positive. This is mainly due to the fact that the relativistic Komar energy density [21] is still positive in a large region of the spacetime. The violation of the three energy conditions in the asymptotically flat regions is a generic feature of the model, independent of the choice of the parameters of the solutions. Spacetime curvature singularities can occur, but the necessary (not sufficient) condition is at least one of the two "polymerization" parameters vanishes. In addition, although it is true that quantum gravitational effects are mainly concentrated in the region near the throat, in this model such effects still can be very large at the black/white hole horizons even for solar mass black/white holes, again depending on the choice of the free parameters. Moreover, in principle the ratio of the two masses (for both of the black/white hole and wormhole spacetimes) can be arbitrarily large.

It should be noted that, despite the fact that in this chapter we consider only a particular model, we believe the main conclusions should hold for more general cases. In particular, the Schwarzschild solution is the unique vacuum solution of GR with a single parameter—the black hole mass, according to the Birkhoff theorem [22]. However, due to the polymerization process, two more free parameters, δ_b and δ_c (or in the present case, λ_1 and λ_2), are introduced. So, the resulted spacetimes should be characterized physically by only three free parameters, although the two polymerization parameters may be completely fixed, when the quantization is carried out explicitly, such as in the case considered in [9, 23]. Clearly, in order for this to be consistent with the Birkhoff theorem, effective matter must be present, purely due to the quantum geometric effects. In addition, to be in harmony with the Hawking-Penrose singularity theorems [20], the effective energy-momentum tensor necessarily violates the weak/strong energy conditions.

The rest of the chapter is organized as follows: In Sec. 3.3, we first review the model built in [17] and then write the corresponding solutions in terms of only three independent combinations of the original five parameters, which are denoted by $\mathcal{D}$, $\mathcal{C}$, x_0, defined explicitly in Eq.(3.9). Then, we study the model in detail over the whole parameter space in Secs. 3.4 - 3.6, respectively, for $\Delta > 0$, $\Delta = 0$, and $\Delta < 0$, as in each case the spacetimes have quite different properties, where Δ is defined by Eq.(3.13). The main results in each of these sections are summarized, respectively, in Tables 3.1 - 3.3. The chapter is ended up in Sec. 3.7, in which we summarize our main conclusions. An appendix is also included, in which the general expressions of the energy density and pressures of the effective energy-momentum tensor are given explicitly.

3.3 Spherically symmetric polymer black holes

Studying spherically symmetric spacetimes inside black holes, Bodendorfer, Mele, and Münch recently obtained the following spherically symmetric black hole solutions [17],

$$d\bar{s}^2 = -\frac{\bar{a}(x)}{L_0^2}d\bar{t}^2 + \frac{\mathcal{L}_0^2}{\bar{a}(x)}dx^2 + \bar{b}^2(x)d\Omega^2, \tag{3.4}$$

where $\mathcal{L}_0 = \sqrt{n},\ \ x \in (-\infty, \infty)$, and

$$\begin{aligned}
\bar{a}(x) &= n\left(\frac{\lambda_2}{\sqrt{n}}\right)^4\left(1+\frac{nx^2}{\lambda_2^2}\right)\left(1-\frac{3CD}{2\lambda_2\sqrt{1+\frac{nx^2}{\lambda_2^2}}}\right)\\
&\times\left[\frac{\lambda_2^6}{16C^2\lambda_1^2n^3}\left(\frac{\sqrt{n}x}{\lambda_2}+\sqrt{1+\frac{nx^2}{\lambda_2^2}}\right)^6+1\right]^{-2/3}\\
&\times\left(\frac{1}{3C^2D\lambda_1^2}\right)^{2/3}\left(\frac{\sqrt{n}x}{\lambda_2}+\sqrt{1+\frac{nx^2}{\lambda_2^2}}\right)^2,\\
\bar{b}(x) &= \frac{\sqrt{n}\left(3C^2D\lambda_1^2\right)^{1/3}}{\lambda_2}\\
&\times\frac{\left[\frac{\lambda_2^6}{16C^2\lambda_1^2n^3}\left(\frac{\sqrt{n}x}{\lambda_2}+\sqrt{1+\frac{nx^2}{\lambda_2^2}}\right)^6+1\right]^{1/3}}{\frac{\sqrt{n}x}{\lambda_2}+\sqrt{1+\frac{nx^2}{\lambda_2^2}}},
\end{aligned}\tag{3.5}$$

where $\lambda_1,\ \lambda_2,\ n,\ C$ and D are real constants with $n > 0$.

As shown in [17], there are two independent Dirac observables, F_Q and $\bar{F}_Q$, which are constants along the trajectories of the effective dynamics, and their on-shell values are given by,

$$\begin{aligned}
F_Q &= \left(\frac{3D}{2}\right)^{4/3}\left(\frac{C}{\sqrt{n}}\right),\\
\bar{F}_Q &= \frac{3CD\sqrt{n}}{\lambda_2^2}\left(3DC^2\lambda_1^2\right)^{1/3}.
\end{aligned}\tag{3.6}$$

It can be shown that both of them are invariant under a fiducial cell rescaling. As a result, the integration constants C and D are independent. In fact, at the limits,

$x \to \pm\infty$, we have

$$\bar{a}(x) \propto \begin{cases} 1 - \frac{F_Q}{\bar{b}}, & x \to \infty, \\ \\ 1 - \frac{\bar{F}_Q}{\bar{b}}, & x \to -\infty. \end{cases} \tag{3.7}$$

Thus, they are essentially related to the black and white hole masses via the relations,

$$\begin{aligned} \bar{M}_{BH} &= \frac{1}{2} F_Q = \left(\frac{3D}{2}\right)^{4/3} \left(\frac{C}{2\sqrt{n}}\right), \\ \bar{M}_{WH} &= \frac{1}{2} \bar{F}_Q = \frac{3CD\sqrt{n}}{2\lambda_2^2} \left(3DC^2\lambda_1^2\right)^{1/3}. \end{aligned} \tag{3.8}$$

Introducing the quantities,

$$\mathcal{D} \equiv \frac{3CD}{2\sqrt{n}}, \quad \mathcal{C} \equiv \left(16C^2\lambda_1^2\right)^{1/6}, \quad x_0 \equiv \frac{\lambda_2}{\sqrt{n}}, \tag{3.9}$$

we find that the metric (3.4) takes the form,

$$\begin{aligned} d\bar{s}^2 &= \left(\frac{3D}{16}\right)^{2/3} ds^2 \\ &\equiv \left(\frac{3D}{16}\right)^{2/3} \left(-a(x)dt^2 + \frac{dx^2}{a(x)} + b^2(x) d\Omega^2\right), \end{aligned} \tag{3.10}$$

with $t \equiv (\sqrt{n}/L_0)\,(16/3D)^{2/3}\,\bar{t}$, and

$$a(x) = \frac{(x^2 - \Delta)\, XY^2}{(X + \mathcal{D})\, Z^2}, \quad b(x) = \frac{Z}{Y}, \tag{3.11}$$

where

$$\begin{aligned} X &\equiv \sqrt{x^2 + x_0^2}, \quad Y \equiv x + X, \\ Z &\equiv \left(Y^6 + \mathcal{C}^6\right)^{1/3}, \end{aligned} \tag{3.12}$$

and

$$\Delta \equiv \mathcal{D}^2 - x_0^2 = \frac{9C^2D^2 - 4\lambda_2^2}{4n}. \tag{3.13}$$

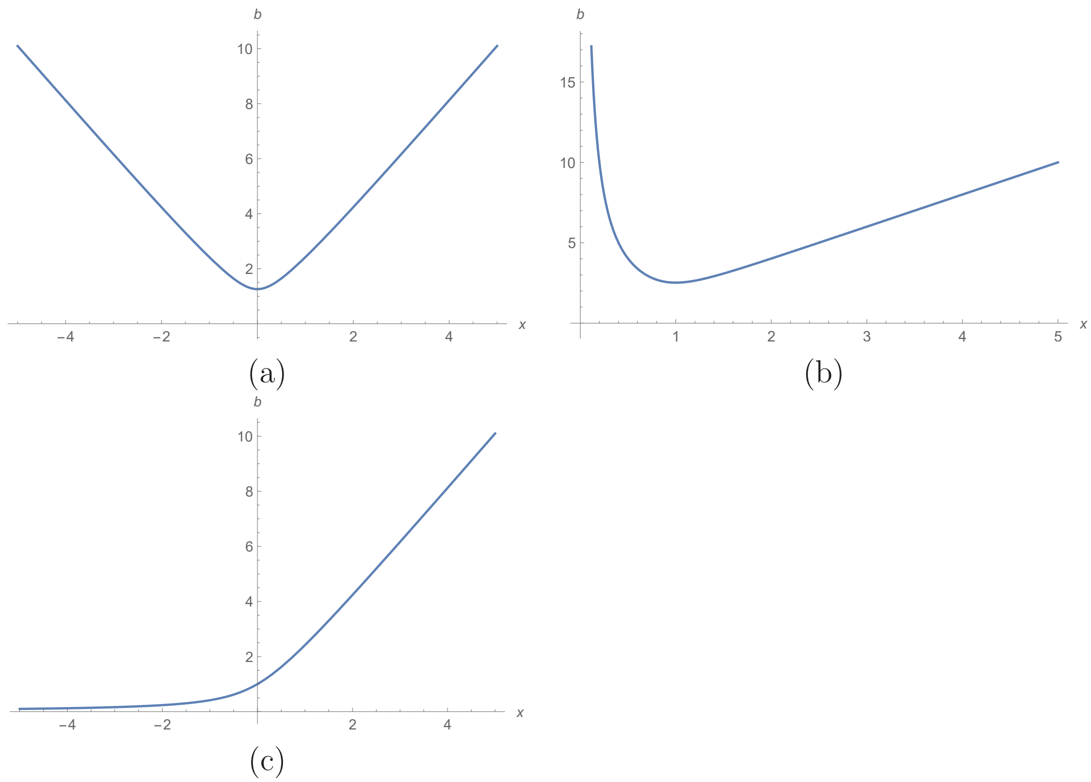

Figure 3.1: The geometric radius $b(x)$ vs x. (a) Upper panel: $\mathcal{C}x_0 \neq 0$. When plotting this curve, we had set $x_0 = 1$, $\mathcal{C} = 1$. (b) Middle panel: $\mathcal{C} \neq 0$, $x_0 = 0$. When plotting this curve, we had set $\mathcal{C} = 2$. (c) Bottom panel: $\mathcal{C} = 0$, $x_0 \neq 0$. When plotting this curve, we had set $x_0 = 1$.

Since ds^2 is related to $d\bar{s}^2$ only by a conformal constant factor $(3D/16)^{2/3}$ [1], without loss of generality, we shall consider only the spacetimes described by ds^2. Then, we can see that only three independent combinations of the five parameters λ_1, λ_2, n, C, and D appear in the metric coefficients, as defined by Eq.(3.9).

It is remarkable to note that in GR, due to the Birkhoff theorem [22], the black hole mass is the only free parameter. However, in LQG, due to the polymerizations (3.3), two new parameters λ_1 and λ_2 are introduced, so now the solutions generically depend on three free parameters. When setting $\lambda_1 = \lambda_2 = 0$ (or $\mathcal{C} = x_0 = 0$), the

[1] Under this rescaling, the Ricci and Kretschmann scalars are scaling, respectively, as $R = (3D/16)^{2/3}\,\bar{R}$ and $K = (3D/16)^{4/3}\,\bar{K}$.

above solutions reduce precisely to the Schwarzschild solution with $\mathcal{D}$ as the black hole mass.

One of our goals in this chapter is to understand their physical and geometrical meanings. To this goal, let us first note the following:

- Since $x \in (-\infty, \infty)$, from Eq.(3.12) we find that

$$X \geq x_0, \quad Y > 0, \quad Z > \mathcal{C}^2. \tag{3.14}$$

- In [17, 18] it was assumed that

$$\mathcal{D} > 0, \quad \Delta > 0, \tag{3.15}$$

  so that two metric horizons always exist at $x_H^{\pm} \equiv \pm\sqrt{\Delta}$, and the asymptotic limits of Eq.(3.7) are always true (See also [24]).

- The solutions were initially derived only in the region $-x_H^- < x < x_H^+$, in which the spacetime is homogeneous, and the Killing vector $\xi \equiv \partial_t$ is space-like. The horizon at $x = x_H^+$ is referred to as the black hole horizon, while the one at $x = x_H^-$ is referred to as the white hole horizon, although in between them, no spacetime singularities exist at all [9, 23]. However, following the standard process of extensions, one can easily extend the solutions beyond these horizons to the regions $|x| > \sqrt{\Delta}$. In the extended regions $x < x_H^-$ and $x > x_H^+$, the metrics will take the same form as that given by Eqs.(3.10)-(3.12), but now the Killing vector ∂_t becomes timelike.

In this chapter, we shall not impose the conditions (3.15), except that we still assume that C and D are real. In particular, since $C,\ D,\ n,\ \lambda_1$, and λ_2 are arbitrary constants, in principle, they can take any real values. However, since $ds^2 = (3D/16)^{2/3}\, d\bar{s}^2$, we shall assume that $D = 0$ holds only in the limiting sense. In addition, the two constants λ_1 and λ_2 originate from the polymerization (3.3), so we also assume that $\lambda_1\lambda_2 \neq 0$, and consider the case $\lambda_1\lambda_2 = 0$ only as some limit cases, as to be explained explicitly below. Recall that we also assumed $n > 0$ in order to have the metric be real.

Then, the geometric radius $b(x)$ and the ranges of x all depend on the choices of the two parameters x_0 and $\mathcal{C}$, which are shown explicitly in Fig. 3.1. In particular, when $\mathcal{C}x_0 \neq 0$, we find that $x \in (-\infty, \infty)$, and a minimal point (the throat) of $b(x)$ always exists, with $b(\pm\infty) = \infty$, as shown by the upper panel of Fig. 3.1. When $\mathcal{C} \neq 0,\ x_0 = 0$, the range of x is restricted to $x \in (0, \infty)$ with $b(0) = \infty$ and $b(\infty) = \infty$. In this case, a minimum (throat) of $b(x)$ also exists, as shown explicitly in the middle panel of Fig. 3.1]. When $\mathcal{C} = 0,\ x_0 \neq 0$, the range of x is $x \in (-\infty, \infty)$, but now $b(x)$ is a monotonically increasing function of x with $b(-\infty) = 0$ and $b(\infty) = \infty$, and a throat does not exists [cf. the bottom panel of Fig. 3.1].

In this chapter, we shall study the main properties of these spherical polymer black hole solutions. In particular, we shall pay particular attention to the locations of the throat and horizons, and the asymptotic behaviors of the spacetimes.

To these purposes, let us first notice that the effective energy-momentum tensor $T_{\mu\nu}$, defined as $T_{\mu\nu} \equiv \kappa^{-1}G_{\mu\nu}$, can be cast in the form,

$$T_{\mu\nu} = \rho u_\mu u_\nu + p_r v_\mu v_\nu + p_\theta\left(\theta_\mu\theta_\nu + \phi_\mu\phi_\nu\right), \tag{3.16}$$

where

$$\begin{aligned} u^+_\mu &= -a^{1/2}(x)\delta^t_\mu, \quad v^+_\mu = a^{-1/2}(x)\delta^x_\mu, \\ \theta_\mu &= b^{1/2}(x)\delta^\theta_\mu, \quad \phi_\mu = b^{1/2}(x)\sin\theta\delta^\phi_\mu,\ (a > 0), \end{aligned} \tag{3.17}$$

and

$$
\begin{aligned}
\kappa\rho^{+} &= -\frac{1}{b^{2}}\Big[b(x)\left(2ab''+a'b'\right)+ab'^{2}-1\Big],\\
\kappa p_{r}^{+} &= \frac{1}{b^{2}}\Big[ba'b'+ab'^{2}-1\Big],\\
\kappa p_{\theta} &= \frac{1}{2b}\Big[ba''+2ab''+2a'b'\Big],\ (a>0),
\end{aligned}
\tag{3.18}
$$

with $\kappa \equiv 8\pi G/c^{4}$, $a' \equiv da(x)/dx$, and so on.

It should be noted that in writing down Eqs.(3.17) and (3.18) we had assumed that $a(x) > 0$, as already indicated in these equations, so the coordinate t is timelike. However, if a (black/white) horizon exists, across this horizon $a(x)$ becomes negative, and the two coordinates t and x exchange their roles. Then, in the region $a(x) < 0$, the effective energy-momentum tensor can be still cast in the form (3.16), but now with

$$
\begin{aligned}
u_{\mu}^{-} &= |a|^{-1/2}\delta_{\mu}^{x}, \quad v_{\mu}^{-} = -|a|^{1/2}\delta_{\mu}^{t},\\
\kappa\rho^{-} &= -\frac{1}{b^{2}}\Big[ba'b'+ab'^{2}-1\Big], \qquad (a<0),\\
\kappa p_{r}^{-} &= \frac{1}{b^{2}}\Big[b(x)\left(2ab''+a'b'\right)+ab'^{2}-1\Big],
\end{aligned}
\tag{3.19}
$$

while θ_{μ}, ϕ_{μ}, and p_{θ} are still given by Eqs.(3.17) and (3.18).

It should be also noted that, although the effective energy-momentum tensor in both of the regions $a > 0$ and $a < 0$ is written in the same form given by Eq.(3.16), the physical interpretations of the quantities $\rho^{\pm}$ and $p_{r}^{\pm}$ are different. In particular, the energy density ρ^{+} in the region $a > 0$ is measured by the observers who are moving along dt-direction, while their x, θ, and ϕ coordinates are fixed. The quantity p_{r}^{+} is the principal pressure along the dx-direction measured by these observers. On the other hand, the energy density ρ^{-} in the region $a < 0$ is measured by the observers who are moving along dx-direction, while their t, θ, and ϕ coordinates are fixed. In addition, the quantity p_r^- now is the principal pressure along the dt-direction. Thus, in general such defined $\rho^\pm$ and $p_r^\pm$ are not continuous across the horizons. One way to avoid such discontinuities is to adopt the Eddington-Finkelstein coordinates, and then define a new set of observers, with respect to whom the energy density and principal pressure along the radial direction are continuous across these horizons. However, since in this chapter we are mainly concerned with the energy conditions of "the effective (quantum) matter," [2] the current considerations are sufficient.

In addition, although this effective energy-momentum tensor is purely due to the polymerization (3.3), and is not related to any real matter fields, it does provide important information on how the spacetime singularity is avoided, and the deviation of the spacetimes from the classical one, as in GR the geometry is uniquely determined by the Schwarzschild spacetime, in which the spacetime is vacuum, and a spacetime curvature singularity is always present at the center of the black hole. In fact, this kind of singularities inevitably occurs in GR, as longer as the corresponding matter fields satisfy some energy conditions, as follows directly from the Hawking-Penrose singularity theorems [20].

The commonly used three energy conditions are *the weak, dominant, and strong energy conditions* [20]. For $T_{\mu\nu}$ given by Eq.(3.16), they can be expressed as follows: The weak energy condition (WEC) is satisfied, when

$$(i)\ \rho \geq 0, \quad (ii)\ \rho + p_r \geq 0, \quad (iii)\ \rho + p_\theta \geq 0, \tag{3.20}$$

[2] As mentioned above, the BMM model has not been obtained from quantizations of gravity yet, but rather obtained by simply applying the "polymerization" (3.3) to the corresponding classical Hamiltonian. So, it is not clear whether these effects are indeed due to quantizations of gravity or not. In the rest of this chapter, whenever we mention "quantum gravitational effects" or "quantum geometric effects" of this model, we always understand them as "polymerization effects" without any further explanations. In the same sense, the expression "quantum black holes" of this model really means polymer black holes.

while the dominant energy condition (DEC) is satisfied, provided that

$$(i)\ \rho \geq 0, \quad (ii)\ -\rho \leq p_r \leq \rho, \quad (iii)\ -\rho \leq p_\theta \leq \rho. \tag{3.21}$$

The strong energy condition (SEC) requires,

$$(i)\ \rho + p_r \geq 0,\ (ii)\ \rho + p_\theta \geq 0,\ (iii)\ \rho + p_r + 2p_\theta \geq 0. \tag{3.22}$$

Moreover, without causing any confusions, in the rest of this chapter we shall absorb κ into $\rho,\ p_r$ and p_θ, i.e.,

$$\kappa\left(\rho,\ p_r,\ p_\theta\right) \rightarrow \left(\rho,\ p_r,\ p_\theta\right). \tag{3.23}$$

To study these solutions in more details, let us consider the cases $\Delta > 0$, $\Delta = 0$ and $\Delta < 0$, separately, in the following three sections.

3.4 Spacetimes with $\Delta > 0$

From Eq.(3.13) we find that this case corresponds to

$$|\lambda_2| < \frac{3}{2}\left|CD\right|. \tag{3.24}$$

However, depending on the choice of the integration constants C and D, there are still the possibilities, $\mathcal{D} > 0$, and $\mathcal{D} < 0$, provided that $\Delta = \mathcal{D}^2 - x_0^2 > 0$. In each of these cases, the physics of the corresponding solutions is quite different, so in the following let us consider them case by case.

3.4.1 $\mathcal{D} > 0$

In this case, we have $CD > 0$, and $\Delta = \mathcal{D}^2 - x_0^2 > 0$ implies,

$$\beta \equiv \frac{\mathcal{D}}{|x_0|} > 1. \tag{3.25}$$

Then, we find that there are two asymptotically flat regions, corresponding to $x \to \pm\infty$, respectively. They are connected by a throat located at

$$b_m \;\equiv\; 2^{1/3}\mathcal{C}, \quad x_m = \frac{1}{2\mathcal{C}}\left(\mathcal{C}^2 - x_0^2\right), \tag{3.26}$$

where $b_m \equiv b(x = x_m)$ and $b'(x = x_m) = 0$ [cf. Fig. 3.1(a)]. It is interesting to note that x_m can be positive, zero or negative, depending on the choice of the two parameters $\mathcal{C}$ and x_0 (or $\lambda_1,\ \lambda_2,\ n$ and C).

On the other hand, in the current case the white and black hole horizons always exist, and are located, respectively, at

$$x_H^{\pm} = \pm\sqrt{\mathcal{D}^2 - x_0^2}. \tag{3.27}$$

Clearly, there exist the possibilities in which $|x_m| \le x_H^+$, or $|x_m| > x_H^+$. When $|x_m| \le x_H^+$, the throat is located in the region between the black and white hole horizons, in which we have $a(x) \le 0$, so the corresponding energy density and radial principal pressure in the region containing the throat are given by ρ^- and p_r^-. When $|x_m| > x_H^+$, the throat is located in the region where $a(x) > 0$, so the corresponding energy density and radial principal pressure at the throat are given by ρ^+ and p_r^+, respectively.

3.4.1.1 $x_H^- \le x_m \le x_H^+$

In this case, we find that $|x_m| \le x_H^+$ implies

$$(i)\ \ \alpha = 1, \qquad \text{or} \tag{3.28}$$

$$(ii)\ \ \beta \ge 1 + \frac{(\alpha - 1)^2}{2\alpha}, \tag{3.29}$$

where $\alpha \equiv \mathcal{C}/|x_0| > 0$. Since now the throat is located inside the black hole horizon, in which we have $a(x) < 0$, we need to use Eq.(3.19) to calculate the effective energy

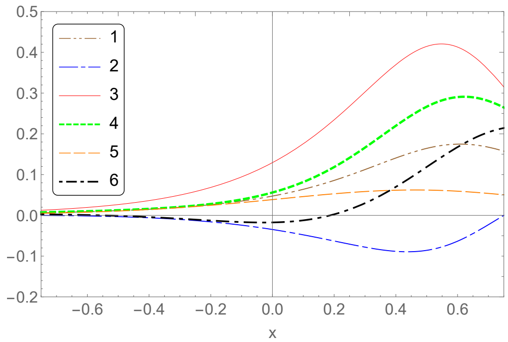

(a)

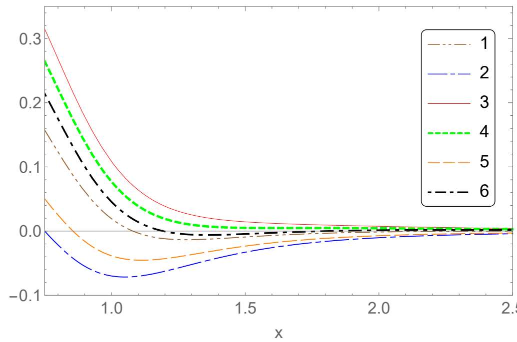

(b)

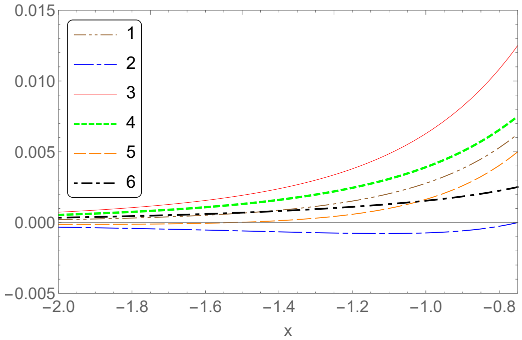

(c)

Figure 3.2: Case $\Delta > 0$, $\mathcal{D} > 0$, $|x_m| < x_H^+$, $\beta = 1 + \frac{(\alpha-1)^2}{2\alpha}, \alpha \neq 1$: The physical quantities, ρ, $(\rho + p_r)$, $(\rho - p_r)$, $(\rho + p_\theta)$, $(\rho - p_\theta)$, and $(\rho + p_r + 2p_\theta)$, represented, respectively, by Curves 1 - 6, vs x: When plotting these curves, we had set $\alpha = 2$, $\beta = 5/4$, $x_0 = 1$, so that the condition (3.33) is satisfied, for which we have $x_m = x_H^+ = -x_H^- = 0.75$. Panel (a): the physical quantities in the region between the white and black horizons, $x_H^- \leq x \leq x_H^+$. Panel (b): the physical quantities in the region outside the black horizon, $x \geq x_H^+ = 0.75$. Panel (c): the physical quantities in the region outside the white horizon, $x \leq x_H^- = -0.75$.

density ρ and pressure p_r at the throat, and find that

$$
\begin{aligned}
\rho &= \frac{1}{2^{2/3}\mathcal{C}^2}, \\
p_r &= -\frac{\mathcal{C}(12\mathcal{D} - 5\mathcal{C}) - 5x_0^2}{2^{2/3}\mathcal{C}^2\left(x_0^2 + \mathcal{C}^2\right)}, \\
p_\theta &= \frac{\left(x_0^2 + \mathcal{C}^2\right)^3 - 4\mathcal{D}x_0^2\mathcal{C}^3}{2^{2/3}\mathcal{C}^2\left(x_0^2 + \mathcal{C}^2\right)^3}.
\end{aligned} \tag{3.30}
$$

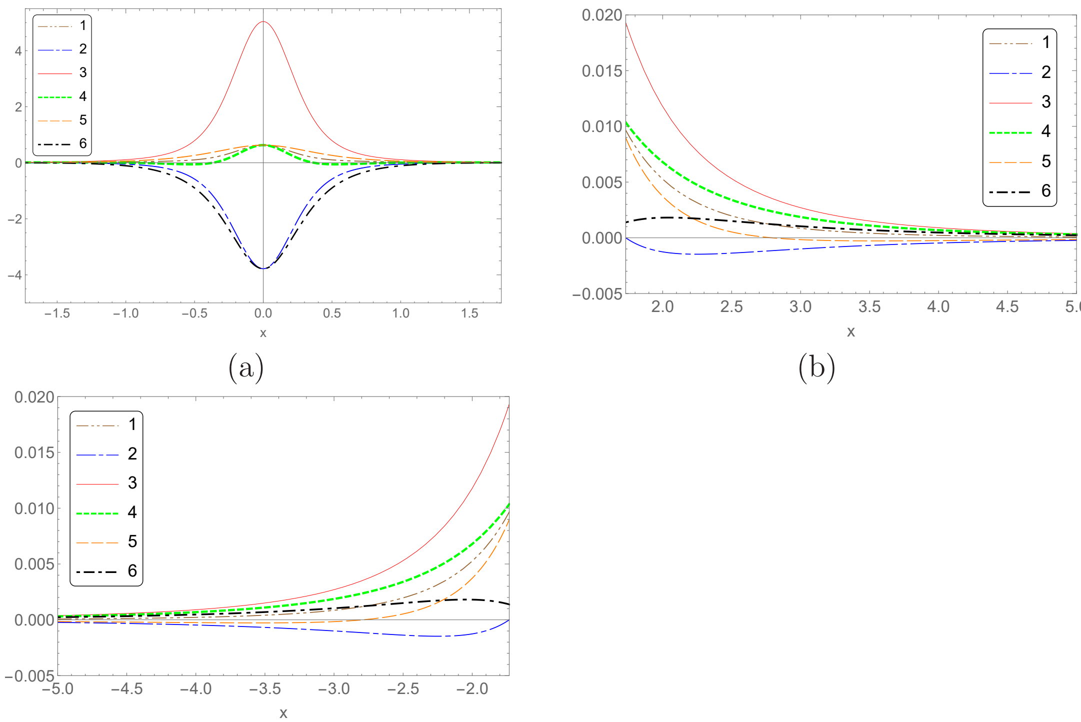

(a) (b)

(c)

Figure 3.3: Case $\Delta > 0$, $\mathcal{D} > 0$, $|x_m| < x_H^+$, $\beta \neq 1 + \frac{(\alpha-1)^2}{2\alpha}$: The physical quantities, ρ, $(\rho + p_r)$, $(\rho - p_r)$, $(\rho + p_\theta)$, $(\rho - p_\theta)$, and $(\rho + p_r + 2p_\theta)$, represented, respectively, by Curves 1 - 6, vs x: When plotting these curves, we had set $\alpha = 1$, $\beta = 2$, $x_0 = 1$, $x_H^\pm = \pm\sqrt{3}$, $x_m = 0$. None of the three energy conditions is satisfied at the throat, although all of them are satisfied at the two horizons $x = x_H^\pm$. Panel (a): the physical quantities in the region between the white and black horizons, $x_H^- \leq x \leq x_H^+$. Panel (b): the physical quantities in the region outside the black horizon, $x \geq x_H^+ = \sqrt{3}$. Panel (c): the physical quantities in the region outside the white horizon, $x \leq x_H^- = -\sqrt{3}$.

Then, we find that at the throat WEC is satisfied for

$$(a) \;\; \beta \leq 1 + \frac{(\alpha-1)^2}{2\alpha}, \qquad \text{or} \tag{3.31}$$

$$(b) \;\; \beta \leq \frac{1}{2}\alpha. \tag{3.32}$$

Combining Eqs.(3.28)-(3.29) with Eqs.(3.31)-(3.32) and considering Eq.(3.25), we find that their common solutions are

$$\beta = 1 + \frac{(\alpha-1)^2}{2\alpha}, \quad \alpha \neq 1, \tag{3.33}$$

which leads to $x_m = x_H^+$.

On the other hand, SEC is also satisfied in the domain given by Eq.(3.33), while DEC requires

$$(a)\ \ 0 < \alpha < 2\beta, \quad \beta \leq \frac{\alpha^2+1}{2\alpha} \leq \frac{3}{2}\beta, \quad \text{or} \tag{3.34}$$

$$(b)\ \ 2\beta \leq \alpha < 3\beta, \quad \beta \geq \frac{1+\alpha^2}{3\alpha}. \tag{3.35}$$

Combining Eqs.(3.28)-(3.29) with Eqs.(3.34)-(3.35), we find that their common solution is also given by Eq.(3.33).

Therefore, at the throat none of the three energy conditions is satisfied, except for the case in which the throat coincides with the black hole horizon, $x_m = x_H^+$, which is a direct result of the condition Eq.(3.33). In Fig. 3.2, we show this case, from which one can see that the three energy conditions are satisfied indeed only at the throat. In Fig. 3.3, we show the case that does not satisfy the condition Eq.(3.33), from which one can see that none of the three energy conditions is satisfied at the throat ($x_m = 0$).

In addition, if we consider the limit to the black hole horizon from outside of it, then we have $\rho = \rho^+$ and $p_r = p_r^+$, and the energy density and pressures are given, respectively, by

$$\begin{aligned}
\rho \ = \ & -p_r = -\frac{Y^3}{XZ^8}\Bigg[\Big(32\mathcal{D}^5\mathcal{C}^6 + 10\mathcal{D}x_0^{10} - 160\mathcal{D}^3x_0^8 \\
& +672\mathcal{D}^5x_0^6 - 1024\mathcal{D}^7x_0^4 + 2\mathcal{D}x_0^4\mathcal{C}^6 + 512\mathcal{D}^9x_0^2 \\
& -24\mathcal{D}^3x_0^2\mathcal{C}^6\Big)\sqrt{\Delta} + 32\mathcal{D}^6\mathcal{C}^6 - x_0^{12} + 50\mathcal{D}^2x_0^{10} \\
& -400\mathcal{D}^4x_0^8 + 1120\mathcal{D}^6x_0^6 - 1280\mathcal{D}^8x_0^4 + 10\mathcal{D}^2x_0^4\mathcal{C}^6 \\
& +512\mathcal{D}^{10}x_0^2 - 40\mathcal{D}^4x_0^2\mathcal{C}^6 + \mathcal{C}^{12}\Bigg],
\end{aligned} \tag{3.36}$$

$$
\begin{aligned}
p_\theta \;&=\; \frac{Y^2}{2X^2Z^8}\Bigg[\Big(128\mathcal{D}^7\mathcal{C}^6 + 2\mathcal{D}\mathcal{C}^{12} + 10\mathcal{D}x_0^{12} \\
&-160\mathcal{D}^3x_0^{10} + 672\mathcal{D}^5x_0^8 - 1024\mathcal{D}^7x_0^6 - 12\mathcal{D}x_0^6\mathcal{C}^6 \\
&+512\mathcal{D}^9x_0^4 + 88\mathcal{D}^3x_0^4\mathcal{C}^6 - 192\mathcal{D}^5x_0^2\mathcal{C}^6\Big)\sqrt{\Delta} \\
&+128\mathcal{D}^8\mathcal{C}^6 + 2\mathcal{D}^2\mathcal{C}^{12} - x_0^{14} + 50\mathcal{D}^2x_0^{12} \\
&-400\mathcal{D}^4x_0^{10} + 1120\mathcal{D}^6x_0^8 + 2x_0^8\mathcal{C}^6 - 1280\mathcal{D}^8x_0^6 \\
&-40\mathcal{D}^2x_0^6\mathcal{C}^6 + 512\mathcal{D}^{10}x_0^4 + 168\mathcal{D}^4x_0^4\mathcal{C}^6 \\
&-256\mathcal{D}^6x_0^2\mathcal{C}^6 - x_0^2\mathcal{C}^{12}\Bigg]. \qquad (3.37)
\end{aligned}
$$

It can be shown that each of the three energy conditions is satisfied provided that $\beta > 1$, which is precisely the condition $\Delta > 0$, as shown in Eq.(3.25). In addition, the surface gravity of the black hole is given by,

$$
\begin{aligned}
\kappa_{BH} \;&\equiv\; \frac{1}{2}a'(x=\sqrt{\Delta}) = \frac{Y^2\,|x_0|^7}{2Z^5} \\
&\times\Bigg[\sqrt{\beta^2-1}\,\Big(32\beta^6 - 48\beta^4 + 18\beta^2 - 1 + \alpha^6\Big) \\
&+2\beta\left(16\beta^6 - 32\beta^4 + 19\beta^2 - 3\right)\Bigg], \qquad (3.38)
\end{aligned}
$$

which is also always positive for $\beta > 1$.

At the white hole horizon ($x = -\sqrt{\Delta}$), taking the limit from the outside of it, so that $\rho = \rho^+$ and $p_r = p_r^+$, we find that

$$
\begin{aligned}
\rho \;&=\; -p_r = -\frac{Y}{\mathcal{D}Z^8}\Bigg(\Big[128\mathcal{D}^7\mathcal{C}^6 + 2\mathcal{D}\mathcal{C}^{12} - 12\mathcal{D}x_0^{12} + 280\mathcal{D}^3x_0^{10} - 1792\mathcal{D}^5x_0^8 \\
&+4608\mathcal{D}^7x_0^6 - 2\mathcal{D}x_0^6\mathcal{C}^6 - 5120\mathcal{D}^9x_0^4 + 48\mathcal{D}^3x_0^4\mathcal{C}^6 + 2048\mathcal{D}^{11}x_0^2 - 160\mathcal{D}^5x_0^2\mathcal{C}^6\Big]\sqrt{\Delta} \\
&-128\mathcal{D}^8\mathcal{C}^6 - 2\mathcal{D}^2\mathcal{C}^{12} - x_0^{14} + 72\mathcal{D}^2x_0^{12} - 840\mathcal{D}^4x_0^{10} + 3584\mathcal{D}^6x_0^8 - 6912\mathcal{D}^8x_0^6 \\
&+14\mathcal{D}^2x_0^6\mathcal{C}^6 + 6144\mathcal{D}^{10}x_0^4 - 112\mathcal{D}^4x_0^4\mathcal{C}^6 - 2048\mathcal{D}^{12}x_0^2 + 224\mathcal{D}^6x_0^2\mathcal{C}^6 + x_0^2\mathcal{C}^{12}\Bigg),
\end{aligned}
$$
(3.39)

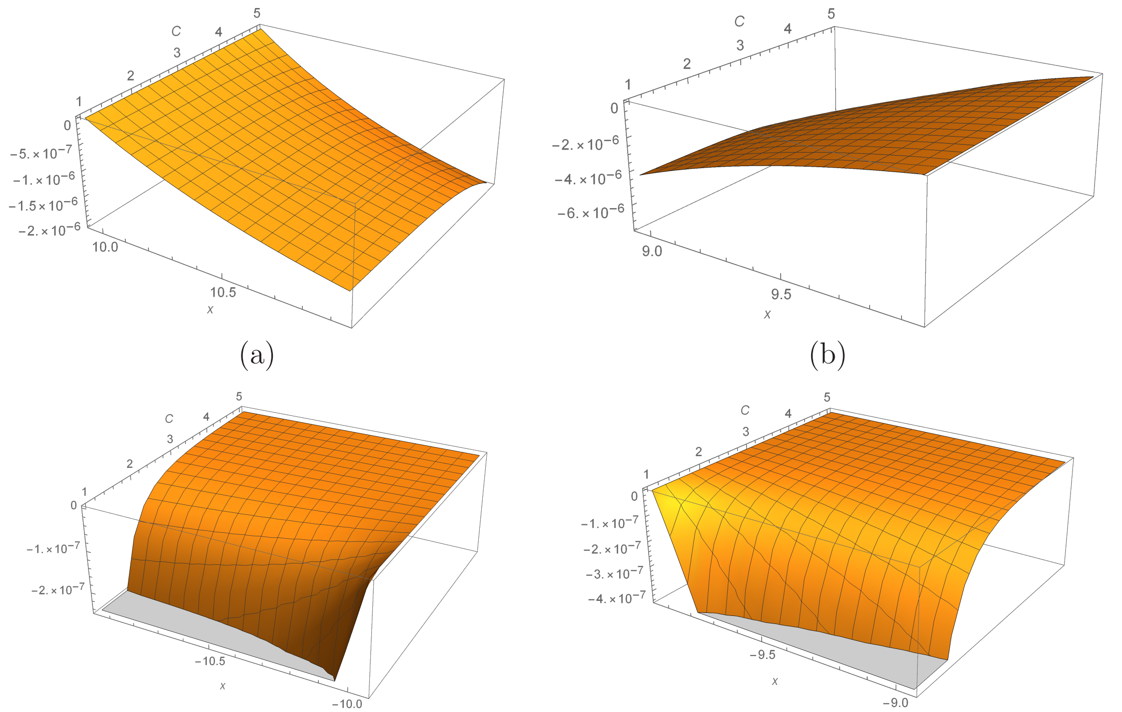

(a) (b) (c) (d)

Figure 3.4: The physical quantity $(\rho+p_r)$ vs the radial coordinate x and the parameter $\mathcal{C}$: (a) outside the black hole horizon; (b) inside the black hole horizon; (c) outside the white hole horizon; and (d) inside the white hole horizon. Graphs are plotted with $x_0=1,\ \mathcal{D}=10$, for which the horizons are at $x_H^{\pm}\approx\pm 10$.

$$\begin{aligned} p_\theta \;=\; \frac{Y^2}{2\mathcal{D}^2Z^8}\Bigg(&\Big[128\mathcal{D}^7\mathcal{C}^6+2\mathcal{D}\mathcal{C}^{12}+10\mathcal{D}x_0^{12}-160\mathcal{D}^3x_0^{10}+672\mathcal{D}^5x_0^8-1024\mathcal{D}^7x_0^6 \\ &-12\mathcal{D}x_0^6\mathcal{C}^6+512\mathcal{D}^9x_0^4+88\mathcal{D}^3x_0^4\mathcal{C}^6-192\mathcal{D}^5x_0^2\mathcal{C}^6\Big]\sqrt{\Delta}-128\mathcal{D}^8\mathcal{C}^6-2\mathcal{D}^2\mathcal{C}^{12} \\ &+x_0^{14}-50\mathcal{D}^2x_0^{12}+400\mathcal{D}^4x_0^{10}-1120\mathcal{D}^6x_0^8-2x_0^8\mathcal{C}^6+1280\mathcal{D}^8x_0^6+40\mathcal{D}^2x_0^6\mathcal{C}^6 \\ &-512\mathcal{D}^{10}x_0^4-168\mathcal{D}^4x_0^4\mathcal{C}^6+256\mathcal{D}^6x_0^2\mathcal{C}^6+x_0^2\mathcal{C}^{12}\Bigg). \end{aligned} \tag{3.40}$$

It can be shown that for $\beta>1$, all the three energy conditions are satisfied at the white hole horizon. Moreover, at this white hole horizon, the surface gravity is given by,

$$
\begin{aligned}
\kappa_{WH} &\equiv \frac{1}{2}a'(x=-\sqrt{\Delta}) \\
&= -\frac{Y^2}{2Z^5}\times\Bigg[\left(32\mathcal{D}^6 - x_0^6 + 18\mathcal{D}^2x_0^4 - 48\mathcal{D}^4x_0^2 + \mathcal{C}^6\right)\sqrt{\Delta} - 32\mathcal{D}^7 + 6\mathcal{D}x_0^6 \\
&\quad -38\mathcal{D}^3x_0^4 + 64\mathcal{D}^5x_0^2\Bigg],
\end{aligned}
\tag{3.41}
$$

which is always negative when the condition (3.25) holds.

In Figs. 3.2 and 3.3, we also show the physical quantities near the two horizons, and find that all the three energy conditions are indeed satisfied at these horizons, no matter whether Eq.(3.33) is satisfied or not. From these figures we can see that $\rho + p_r$ is the key quantity to determine the energy conditions. In particular, it is zero only at the two horizons and negative at other locations. Thus, the energy conditions are normally satisfied only at horizons. To show this more clearly, we plot $\rho + p_r$ vs x and the parameter $\mathcal{C}$ in Fig. 3.4, from which we can see that even with different choices of the free parameter, $\rho + p_r$ is non-negative only on the two horizons.

In addition, as $x \to \pm\infty$, we find that

$$
\begin{aligned}
\rho(x) &= \begin{cases} \frac{\mathcal{D}x_0^2}{8x^5} + \mathcal{O}\left(\epsilon^6\right), & x\to\infty, \\ -\frac{\mathcal{D}x_0^6}{8x^5\mathcal{C}^4} + \mathcal{O}\left(\epsilon^6\right), & x\to-\infty, \end{cases} \\
p_r(x) &= \begin{cases} -\frac{x_0^2}{4x^4} + \frac{\mathcal{D}x_0^2}{8x^5} + \mathcal{O}\left(\epsilon^6\right), & x\to\infty, \\ -\frac{x_0^6}{4x^4\mathcal{C}^4} - \frac{\mathcal{D}x_0^6}{8x^5\mathcal{C}^4} + \mathcal{O}\left(\epsilon^6\right), & x\to-\infty, \end{cases} \\
p_\theta(x) &= \begin{cases} \frac{x_0^2}{4x^4} - \frac{\mathcal{D}x_0^2}{4x^5}, & x\to\infty, \\ \frac{x_0^6}{4x^4\mathcal{C}^4} + \frac{\mathcal{D}x_0^6}{4x^5\mathcal{C}^4} + \mathcal{O}\left(\epsilon^6\right), & x\to-\infty, \end{cases}
\end{aligned}
\tag{3.42}
$$

where $\epsilon \equiv 1/|x|$. Thus, in these two asymptotically flat regions, none of these three energy conditions holds. On the other hand, at these limits, we also have,

$$
\begin{aligned}
a(x) &= \begin{cases} \frac{1}{4}\left(1-\frac{2\mathcal{D}}{b}\right)+\mathcal{O}\left(\epsilon^2\right), & x\to\infty, \\ \frac{x_0^4}{4\mathcal{C}^4}\left(1-\frac{\left(2\mathcal{D}\mathcal{C}^2/x_0^2\right)}{b}\right)+\mathcal{O}\left(\epsilon^2\right), & x\to-\infty, \end{cases} \\
b(x) &\simeq \begin{cases} 2x, & x\to\infty, \\ -2\left(\mathcal{C}^2/x_0^2\right)x, & x\to-\infty, \end{cases}
\end{aligned}
\tag{3.43}
$$

from which we find that the masses of the black and white holes are given, respectively, by

$$
M_{BH} = \mathcal{D}, \quad M_{WH} = \frac{\mathcal{D}\mathcal{C}^2}{x_0^2}. \tag{3.44}
$$

To study the quantum gravitational effects further, let us turn to consider the Ricci scalar R and the relative difference $\Delta\mathcal{K}$ of the Kretschmann scalar, defined by

$$
\Delta\mathcal{K} \equiv \frac{\mathcal{K}-\mathcal{K}^{GR}}{\mathcal{K}^{GR}}, \tag{3.45}
$$

where $\mathcal{K}^{GR}$ denotes the Kretschmann scalar of the Schwarzschild solution, given by,

$$
\mathcal{K}^{GR} \equiv R_{\alpha\beta\mu\nu}R^{\alpha\beta\mu\nu} = \begin{cases} \frac{48M_{BH}^2}{b^6(x)}, & x > x_m, \\ \frac{48M_{WH}^2}{b^6(x)}, & x < x_m. \end{cases} \tag{3.46}
$$

In GR, we have $R^{GR}=0$, But due to the quantum geometric effects, clearly now we have $R\neq 0$. Therefore, both quantities, R and $\Delta\mathcal{K}$, will describe the deviations of the quantum black holes from the classical one. Before proceeding further, we would like to point out that Eqs.(3.45) and (3.46) are applicable when the two horizons and asymptotic regions exist. In some particular cases, this is not true, and a proper modification for $\Delta\mathcal{K}$ is needed, as to be shown below.

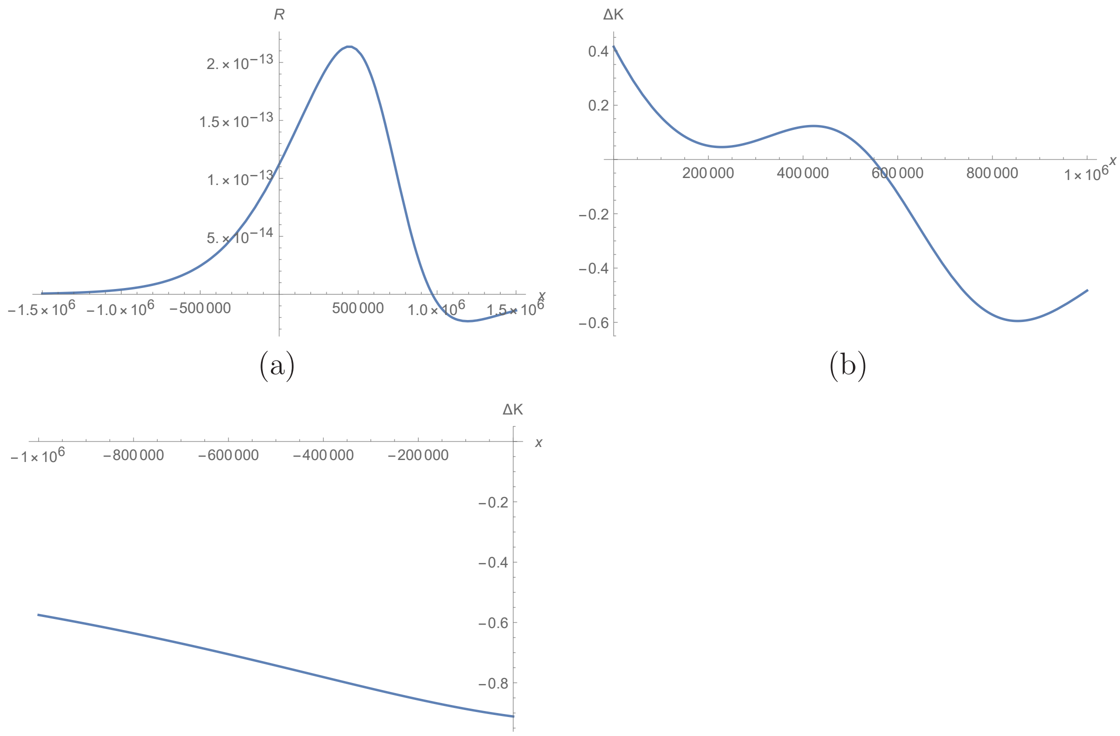

(a) (b) (c)

Figure 3.5: Case $\Delta > 0,\ \mathcal{D} > 0,\ |x_m| \leq x_H^+,\ \beta = 1 + \frac{(\alpha-1)^2}{2\alpha}, \alpha \neq 1$: The quantities R and $\Delta\mathcal{K}$ vs x. Here we choose $\mathcal{C} = 2 \times 10^6,\ x_0 = 10^6,\ \mathcal{D} = \frac{5}{4} \times 10^6$, for which the horizons are located at $x_H^{\pm} = \pm 0.75 \times 10^6$, and the throat is at $x_m = x_H^+$, while the black and white hole masses are $M_{BH} = \frac{5}{4} \times 10^6\ M_{Pl}$ and $M_{WH} = 5 \times 10^6\ M_{Pl}$, respectively.

In addition, another important quantity is the scalar

$$C_{\mu\nu\alpha\beta}C^{\mu\nu\alpha\beta} = \mathcal{K}^2 + \frac{1}{3}R^2 - 2R_{\mu\nu}R^{\mu\nu}, \tag{3.47}$$

where $C_{\mu\nu\alpha\beta}$ denotes the Weyl tensor. However, for the sake of simplicity, in the following we shall consider only the quantities $\Delta\mathcal{K}$ and R, which are sufficient for our current purpose.

In Fig. 3.5, the quantities R and $\Delta\mathcal{K}$ are plotted in the region between the two horizons ($x_H^{\pm} = \pm 0.75 \times 10^6$), from which it can be seen that the deviation from GR are still large near these two horizons, although the curvature decays rapidly when away from them in both directions. In particular, for $M_{BH} = 2 \times 10^6\ M_{Pl}$ and

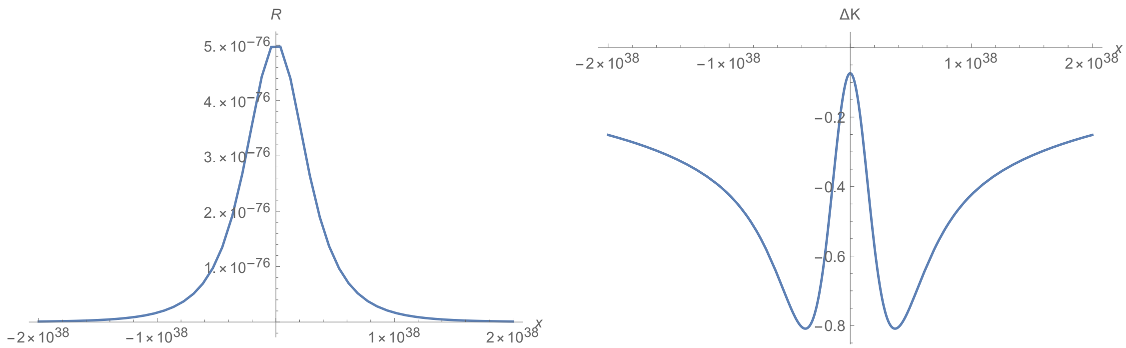

(a) (b)

Figure 3.6: Case $\Delta > 0$, $\mathcal{D} > 0$, $|x_m| < x_H^+$, $\beta \neq 1 + \frac{(\alpha-1)^2}{2\alpha}$: The quantities R and $\Delta\mathcal{K}$ vs x. Here we choose $\mathcal{C} = 10^{38}$, $x_0 = 10^{38}$, $\mathcal{D} = 2 \times 10^{38}$, for which the horizons are located at $x_H^{\pm} = \pm\sqrt{3} \times 10^{38}$, and the throat is at $x_m = 0$, while the black and white hole masses are $M_{BH} = 2 \times 10^{38}\ M_{Pl}$ and $M_{WH} = 2 \times 10^{38}\ M_{Pl}$, respectively.

$M_{WH} = 32 \times 10^6\ M_{Pl}$, near the horizons we find that $R(x_H^+) \lesssim 10^{-13}$, $R(x_H^-) \lesssim 10^{-14}$, and $\left|\Delta\mathcal{K}(x_H^+)\right| \lesssim 0.50$, $\left|\Delta\mathcal{K}(x_H^-)\right| \lesssim 0.65$, respectively. This is because now the throat coincides with the black hole horizon ($x_m = x_H^+ = 0.75 \times 10^6$), and to keep the throat open, the quantum effects at this point must be strong enough.

In Fig. 3.6, we plot R and $\Delta\mathcal{K}$ in the region that covers the throat ($x_m = 0$) as well as the two horizons ($x_H^{\pm} = \pm\sqrt{3} \times 10^{38}$). Thus, in the current case the throat is located far away from both of the two horizons. But, the deviations of the curvature near the two horizons are still large. In particular, we find that $R(x_H^+) \lesssim 10^{-76}$, $R(x_H^-) \lesssim 10^{-76}$, and $\left|\Delta\mathcal{K}(x_H^+)\right| \lesssim 0.2$ and $\left|\Delta\mathcal{K}(x_H^-)\right| \lesssim 0.2$ for solar mass $M_{BH} = 2 \times 10^{38}\ M_{Pl}$ and $M_{WH} = 2 \times 10^{38}\ M_{Pl}$. Therefore, in the current model the quantum gravitational effects can be still large near the horizons even for astrophysical black holes. More detailed analyses show that this is due to the fact that in the current case both x_0 and $\mathcal{C}$ are large ($x_0 = \mathcal{C} = 10^{38}$). Since large x_0 and $\mathcal{C}$ implies large λ_1 and λ_2, as one can see from the relations $\mathcal{C} \equiv (16C^2\lambda_1^2)^{1/6}$ and $x_0 \equiv \frac{\lambda_2}{\sqrt{n}}$. As mentioned above, the two parameters λ_1, λ_2 control quantum gravitational corrections. In particular, large λ_1 and λ_2 will lead to large quantum effects.

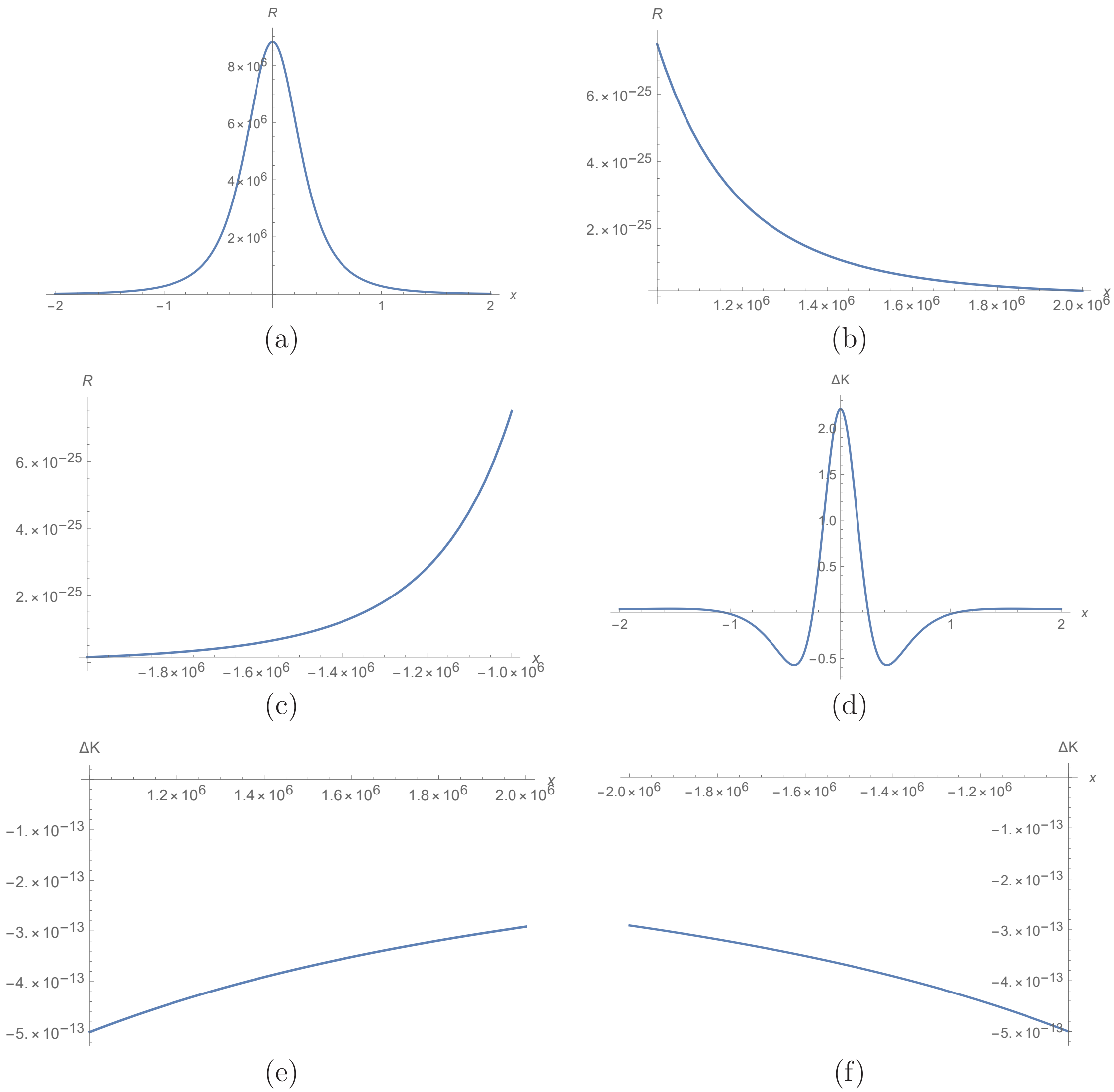

Figure 3.7: Case $\Delta > 0$, $\mathcal{D} > 0$, $|x_m| \leq x_H^+, \beta \neq 1 + \frac{(\alpha-1)^2}{2\alpha}$: The quantities R and $\Delta\mathcal{K}$ vs x. Here we choose $\mathcal{C} = 1$, $x_0 = 1$, $\mathcal{D} = 2 \times 10^6$, for which the throat is at $x_m = 0$ and the black/white hole horizons are located at $x_H^{\pm} \approx \pm 2 \times 10^6$, respectively. The black and white hole masses are $M_{BH} = M_{WH} = 2 \times 10^6 \ M_{Pl}$.

Therefore, to have negligible quantum gravitational effects, we must consider the cases where λ_1 and λ_2 are effectively small. In Fig. 3.7, we plot R and $\Delta\mathcal{K}$ in the region between the two horizons for $\mathcal{C} = 1,\ x_0 = 1,\ \mathcal{D} = 2 \times 10^6$, for which the horizons are located at $x_H^{\pm} \approx \pm 2 \times 10^6$, and the throat is at $x_m = 0$, while the black and white hole masses are $M_{BH} = M_{WH} = 2 \times 10^6\ M_{Pl}$. From this figure we can see that now the deviations from GR decays rapidly when away from the throat in both directions, and near the two horizons the quantum effects already become extremely small. In fact, near the two horizons now we find that $R(x_H^+) \lesssim 10^{-25},\ R(x_H^-) \lesssim 10^{-25}$, and $\left|\Delta\mathcal{K}(x_H^+)\right| \lesssim 10^{-13}$ and $\left|\Delta\mathcal{K}(x_H^-)\right| \lesssim 10^{-13}$. Therefore, in the current case, the quantum gravitational effects are mainly concentrated in the neighborhood of the throat.

On the other hand, in Fig. 3.8 we plot R and $\Delta\mathcal{K}$ in the region between the two horizons for $\mathcal{C} = 10^{-6},\ x_0 = 1,\ \mathcal{D} = 10^6$, for which the horizons are located at $x_H^{\pm} \approx \pm 10^6$, and the throat is at $x_m \approx -\frac{1}{2} \times 10^6$, while the black and white hole masses are $M_{BH} = 10^6\ M_{Pl},\ M_{WH} = 10^{-6}\ M_{Pl}$, respectively. From this figure we can see that now the deviations from GR decays rapidly when away from the throat only in the black hole direction, that is, only for $x > x_H^+$, and near the white hole horizon the quantum effects become very large again. In fact, near the two horizons now we find that $R(x_H^+) \lesssim 10^{-25},\ R(x_H^-) \simeq 10^{10}$, and $\left|\Delta\mathcal{K}(x_H^+)\right| \lesssim 10^{-12}$ and $\left|\Delta\mathcal{K}(x_H^-)\right| \simeq 0.05$. Thus, in the current case the quantum gravitational effects are negligible only at the black hole horizon but still very large at the white hole horizon. This is due to the fact that the throat is now very close to the white hole horizon.

The above examples show clearly that, depending on the values of the three free parameters $\mathcal{C},\ \mathcal{D},\ x_0$ (or $\mathcal{D},\ \lambda_1,\ \lambda_2$), quantum gravitational effects can be large, even for the cases in which the black/white hole masses are of order of solar masses.

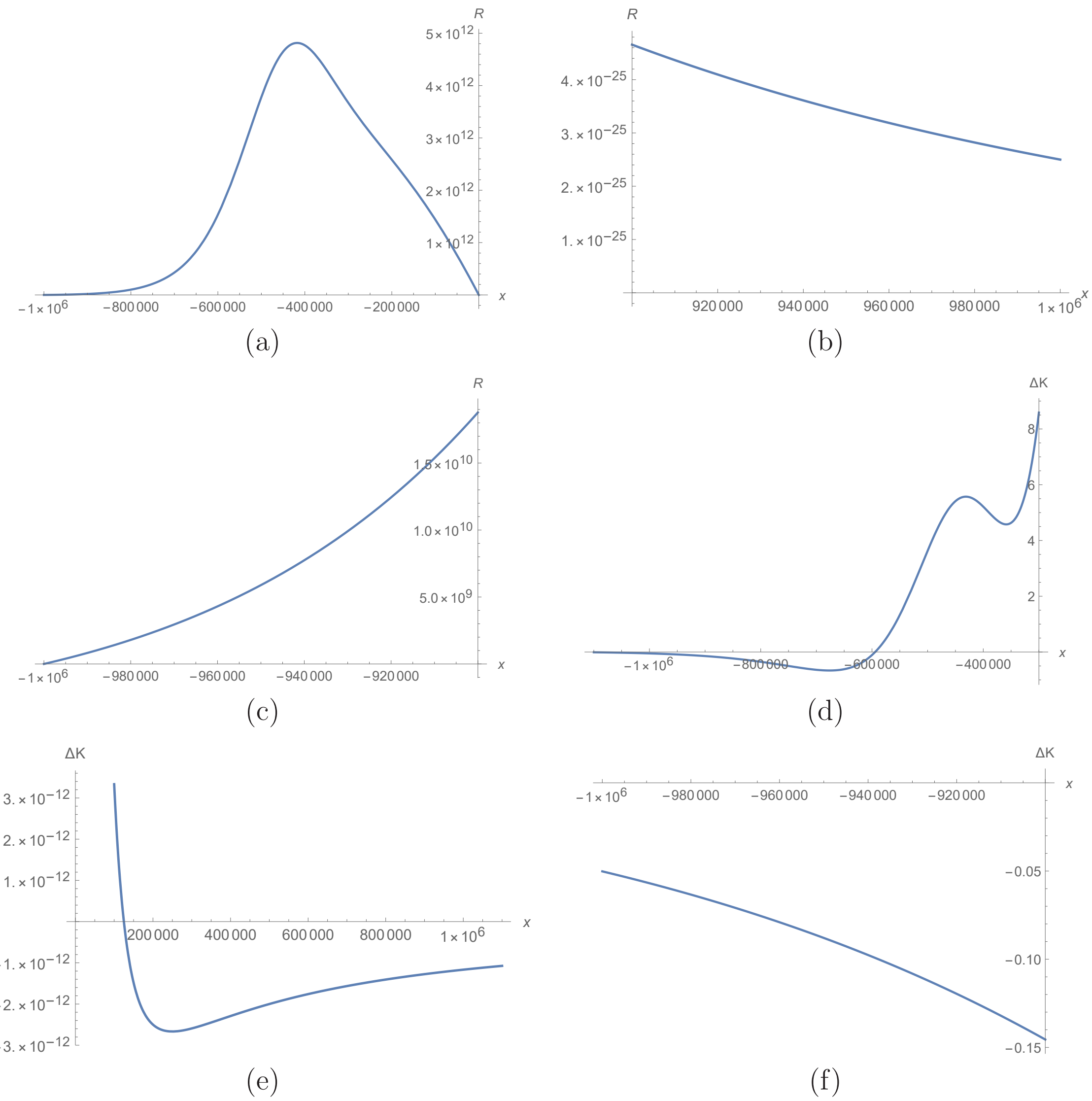

Figure 3.8: Case $\Delta > 0,\ \mathcal{D} > 0,\ |x_m| \leq x_H^+, \beta \neq 1 + \frac{(\alpha-1)^2}{2\alpha}$: The quantities R and $\Delta\mathcal{K}$ vs x. Here we choose $\mathcal{C} = 10^{-6},\ x_0 = 1,\ \mathcal{D} = 10^6$, for which the throat is at $x_m \approx -\frac{1}{2} \times 10^6$ and the black/white hole horizons are located at $x_H^{\pm} \approx \pm 10^6$, respectively. The black and white hole masses are $M_{BH} = 10^6\ M_{Pl}$, $M_{WH} = 10^{-6}\ M_{Pl}$.

In particular, near the two horizons $x = x_H^{\pm}$, we find

$$R = \begin{cases} -\frac{x_0^6}{\mathcal{D}^2\left(2\mathcal{D}\left(\sqrt{\mathcal{D}^2 - x_0^2} - \mathcal{D}\right) + x_0^2\right)\mathcal{R}_H^+}, & x = x_H^+, \\ \frac{x_0^6}{\mathcal{D}^2\left(2\mathcal{D}\left(\mathcal{D} + \sqrt{\mathcal{D}^2 - x_0^2}\right) - x_0^2\right)\mathcal{R}_H^-}, & x = x_H^-, \end{cases} \tag{3.48}$$

where $\mathcal{R}_H^{\pm} \equiv \left(\left(\mathcal{D} \pm \sqrt{\mathcal{D}^2 - x_0^2}\right)^6 + \mathcal{C}^6\right)^{2/3}$. Thus, for $\mathcal{D} \gg |x_0|$, we have

$$R \;\simeq\; \begin{cases} \frac{4x_0^2}{[(2\mathcal{D})^6+\mathcal{C}^6]^{2/3}}, & x = x_H^+, \\ \frac{x_0^6}{4\mathcal{D}^4\mathcal{C}^4}, & x = x_H^-. \end{cases} \tag{3.49}$$

Therefore, to have the effects negligibly small near the two horizons, we must require

$$\mathcal{C} \gtrsim |x_0|, \quad \mathcal{D} \gg |x_0|. \tag{3.50}$$

On the other hand, as $x \to \pm\infty$, we find that

$$R \;\simeq\; \begin{cases} -\frac{x_0^2}{4x^4} + \frac{\mathcal{D}x_0^2}{2x^5} + \mathcal{O}\left(\epsilon^6\right), & x \to \infty, \\ -\frac{x_0^6}{4x^4\mathcal{C}^4} - \frac{\mathcal{D}x_0^6}{2x^5\mathcal{C}^4} + \mathcal{O}\left(\epsilon^6\right), & x \to -\infty, \end{cases} \tag{3.51}$$

and

$$\Delta\mathcal{K} \;\simeq\; \begin{cases} -\frac{4x_0^2}{3M_{BH}x} + \mathcal{O}\left(\epsilon^2\right), & x \to \infty, \\ +\frac{4\mathcal{C}^2}{3M_{WH}x} + \mathcal{O}\left(\epsilon^2\right), & x \to -\infty, \end{cases} \tag{3.52}$$

where M_{BH} and M_{WH} are given by Eq.(3.44). Then, we have $|\Delta\mathcal{K}_+/\Delta\mathcal{K}_-| = 1 + \mathcal{O}\left(\epsilon^2\right)$, as $|x| \to \infty$. That is, whether $M_{WH} \gg M_{BH}$ or not, $|\Delta\mathcal{K}_+|$ will always have the same asymptotic magnitude as $|\Delta\mathcal{K}_-|$, and both of them approach their GR limits as $\mathcal{O}(1/|x|)$.

Therefore, in the present case we find the following:

- The throat is always located in the region between the black and white hole horizons, $x_H^- \leq x_m \leq x_H^+$, and each of the three energy conditions, WEC, DEC, and SEC, is satisfied at the throat only in the case where the condition (3.33) holds. In this case the quantum gravitational effects are always large at the black hole horizon $x = x_H^+$. This is expected, as at the throat the quantum effects need to be strong, in order to keep the throat open, and when the condition (3.33) is satisfied, the black hole horizon always coincides with the throat, $x_m = x_H^+$.

- Even the condition (3.33) does not hold, and the throat is far from both of the white and black hole horizons, that is, $|x_m| \ll \left|x_H^{\pm}\right|$, the quantum gravitational effects can be still large at the two horizons, including the cases in which both of the white and black hole masses are large, $M_{BH},\ M_{WH} \gg 10^6\ M_{Pl}$. Only in the case where the conditions (3.50) hold, can the effects become negligible at the two horizons.
- In general, none of the three energy conditions is satisfied in the neighborhoods of the white and black hole horizons, $x = x_H^{\pm}$, except precisely at these two surfaces. However, the surface gravity at the black (white) hole horizon is always positive (negative), as now the condition $\rho + p_r + 2p_\theta > 0$ is still satisfied in the most part of the spacetime [21], as can be seen from Figs. 3.2 and 3.3. So, the trapped region ($x_H^- < x < x_H^+$) is still attractive to observers outside of it.
- In the two asymptotically flat regions $x \to \pm\infty$, for which the geometrical radius becomes infinitely large, $b(\pm\infty) = \infty$, none of the three energy conditions is satisfied.
- The black and white hole masses read off from these two asymptotically flat regions are given by Eq.(3.44), which are always positive, no matter the condition (3.33) is satisfied or not. Again, this is because the relativistic Komar mass density $\rho + p_r + 2p_\theta$ is still positive in a large part of the spacetime. As a result, the total masses of the spacetime read off at the two asymptotically flat region are positive.

It should be noted that the absence of spacetime singularities in this case does not contradict to the Hawking-Penrose singularity theorems [20], as now none of the three energy conditions is satisfied in the two asymptotically flat regions, including the case in which the condition (3.33) holds, as shown in the above explicitly.

3.4.1.2 $|x_m| > x_H^+$

Now, let us turn to consider the case $|x_m| > x_H^+$, which implies that

$$\beta < 1 + \frac{(\alpha - 1)^2}{2\alpha}. \tag{3.53}$$

In this case, since the throat is located in the region where $a(x) > 0$, then at the throat we have $\rho = \rho^+$ and $p_r = p_r^+$. Hence, from Eq.(3.18) we find that the effective energy density ρ and pressures p_r and p_θ at the throat are given by

$$\begin{aligned}
\rho &= \frac{\mathcal{C}(12\mathcal{D} - 5\mathcal{C}) - 5x_0^2}{2^{2/3}\mathcal{C}^2\left(x_0^2 + \mathcal{C}^2\right)}, \\
p_r &= -\frac{1}{2^{2/3}\mathcal{C}^2}, \\
p_\theta &= \frac{\left(x_0^2 + \mathcal{C}^2\right)^3 - 4\mathcal{D}x_0^2\mathcal{C}^3}{2^{2/3}\mathcal{C}^2\left(x_0^2 + \mathcal{C}^2\right)^3}.
\end{aligned} \tag{3.54}$$

From these expressions, we find that in the 3D parameter space, WEC is satisfied when,

$$\beta \geq 1 + \frac{(\alpha - 1)^2}{2\alpha}, \quad \text{and} \quad \beta > \frac{1}{2}\alpha. \tag{3.55}$$

Clearly, these conditions contradict to the condition $|x_m| > x_H^+$, as it can be seen from Eq.(3.53). Therefore, in the current case WEC is always violated at the throat. In addition, for ρ, p_r and p_θ given by Eq.(3.54), we also find that neither DEC nor SEC is satisfied, after the conditions (3.53) are taken into account. Therefore, in the current case, *none of the three energy conditions is satisfied at the throat.*

On the other hand, following the analyses provided in the last subsection, it can be also shown that in the current case the following is true: (i) All the three energy conditions are not satisfied generically in the regions near the black hole and white hole horizons in the whole 3D phase space. But, the surface gravity at the black (white) hole horizon can be still positive (negative), as the relativistic Komar mass density can be still positive over a large region of the spacetime, so that its integration over the 3D spatial space can be positive, $\int_V (\rho + p_r + 2p_\theta)\, dV > 0$. (ii) In the two asymptotically flat regions $x \to \pm\infty$, none of the three energy conditions is satisfied for any given values of $\mathcal{C}$, $\mathcal{D}$ and x_0, as longer as the condition (3.25) holds, which is resulted from the condition $\Delta > 0$. (iii) The black/white hole masses are also given by Eq.(3.44), which are all positive in the current case, too. (iv) The quantum effects are mainly concentrated near the throat. Since now the throat is always located either outside the black hole horizon ($x_m > x_H^+$) or outside the white hole horizon ($x_m < x_H^-$), the quantum effects can be large near the two horizons, even for the cases where the white/black hole masses are of order of solar masses.

It should be noted that the above analysis is not valid for the limit cases $x_0 \to 0$ and $\mathcal{C} \to 0$. So, in the following, let us consider these particular cases, separately.

3.4.1.3 $x_0 = 0,\ \mathcal{C} \neq 0$

If we assume that $\lambda_2 \neq 0$, from Eq.(3.9) we can see that this corresponds to the limit $\sqrt{n} \to \infty$. However, to keep $\mathcal{D} > 0$ and finite, we must require $D/\sqrt{n} \to$ finite and $CD > 0$. Then, we find that $\Delta = \mathcal{D}^2$, and from Eq.(3.12) we find $X = |x|$, and

$$Y = x + |x| = \begin{cases} 2x, & x \geq 0, \\ \\ 0, & x < 0. \end{cases} \tag{3.56}$$

Hence, Eq.(3.11) implies $a(x) = 0$ and $b(x) = \infty$ for $x \leq 0$, that is, the metric becomes singular for $x \leq 0$. However, since $b(0) = \infty$, it is clear that now $x = 0$ already represents the spatial infinity. Therefore, in this case we only need to consider the region $x \in (0, \infty)$ [cf. Fig. 3.1(b)]. Then, we find that

$$X = x, \ \ Y = 2x, \ \ Z = 4\left(x^6 + \hat{\mathcal{C}}^6\right)^{1/3}, \ (x \geq 0), \tag{3.57}$$

where $\hat{\mathcal{C}} \equiv \mathcal{C}/2$, and

$$\begin{aligned} a(x) &= \frac{x^3\,(x - \mathcal{D})}{4\left(x^6 + \hat{\mathcal{C}}^6\right)^{2/3}}, \\ b(x) &= \frac{2}{x}\left(x^6 + \hat{\mathcal{C}}^6\right)^{1/3}. \end{aligned} \tag{3.58}$$

Clearly, $a(x) = 0$ leads to two roots,

$$x_H^- = 0, \quad x_H^+ = \mathcal{D}, \tag{3.59}$$

while the minimum of $b(x)$ now is located at $x_m \equiv \hat{\mathcal{C}}$, so we have

$$b(x) = \begin{cases} \infty, & x = 0, \\ \\ 2^{4/3}\hat{\mathcal{C}}, & x = \hat{\mathcal{C}}, \\ \\ \infty, & x = \infty. \end{cases} \tag{3.60}$$

It is interesting to note that the outer (black hole) horizon located at $x = x_H^+$ can be smaller than the throat $x = x_m$, that is, $\hat{\mathcal{C}} > \mathcal{D}$. In addition, the spacetime becomes antitrapped at $x_H^- = 0$. Since $b(x = 0) = \infty$, this antitrapped point now also corresponds to the spatial infinity at the other side (the white hole side) of the throat.

To study the solutions further, in the following let us consider the cases $\mathcal{D} \geq \hat{\mathcal{C}}$ and $\mathcal{D} < \hat{\mathcal{C}}$, separately.

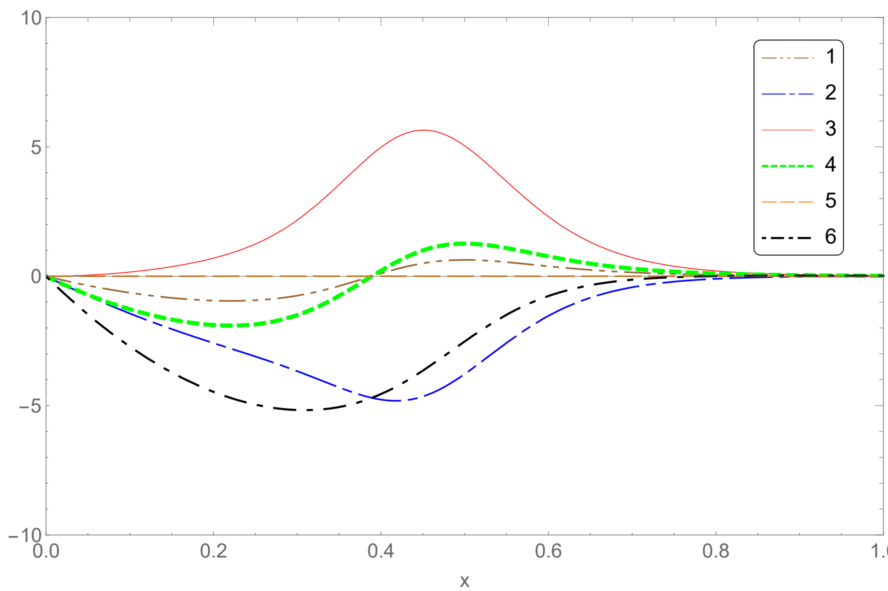

Figure 3.9: Case $\Delta > 0$, $\mathcal{D} > 0$, $x_0 = 0$, $\mathcal{C} \neq 0$: The physical quantities, ρ, $(\rho + p_r)$, $(\rho - p_r)$, $(\rho + p_\theta)$, $(\rho - p_\theta)$, and $(\rho + p_r + 2p_\theta)$, represented, respectively, by Curves 1 - 6, vs x in the neighborhood of the throat. All curves are plotted with $\mathcal{C} = 1$, $\mathcal{D} = 1$, for which the throat is at $x_m = 0.5$, and the outer horizon is at $x_H^+ = 1$.

(Case III.3.1) $\mathcal{D} \geq \hat{\mathcal{C}}$*:* In this case the throat locates always inside the black hole horizon, so in the region $x < x_H^+$ we always have $a(x) < 0$, and the corresponding

effective energy density and pressures are given by

$$\begin{aligned}
\rho(x) &= \frac{\mathcal{C}^6\left[64\mathcal{D}x^6+\mathcal{C}^6(2x-\mathcal{D})\right]x}{2^{13}\left(x^6+\hat{\mathcal{C}}^6\right)^{8/3}},\\
p_r(x) &= -\frac{\mathcal{C}^6\left(\mathcal{D}\mathcal{C}^6-640x^7+704\mathcal{D}x^6\right)x}{2^{13}\left(x^6+\hat{\mathcal{C}}^6\right)^{8/3}},\\
p_\theta(x) &= \frac{\mathcal{C}^6\left[64\mathcal{D}x^6+\mathcal{C}^6(2x-\mathcal{D})\right]x}{2^{13}\left(x^6+\hat{\mathcal{C}}^6\right)^{8/3}}. \qquad (3.61)
\end{aligned}$$

In particular, at the throat ($x=\hat{\mathcal{C}}$), we have

$$\rho = p_\theta = \frac{1}{2^{2/3}\mathcal{C}^2},\quad p_r = \frac{5\mathcal{C}-12\mathcal{D}}{2^{2/3}\mathcal{C}^3}, \qquad (3.62)$$

from which we find that the WEC, SEC, and DEC are satisfied in the domain,

$$2\mathcal{D} \le \mathcal{C} \le 3\mathcal{D}. \qquad (3.63)$$

Combining Eq.(3.63) with $\mathcal{C}/2 \le \mathcal{D}$, we have $\mathcal{C}/2 = \mathcal{D}$, which implies that the effective energy-momentum tensor satisfies all the three energy conditions at the throat only when the location of the throat and location of the black hole horizon coincide.

In Fig. 3.9 we plot the physical quantities $\rho,\ \rho \pm p_r,\ \rho \pm p_\theta$ and $\rho + p_r + 2 \pm p_\theta$ in the neighborhood of the throat.

In addition, as $x \to 0$ (or $b(x) \to \infty$), we find that

$$\begin{aligned}
\rho &= p_\theta = -\frac{8\mathcal{D}x}{\mathcal{C}^4} + \frac{16x^2}{\mathcal{C}^4} + \mathcal{O}\left(x^3\right),\\
p_r &= -\frac{8\mathcal{D}x}{\mathcal{C}^4} + \mathcal{O}\left(x^3\right), \qquad (3.64)
\end{aligned}$$

from which we find that the WEC, SEC, and DEC are satisfied only at $x=0$.

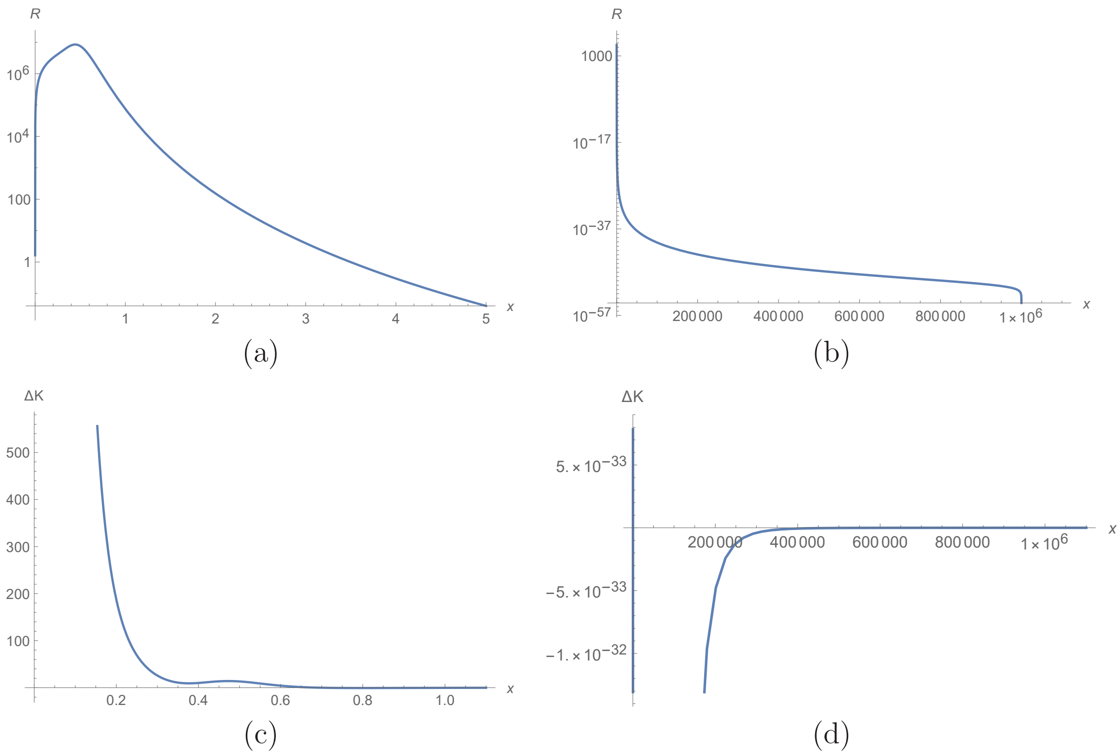

Figure 3.10: Case $\Delta > 0,\ \mathcal{D} > 0,\ x_0 = 0,\ \mathcal{C} \neq 0$: The physical quantities R and $\Delta\mathcal{K}$. Here we choose $\mathcal{C} = 1,\ \mathcal{D} = 10^6$, so that $M_{BH} = 10^6\ M_{Pl},\ x_H^+ = \mathcal{D} = 10^6,\ x_m = \hat{\mathcal{C}} = 1/2$.

On the other hand, outside of the black hole horizon ($x > x_H^+$), we always have $a(x) > 0$, and the corresponding effective energy density and pressures are given by

$$\begin{aligned}
\rho(x) &= \frac{\mathcal{C}^6\left(\mathcal{D}\mathcal{C}^6 - 640x^7 + 704\mathcal{D}x^6\right)x}{2^{13}\left(x^6 + \hat{\mathcal{C}}^6\right)^{8/3}}, \\
p_r(x) &= -\frac{\mathcal{C}^6\left[64\mathcal{D}x^6 + \mathcal{C}^6(2x - \mathcal{D})\right]x}{2^{13}\left(x^6 + \hat{\mathcal{C}}^6\right)^{8/3}}, \\
p_\theta(x) &= \frac{\mathcal{C}^6\left[64\mathcal{D}x^6 + \mathcal{C}^6(2x - \mathcal{D})\right]x}{2^{13}\left(x^6 + \hat{\mathcal{C}}^6\right)^{8/3}}.
\end{aligned} \tag{3.65}$$

In particular, at the black hole horizon ($x_H^+ = \mathcal{D}$), we have

$$\rho = -p_r = p_\theta = \frac{8\mathcal{D}^2\mathcal{C}^6}{\left(64\mathcal{D}^6 + \mathcal{C}^6\right)^{5/3}}, \tag{3.66}$$

so all the three energy conditions, WEC, SEC, and DEC, are satisfied at the black hole horizon. The surface gravity now is given by,

$$\kappa_{BH} \equiv \frac{1}{2} a'(x = \mathcal{D}) = \frac{2\mathcal{D}^3}{(64\mathcal{D}^6 + \mathcal{C}^6)^{2/3}}, \tag{3.67}$$

which is always positive, as now we have $\mathcal{D} > 0$.

At the spatial infinity $x \to \infty$, we find

$$\begin{aligned} \rho &\approx -\frac{5\mathcal{C}^6}{64x^8} + \frac{11\mathcal{D}\mathcal{C}^6}{128x^9} + \mathcal{O}\left(\epsilon^{10}\right), \\ \rho + p_r &\approx -\frac{5\mathcal{C}^6}{64x^8} + \frac{5\mathcal{D}\mathcal{C}^6}{64x^9} + \mathcal{O}\left(\epsilon^{10}\right), \\ \rho + p_\theta &\approx -\frac{5\mathcal{C}^6}{64x^8} + \frac{3\mathcal{D}\mathcal{C}^6}{32x^9} + \mathcal{O}\left(\epsilon^{10}\right), \\ \rho + p_r + 2p_\theta &\approx -\frac{5\mathcal{C}^6}{64x^8} + \frac{3\mathcal{D}\mathcal{C}^6}{32x^9} + \mathcal{O}\left(\epsilon^{10}\right), \end{aligned} \tag{3.68}$$

from which we can see that none of the three energy conditions is satisfied. In addition, we also have

$$\begin{aligned} a(x) &= \begin{cases} \frac{1}{4}\left(1 - \frac{2\mathcal{D}}{b}\right) + \mathcal{O}\left(\epsilon^2\right), & x \to \infty, \\ -\frac{4\mathcal{D}x^3}{\mathcal{C}^4} + \frac{4x^4}{\mathcal{C}^4} + \mathcal{O}\left(x^6\right), & x \to 0, \end{cases} \\ b(x) &\simeq \begin{cases} 2x, & x \to \infty, \\ \frac{\mathcal{C}^2}{2x} + \frac{32x^5}{3\mathcal{C}^4} + \mathcal{O}\left(x^6\right), & x \to 0. \end{cases} \end{aligned} \tag{3.69}$$

Therefore, the mass of the black hole is given by

$$M_{BH} = \mathcal{D}. \tag{3.70}$$

To study the quantum gravitational effects further, in Fig. 3.10 we plot R and $\Delta\mathcal{K}$ in the region that covers the throat and the horizon, from which it can be seen that the deviation from GR quickly becomes vanishingly small around the horizon.

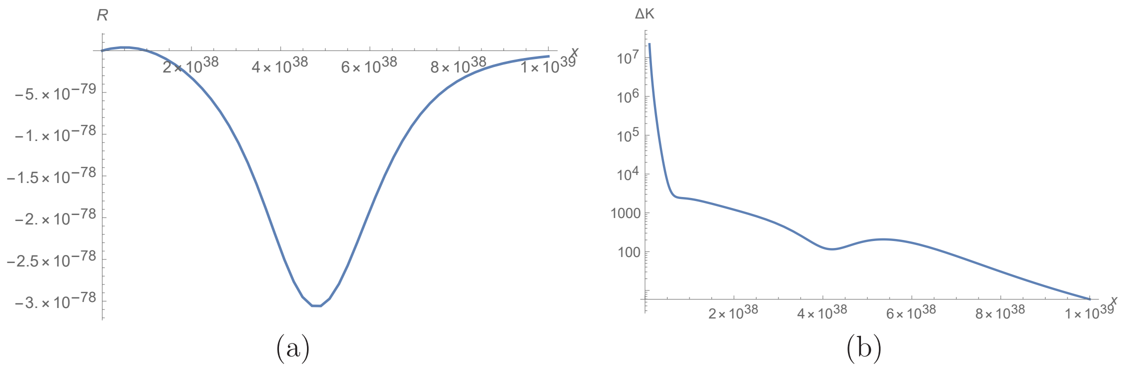

Figure 3.11: Case $\Delta > 0$, $\mathcal{D} > 0$, $x_0 = 0$, $x_m > x_H^+$, : The quantities R and $\Delta\mathcal{K}$ vs x. Here we choose $\mathcal{C} = 10^{39}$, $\mathcal{D} = 10^{38}$, for which the outer horizon is located at $x_H^+ = 10^{38}$, and the throat is at $x_m = 5 \times 10^{38}$, while the black hole mass is $M_{BH} = 10^{38}\ M_{Pl}$.

In addition, as $x \to \infty$, we find that

$$\begin{aligned} R &\simeq -\frac{20\mathcal{C}^6}{b^8} + \mathcal{O}\left(\epsilon^9\right), \\ \Delta\mathcal{K} &\simeq \frac{32\mathcal{C}^6}{3M_{BH}b^5} + \mathcal{O}\left(\epsilon^6\right), \end{aligned} \tag{3.71}$$

from which we can see that quantum corrections are decaying rapidly when $x \to \infty$.

When $x \to 0$ ($b \to \infty$), we have

$$\begin{aligned} R &\simeq \frac{8\mathcal{D}}{\mathcal{C}^2 b} + \mathcal{O}\left(b^{-2}\right), \\ \mathcal{K} &\simeq \frac{240\mathcal{D}^2}{\mathcal{C}^4 b^2} + \mathcal{O}\left(b^{-3}\right), \end{aligned} \tag{3.72}$$

which decays much less slowly than that in the Schwarzschild case, $\mathcal{K}^{GR} \to b^{-6}$. [3] It is even slower than that of the loop quantum black hole solution found by Ashtekar, Olmedo and Singh [9, 23], in which $R \to b^{-2}$ and $\mathcal{K} \to b^{-4}$ [25].

(Case III.3.2) $\mathcal{D} < \hat{\mathcal{C}}$: In this case the throat locates always outside the black hole horizon, so in the region $x > x_H^+$ we always have $a(x) > 0$, and the corresponding effective energy density and pressures are given by Eq.(3.65). In particular, at the

[3] In [17] a different conclusion was derived, as the authors implicitly assumed that $x_0\mathcal{C} \neq 0$. Therefore, our conclusion in this case does not essentially contradict to the one obtained in [17].

throat ($x = \hat{\mathcal{C}}$), we have

$$\rho = \frac{6\mathcal{D} - 5\hat{\mathcal{C}}}{2^{8/3}\hat{\mathcal{C}}^3}, \quad p_r = -p_\theta = -\frac{1}{2^{8/3}\hat{\mathcal{C}}^2}, \tag{3.73}$$

from which we find that the WEC, SEC, and DEC are satisfied in the domain,

$$0 < \mathcal{C}/2 < \mathcal{D}. \tag{3.74}$$

Combining Eq.(3.74) with $\mathcal{D} < \hat{\mathcal{C}}$, we find that in this case, all the energy conditions are violated at the throat.

In addition, as $x \to 0$ (or $b(x) \to \infty$), we still have Eq.(3.64), from which we find that the WEC, SEC, and DEC are satisfied only at $x = 0$. At the spatial infinity $x \to \infty$, we still have Eq.(3.68), from which we can see that none of the three energy conditions is satisfied. In addition, we also have Eq.(3.69), thus the mass of the black hole is given by Eq.(3.70).

For the quantum gravitational effects, we still have Eqs.(3.71) and (3.72). In Fig. 3.11 we plot R and $\Delta\mathcal{K}$ in the region that covers the throat and the horizon, from which it can be seen that the deviation from GR is still large around the horizon even for solar mass black holes, due to the fact that $\mathcal{C}$ is very large in this case and thus makes $\Delta\mathcal{K}$ large around horizon which can be seen from Eq.(3.71).

3.4.1.4 $\mathcal{C} = 0,\ x_0 \neq 0$

If we assume that $\lambda_1 \neq 0$, from Eq.(3.9) we can see that this corresponds to the limit $C \to 0$. However, to keep $\mathcal{D} > 0$ and finite, we must require $DC \to$ finite and positive. Thus, we have

$$a(x) = \frac{(x^2 - \Delta)\, X}{(X + \mathcal{D})\, Y^2}, \quad b(x) = Y. \tag{3.75}$$

Clearly, $a(x) = 0$ leads to two real roots,

$$x_H^{\pm} = \pm\sqrt{\Delta}, \tag{3.76}$$

while $b(x)$ is a monotonically increasing function with $b(x = -\infty) = 0$ [cf. Fig. 3.1(c)]. Therefore, in contrast to the above cases, now the spacetime is not asymptotically flat as $x \to -\infty$, but rather it represents the center of the spacetime, at which a spacetime curvature singularity appears, as to be shown below. Therefore, in the current case the spacetime represents a black hole with two horizons located at $x = \pm\sqrt{\Delta}$. This is quite similar to the charged Reissner-Nordström (RN) solution.

In the trapped region, $x_H^- < x < x_H^+$, the effective energy density and pressures are given by

$$\begin{aligned}
\rho(x) &= \frac{x_0^2 Y^3}{X^2 \left(Y^6\right)^{8/3}} \Bigg(\Big[1024x^{10} - 512\mathcal{D}x^9 + 2560x^8x_0^2 - 1024\mathcal{D}x^7x_0^2 + 2240x^6x_0^4 \\
&\quad -672\mathcal{D}x^5x_0^4 + 800x^4x_0^6 - 160\mathcal{D}x^3x_0^6 + 100x^2x_0^8 - 10\mathcal{D}xx_0^8 + 2x_0^{10}\Big] X \\
&\quad +1024x^{11} - 512\mathcal{D}x^{10} + 3072x^9x_0^2 - 1280\mathcal{D}x^8x_0^2 + 3392x^7x_0^4 - 1120\mathcal{D}x^6x_0^4 \\
&\quad +1664x^5x_0^6 - 400\mathcal{D}x^4x_0^6 + 340x^3x_0^8 - 50\mathcal{D}x^2x_0^8 + 20xx_0^{10} - \mathcal{D}x_0^{10} \Bigg), \\
p_r(x) &= -\frac{\mathcal{D}x_0^2 Y}{X^2 \left(Y^6\right)^{2/3}}, \\
p_\theta(x) &= \frac{x_0^2 Y^2}{2X^3 \left(Y^6\right)^{8/3}} \Bigg(\Big[4096x^{12} - 4096\mathcal{D}x^{11} + 13312x^{10}x_0^2 - 10752\mathcal{D}x^9x_0^2 + 16384x^8x_0^4 \\
&\quad -10240\mathcal{D}x^7x_0^4 + 9408x^6x_0^6 - 4256\mathcal{D}x^5x_0^6 + 2480x^4x_0^8 - 720\mathcal{D}x^3x_0^8 \\
&\quad +244x^2x_0^{10} - 34\mathcal{D}xx_0^{10} + 4x_0^{12}\Big] X + 4096x^{13} - 4096\mathcal{D}x^{12} + 15360x^{11}x_0^2 \\
&\quad -12800\mathcal{D}x^{10}x_0^2 + 22528x^9x_0^4 - 15104\mathcal{D}x^8x_0^4 + 16192x^7x_0^6 - 8288\mathcal{D}x^6x_0^6 \\
&\quad +5808x^5x_0^8 - 2080\mathcal{D}x^4x_0^8 + 924x^3x_0^{10} - 194\mathcal{D}x^2x_0^{10} + 44xx_0^{12} - 3\mathcal{D}x_0^{12} \Bigg).
\end{aligned} \tag{3.77}$$

On the other hand, in the region $x < x_H^-$ or $x > x_H^+$, the effective energy density and pressures are given by

$$
\begin{aligned}
\rho(x) &= \frac{\mathcal{D}x_0^2 Y}{X^2\left(Y^6\right)^{2/3}},\\
p_r(x) &= -\frac{x_0^2 Y^3}{X^2\left(Y^6\right)^{8/3}}\Bigg(\Big[1024x^{10} - 512\mathcal{D}x^9 + 2560x^8x_0^2 - 1024\mathcal{D}x^7x_0^2 + 2240x^6x_0^4\\
&\quad -672\mathcal{D}x^5x_0^4 + 800x^4x_0^6 - 160\mathcal{D}x^3x_0^6 + 100x^2x_0^8 - 10\mathcal{D}xx_0^8 + 2x_0^{10}\Big]X\\
&\quad +1024x^{11} - 512\mathcal{D}x^{10} + 3072x^9x_0^2 - 1280\mathcal{D}x^8x_0^2 + 3392x^7x_0^4 - 1120\mathcal{D}x^6x_0^4\\
&\quad +1664x^5x_0^6 - 400\mathcal{D}x^4x_0^6 + 340x^3x_0^8 - 50\mathcal{D}x^2x_0^8 + 20xx_0^{10} - \mathcal{D}x_0^{10}\Bigg),\\
p_\theta(x) &= \frac{x_0^2 Y^2}{2X^3\left(Y^6\right)^{8/3}}\Bigg(\Big[4096x^{12} - 4096\mathcal{D}x^{11} + 13312x^{10}x_0^2 - 10752\mathcal{D}x^9x_0^2 + 16384x^8x_0^4\\
&\quad -10240\mathcal{D}x^7x_0^4 + 9408x^6x_0^6 - 4256\mathcal{D}x^5x_0^6 + 2480x^4x_0^8 - 720\mathcal{D}x^3x_0^8\\
&\quad +244x^2x_0^{10} - 34\mathcal{D}xx_0^{10} + 4x_0^{12}\Big]X + 4096x^{13} - 4096\mathcal{D}x^{12} + 15360x^{11}x_0^2\\
&\quad -12800\mathcal{D}x^{10}x_0^2 + 22528x^9x_0^4 - 15104\mathcal{D}x^8x_0^4 + 16192x^7x_0^6 - 8288\mathcal{D}x^6x_0^6\\
&\quad +5808x^5x_0^8 - 2080\mathcal{D}x^4x_0^8 + 924x^3x_0^{10} - 194\mathcal{D}x^2x_0^{10} + 44xx_0^{12} - 3\mathcal{D}x_0^{12}\Bigg). \quad (3.78)
\end{aligned}
$$

In Fig. 3.12 we plot the physical quantities ρ, $\rho{\pm}p_r$, $\rho{\pm}p_\theta$, and $\rho{+}p_r{+}2{\pm}p_\theta$ in the neighborhood of the two horizons, from which we can see that all these quantities become unbounded as $x \to -\infty$ (or $b(x) \to 0$).

In particular, at the horizon ($x = \sqrt{\Delta}$), we have

$$
\begin{aligned}
\rho &= -p_r = \frac{\left(\sqrt{\Delta} + \mathcal{D}\right)x_0^2}{\mathcal{D}Z^2},\\
p_\theta &= \frac{x_0^4}{2\mathcal{D}^2Z^2}, \qquad (3.79)
\end{aligned}
$$

so all the three energy conditions, WEC, SEC, and DEC, are satisfied in the domain

$$|x_0| < \mathcal{D},\ (x_0 \neq 0)\,. \qquad (3.80)$$

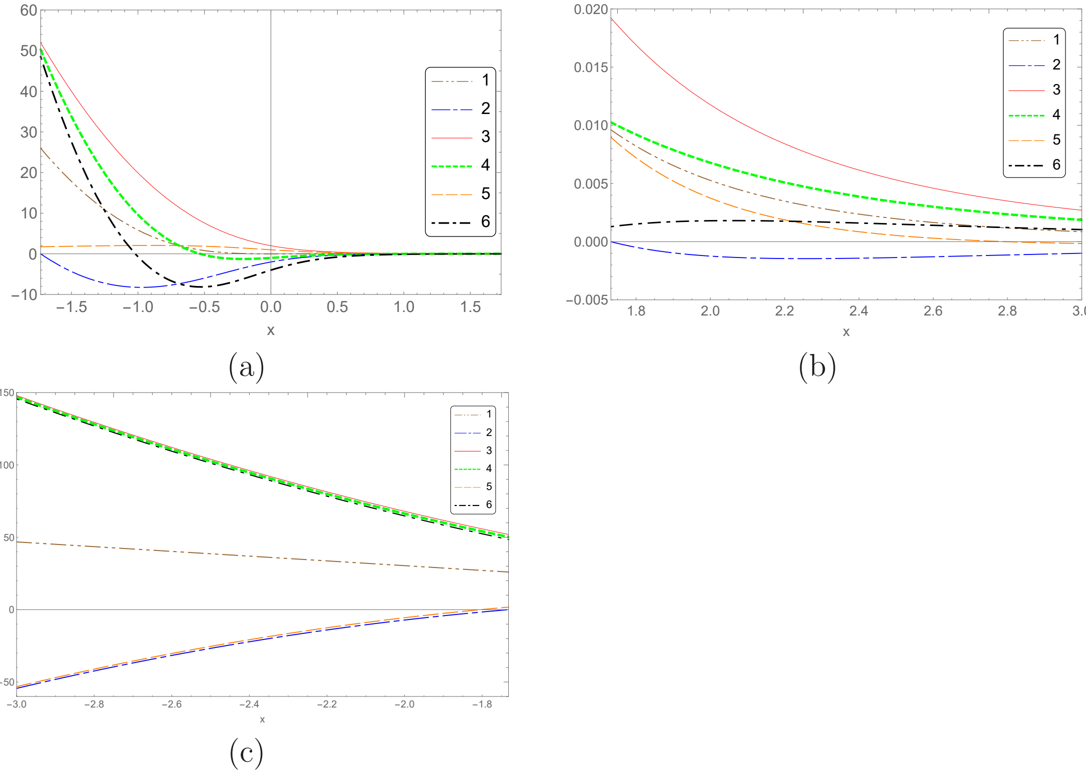

Figure 3.12: Case $\Delta > 0$, $\mathcal{D} > 0$, $x_0 \neq 0$, $\mathcal{C} = 0$: The physical quantities, ρ, $(\rho + p_r)$, $(\rho - p_r)$, $(\rho + p_\theta)$, $(\rho - p_\theta)$, and $(\rho + p_r + 2p_\theta)$, represented, respectively, by Curves 1 - 6, vs x: (a) between the white and black horizons, $x_H^- \leq x \leq x_H^+$; (b) outside the black horizon, $x \geq x_H^+ = \sqrt{3}$; (c): outside the white horizon, $x \leq x_H^- = -\sqrt{3}$. All curves are plotted with $x_0 = 1$, $\mathcal{D} = 2$, for which the two horizons are located respectively at $x_H^\pm = \pm\sqrt{\Delta} = \pm\sqrt{3}$.

The surface gravity at this horizon is given by,

$$\begin{aligned}
\kappa_{BH} &\equiv \frac{1}{2} a'(x = \sqrt{\Delta}) \\
&= \frac{Y^2}{2Z^5} \Bigg(\Big[32\mathcal{D}^6 - x_0^6 + 18\mathcal{D}^2 x_0^4 - 48\mathcal{D}^4 x_0^2 \Big] \sqrt{\Delta} \\
&\quad + 32\mathcal{D}^7 - 6\mathcal{D} x_0^6 + 38\mathcal{D}^3 x_0^4 - 64\mathcal{D}^5 x_0^2 \Bigg),
\end{aligned} \tag{3.81}$$

which is always positive, provided that the conditions (3.80) hold.

On the other hand, at the horizon $x = -\sqrt{\Delta}$, we have

$$
\begin{aligned}
\rho &= -p_r = \frac{Y}{\mathcal{D}x_0^8}\Bigg(16\mathcal{D}^4\left(\mathcal{D}+\sqrt{\Delta}\right) + x_0^4\left(5\mathcal{D}+\sqrt{\Delta}\right) \\
&\qquad - 4\mathcal{D}^2 x_0^2\left(5\mathcal{D}+3\sqrt{\Delta}\right)\Bigg), \\
p_\theta &= \frac{x_0^4}{2\mathcal{D}^2 Y^2},
\end{aligned} \tag{3.82}
$$

so all the three energy conditions, WEC, SEC, and DEC, are satisfied in the domain given by Eq.(3.80). The surface gravity at this horizon is given by,

$$
\begin{aligned}
\kappa_{BH} \quad &\equiv \frac{1}{2}a'(x = -\sqrt{\Delta}) \\
&= -\frac{Y^2}{2Z^5}\Bigg(\left[32\mathcal{D}^6 - x_0^6 + 18\mathcal{D}^2 x_0^4 - 48\mathcal{D}^4 x_0^2\right]\sqrt{\Delta} \\
&\quad -32\mathcal{D}^7 + 6\mathcal{D}x_0^6 - 38\mathcal{D}^3 x_0^4 + 64\mathcal{D}^5 x_0^2\Bigg),
\end{aligned} \tag{3.83}
$$

which is always negative when the conditions (3.80) hold.

As $x \to \pm\infty$, we find that

$$
\begin{aligned}
\rho(x) &= \begin{cases} \frac{\mathcal{D}x_0^2}{8x^5} + \mathcal{O}\left(\epsilon^6\right), & x \to \infty, \\ -\frac{8\mathcal{D}x}{x_0^4} + \mathcal{O}\left(\epsilon\right), & x \to -\infty, \end{cases} \\
p_r(x) &= \begin{cases} -\frac{x_0^2}{4x^4} + \frac{\mathcal{D}x_0^2}{8x^5} + \mathcal{O}\left(\epsilon^6\right), & x \to \infty, \\ -\frac{16x^2}{x_0^4} - \frac{8\mathcal{D}x}{x_0^4} - \frac{4}{x_0^2} + \mathcal{O}\left(\epsilon\right), & x \to -\infty, \end{cases} \\
p_\theta(x) &= \begin{cases} \frac{x_0^2}{4x^4} - \frac{\mathcal{D}x_0^2}{4x^5}, & x \to \infty, \\ \frac{16x^2}{x_0^4} + \frac{8\mathcal{D}x}{x_0^4} + \frac{4}{x_0^2} + \mathcal{O}\left(\epsilon\right), & x \to -\infty, \end{cases}
\end{aligned} \tag{3.84}
$$

from which we can show that none of the three energy conditions, WEC, SEC, and DEC, is satisfied at spatial infinity $x = \infty$ as well as at the center $b(x = -\infty) = 0$.

In addition, we also have

$$
a(x) = \begin{cases} \frac{1}{4}\left(1-\frac{2\mathcal{D}}{b}\right)+\mathcal{O}\left(\epsilon^2\right), & x\to\infty, \\ \frac{4x^4}{x_0^4}+\frac{4\mathcal{D}x^3}{x_0^4}+\frac{6x^2}{x_0^2}+\frac{4\mathcal{D}x}{x_0^2} & \\ +\frac{7}{4}+\frac{\mathcal{D}}{4x}+\mathcal{O}\left(\epsilon^2\right), & x\to-\infty, \end{cases}
$$

$$
b(x) \simeq \begin{cases} 2x, & x\to\infty, \\ -\frac{x_0^2}{2x}+\frac{x_0^4}{8x^3}+\mathcal{O}\left(\epsilon^4\right), & x\to-\infty. \end{cases} \tag{3.85}
$$

Thus, the mass of the black hole is given by

$$
M_{BH} = \mathcal{D}. \tag{3.86}
$$

However, at $x=-\infty$ we have $b(-\infty)=0$, and the physical quantities, ρ, p_r and p_θ, all become unbounded, so a spacetime curvature singularity appears at $x=-\infty$, and the solution has a RN-like structure, i.e., two horizons, one is inner and the other is outer, located, respectively, at $x=\pm\sqrt{\Delta}$. The spacetime singularity located at $b(-\infty)=0$ is timelike.

On the other hand, in Fig. 3.13 we plot R and $\Delta\mathcal{K}$ in the region that covers the throat and the horizons, from which it can be seen that the deviation from GR quickly becomes vanishing small around the outer horizon, but around the inner horizon, R deviates from GR significantly. In fact, as $x\to\pm\infty$, we find that

$$
R \simeq \begin{cases} -\frac{x_0^2}{4x^4}+\frac{\mathcal{D}x_0^2}{2x^5}+\mathcal{O}\left(\epsilon^6\right), & x\to\infty, \\ -\frac{16x^2}{x_0^4}-\frac{16\mathcal{D}x}{x_0^4}-\frac{4}{x_0^2}+\mathcal{O}\left(\epsilon\right), & x\to-\infty, \end{cases} \tag{3.87}
$$

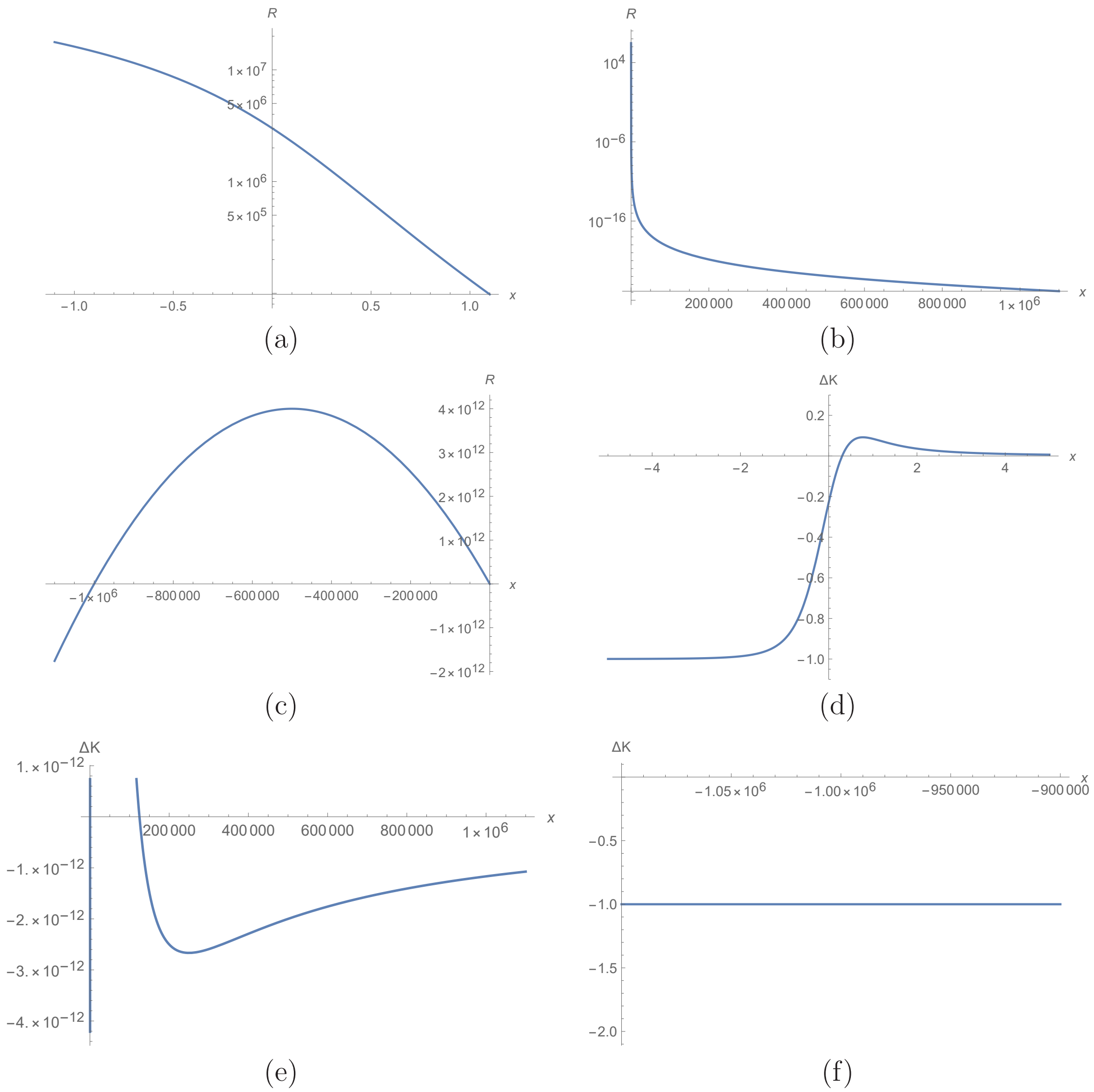

Figure 3.13: Case $\Delta > 0,\ \mathcal{D} > 0,\ x_0 \neq 0,\ \mathcal{C} = 0$: The physical quantities R and $\Delta\mathcal{K}$ vs x. Here we choose $x_0 = 1$, $\mathcal{D} = 10^6$, so that $M_{BH} = 10^6\ M_{Pl}$, and the horizons are located at $x = \pm\mathcal{D} = \pm 10^6$.

and

$$\mathcal{K} \ \simeq \ \begin{cases} \frac{3\mathcal{D}^2}{4x^6} + \mathcal{O}\left(\epsilon^7\right), & x \to \infty, \\ \frac{2816x^4}{x_0^8} + \frac{3072\mathcal{D}x^3}{x_0^8} + \frac{64x^2\left(15\mathcal{D}^2+22x_0^2\right)}{x_0^8} & \\ +\frac{640\mathcal{D}x}{x_0^6} + \frac{16\left(11x_0^2-8\mathcal{D}^2\right)}{x_0^6} + \mathcal{O}\left(\epsilon\right), & x \to -\infty, \end{cases} \tag{3.88}$$

from which we can see that, as $x \to -\infty$, both of the Ricci and Kretschmann scalars become unbounded, and a spacetime singularity appears at $b(x = -\infty) = 0$.

It is interesting to note that $\Delta\mathcal{K}$ is bounded and approaches a nonzero constant -1, as $x \to -\infty$. In fact, we have

$$\Delta\mathcal{K} \simeq \begin{cases} -\frac{4x_0^2}{3M_{BH}x} + \mathcal{O}\left(\epsilon^2\right), \; x \to \infty, \\ \\ -1 + \frac{11x_0^4}{12M_{BH}^2x^2} + \mathcal{O}\left(\epsilon^3\right), \qquad x \to -\infty, \end{cases} \tag{3.89}$$

where in writing the above expressions we had set $\mathcal{K}^{GR} = 48M_{BH}/b^6$ over the whole region $x \in (-\infty, \infty)$. Thus, near the singular point $b(x = -\infty) = 0$, the Kretschmann scalar of the quantum black hole diverges much more slowly than that of the Schwarzschild black hole. This can be seen from Eqs.(3.85) and (3.88), from which we find that $\mathcal{K} \propto b^{-4}$ as $x \to -\infty$.

3.4.1.5 $\quad x_0 = \mathcal{C} = 0$

Since $\lambda_1\lambda_2 \neq 0$, from Eq.(3.9) we can see that this corresponds to the limits $C \to 0$ and $\sqrt{n} \to \infty$. However, to keep $\mathcal{D} > 0$, at these limits, we must require $DC/\sqrt{n} \to$ finite and positive. Then, we find that $\Delta = \mathcal{D}^2$, and from Eq.(3.12) we find $X = |x|$, and

$$Y = x + |x| = \begin{cases} 2x, & x \geq 0, \\ \\ 0, & x < 0. \end{cases} \tag{3.90}$$

Therefore, the spacetime must be restricted to the region $x \geq 0$, in which we have

$$\begin{aligned} a(x) &= \frac{x - \mathcal{D}}{4x} = \frac{1}{4}\left(1 - \frac{2\mathcal{D}}{b}\right), \\ b(x) &= (x + \sqrt{x^2}) = 2x, \end{aligned} \tag{3.91}$$

and

$$\rho(x) = p_r = p_\theta(x) = 0. \tag{3.92}$$

In fact, this is precisely the Schwarzschild solution, and will take its standard form, by setting $r = 2x$ and rescaling t,

$$ds^2 = \left(1 - \frac{2m}{r}\right) dt^2 + \left(1 - \frac{2m}{r}\right)^{-1} dr^2 + r^2 d\Omega^2, \tag{3.93}$$

where $m \equiv \mathcal{D}$. This case can be also considered as the limit of $\lambda_{1,2} \to 0$, for which the GR limit is obtained. Therefore, the results are consistent with the effective theory of quantum black holes, as the singularities are always avoided exactly because of the replacement (3.3). When $\lambda_{1,2} \to 0$, the classical limits are recovered.

3.4.2 $\mathcal{D} < 0$

In this case, similar to the last one, let us consider $x_0\mathcal{C} \neq 0$ and $x_0\mathcal{C} = 0$, separately.

3.4.2.1 $x_0\mathcal{C} \neq 0$

Then, since $\Delta = \mathcal{D}^2 - x_0^2 > 0$, we must have

$$\mathcal{D} < -|x_0|. \tag{3.94}$$

Thus, from Eq.(3.11) we find that

$$a(x) = \frac{(X + |\mathcal{D}|)\, XY^2}{Z^2}, \quad b(x) = \frac{Z}{Y}, \tag{3.95}$$

where X, Y, and Z are given by Eq.(3.12). From the above expressions, it can be shown that there are two asymptotically flat regions, corresponding to $x \to \pm\infty$, respectively. They are still connected by a throat located at x_m given by Eq.(3.26) [cf. Fig. 3.1(a)]. But since $a(x) \neq 0$ for any given x, horizons, either WHs or BHs, do not exist.

At the throat, the effective energy density ρ and pressures p_r and p_θ are still given by Eq.(3.54). Then, it can be easily shown that none of the three energy conditions can be satisfied in the current case, because condition Eq.(3.55) is always violated for $\mathcal{D} < 0$.

At the spatial infinities $x \to \pm\infty$, we find that the expression of ρ, p_r, p_θ are still given by Eq.(3.42), from which we can see that *none of the three energy conditions is satisfied either*. The asymptotic expressions of $a(x)$ and $b(x)$ are still given by Eq.(3.43), and the total masses measured at $x \to \pm\infty$ are

$$M_+ \;=\; \mathcal{D}, \quad M_- = \frac{\mathcal{D}\mathcal{C}^2}{x_0^2}, \tag{3.96}$$

but since we now have $\mathcal{D} < 0$, they are all negative. Note that from now on, we use $M_\pm$ to denote the total masses of the spacetimes measured at $x = \pm\infty$, when no horizons (either BHs or WHs) exist, while reserve $M_{BH/WH}$ to denote the black (white) hole masses.

It can be shown that in the present case the deviation from GR decays rapidly when away from the throat from both directions of it only for some particular choice of the free parameters. In particular, as $x \to \pm\infty$, we find that the asymptotic expressions of $R(x)$ and $\Delta\mathcal{K}(x)$ are still given by Eq.(3.51) and Eq.(3.52), with $M_{BH}(M_{WH})$ being replaced by $M_+(M_-)$. Therefore, we still have $|\Delta\mathcal{K}_+/\Delta\mathcal{K}_-| = 1 + \mathcal{O}\left(\epsilon^2\right)$, as $|x| \to \infty$. That is, whether $M_- \gg M_+$ or not, $|\Delta\mathcal{K}_+|$ will always have the same asymptotic magnitude as $|\Delta\mathcal{K}_-|$, and both of them approach their GR limits as $\mathcal{O}(1/|x|)$.

3.4.2.2 $x_0 = 0, \;\; \mathcal{C} \neq 0$

In this case $a(x)$ and $b(x)$ are still given by Eq.(3.58), but since $\mathcal{D} < 0$, $a(x) = 0$ is possible only when

$$x_H = 0, \tag{3.97}$$

where $b(x = 0) = \infty$. Therefore, in the current case there is no black/white hole horizon either, while the minimum of $b(x)$ now is still located at $x_m \equiv \hat{\mathcal{C}}$ [cf. Fig. 3.1(b)]. On the other hand, in this case the effective energy density and pressures are still given by Eq.(3.65), which are all become zero as $x \to 0$.

At the throat ($x = \hat{\mathcal{C}}$), ρ, p_r, p_θ are given by Eq.(3.73), but since now we have $\mathcal{D} < 0$, none of the three energy conditions is satisfied at the throat.

At the spatial infinity $x \to \infty$, on the other hand, we have the same expressions as given by Eq.(3.68), from which we can see that none of the three energy conditions is satisfied. The asymptotic behavior of $a(x)$ and $b(x)$ are still given by Eq.(3.69). Therefore, the total mass at $x \to \infty$ is given by

$$M_+ \;\; = \;\; \mathcal{D} < 0. \tag{3.98}$$

On the other hand, to study the quantum gravitational effects further, we consider the physical quantities R and $\Delta\mathcal{K}$ and find that the deviation from GR also quickly becomes vanishingly small as $x \to \infty$ for some particular choice of the free parameters. In particular, as $x \to \infty$, we find that the asymptotic expressions of $R(x)$ and $\Delta\mathcal{K}(x)$ are still given by Eq.(3.71), with M_{BH} being replaced by M_+.

3.4.2.3 $x_0 \neq 0, \; \mathcal{C} = 0$

Table 3.1: The main properties of the solutions given by Eqs.(3.10)-(3.13) with $\Delta > 0$ in various cases, where bhH $\equiv$ black hole horizon, whH $\equiv$ white hole horizon, ECs $\equiv$ energy conditions, SAF $\equiv$ spacetime is asymptotical flat, SCS $\equiv$ spacetime curvature singularity, and Sch.S $\equiv$ Schwarzschild solution. In addition, "✓" means yes, "×" means no, while "N/A" means not applicable.

Properties	$\Delta > 0$							
	$\mathcal{D} > 0$				$\mathcal{D} < 0$			
	$\mathcal{C} \neq 0$, $x_0 \neq 0$	$\mathcal{C} \neq 0$, $x_0 = 0$	$\mathcal{C} = 0$, $x_0 \neq 0$	$\mathcal{C} = x_0 = 0$ (Sch.S)	$\mathcal{C} \neq 0$, $x_0 \neq 0$	$\mathcal{C} \neq 0$, $x_0 = 0$	$\mathcal{C} = 0$, $x_0 \neq 0$	$\mathcal{C} = x_0 = 0$ (Sch.S)
bhH exists?	✓	✓	✓	✓	×	×	×	×
ECs at bhH	Eq.(3.25)	✓	Eq.(3.80)	✓	N/A	N/A	N/A	N/A
whH exists?	✓	×	✓	×	×	×	×	×
ECs at whH	Eq.(3.25)	N/A	Eq.(3.80)	N/A	N/A	N/A	N/A	N/A
Throat exists?	✓	✓	×	×	✓	✓	×	×
ECs at throat	Eq.(3.33)	$\mathcal{C} = 2\mathcal{D}$	N/A	N/A	×	×	N/A	N/A
ECs at $x = \infty$	×	×	×	✓	×	×	×	✓
Mass at $x = \infty$	$\mathcal{D}$	$\mathcal{D}$	$\mathcal{D}$	$\mathcal{D}$	$\mathcal{D}$	$\mathcal{D}$	$\mathcal{D}$	$\mathcal{D}$
ECs at $x = -\infty$	×	N/A ($x \geq 0$)	×	N/A ($x \geq 0$)	×	N/A ($x \geq 0$)	×	N/A ($x \geq 0$)
Mass at $x = -\infty$	$\frac{\mathcal{D}\mathcal{C}^2}{x_0^2}$	SAF at $x = 0$	SCS	SCS at $x = 0$	$\frac{\mathcal{D}\mathcal{C}^2}{x_0^2}$	SAF at $x = 0$	SCS	SCS at $x = 0$

From Eq.(3.11) we find that

$$a(x) = \frac{(X + |\mathcal{D}|)\, X}{Y^2}, \quad b(x) = Y, \tag{3.99}$$

where X, Y, and Z are given by Eq.(3.12). Clearly, $a(x) = 0$ has no real roots, thus no horizons exist, while $b(x)$ is still a monotonically increasing function with $b(x = -\infty) = 0$ [cf. Fig. 3.1(c)].

On the other hand, in this case the effective energy density and pressures are still given by Eq.(3.78). In particular, at the spatial infinities $x \to \pm\infty$, they stall take the forms of Eq.(3.84), from which we find none of the three energy conditions, WEC, SEC, and DEC, is satisfied. In addition, the asymptotic behaviors of $a(x)$ and $b(x)$ are given by Eq.(3.85). Therefore, the total mass at $x = \infty$ is still given by Eq.(3.86), which is always negative.

However, at $x = -\infty$ we have $b(-\infty) = 0$, and the physical quantities, ρ, p_r and p_θ, all become unbounded, so a spacetime curvature singularity appears at $x = -\infty$.

In addition, from R and $\Delta\mathcal{K}$ we find that the deviation from GR quickly becomes vanishingly small as $x \to +\infty$, but as $x \to -\infty$, R deviates from GR significantly, as a spacetime curvature singularity now appears at $x = -\infty$, at which we have $b(x = -\infty) = 0$.

3.4.2.4 $x_0 = \mathcal{C} = 0$

In this case, the solution is precisely the Schwarzschild solution with negative mass, and will take its standard form, by setting $r = 2x$ and rescaling t,

$$ds^2 = \left(1 - \frac{2m}{r}\right) dt^2 + \left(1 - \frac{2m}{r}\right)^{-1} dr^2 + r^2 d\Omega^2, \tag{3.100}$$

where $m \equiv \mathcal{D} < 0$.

This completes the analysis of the solutions in the case $\Delta > 0$. In Table 3.1, we summarize the main properties of these solutions.

3.5 Spacetimes with $\Delta = 0$

From Eq.(3.13) we find that this case corresponds to

$$|\lambda_2| = \frac{3}{2}\,|CD|\,, \quad \text{or} \quad |\mathcal{D}| = |x_0|\,. \tag{3.101}$$

Then, from Eqs.(3.11) and (3.12) we obtain

$$a(x) \;=\; \frac{x^2 X Y^2}{(X + \mathcal{D})\, Z^2}, \quad b(x) = \frac{Z}{Y}, \tag{3.102}$$

where

$$\begin{aligned} X &\equiv \sqrt{x^2 + \mathcal{D}^2}, \quad Y \equiv x + X, \\ Z &\equiv \left(Y^6 + \mathcal{C}^6\right)^{1/3}. \end{aligned} \tag{3.103}$$

To study these solutions further, in the following let us consider the three possibilities, $\mathcal{D} > 0$, $\mathcal{D} = 0$ and $\mathcal{D} < 0$, separately.

3.5.1 $\mathcal{D} > 0$

In this subcase, there are still two possibilities, $\mathcal{C} \neq 0$ and $\mathcal{C} = 0$.

3.5.1.1 $\mathcal{C} \neq 0$

In this case, since we also have $\mathcal{D} > 0$, we find that

$$b(x) = \begin{cases} \infty, & x = \infty, \\ 2^{1/3}\mathcal{C}, & x = x_m, \\ \infty, & x = -\infty, \end{cases} \tag{3.104}$$

where $x_m \equiv (\mathcal{C}^2 - \mathcal{D}^2)/(2\mathcal{C})$ [cf. Fig. 3.1(a)].

On the other hand, $a(x) = 0$ leads to $x_H^{\pm} = 0$, which is a double root. This is similar to the charged RN solution in the extreme case $|e| = m$. At the horizon, we have

$$b(0) = \frac{(\mathcal{C}^6 + \mathcal{D}^6)^{1/3}}{|\mathcal{D}|}, \tag{3.105}$$

and

$$\rho = -p_r = 2p_\theta = \frac{\mathcal{D}^2}{(\mathcal{D}^6 + \mathcal{C}^6)^{2/3}}, \tag{3.106}$$

from which we find that all the WEC, SEC, and DEC are satisfied. In addition, the surface gravity at the horizon is,

$$\kappa_{BH} \equiv \frac{1}{2}a'(x = 0) = 0, \tag{3.107}$$

as in the extremal case of the RN solution.

At the throat, the effective energy density ρ and pressures p_r and p_θ are given by

$$\begin{aligned}
\rho &= \frac{-5\mathcal{D}^2 + 12\mathcal{D}\mathcal{C} - 5\mathcal{C}^2}{2^{2/3}\mathcal{C}^2\left(\mathcal{D}^2 + \mathcal{C}^2\right)}, \quad p_r = -\frac{1}{2^{2/3}\mathcal{C}^2}, \\
p_\theta &= \frac{\left(\mathcal{D}^2 + \mathcal{C}^2\right)^3 - 4\mathcal{D}^3\mathcal{C}^3}{2^{2/3}\left(\mathcal{D}^2 + \mathcal{C}^2\right)^3},
\end{aligned} \tag{3.108}$$

from which we find that WEC, SEC, and DEC are satisfied only when

$$\mathcal{D} = \mathcal{C}. \tag{3.109}$$

Then, from the expression $x_m = (\mathcal{C}^2 - \mathcal{D}^2)/(2\mathcal{C})$, we can see when $\mathcal{D} = \mathcal{C}$ we also have $x_m = 0$, i.e., the black hole horizon now coincides with the throat.

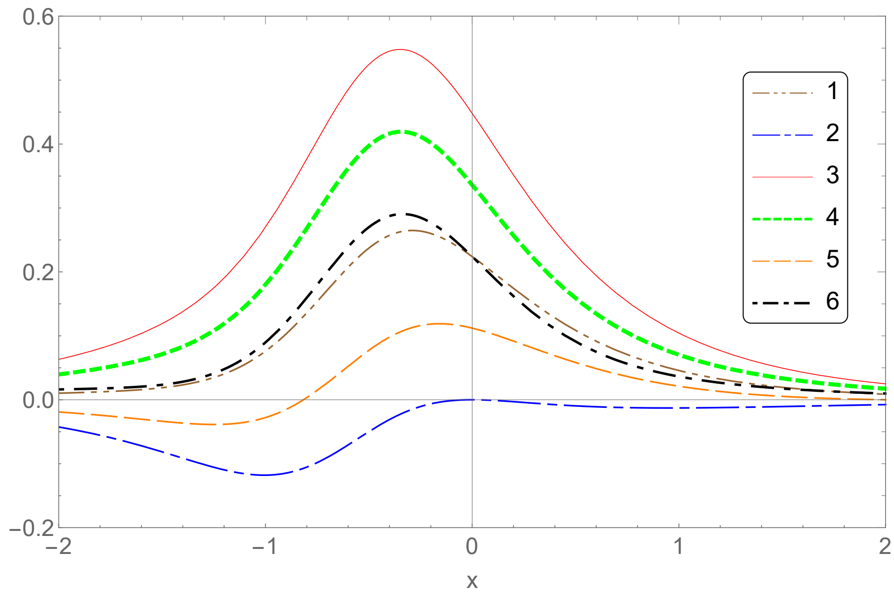

Figure 3.14: Case $\Delta = 0$, $\mathcal{D} > 0$, $\mathcal{C} \neq 0$: The physical quantities, ρ, $(\rho + p_r)$, $(\rho - p_r)$, $(\rho + p_\theta)$, $(\rho - p_\theta)$, and $(\rho + p_r + 2p_\theta)$, represented, respectively, by Curves 1 - 6, vs x in the neighborhood of the throat. All graphs are plotted with $\mathcal{C} = 1.5$, $\mathcal{D} = 2$, for which the throat is at $x_m \approx -0.437$, and horizons are at $x_H^{\pm} = 0$.

In Fig. 3.14 we plot out the quantities ρ, $\rho \pm p_r$, $\rho \pm p_\theta$ and $\rho + p_r + 2p_\theta$ vs x in the neighborhood of the throat for $\mathcal{C} = 1.5$, $\mathcal{D} = 2$. With these choices, the throat is located at $x_m \approx -0.437$, and the horizon is at $x_H^{\pm} = 0$. From these curves we can see clearly that the three energy conditions, WEC, SEC, and DEC, are satisfied only at the horizon.

At the spatial infinities $x \to \pm\infty$, we find that

$$\begin{aligned}
\rho(x) &= \begin{cases} \frac{\mathcal{D}^3}{8x^5} + \mathcal{O}\left(\epsilon^6\right), & x \to \infty, \\ -\frac{\mathcal{D}^7}{8x^5\mathcal{C}^4} + \mathcal{O}\left(\epsilon^6\right), & x \to -\infty, \end{cases} \\
p_r(x) &= \begin{cases} -\frac{\mathcal{D}^2}{4x^4} + \frac{\mathcal{D}^3}{8x^5} + \mathcal{O}\left(\epsilon^6\right), & x \to \infty, \\ -\frac{\mathcal{D}^6}{4x^4\mathcal{C}^4} - \frac{\mathcal{D}^7}{8x^5\mathcal{C}^4} + \mathcal{O}\left(\epsilon^6\right), & x \to -\infty, \end{cases} \\
p_\theta(x) &= \begin{cases} \frac{\mathcal{D}^2}{4x^4} - \frac{\mathcal{D}^3}{4x^5} + \mathcal{O}\left(\epsilon^6\right), & x \to \infty, \\ \frac{\mathcal{D}^6}{4x^4\mathcal{C}^4} + \frac{\mathcal{D}^7}{4x^5\mathcal{C}^4} + \mathcal{O}\left(\epsilon^6\right), & x \to -\infty, \end{cases}
\end{aligned} \tag{3.110}$$

and

$$\begin{aligned}
a(x) &= \begin{cases} \frac{1}{4}\left(1 - \frac{2\mathcal{D}}{b}\right) + \mathcal{O}\left(\epsilon^2\right), & x \to \infty, \\ \frac{\mathcal{D}^4}{4\mathcal{C}^4}\left(1 - \frac{\left(2\mathcal{C}^2/\mathcal{D}\right)}{b}\right) + \mathcal{O}\left(\epsilon^2\right), & x \to -\infty, \end{cases} \\
b(x) &\simeq \begin{cases} 2x + \mathcal{O}\left(\epsilon\right), & x \to \infty, \\ -2\left(\mathcal{C}^2/\mathcal{D}^2\right)x + \mathcal{O}\left(\epsilon\right), & x \to -\infty, \end{cases}
\end{aligned} \tag{3.111}$$

where $\epsilon \equiv 1/x$. Therefore, the masses of the black and white holes are given, respectively, by

$$M_{BH} = \mathcal{D}, \quad M_{WH} = \frac{\mathcal{C}^2}{\mathcal{D}}. \tag{3.112}$$

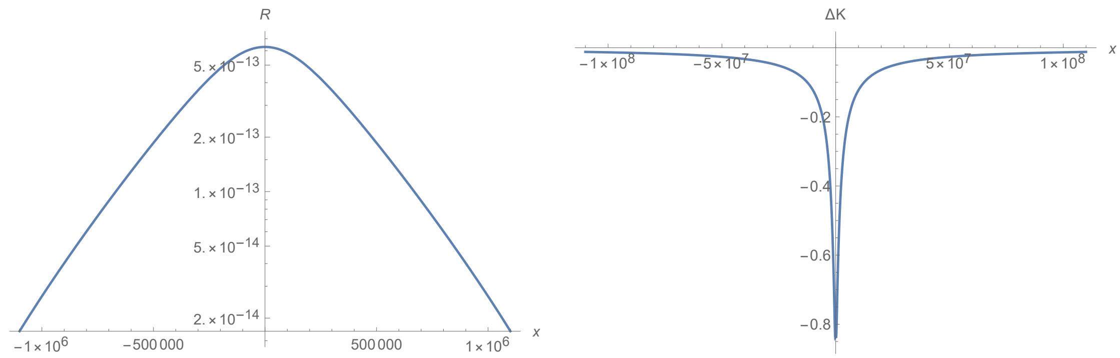

(a) (b)

Figure 3.15: Case $\Delta = 0$, $\mathcal{D} > 0$, $\mathcal{C} \neq 0$: R and $\Delta\mathcal{K}$ vs x. Here we choose $\mathcal{C} = x_0 = 10^6$, for which the horizon and the throat are all located at $x_H^{\pm} = x_m = 0$.

On the other hand, from Eq.(3.110) we find that in the limit $x \to \infty$ we have

$$
\begin{aligned}
\rho &\approx \frac{\mathcal{D}^3}{8x^5} + \mathcal{O}\left(\epsilon^6\right), \\
\rho + p_r &\approx -\frac{\mathcal{D}^2}{4x^4} + \frac{\mathcal{D}^3}{4x^5} + \mathcal{O}\left(\epsilon^6\right), \\
\rho + p_\theta &\approx \frac{\mathcal{D}^2}{4x^4} - \frac{\mathcal{D}^3}{8x^5} + \mathcal{O}\left(\epsilon^6\right), \\
\rho + p_r + 2p_\theta &\approx \frac{\mathcal{D}^2}{4x^4} - \frac{\mathcal{D}^3}{4x^5} + \mathcal{O}\left(\epsilon^6\right),
\end{aligned} \tag{3.113}
$$

while in the limit $x \to -\infty$, we have

$$
\begin{aligned}
\rho &\approx -\frac{\mathcal{D}^7}{8x^5\mathcal{C}^4} + \mathcal{O}\left(\epsilon^6\right), \\
\rho + p_r &\approx -\frac{\mathcal{D}^6}{4x^4\mathcal{C}^4} - \frac{\mathcal{D}^7}{4x^5\mathcal{C}^4} + \mathcal{O}\left(\epsilon^6\right), \\
\rho + p_\theta &\approx \frac{\mathcal{D}^6}{4x^4\mathcal{C}^4} + \frac{\mathcal{D}^7}{8x^5\mathcal{C}^4} + \mathcal{O}\left(\epsilon^6\right), \\
\rho + p_r + 2p_\theta &\approx \frac{\mathcal{D}^6}{4x^4\mathcal{C}^4} + \frac{\mathcal{D}^7}{4x^5\mathcal{C}^4} + \mathcal{O}\left(\epsilon^6\right).
\end{aligned} \tag{3.114}
$$

Therefore, *none of the three energy conditions is satisfied at both $x = -\infty$ and $x = \infty$.*

In Fig. 3.15, we plot R and $\Delta\mathcal{K}$ for solar mass black/white holes in the region that covers the throat, with $\mathcal{C} = \mathcal{D} = x_0 = 10^6$, for which the horizon and the throat are all located at $x_H^{\pm} = x_m = 0$. In this case, it can be seen that the deviations from

GR decay rapidly when away from the throat from both directions, and the quantum gravitational effects are mainly concentrated in the neighborhood of it.

In addition, as $x \to \pm\infty$, we find that

$$R \simeq \begin{cases} -\frac{\mathcal{D}^2}{4x^4} + \frac{\mathcal{D}^3}{2x^5} + \mathcal{O}\left(\epsilon^6\right), & x \to \infty, \\ -\frac{\mathcal{D}^6}{4x^4\mathcal{C}^4} - \frac{\mathcal{D}^7}{2x^5\mathcal{C}^4} + \mathcal{O}\left(\epsilon^6\right), & x \to -\infty, \end{cases} \tag{3.115}$$

and

$$\Delta\mathcal{K} \simeq \begin{cases} -\frac{4M_{BH}}{3x} + \mathcal{O}\left(\epsilon^2\right), & x \to \infty, \\ +\frac{4\mathcal{C}^2}{3M_{WH}x} + \mathcal{O}\left(\epsilon^2\right), & x \to -\infty, \end{cases} \tag{3.116}$$

where M_{BH} and M_{WH} are given by Eq.(3.112).

3.5.1.2 $\mathcal{C} = 0$

In this case, we have

$$a(x) = \frac{x^2 X}{(X + \mathcal{D})\, Y^2}, \quad b(x) = Y. \tag{3.117}$$

Then, $a(x) = 0$ leads to $x = 0$, which is a double root, as mentioned above. The geometric radius $b(x)$ is a monotonically increasing function with $b(x = -\infty) = 0$ [cf. Fig. 3.1(c)].

In Fig. 3.16 we plot the physical quantities $\rho,\ \rho \pm p_r,\ \rho \pm p_\theta$ and $\rho + p_r + 2 \pm p_\theta$ in the neighborhood of the horizon $x_H = 0$, at which, we have

$$\rho = -p_r = 2p_\theta = \frac{1}{\mathcal{D}^2}, \tag{3.118}$$

so all the three energy conditions, WEC, SEC, and DEC, are satisfied. In addition, the surface gravity at this horizon also vanishes.

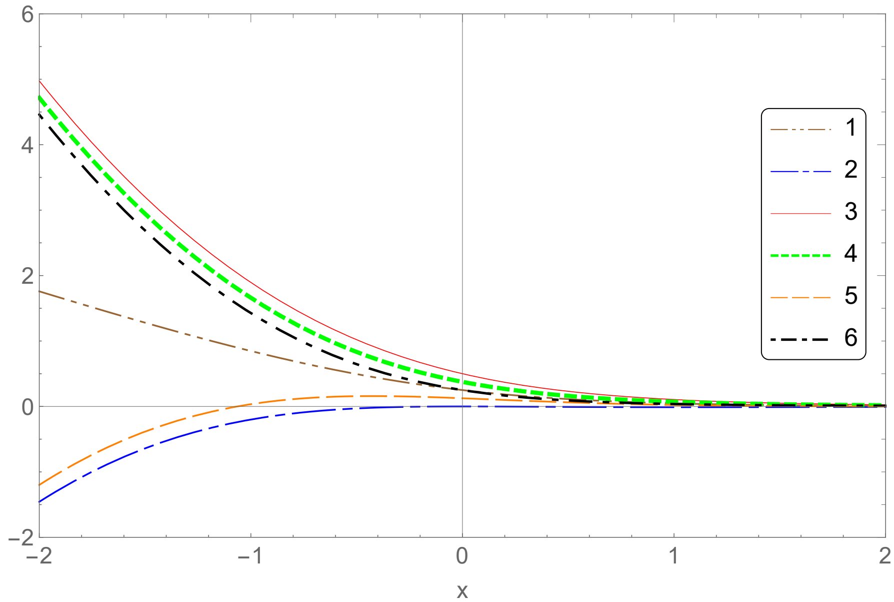

Figure 3.16: Case $\Delta = 0,\ \mathcal{D} > 0,\ \mathcal{C} = 0$: The physical quantities, ρ, $(\rho + p_r)$, $(\rho - p_r)$, $(\rho + p_\theta)$, $(\rho - p_\theta)$, and $(\rho + p_r + 2p_\theta)$, represented, respectively, by Curves 1 - 6, vs x in the neighborhood of the horizon $x_H^{\pm} = 0$. All graphs are plotted with $\mathcal{D} = 2$.

At the spatial infinities $x \to \pm\infty$, we find that

$$
\begin{aligned}
\rho(x) &= \begin{cases} \frac{\mathcal{D}^3}{8x^5} + \mathcal{O}\left(\epsilon^6\right), & x \to \infty, \\[2ex] -\frac{8x}{\mathcal{D}^3} + \mathcal{O}\left(\epsilon\right), & x \to -\infty, \end{cases} \\
p_r(x) &= \begin{cases} -\frac{\mathcal{D}^2}{4x^4} + \frac{\mathcal{D}^3}{8x^5} + \left(\epsilon^6\right), & x \to \infty, \\[2ex] -\frac{16x^2}{\mathcal{D}^4} - \frac{8r}{\mathcal{D}^3} - \frac{4}{\mathcal{D}^2} + \mathcal{O}\left(\epsilon\right), & x \to -\infty, \end{cases} \\
p_\theta(x) &= \begin{cases} \frac{\mathcal{D}^2}{4x^4} - \frac{\mathcal{D}^3}{4x^5} + \mathcal{O}\left(\epsilon^6\right), & x \to \infty, \\[2ex] \frac{16x^2}{\mathcal{D}^4} + \frac{8x}{\mathcal{D}^3} + \frac{4}{\mathcal{D}^2} + \mathcal{O}\left(\epsilon\right), & x \to -\infty, \end{cases}
\end{aligned} \tag{3.119}
$$

from which we can see that none of the three energy conditions, WEC, SEC, and DEC, is satisfied at the spatial infinities. In addition, we also have

$$
\begin{aligned}
a(x) &= \begin{cases} \frac{1}{4}\left(1-\frac{2\mathcal{D}}{b}\right)+\mathcal{O}\left(\epsilon^2\right), & x\rightarrow\infty, \\ \frac{4x^4}{\mathcal{D}^4}+\frac{4x^3}{\mathcal{D}^3}+\frac{6x^2}{\mathcal{D}^2}+\frac{4x}{\mathcal{D}} & \\ +\frac{7}{4}+\frac{\mathcal{D}}{4x}+\mathcal{O}\left(\epsilon^2\right), & x\rightarrow -\infty, \end{cases} \\
b(x) &\simeq \begin{cases} 2x+\mathcal{O}\left(\epsilon\right), & x\rightarrow\infty, \\ -\frac{\mathcal{D}^2}{2x}+\frac{\mathcal{D}^4}{8x^3}+\mathcal{O}\left(\epsilon^4\right), & x\rightarrow -\infty. \end{cases}
\end{aligned} \tag{3.120}
$$

Therefore, the mass of the black hole is given by

$$
M_{BH} = \mathcal{D}. \tag{3.121}
$$

However, at $x=-\infty$ we have $b(-\infty)=0$, and the physical quantities, ρ, p_r and p_θ, all become unbounded, so a spacetime curvature singularity appears at $x=-\infty$.

To study the quantum gravitational effects further, in Fig. 3.17 we plot R and $\Delta\mathcal{K}$, from which it can be seen that the deviation from GR quickly becomes vanishingly small as $x\rightarrow\infty$. However, as $x\rightarrow-\infty$, R diverges, as now the spacetime is singular at $b(x=-\infty)=0$. In fact, as $x\rightarrow\pm\infty$, we find that

$$
R \simeq \begin{cases} -\frac{\mathcal{D}^2}{4x^4}+\frac{\mathcal{D}^3}{2x^5}+\mathcal{O}\left(\epsilon^6\right), & x\rightarrow\infty, \\ -\frac{16x^2}{\mathcal{D}^4}-\frac{16x}{\mathcal{D}^3}-\frac{4}{\mathcal{D}^2}+\mathcal{O}\left(\epsilon\right), & x\rightarrow -\infty, \end{cases} \tag{3.122}
$$

$$
\mathcal{K} \simeq \begin{cases} \frac{3\mathcal{D}^2}{4x^6}-\frac{\mathcal{D}^3}{x^7}+\mathcal{O}\left(\epsilon^8\right), & x\rightarrow\infty, \\ \frac{2816x^4}{\mathcal{D}^8}+\frac{3072x^3}{\mathcal{D}^7}+\frac{2368x^2}{\mathcal{D}^6} & \\ +\frac{640x}{\mathcal{D}^5}+\frac{48}{\mathcal{D}^4}+\mathcal{O}\left(\epsilon\right), & x\rightarrow -\infty, \end{cases} \tag{3.123}
$$

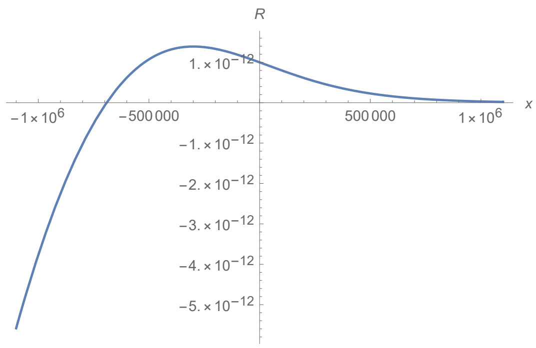

(a)

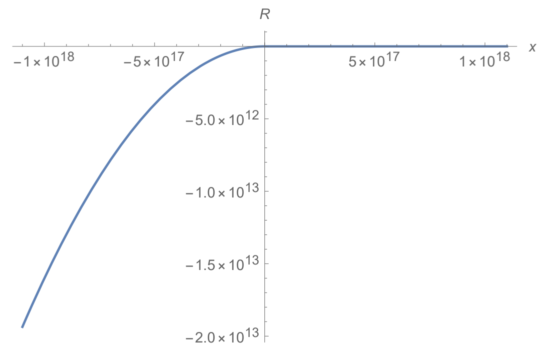

(b)

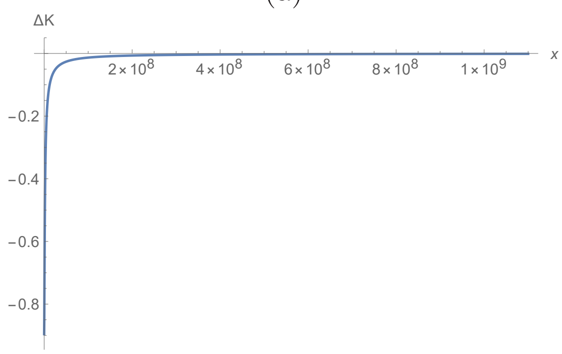

(c)

Figure 3.17: Case $\Delta = 0$, $\mathcal{D} > 0$, $\mathcal{C} = 0$: R and $\Delta\mathcal{K}$ vs x. Here we choose $x_0 = 10^6$, $\mathcal{D} = 10^6$, so that $M_{BH} = 10^6\ M_{Pl}$. Note that the horizon is located at $x_H^{\pm} = 0$, and the spacetime is singular at $b(x = -\infty) = 0$.

and

$$\Delta\mathcal{K} \simeq \begin{cases} -\frac{4M_{BH}}{3x} + \mathcal{O}\left(\epsilon^2\right), & x \to \infty, \\ \\ -1 + \frac{11\mathcal{D}^4}{12M_{BH}^2 x^2} + \mathcal{O}\left(\epsilon^3\right), & x \to -\infty. \end{cases} \tag{3.124}$$

3.5.2 $\mathcal{D} = 0$

In this case, since $|\mathcal{D}| = |x_0|$, we also have $x_0 = 0$. Then, from Eq.(3.9), this corresponds to the limit $n \to \infty$. Again, to study the solutions further, we consider the two cases $\mathcal{C} \neq 0$ and $\mathcal{C} = 0$, separately.

3.5.2.1 $\mathcal{C} \neq 0$

From Eq.(3.12) we find $X = |x|$, and

$$Y = x + |x| = \begin{cases} 2x, & x \geq 0, \\ \\ 0, & x < 0. \end{cases} \tag{3.125}$$

Thus, from Eq.(3.11) we find $a(x) = 0$ and $b(x) = \infty$ for $x \leq 0$, that is, the metric becomes singular for $x \leq 0$. However, since $b(0) = \infty$, it is clear that now $x = 0$ already represents the spatial infinity. Therefore, in this case we only need to consider the region $x \in (0, \infty)$ [cf. Fig. 3.1(b)]. In this case we have

$$a(x) = \frac{x^2 Y^2}{Z^2}, \quad b(x) = \frac{Z}{Y}. \tag{3.126}$$

Clearly, $a(x) = 0$ leads to a double root, $x_H^{\pm} = 0$, while the minimum of $b(x)$ now is located at $x_m \equiv \hat{\mathcal{C}} = \mathcal{C}/2$, so we have

$$b(x) = \begin{cases} \infty, & x = 0, \\ \\ 2^{4/3}\hat{\mathcal{C}}, & x = \hat{\mathcal{C}}, \\ \\ \infty, & x = \infty. \end{cases} \tag{3.127}$$

The spacetime becomes antitrapped at $x = 0$. Since $b(x = 0) = \infty$, this antitrapped point now also corresponds to the spatial infinity at the other side of the throat, located at $x_m = \hat{\mathcal{C}}$.

On the other hand, the effective energy density and pressures are now given by

$$\begin{aligned} \rho(x) &= -\frac{5120 x^8 \mathcal{C}^6}{(64x^6 + \mathcal{C}^6)^{8/3}}, \\ p_r(x) &= -\frac{16 x^2 \mathcal{C}^{12}}{(64x^6 + \mathcal{C}^6)^{8/3}}, \\ p_\theta(x) &= \frac{16 x^2 \mathcal{C}^{12}}{(64x^6 + \mathcal{C}^6)^{8/3}}, \end{aligned} \tag{3.128}$$

which all become zero as $x \to 0$. They are also vanishing as $x \to \infty$.

At the throat ($x = \hat{\mathcal{C}}$), we have

$$\rho = -\frac{5}{2^{8/3}\hat{\mathcal{C}}^2}, \quad p_r = -p_\theta = -\frac{1}{2^{8/3}\hat{\mathcal{C}}^2}, \tag{3.129}$$

so we find that none of the WEC, SEC, and DEC is satisfied.

At the spatial infinity $x \to \infty$, on the other hand, we find

$$\begin{aligned} \rho &\approx -\frac{5\mathcal{C}^6}{64x^8} + \mathcal{O}\left(\epsilon^9\right), \\ \rho + p_r &\approx -\frac{5\mathcal{C}^6}{64x^8} + \mathcal{O}\left(\epsilon^9\right), \\ \rho + p_\theta &\approx -\frac{5\mathcal{C}^6}{64x^8} + \mathcal{O}\left(\epsilon^9\right), \\ \rho + p_r + 2p_\theta &\approx -\frac{5\mathcal{C}^6}{64x^8} + \mathcal{O}\left(\epsilon^9\right), \end{aligned} \tag{3.130}$$

while as $x \to 0$ (or $b(x) \to \infty$), we find that

$$\begin{aligned} \rho &\approx -\frac{5120x^8}{\mathcal{C}^{10}} + \mathcal{O}\left(x^{11}\right), \\ \rho + p_r &\approx -\frac{16x^2}{\mathcal{C}^4} - \frac{7168x^8}{3\mathcal{C}^{10}} + \mathcal{O}\left(x^{11}\right), \\ \rho + p_\theta &\approx \frac{16x^2}{\mathcal{C}^4} - \frac{23552x^8}{3\mathcal{C}^{10}} + \mathcal{O}\left(x^{11}\right), \\ \rho + p_r + 2p_\theta &\approx \frac{16x^2}{\mathcal{C}^4} - \frac{23552x^8}{3\mathcal{C}^{10}} + \mathcal{O}\left(x^{11}\right), \end{aligned} \tag{3.131}$$

from which we can see that none of the three energy conditions is satisfied.

In addition, we also have

$$\begin{aligned} a(x) &= \begin{cases} \frac{1}{4}\left(1 - \frac{2\mathcal{C}^6}{3b^6}\right) + \mathcal{O}\left(\epsilon^7\right), & x \to \infty, \\ \frac{4x^4}{\mathcal{C}^4} + \mathcal{O}\left(x^6\right), & x \to 0, \end{cases} \\ b(x) &\simeq \begin{cases} 2x + \mathcal{O}\left(\epsilon\right), & x \to \infty, \\ \frac{\mathcal{C}^2}{2x} + \frac{32x^5}{3\mathcal{C}^4} + \mathcal{O}\left(x^6\right). & x \to 0. \end{cases} \end{aligned} \tag{3.132}$$

Thus, the space-time is asymptotically flat as $x \to \infty$, with a black/hole mass given by

$$M_{BH/WH} = 0. \tag{3.133}$$

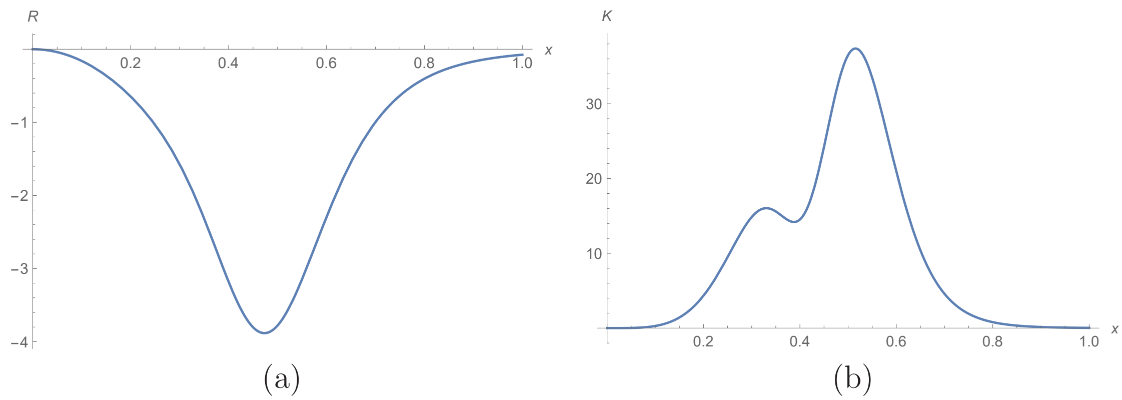

Figure 3.18: Case $\Delta = 0$, $\mathcal{D} = 0$, $\mathcal{C} \neq 0$: R and $\mathcal{K}$ vs x. Here we choose $\mathcal{C} = 1$. Note that now the throat is at $x = \hat{\mathcal{C}} = 1/2$.

On the other hand, to study the quantum gravitational effects, in Fig. 3.18 we plot R and $\mathcal{K}$ in the region that covers the throat, and in the asymptotical regions $x \to 0$ and $x \to \infty$, from which it can be seen that the deviation from GR is mainly in the region near the throat, and quickly becomes vanishingly small as $x \to \infty$ or $x \to 0$.

The spacetime is also asymptotically flat as $x \to 0$ ($b(0) = \infty$). In fact, we find

$$\begin{aligned}
R &\simeq \begin{cases} -\frac{5\mathcal{C}^6}{64x^8} + \mathcal{O}\left(\epsilon^9\right), & x \to \infty, \\ -\frac{16x^2}{\mathcal{C}^4} + \mathcal{O}\left(x^4\right), & x \to 0, \end{cases} \\
\mathcal{K} &\simeq \begin{cases} \frac{127\mathcal{C}^{12}}{4096x^{16}} + O\left(\epsilon^{19}\right), & x \to \infty, \\ \frac{2816x^4}{\mathcal{C}^8} + O\left(x^6\right), & x \to 0. \end{cases}
\end{aligned} \tag{3.134}$$

Table 3.2: The main properties of the solutions given by Eqs.(3.10)-(3.13) with $\Delta = 0$, for which we have $x_H^{\pm} = 0$, and the white and black hole horizons always coincide. Here bhH $\equiv$ black hole horizon, whH $\equiv$ white hole horizon, ECs $\equiv$ energy conditions, SAF $\equiv$ spacetime is asymptotical flat, and SCS $\equiv$ spacetime curvature singularity. In addition, "✓" means yes, "×" means no, while "N/A" means not applicable.

Properties	$\Delta = 0$					
	$\mathcal{D} > 0$		$\mathcal{D} = 0$		$\mathcal{D} < 0$	
	$\mathcal{C} \neq 0$	$\mathcal{C} = 0$	$\mathcal{C} \neq 0$	$\mathcal{C} = 0$	$\mathcal{C} \neq 0$	$\mathcal{C} = 0$
bhH/whH exists?	✓	✓	✓	(Minkowski)	×	×
ECs at bhH/whH	✓	✓	×	N/A	N/A	N/A
Throat exists?	✓	×	✓	N/A	✓	×
ECs at throat	Eq.(3.109)	N/A	×	N/A	×	N/A
ECs at $x = \infty$	×	×	×	N/A	×	×
Mass at $x = \infty$	$\mathcal{D}$	$\mathcal{D}$	0	0	$\mathcal{D}$	$\mathcal{D}$
ECs at $x = -\infty$	×	×	N/A($x \geq 0$)	N/A	×	×
Mass at $x = -\infty$	$\frac{\mathcal{C}^2}{\mathcal{D}}$	SCS($b(-\infty) = 0$)	SAF($x = 0$)	N/A	$\frac{\mathcal{C}^2}{\mathcal{D}}$	SCS($b(-\infty) = 0$)

3.5.2.2 $\mathcal{C} = 0$

From Eq.(3.12) we find

$$Y = x + |x| = \begin{cases} 2x, & x \geq 0, \\ 0, & x < 0. \end{cases} \tag{3.135}$$

Therefore, the spacetime must be restricted to the region $x \geq 0$, in which we have

$$a(x) = \frac{1}{4}, \quad b(x) = (x + \sqrt{x^2}) = 2x, \tag{3.136}$$

and

$$\rho(x) = p_r = p_\theta(x) = 0. \tag{3.137}$$

In fact, this is precisely the Minkowski solution, and will take its standard form, by setting $r = 2x$ and rescaling t.

3.5.3 $\mathcal{D} < 0$

Similar to the last subcase, now we also need to consider the cases $\mathcal{C} \neq 0$ and $\mathcal{C} = 0$ separately.

3.5.3.1 $\mathcal{C} \neq 0$

When $\mathcal{D} < 0$, we find that

$$b(x) = \begin{cases} \infty, & x = \infty, \\ 2^{1/3}\mathcal{C}, & x = x_m, \\ \infty, & x = -\infty, \end{cases} \tag{3.138}$$

where $x_m \equiv (\mathcal{C}^2 - \mathcal{D}^2)/(2\mathcal{C})$ [cf. Fig. 3.1(a)]. On the other hand, $a(x) = 0$ has no real roots, thus in the current case no black/white hole horizons exist.

But, as shown by Eq.(3.138), a throat still exists at $x = x_m$, at which the effective energy density ρ and pressures p_r and p_θ are still given by Eq.(3.108), from which we find that none of the three energy conditions is satisfied at this point.

At the spatial infinities $x \to \pm\infty$, we find that the effective energy density ρ and pressures p_r and p_θ are still given by Eqs.(3.110), (3.113), and(3.114), from which we can see that *none of the three energy conditions is satisfied at both $x = -\infty$ and $x = \infty$*. In addition, the asymptotic expression of $a(x)$ and $b(x)$ are still given by Eq.(3.111). Therefore, the total mass at $x \to \infty$ is given by

$$M_+ \quad = \quad \mathcal{D} < 0, \tag{3.139}$$

while the total mass at $x \to -\infty$ is given by

$$M_- = \frac{\mathcal{C}^2}{\mathcal{D}} < 0. \tag{3.140}$$

It can be shown that in the present case the quantum gravitational effects are also concentrated in the region near the throat, and are vanishing rapidly when away from it in each side of the throat.

3.5.3.2 $\mathcal{C} = 0$

In this case, we have

$$a(x) \;=\; \frac{(X+|\mathcal{D}|)\,X}{Y^2}, \quad b(x)=Y. \tag{3.141}$$

Thus, $a(x) = 0$ has no real roots, and $b(x)$ becomes a monotonically increasing function with $b(-\infty)=0$ and $b(\infty)=\infty$ [cf. Fig. 3.1(c)]. Therefore, in this case a throat does not exist.

At the spatial infinities $x \to \pm\infty$, we find that the effective energy density ρ and pressures p_r and p_θ are still given by Eq.(3.119), from which we find that none of the three energy conditions, WEC, SEC and DEC, is satisfied at the spatial infinity. In addition, the asymptotic expressions of $a(x)$ and $b(x)$ are still given by Eq.(3.120). Therefore, the total mass at $x\to\infty$ is given by

$$M_+ \;=\; \mathcal{D} < 0. \tag{3.142}$$

However, at $x=-\infty$ we have $b(-\infty)=0$, and the physical quantities, $\rho,\ p_r$ and p_θ, all become unbounded, so a spacetime curvature singularity appears at $x = -\infty$. Since no horizon exists, such a singularity is also naked.

This completes our analysis for the case $\Delta = 0$, and the main properties of these solutions are summarized in Table 3.2.

3.6 Spacetimes with $\Delta < 0$

In this case we have

$$a(x) = \frac{(x^2+|\Delta|)\,XY^2}{(X+\mathcal{D})\,Z^2}, \quad b(x) = \frac{Z}{Y}, \tag{3.143}$$

where $X,\ Y,\ Z$ are given by Eq.(3.12), while Δ is given by Eq.(3.13), from which we find $\Delta < 0$ implies

$$|\mathcal{D}| < |x_0|\,. \tag{3.144}$$

Then, we find that

$$b(x) = \begin{cases} \infty, & x = \infty, \\ 2^{1/3}\mathcal{C}, & x = x_m, \\ \infty, & x = -\infty, \end{cases} \tag{3.145}$$

where $x_m \equiv (\mathcal{C}^2 - x_0^2)/(2\mathcal{C})$ [cf. Fig. 3.1(a)].

To study the solutions further, as what we did in the last case, let us consider the solutions with $\mathcal{D} > 0$, $\mathcal{D} = 0$ and $\mathcal{D} < 0$, separately.

3.6.1 $\mathcal{D} > 0$

Then, we find $a(x)$ is nonzero for any $x \in (-\infty, \infty)$, and in particular we have

$$a(x) = \begin{cases} \frac{1}{4}, & x = \infty, \\ \frac{x_0^4}{4\mathcal{C}^2}, & x = -\infty. \end{cases} \tag{3.146}$$

Thus, in the current case horizons do not exist. But, a throat does exist, as shown by Eq.(3.145). At the throat, the effective energy density ρ and pressures p_r and p_θ are still given by Eq.(3.54), from which we find that WEC, SEC and DEC are still satisfied, provided that

$$|x_0| \leq \sqrt{\mathcal{C}(2\mathcal{D} - \mathcal{C})}\ , \ 0 < \mathcal{C} \leq 2\mathcal{D}. \tag{3.147}$$

In addition, we also have the constraint $|\mathcal{D}| < |x_0|$, as now we are considering the case $\Delta < 0$.

At the spatial infinities $x \to \pm\infty$, we find that the effective energy density ρ and pressures p_r and p_θ can be also written in the forms of Eq.(3.42), from which we can see that *none of the three energy conditions is satisfied at both* $x = -\infty$ *and* $x = \infty$.

The asymptotic expressions of $a(x)$ and $b(x)$ are still given by Eq.(3.43). Therefore, the total mass at $x \to \infty$ is given by

$$M_+ = \mathcal{D}, \tag{3.148}$$

while the total mass at $x \to -\infty$ is given by

$$M_- = \frac{\mathcal{D}\mathcal{C}^2}{x_0^2}. \tag{3.149}$$

It can be shown that the quantum gravitational effects are concentrated in the region near the throat, and are rapidly vanishing as away from the throat in each side of it only by proper choice of the free parameters involved in the solutions, as in the corresponding case $\Delta > 0,\ \mathcal{D} > 0$ and $x_0\mathcal{C} \neq 0$.

Although no horizons exist in the present case, the corresponding solution is very interesting on its own rights: *it represents a wormhole spacetime, in which all the three energy conditions, WEC, SEC, and DEC, are satisfied in the neighborhood of the throat, provided that Eq.(3.147) holds, while none of them is satisfied at the asymptotically flat regions (spatial infinities) $x \to \pm\infty$.*

It should be also noted that the above analysis does not cover the limit cases $x_0 \to 0$ and $\mathcal{C} \to 0$. However, since now $|\mathcal{D}| < |x_0|$, the cases $x_0 = 0,\ \mathcal{C} \neq 0$ and $x_0 = \mathcal{C} = 0$ do not exist. So, only the limiting case, $\mathcal{C} = 0,\ x_0 \neq 0$, exists.

• $\mathcal{C} = 0,\ x_0 \neq 0$**:** In this case, we have

$$a(x) = \frac{(x^2 + |\Delta|)\, X}{(X + \mathcal{D})\, Y^2}, \quad b(x) = Y. \tag{3.150}$$

Clearly, $a(x) = 0$ does not have real solutions, while $b(x)$ is a monotonically increasing function with $b(x = -\infty) = 0$, as shown in Fig. 3.1(c).

At the spatial infinities $x \to \pm\infty$, we find that the effective energy density ρ and pressures p_r and p_θ are still given by Eq.(3.84), from which we can see that *none of the three energy conditions is satisfied at both $x = -\infty$ and $x = \infty$.*

The asymptotic expression of $a(x)$ and $b(x)$ are still given by Eq.(3.85). Therefore, the total mass at $x \to \infty$ is given by

$$M_+ \;=\; \mathcal{D}. \tag{3.151}$$

However, at $x = -\infty$ we have $b(-\infty) = 0$, and the physical quantities, ρ, p_r and p_θ, all become unbounded, so a spacetime curvature singularity appears at $x = -\infty$.

3.6.2 $\mathcal{D} = 0$

From Eq.(3.11) we find that

$$a(x) = \frac{X^2Y^2}{Z^2}, \quad b(x) = \frac{Z}{Y}, \tag{3.152}$$

where X, Y, and Z are given by Eq.(3.12). From the above expressions, it can be shown that there are two asymptotically flat regions, corresponding to $x \to \pm\infty$, respectively. They are still connected by a throat located at x_m given by Eq.(3.26) [cf. Fig. 3.1(a)]. But since $a(x) \neq 0$ for any given $x \in (-\infty, \infty)$, as it can be seen from the above expression, horizons, either WHs or BHs, do not exist.

At the throat, the effective energy density ρ and pressures p_r and p_θ are given by

$$\rho = -\frac{5}{2^{8/3}\hat{\mathcal{C}}^2}, \;\; p_r = -p_\theta = -\frac{1}{2^{8/3}\hat{\mathcal{C}}^2}, \tag{3.153}$$

so none of the WEC, SEC, and DEC is satisfied.

At the spatial infinities $x \to \pm\infty$, we find that the effective energy density ρ and pressures p_r and p_θ take the forms,

$$
\begin{aligned}
\rho(x) &= \begin{cases} -\frac{5\mathcal{C}^6}{64x^8} + \mathcal{O}\left(\epsilon^9\right), & x \to \infty, \\ -\frac{5x_0^{16}}{64x^8\mathcal{C}^{10}} + \mathcal{O}\left(\epsilon^9\right), & x \to -\infty, \end{cases} \\
p_r(x) &= \begin{cases} -\frac{x_0^2}{4x^4} + \mathcal{O}\left(\epsilon^6\right), & x \to \infty, \\ -\frac{x_0^6}{4x^4\mathcal{C}^4} + \mathcal{O}\left(\epsilon^6\right), & x \to -\infty, \end{cases} \\
p_\theta(x) &= \begin{cases} \frac{x_0^2}{4x^4} + \mathcal{O}\left(\epsilon^6\right), & x \to \infty, \\ \frac{x_0^6}{4x^4\mathcal{C}^4} + \mathcal{O}\left(\epsilon^6\right), & x \to -\infty, \end{cases}
\end{aligned} \tag{3.154}
$$

from which we can see that *none of the three energy conditions is satisfied at both* $x = -\infty$ *and* $x = \infty$.

In addition, we also have

$$
\begin{aligned}
a(x) &= \begin{cases} \frac{1}{4}\left(1 + \frac{2x_0^2}{b^2}\right) + \mathcal{O}\left(\epsilon^3\right), & x \to \infty, \\ \frac{x_0^4}{4\mathcal{C}^4}\left(1 + \frac{2\mathcal{C}^4}{x_0^2 b^2}\right) + \mathcal{O}\left(\epsilon^2\right), & x \to -\infty, \end{cases} \\
b(x) &\simeq \begin{cases} 2x + \mathcal{O}\left(\epsilon\right), & x \to \infty, \\ -\frac{2x\mathcal{C}^2}{x_0^2} + \mathcal{O}\left(\epsilon\right). & x \to -\infty, \end{cases}
\end{aligned} \tag{3.155}
$$

from which we can see that the space-time is asymptotically flat as $x \to \pm\infty$.

Similar to the last subcase, the quantum gravitational effects are concentrated in the region near the throat, and are rapidly vanishing as away from the throat in each side of it for the proper choice of the free parameters, as in the corresponding case $\Delta > 0$, $\mathcal{D} = 0$ and $x_0\mathcal{C} \neq 0$.

In addition, the above analysis is valid only for $x_0\mathcal{C} \neq 0$. Otherwise, we have the following limiting case.

• $x_0 \neq 0,\ \mathcal{C} = 0$**:** Then, we have

$$a(x) = \frac{X^2}{Y^2}, \quad b(x) = Y. \tag{3.156}$$

Since $a(x) \neq 0$ for any given real value of x, as it can be seen from the above expression, horizons, either WHs or BHs, do not exist, but $b(x)$ is still a monotonically increasing function with $b(x = -\infty) = 0$, as shown in Fig. 3.1(c).

At the spatial infinities $x \to \pm\infty$, we find that the effective energy density ρ and pressures p_r and p_θ are given by

$$\begin{aligned}
\rho(x) &= \begin{cases} 0, \quad x \to \infty, \\ 0, \quad x \to -\infty, \end{cases} \\
p_r(x) &= \begin{cases} -\frac{x_0^2}{4x^4} + \mathcal{O}\left(\epsilon^6\right), & x \to \infty, \\ -\frac{16x^2}{x_0^4} - \frac{4}{x_0^2} + \frac{x_0^2}{4x^4} + \mathcal{O}\left(\epsilon^6\right), & x \to -\infty, \end{cases} \\
p_\theta(x) &= \begin{cases} \frac{x_0^2}{4x^4} + \mathcal{O}\left(\epsilon^6\right), & x \to \infty, \\ \frac{16x^2}{x_0^4} + \frac{4}{x_0^2} - \frac{x_0^2}{4x^4} + \mathcal{O}\left(\epsilon^6\right), & x \to -\infty, \end{cases}
\end{aligned} \tag{3.157}$$

from which we can see that *none of the three energy conditions is satisfied to the leading order of* $(1/x)$ *at both* $x = -\infty$ *and* $x = \infty$.

In addition, we also have

$$\begin{aligned}
a(x) &= \begin{cases} \frac{1}{4}\left(1 + \frac{2x_0^2}{b^2}\right) + \mathcal{O}\left(\epsilon^3\right), & x \to \infty, \\ \frac{4x^4}{x_0^4} + \frac{6x^2}{x_0^2} + \frac{7}{4} + \mathcal{O}\left(\epsilon^2\right), & x \to -\infty, \end{cases} \\
b(x) &\simeq \begin{cases} 2x + \mathcal{O}\left(\epsilon\right), & x \to \infty, \\ -\frac{x_0^2}{2x} + \mathcal{O}\left(\epsilon^3\right), & x \to -\infty, \end{cases}
\end{aligned} \tag{3.158}$$

from which we can see that the space-time is asymptotically flat as $x \to +\infty$, but a spacetime curvature singularity appears at $x = -\infty$, where $b(x = -\infty) = 0$, as it can be seen from the above expressions.

3.6.3 $\mathcal{D} < 0$

From Eq.(3.11) we find that

$$a(x) = \frac{(X + |\mathcal{D}|)\, XY^2}{Z^2}, \quad b(x) = \frac{Z}{Y}, \tag{3.159}$$

where X, Y, and Z are given by Eq.(3.12). From the above expressions, it can be shown that there are two asymptotically flat regions, corresponding to $x \to \pm\infty$, respectively. They are still connected by a throat located at x_m given by Eq.(3.26) [cf. Fig. 3.1(a)]. But since $a(x) \neq 0$ for any given x, horizons, either WHs or BHs, do not exist.

At the throat, the effective energy density ρ and pressures p_r and p_θ are given by Eq.(3.54). Then, it can be easily shown that none of the three energy conditions, WEC, SEC, and DEC, can be satisfied in the current case.

Similarly, the quantum gravitational effects are concentrated in the region near the throat for only when the free parameters are properly chosen, and are rapidly vanishing as away from the throat in each side of it.

At the spatial infinities $x \to \pm\infty$, we find that the expression of ρ, p_r, p_θ are still given by Eq.(3.42), from which we can see that *none of the three energy conditions is satisfied to the leading order of* $(1/x)$.

The asymptotic expressions of $a(x)$ and $b(x)$ are given by Eq.(3.43), and the total mass at $x \to \pm\infty$ is still given by Eq.(3.44), but since we now have $\mathcal{D} < 0$, the total mass becomes negative.

Similar to the last case, the above analysis holds only for $x_0\mathcal{C} \neq 0$. When $x_0\mathcal{C} = 0$, we find that only the possibility, $x_0 \neq 0$, $\mathcal{C} = 0$, is allowed.

- $x_0 \neq 0,\ \mathcal{C} = 0$**:** From Eq.(3.11) we find that

$$a(x) = \frac{(X + |\mathcal{D}|)\, X}{Y^2}, \quad b(x) = Y, \tag{3.160}$$

where X, Y, and Z are given by Eq.(3.12). Clearly, $a(x) = 0$ has no real roots, thus no horizons exist. On the other hand, $b(x)$ is still a monotonically increasing function with $b(x = -\infty) = 0$, as shown in Fig. 3.1(c).

At the spatial infinities $x \to \pm\infty$, we find that the effective energy density and pressures are still given by Eq.(3.84), from which we find that none of the three energy conditions, WEC, SEC, and DEC, is satisfied at the spatial infinities. In addition, the asymptotic behaviors of $a(x)$ and $b(x)$ are still given by Eq.(3.85). Therefore, the total mass at $x = \infty$ is still given by Eq.(3.71), which is always negative.

However, at $x = -\infty$ we have $b(-\infty) = 0$, and the physical quantities, ρ, p_r, and p_θ, all become unbounded, so a spacetime curvature singularity appears at $x = -\infty$.

This completes our analysis for the solutions with $\Delta < 0$, and the main properties of these solutions are summarized in Table 3.3.

3.7 Conclusions

In this chapter, we have studied in detail the main properties of spherically symmetric black/white hole solutions, found recently by Bodendorfer, Mele, and Münch [17], inspired by the effective loop quantum gravity, and paid particular attention to their local and global properties, as well as to the energy conditions of the

Table 3.3: The main properties of the solutions given by Eqs.(3.10)-(3.13) with $\Delta < 0$, for which no horizons exist in all these solutions. Here bhH $\equiv$ black hole horizon, whH $\equiv$ white hole horizon, ECs $\equiv$ energy conditions, SAF $\equiv$ spacetime is asymptotical flat, and SCS $\equiv$ spacetime curvature singularity. In addition, "✓" means yes, "×" means no, while "N/A" means not applicable.

Properties	$\Delta < 0$					
	$\mathcal{D} > 0$		$\mathcal{D} = 0$		$\mathcal{D} < 0$	
	$\mathcal{C}x_0 \neq 0$	$\mathcal{C} = 0,\ x_0 \neq 0$	$x_0\mathcal{C} \neq 0$	$\mathcal{C} = 0,\ x_0 \neq 0$	$\mathcal{C}x_0 \neq 0,$	$\mathcal{C} = 0,\ x_0 \neq 0$
bhH/whH exists?	×	×	×	×	×	×
Throat exists?	✓	×	✓	×	✓	×
ECs at throat	Eq.(3.147)	N/A	×	N/A	×	N/A
ECs at $x = \infty$	×	×	×	×	×	×
Mass at $x = \infty$	$\mathcal{D}$	$\mathcal{D}$	$-x_0^2$	$-x_0^2$ (SAF)	$\mathcal{D}$	$\mathcal{D}$
ECs at $x = -\infty$	×	×	×	×	×	×
Mass at $x = -\infty$	$\frac{\mathcal{D}\mathcal{C}^2}{x_0^2}$	SCS	$-\frac{\mathcal{C}^4}{x_0^2}$	SCS	$\frac{\mathcal{D}\mathcal{C}^2}{x_0^2}$	SCS

effective energy-momentum tensor of the spacetimes. Although this effective energy-momentum tensor is purely due to the quantum geometric effects, and is not related to any real matter fields, it does provide important information on how the spacetime singularity is avoided, and the deviations of the spacetimes from the classical one (the Schwarzschild solution). In particular, spacetime singularities inevitably occur in general relativity, as longer as matter fields satisfy some energy conditions, as follows directly from the Hawking-Penrose singularity theorems [20]. In addition, due to the Birkhoff theorem, the spacetime is uniquely described by the Schwarzschild black hole solution in general relativity. Therefore, the presence of this effective energy-momentum tensor also characterizes the deviations of the quantum solutions from the classical one.

The most general metric for static spherically symmetric spacetimes, without loss of the generality, can be always cast in the form,

$$ds^2 = -a(x)dt^2 + \frac{dx^2}{a(x)} + b^2(x)\left(d^2\theta + \sin^2\theta d^2\phi\right),$$

subjected to the following additional gauge transformations (gauge residuals),

$$t = \alpha\tilde{t} + t_0, \quad x = \xi(\tilde{x}), \tag{3.161}$$

where α and t_0 are constant, and $\xi(\tilde{x})$ is an arbitrary function of $\tilde{x}$. Therefore, in general the phase space are four-dimensional, spanned by (a, b, p_a, p_b), but with one constraint, the Hamiltonian constraint, $H_{\text{eff}} = 0$. So, the phase space is actually three-dimensional, and the trajectories of the system are uniquely determined once the three "initial" conditions are given. However, due to the polymerization (3.3), two new parameters are introduced, so the phase space is enlarged to five-dimensional, due to the polymerization quantizations. Nevertheless, the trajectories of the system are also gauge-invariant under the transformations (3.161), which reduce the dimensions of the phase space from five to three again. Therefore, *the phase space in this model is generically three-dimensional.*

The above general arguments can be seen clearly from the particular solutions considered in this chapter, and the three physically independent free parameters now can be chosen as $(\mathcal{C},\ \mathcal{D},\ x_0)$, defined explicitly by Eq.(3.9),

$$\mathcal{D} \equiv \frac{3CD}{2\sqrt{n}}, \quad \mathcal{C} \equiv \left(16C^2\lambda_1^2\right)^{1/6}, \quad x_0 \equiv \frac{\lambda_2}{\sqrt{n}}, \tag{3.162}$$

out of the five parameters, λ_1, λ_2, n, C, and D, introduced in [17]. Thus, in comparison with the relativistic case, the polymerizations introduce two more free parameters, and only when they vanish, i.e., $\lambda_1 = \lambda_2 = 0$ (or $\mathcal{C} = x_0 = 0$), can the solutions reduce to the Schwarzschild one with its mass $M_{BH} = \mathcal{D}$, and a spacetime curvature singularity located at the center ($b = 0$) appears. If any of them vanishes, the corresponding moment conjugate, P_1 or P_2, can become unbounded at some points (or in some regions) of the spacetime. As a result, spacetime curvature singularities will appear. From Tables II - IV it can be seen that in the current model the condition for such singularities to appear is indeed $\lambda_1 = 0$ (or $\mathcal{C} = 0$), the cases corresponding to Fig. 1(c).

The asymptotical properties of the spacetimes also depend on the choices of the two parameters $\mathcal{C}$ and x_0. In particular, when $\mathcal{C}x_0 \neq 0$, we have $x \in (-\infty, \infty)$, and a minimal point (throat) of $b(x)$ always exists, with $b(\pm\infty) = \infty$ [cf. Fig. 3.1(a)]. When $\mathcal{C} \neq 0$ but $x_0 = 0$, the range of x is restricted to $x \in (0, \infty)$ with $b(0) = \infty$ and $b(\infty) = \infty$. In this case, a minimum of $b(x)$ also exists [cf. Fig. 3.1(b)]. When $\mathcal{C} = 0$ and $x_0 \neq 0$, the range of x is also $x \in (-\infty, \infty)$, but now $b(x)$ is a monotonically increasing function of x with $b(-\infty) = 0$ and $b(\infty) = \infty$ [cf. Fig. 3.1(c)].

In [17, 18, 24], the authors considered the case

$$\Delta \equiv \mathcal{D}^2 - x_0^2 > 0,\ \mathcal{D} > 0,\ \mathcal{C}x_0 \neq 0, \tag{3.163}$$

for which the black and white hole horizons always exist, located at

$$x_H^{\pm} = \pm\sqrt{\Delta},$$

respectively, as shown in Sec. 3.4.1 [See also Table 3.1]. The corresponding spacetime has two asymptotically flat regions $x \to \pm\infty$, which are connected by a throat located at

$$x_m = \frac{1}{2\mathcal{C}}\left(\mathcal{C}^2 - x_0^2\right),$$

as can be seen from Eq.(3.26) and Fig. 3.1(a)]. It is remarkable to note that in this case the surface gravity at the black hole horizon $x = x_H^+$ is always positive, while at the white hole horizon $x = x_H^-$, it is always negative, as the latter represents an antitrapped surface. In the asymptotical region $x \to +\infty$, the ADM mass reads

$$M_{BH} = \mathcal{D}, \tag{3.164}$$

while in the asymptotical region $x \to -\infty$, it reads

$$M_{WH} = \frac{\mathcal{D}\mathcal{C}^2}{x_0^2}, \tag{3.165}$$

as given explicitly in Eq.(3.44), which are all positive, too. All the above properties are mainly due to the fact that the Komar energy density [21] $(\rho + \sum_i p_i)$ remains positive over a large region of the spacetime, despite that all the three energy conditions are violated in most part of the spacetime, including the regions near the throat and horizons, as well as in the two asymptotically flat regions.

In addition, the quantum gravitational effects are mainly concentrated in the neighborhood of the throat. However, in the current model, such effects can be still large at the two horizons even for solar mass black/white hole spacetimes, depending on the choice of the free parameters. They become negligible near the black/white hole horizons only for some particular choices of these free parameters [cf. Eq.(3.50)].

Moreover, the ratio M_{BH}/M_{WH} can take in principle any value, $M_{BH}/M_{WH} \in (0, \infty)$, as the three parameters $\mathcal{C},\ \mathcal{D},\ x_0$ now are all arbitrary (subjected only to the constraint $\mathcal{C} \geq 0$ as can be seen from Eq.(3.162)) [18].

It should be also noted that the region defined by Eq.(3.163) is quite small in the whole three-dimensional phase space, spanned by $(\mathcal{C},\ \mathcal{D},\ x_0)$, where

$$\mathcal{D},\ x_0 \in (-\infty, \infty), \quad \mathcal{C} \in [0, \infty), \tag{3.166}$$

although the cases with $\mathcal{D} = 0$, or $\mathcal{C} = 0$, or $x_0 = 0$ can be obtained only by taking certain proper limits of the five free parameters, $\lambda_1,\ \lambda_2,\ n,\ C$, and D, as explained explicitly in the content.

With all the above in mind, we have explored the whole three-dimensional phase space of the three free parameters $(\mathcal{C},\ \mathcal{D},\ x_0)$, and found that the solutions have very rich physics. In particular, the existence of the black/white horizons crucially depends on the values of Δ. When $\Delta > 0$, they always exist and are located at $x_H^{\pm} = \pm\sqrt{\Delta}$, respectively. The spacetime in the region $x_H^- < x < x_H^+$ becomes trapped. When $\Delta = 0$, they also exist, but now become degenerate, $x_H^{\pm} = 0$, that is, $a(x) = 0$ now has a double root, the trapped region $(a(x) < 0)$ disappears, and the surface gravity at the horizon is always zero now, quite similar to the extreme case of the charged RN solution with $|e| = m$. When $\Delta < 0$, the equation $a(x) = 0$ has no real roots, and, as a result, in this case no horizons exist at all, neither a trapped region.

Thus, depending on the choices of the three free parameters, $\mathcal{C},\ \mathcal{D},\ x_0$, there are various cases that all have different (local and global) properties. In Secs. 3.4 - 3.6, we have studied the cases $\Delta > 0$, $\Delta = 0$, and $\Delta < 0$, separately, and in each of which all the three possible choices of $\mathcal{C}$ and x_0, as illustrated in Fig. 3.1, raise and have been studied in detail. Their main properties are summarized in the three tables, Tables 3.1 - 3.3. From these tables, the following interested cases are worthwhile of particularly mentioning:

- **$\Delta > 0,\ \mathcal{D} > 0,\ \mathcal{C}x_0 \neq 0$:** As mentioned above, in this case the solutions were first studied in [17,18,24], and in the present chapter we have studied them in detail, and found the remarkable features stated above. In particular, we have shown explicitly that the quantum geometric efforts are mainly concentrated in the region near the throat (transition surface). However, in the current model such effects can be still large at the black/white hole horizons even for solar mass black/white holes. They become negligible only in a restricted region of the 3D phase space, defined by Eq.(3.50).

- $\Delta = 0,\ \mathcal{D} > 0,\ \mathcal{C}x_0 \neq 0$**:** In this case, the black/white horizons coincide and all are located at $x_H^{\pm} = 0$, so the surface gravity at the horizon is zero, quite similar to the extreme case $|e| = m$ of the RN solution in general relativity. But, it is fundamentally different from the RN solution, as now there are no spacetime curvature singularities, and the spacetime becomes asymptotically flat in both of the regions $x \to \pm\infty$.
In addition, all the three energy conditions are satisfied at the horizon, but at the throat $x = x_m$, they are satisfied only when $\mathcal{D} = \mathcal{C}$, for which the throat coincides with the horizon, i.e., $x_m = x_H^{\pm} = 0$.
Similar to the last case (in fact, in all the cases, including $\Delta > 0$ and $\Delta < 0$), none of the three energy conditions is satisfied at the spatial infinities $b(\pm\infty) = \infty$, although the quantum gravitational effects are also mainly concentrated at the throat, as shown in Fig. 3.15. In this case, the black/white hole masses are also given by Eqs.(3.164) and (3.165) but now with $|x_0| = \mathcal{D}$.

- $\Delta < 0,\ \mathcal{D} > 0,\ \mathcal{C}x_0 \neq 0$**:** In this case, the function $a(x)$ is always positive, and no horizons exist, although a throat does exist, as shown in Fig. 3.1(a), at which all the three energy conditions are satisfied, as long as the conditions (3.147) hold. By properly choosing the free parameters, the quantum geometric effects can be made to be mainly concentrated at the throat, and the spacetime is asymptotically flat at both of the two limits, $x \to \pm\infty$, with the ADM masses, given, respectively, by Eqs.(3.164) and (3.165), which can be all positive. However, since no horizons exist, the spacetimes now represent wormholes without any spacetime curvature singularities. Again, this is not in conflict to the Hawking-Penrose singularity theorems [20], as none of the three energy conditions holds at the asymptotically flat regions, $x = \pm\infty$.

The main properties of other interesting cases can be found in Tables 3.1 - 3.3.

It should be noted that, although in this chapter we have studied only the solutions found recently in [17], we expect that quantum black hole solutions share similar properties. In particular, due to the quantum geometric effects, an effective energy-momentum tensor inevitably appears, which generically violates the weak/strong energy conditions at the throat, so the spacetime is opened up by such repulsive forces. As a result, the throat will connect two asymptotically flat regions. For spherical spacetimes [26], such effects are uniquely characterized by the two quantum parameters λ_1 and λ_2. The classical limit is obtained by setting $\lambda_1 = \lambda_2 = 0$. Therefore, the singularities inside the classical black holes are resolved by the polymerization [4], given by Eq.(3.3), provided that

$$\lambda_1 \lambda_2 \neq 0. \tag{3.167}$$

If any of these two parameters vanishes, a spacetime curvature singularity can appear, as it is shown explicitly by the current model.

Therefore, spherically quantum black holes should generically also contain three free parameters, which uniquely determine the location of the throat and the two masses, measured by observers located in the two asymptotically flat regions. Here we use "black holes" to emphasize the fact that in such resultant spacetimes white/black hole horizons are not necessarily always present, and spacetimes with wormhole structures (without horizons) can be equally possible, unless the two free parameters λ_1 and λ_2 are fixed by some physical considerations [9, 23, 26]. It is also equally true that the two (Komar) masses are independent and can be assigned arbitrary values, unless additional physics is taken into account [9, 17, 18, 23]. To understand these issues further, one way is to consider the formation of such spacetimes from gravitational collapse of realistic matter fields [27–34].

Finally, we would like to mention that to get a universal curvature upper bound in these polymer black holes, we need to impose specific relations between black and white hole masses [17], which amounts to impose further constraint in the parameter space. In this chapter, we did not impose this condition in order to study properties in the whole parameter space. To overcome this problem, recently BMM proposed another set of canonical variables in which one of the canonical momentum is precisely the square root of the Kretschmann scalar [18]. In this new model, a universal curvature upper bound can be obtained without any further constraint on the relation between black and white hole masses.

CHAPTER FOUR

Understanding quantum black holes from quantum reduced loop gravity

This chapter is published in [2]: W. C. Gan, G. Ongole, E. Alesci, Y. An, F. W. Shu and A. Wang, Understanding quantum black holes from quantum reduced loop gravity, Phys. Rev. D **106**, no.12, 126013 (2022).

4.1 Abstract

In this chapter, we systematically study the top-down model of loop quantum black holes (LQBHs), recently derived by Alesci, Bahrami and Pranzetti (ABP). Starting from the full theory of loop quantum gravity, ABP constructed a model with respect to coherent states peaked around spherically symmetric geometry, in which both holonomy and inverse volume corrections are taken into account, and shown that the classical singularity used to appear inside the Schwarzschild black hole is replaced by a regular transition surface. To understand the structure of the model, we first derive several well-known LQBH solutions by taking proper limits. These include the Böhmer-Vandersloot and Ashtekar-Olmedo-Singh models, which were all obtained by the so-called bottom-up polymerizations within the framework of the minisuperspace quantizations. Then, we study the ABP model, and find that the inverse volume corrections become important only when the radius of the two-sphere is of the Planck size. For macroscopic black holes, the minimal radius obtained at the transition surface is always much larger than the Planck scale, and hence these corrections are always sub-leading. The transition surface divides the whole spacetime into two regions, and in one of them the spacetime is asymptotically Schwarzschild-like, while in the other region, the asymptotical behavior sensitively depends on the ratio of two

spin numbers involved in the model, and can be divided into three different classes. In one class, the spacetime in the 2-planes orthogonal to the two spheres is asymptotically flat, and in the second one it is not even conformally flat, while in the third one it can be asymptotically conformally flat by properly choosing the free parameters of the model. In the latter, it is asymptotically de Sitter. However, in any of these three classes, sharply in contrast to the models obtained by the bottom-up approach, the spacetime is already geodesically complete, and no additional extensions are needed in both sides of the transition surface. In particular, identical multiple black hole and white hole structures do not exist.

4.2 Introduction

Recently, a new technique (Quantum Reduced Loop Gravity - QRLG) aimed to disentangle those ambiguities was proposed by Alesci, Bahrami and Pranzetti (ABP), the so-called top-down approach [35]. QRLG is based on the tentative of reverting the reduction-quantization process to implement a quantum symmetry reduction. Performing gauge fixing to adapt the full quantization to the symmetry compatible coordinates, QRLG allows to study the homogeneous spacetimes as coherent states of the full theory retaining all the quantum degrees of freedom of LQG. In this sense, QRLG doesn't need an external area gap or an ad-hoc Hilbert space, because it just uses the full LQG Hilbert space. QRLG program has been successfully applied to cosmology [36] and a direct link to LQC has been unveiled [37]. However, the inclusion of new degrees of freedom also opens the possibility for new scenarios as the replacement of the big bounce scenario [38] with the emergent bouncing one [39]. The application of QRLG to the interior of a black hole [40,41] has been recently performed and showed a completely new possibility. The black hole singularity is replaced by a bounce followed by an expanding Universe that could be asymptotically de Sitter [42].

In this chapter, we shall study the ABP model in detail and confirm several major conclusions obtained in [41, 42], and meanwhile clarify some silent points. In particular, the article is organized as follows. In Sec. 4.3, we provide a brief review of the ABP model [40–42], by paying particular attention to its semi-classical limit conditions, which are essential in order to understand the physical implications of the model. In Sec. 4.4, we first consider its classical limit, whereby the physical interpretation of quantities of the ABP model become clear, and then obtain the Böhmer-Vandersloot (BV) [15] and Ashtekar-Olmedo-Singh (AOS) models [9, 23] by taking proper limits and replacements. In doing so, we look for the possible relation among these models. Although formally we can obtain all these models, they all fall to the case where the semi-classical limit conditions of the ABP model are not satisfied. As a result, these models cannot be embedded properly into the ABP model. However, we do find that such derivation is helpful in understanding the structure of the ABP model. In Sec. 4.5, we study the ABP model without the inverse volume corrections in detail, by first showing that such corrections become important only when the curvature becomes the order of the Planck scale. The subsequent detailed analysis shows that the minimal radius of the two-sphere obtained at the transition surface is always much larger than the Planck scale for macroscopic black holes. As a result, the inverse volume corrections should be always sub-leading for such black holes. In Sec. 4.6, we confirm this by focusing only on the cases with $\gamma = 0.274$ obtained by the considerations of black hole entropy [43], and j_x and j given by Eq.(4.21) below, obtained by demanding that the spatial manifold triangulation remain consistent on both sides of the black hole horizons [42]. Our main results are summarized in Sec. 4.7, while in Appendix B, we provide some properties of the Struve functions.

In this chapter, we shall use ℓ_p, m_p, τ_p to denote, respectively, the Planck length, mass and time. In all the numerical plots, we shall use them as the units. For example, when plotting a figure with $m = 1$ we always mean $m/m_p = 1$, and so on.

4.3 Effective Hamiltonian of Internal spherical Black Hole Spacetimes

Spherically symmetric spacetimes inside black holes can be written in the form

$$ds^2 = -N(\tau)^2 d\tau^2 + \Lambda(\tau)^2 dx^2 + R(\tau)^2 d\Omega^2, \tag{4.1}$$

where $N(\tau)$ is the lapse function and $d\Omega^2 \equiv d\theta^2 + \sin^2\theta d\phi^2$. Clearly, the above metric is invariant under the following transformations

$$\tau = \xi(\tau'), \quad x = a_0 x' + b_0, \tag{4.2}$$

where $\xi(\tau')$ is an arbitrary function of τ' and a_0 and b_0 are arbitrary constants.

4.3.1 Classical Spherical Spacetimes and Canonical Variables

It should be noted that, instead of using the canonic variables (Λ, R) and their momentum conjugates (P_Λ, P_R), one often uses (p_b, b, p_c, c) [23], which can be obtained by comparing the gravitational connection $A^i_a \tau_i dx^a$ and the spatial triads $E^a_i \tau^i \partial_a$, given in [23, 42], and yield

$$\begin{aligned} p_c &= R^2, \quad p_b = L_0 R\Lambda, \quad b = -\frac{\gamma G}{R} P_\Lambda, \\ c &= -\frac{\gamma G L_0}{R}\left(P_R - \frac{\Lambda P_\Lambda}{R}\right), \end{aligned} \tag{4.3}$$

where L_0 is a constant, and related to $\mathcal{L}_0$ introduced in [42] by $L_0 = 2\mathcal{L}_0$. Note that in writing down the above expressions we assumed $p_c > 0$. With the choice of the lapse function [9, 23]

$$N_{cl} = \gamma b^{-1}\text{sgn}(p_c)\,|p_c|^{1/2} = -\frac{R^2}{GP_\Lambda}, \tag{4.4}$$

we find that the metric (4.1) takes the form

$$ds^2 = -\frac{\gamma^2 p_c(T)}{b^2(T)}dT^2 + \frac{p_b^2(T)}{L_0^2 p_c(T)}dx^2 + p_c(T)d\Omega^2, \tag{4.5}$$

where [1]

$$T \equiv \frac{\tau}{2Gm} + \log(2Gm). \tag{4.6}$$

Then, the corresponding classical Hamiltonian is given by

$$\begin{aligned} H_{cl}[N_{cl}] &\equiv N_{cl}\mathcal{H}_c \\ &= -\frac{1}{2G\gamma}\left(2c\,p_c + \left(b + \frac{\gamma^2}{b}\right)p_b\right) \\ &= \frac{L_0 R^2}{GP_\Lambda}\left(\frac{GP_\Lambda P_R}{R} - \frac{GP_\Lambda^2\Lambda}{2R^2} + \frac{\Lambda}{2G}\right). \end{aligned} \tag{4.7}$$

4.3.2 Quantum Black Holes in QRLG

Within the framework of QRLG, starting from a partial gauge fixing of the full LQG Hilbert space, ABP [40–42] studied the interior of a Schwarzschild black hole, and derived an effective Hamiltonian by including the inverse volume and coherent state sub-leading corrections, which differs crucially from the ones introduced previously in the minisuperspace models. In particular, by fixing the quantum parameters associated with the structure of coherent states through geometrical considerations, the authors found that the post-bounce interior geometry sensitively depends on the value of the Barbero-Immirzi parameter γ, and that the value $\gamma \simeq 0.274$, deduced

[1] It should be noted that the parameter m used in [9, 15, 23] corresponds to Gm introduced in this chapter.

from the SU(2) black hole entropy calculations in LQG [43,44], gives rise to an asymptotically de Sitter geometry in the interior region [2].

Introducing the following parameters

$$\begin{aligned}
A &\equiv 2{\ell_p}^2\left(\frac{{\ell_p}^2\gamma^2}{\beta^2}-\frac{4\gamma^2}{\delta_x}+\frac{4(3-\nu)\gamma^2}{\delta}\right),\\
B &\equiv {\ell_p}^2\left(\frac{{\ell_p}^2\gamma^2}{\beta^2}-\frac{8\gamma^2}{\delta_x}+\frac{8(3\nu-1)\gamma^2}{\delta}\right),\\
C &\equiv 2{\ell_p}^2\left(\frac{{\ell_p}^2\gamma^2}{\alpha^2}+\frac{12\gamma^2}{\delta_x}-\frac{4(1+\nu)\gamma^2}{\delta}\right),
\end{aligned} \tag{4.8}$$

and the functions

$$\begin{aligned}
X &\equiv \alpha\gamma G\left(\frac{P_\Lambda}{R^2}\right), \quad Y\equiv\beta\gamma G\left(\frac{P_R}{R\Lambda}-\frac{P_\Lambda}{R^2}\right),\\
Z &\equiv 8\gamma^2\cos\left(\frac{\alpha}{R}\right)\sin^2\left(\frac{\alpha}{2R}\right),
\end{aligned} \tag{4.9}$$

we find that the effective Hamiltonian of the ABP model can be cast in the form

$$\mathcal{H}_{int}^{IV+CS} = -\frac{\mathcal{L}_0 R^2\Lambda}{2\alpha^2\gamma^2 G}\mathcal{C}(\tau), \tag{4.10}$$

where

$$\begin{aligned}
\mathcal{C}(\tau) \equiv \frac{\alpha}{\beta}\sin[Y]\Bigg\{&\left(1+\frac{A}{R^2}\right)\pi h_0[X]\\
&+2\left(1+\frac{B}{R^2}\right)\sin[X]\Bigg\}\\
&+Z+\left(1+\frac{C}{R^2}\right)\pi\sin[X]h_0[X],
\end{aligned} \tag{4.11}$$

and $\mathcal{L}_0$ denotes the length of the fiducial cell with $x\in[-\mathcal{L}_0,\mathcal{L}_0]$, and ℓ_p is the Planck length with $\ell_p\equiv\sqrt{\hbar G/c^3}$, while G and c are the Newton's constant and the speed of light, respectively. The super indices "IV" and "CS" stand for, respectively, the inverse volume and coherent state, while the dimensionless parameters $\delta,\ \delta_x$ and ν are

[2] Note that, instead of using the SU(2) black hole entropy as done in [43, 44], if one uses the U(1) black hole entropy arguments, the parameter γ was found to be $\gamma\simeq 0.2375$ [11].

the spread parameters, characterizing the coherent state corrections. The terms proportional to the constants A, B and C characterize the inverse volume corrections and are subdominant [42]. The function $h_0[X]$ denotes the zeroth-order Struve function and its series expansion reads [45]

$$h_0[z] = \frac{2}{\pi}\left(z - \frac{z^3}{1^2 \cdot 3^2} + \frac{z^5}{1^2 \cdot 3^2 \cdot 5^2} - ...\right). \tag{4.12}$$

In Fig. 4.1, we plot out the Struve function h_0 together with h_{-1}, as the latter will appear in the dynamical equations. In general, the ν-th order Struve functions are defined by Eq.(B.1) in Appendix A, in which some of their properties are also given. For more details, we refer readers to [45].

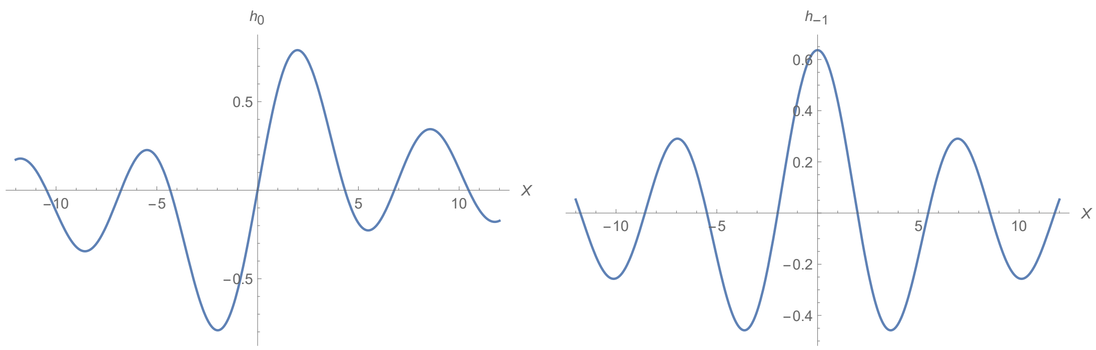

(a) (b)

Figure 4.1: The Struve functions $h_0[X]$ and $h_{-1}[X]$.

In terms of the spin numbers j and j_x, the parameters α and β are given by

$$\alpha \equiv 2\pi\sqrt{\gamma j_x}\,\ell_p, \quad \beta \equiv 4\sqrt{\frac{8\pi\gamma}{j_x}}\,j\,\ell_p, \tag{4.13}$$

where j_x denotes the averaged spin number of all plaquettes that tessellate the 2-sphere S^2 spanned by (θ, ϕ), while j is the averaged spin number associated with the links dual to the plaquettes in both (θ, x) and (ϕ, x) planes. It must be noted that this effective Hamiltonian is valid only in the semi-classical limits [42]

$$j,\ j_x \gg 1. \tag{4.14}$$

To understand further the geometrical meaning of j and j_x, we introduce the coordinate lengths along $x,\ \theta,\ \phi$ directions by $\epsilon_x,\ \epsilon_\theta,\ \epsilon_\phi$, respectively. Due to the spherical symmetry, we have $\epsilon_\theta = \epsilon_\phi \equiv \epsilon$. Then, we introduce two new quantities $\mathcal{N}$ and $\mathcal{N}_x$, in terms of which ϵ and ϵ_x can be written as

$$\epsilon \equiv \frac{2\pi}{\mathcal{N}}, \quad \epsilon_x \equiv \frac{\mathcal{L}_0}{\mathcal{N}_x}, \tag{4.15}$$

where $\mathcal{N}^2/2$ is the total number of the plaquettes on S^2, and $\mathcal{N}_x$ denotes the total number of plaquettes in the x direction for a given fiducial length $\mathcal{L}_0$. The effective Hamiltonian (4.10) was obtained under the assumption

$$\mathcal{N},\ \mathcal{N}_x \gg 1 \quad \text{or} \quad \epsilon,\ \epsilon_x \ll 1. \tag{4.16}$$

To find the relations between $(\mathcal{N},\ \mathcal{N}_x)$ and (j, j_x), we can calculate the area of a given S^2 and the volume of a given spatial three-surface spanned by x, θ, ϕ, which are given, respectively, by

$$A(R) = 4\pi R^2 = 8\pi\gamma\ell_p^2 \sum_{p\in S^2} \tilde{j}_x^p \simeq 8\pi\gamma\ell_p^2 \left(\frac{\mathcal{N}^2}{2} j_x\right), \tag{4.17}$$

$$V(\Sigma) = 8\pi\mathcal{L}_0\Lambda R^2 \simeq 4\left(8\pi\gamma\ell_p^2\right)^{3/2} j\sqrt{j_x}\mathcal{N}_x\mathcal{N}^2, \tag{4.18}$$

where $\tilde{j}_x^p$ is the spin number associated with the link dual to the given plaquettes p on S^2. In the limit $\mathcal{N} \gg 1$, the sum of $\tilde{j}_x^p$ in Eq.(4.17) was approximated by the average spin j_x of a single cell times the total number of the plaquettes in S^2. In the last step of Eq.(4.18), the average spin number j is associated with the links dual to the plaquettes in both (x, θ)- and (x, ϕ)-planes. Therefore, we find

$$\mathcal{N} = \frac{R}{\sqrt{\gamma\ell_p^2}}\left(\frac{1}{\sqrt{j_x}}\right), \quad \mathcal{N}_x = \frac{\mathcal{L}_0\Lambda}{4\sqrt{8\pi\gamma\ell_p^2}}\left(\frac{\sqrt{j_x}}{j}\right). \tag{4.19}$$

Inserting Eq.(4.19) into Eq.(4.15), we obtain

$$\epsilon = \frac{\alpha}{R}, \quad \epsilon_x = \frac{\beta}{\Lambda}, \tag{4.20}$$

where α and β are defined by Eq.(4.13).

It should be noted that the understanding of the geometrical meaning of $\mathcal{N}, \mathcal{N}_x, j$ and j_x is important for our following discussions, especially when we consider some specific models within the framework of QRLG. As to be seen below, both of the semi-classical limit conditions (4.14) and (4.16) must be fulfilled, in order to have the effective Hamiltonian (4.10) valid. These also provide the keys for us to understand the semi-classical structures of black holes in the framework of LQG.

We further note that, by demanding that the spatial manifold triangulation remain consistent on both sides of the black hole horizons, ABP found [42]

$$j = \gamma j_x, \tag{4.21}$$

for which we have

$$\eta \equiv \frac{\alpha}{\beta} = \frac{\sqrt{2\pi}}{8\gamma}, \tag{4.22}$$

as can be seen from Eq.(4.13). Then, in the effective Hamiltonian (4.10) five new parameters

$$(\gamma, j; \nu, \delta, \delta_x) \quad \text{or} \quad (\gamma, \alpha; \nu, \delta, \delta_x),$$

are present in addition to $G, c, \hbar$, where (ν, δ, δ_x) are related to the inverse volume corrections. One of the purposes of this chapter is to understand their effects on the local and global properties of the spacetimes.

It should be noted that the two spin numbers j and j_x used in this chapter, which are consistent with those used in [42], are different from the ones $(\hat{j}, \hat{j}_0)$

introduced in [41] [3]. In particular, we have

$$\hat{j} = \sqrt{8\pi}\, j, \quad \hat{j}_0 = \frac{\pi}{2} j_x. \tag{4.23}$$

To write down the corresponding dynamic equations for the effective Hamiltonian (4.10), using the gauge freedom (4.2), ABP chose the lapse function $N(\tau)$ as

$$N(\tau) = -\frac{2\alpha\gamma}{mGW}, \tag{4.24}$$

where m is a mass parameter, and W is defined as

$$W = \pi h_0[X] + 2\sin[X]. \tag{4.25}$$

Taking $\hbar \to 0$, it reduces to

$$N_c \equiv \lim_{\hbar \to 0} N = -\frac{R^2}{2mG^2 P_\Lambda}, \tag{4.26}$$

which corresponds to the classical limit, and m represents the mass of the Schwarzschild black hole. Taking Eq.(4.6) into account, we find that

$$N_c^2 d\tau^2 = N_{cl}^2 dT^2, \quad N_{cl} = 2GmN_c, \tag{4.27}$$

where N_{cl} and N_c are given, respectively, by Eqs.(4.4) and (4.26).

Then, the smeared effective Hamiltonian of Eq.(4.10) with the choice of the lapse function (4.24) is given by

$$H_{int}^{IV+CS}[N] \equiv N(\tau)\mathcal{H}_{int}^{IV+CS} = \frac{\mathcal{L}_0 R^2 \Lambda}{\alpha\gamma m G^2 W}\mathcal{C}(\tau). \tag{4.28}$$

Hence, the corresponding dynamical equations can be cast in the form

$$-2Gm\frac{z}{\ell}R' = \frac{R\cos[Y]}{W}\mathcal{D}, \tag{4.29}$$

$$-2Gm\frac{z}{\ell}P_\Lambda' = \frac{RP_R\cos[Y]}{\Lambda W}\mathcal{D}, \tag{4.30}$$

[3] Note that, instead of using (j, j_0) as those adopted in [41], here we use the symbols with hats, in order to distinguish them from the ones used in this chapter.

$$
\begin{aligned}
-2Gm\frac{z}{\ell}\frac{\Lambda'}{\Lambda} &= -\frac{\cos[Y]}{W}\mathcal{D} + \frac{1}{W^2}\Bigg\{\pi h_{-1}[X]\left[2\left(1+\frac{C}{R^2}\right)\sin^2[X] - Z\right] \\
&+\cos[X]\left[\left(1+\frac{C}{R^2}\right)\pi^2 h_0^2[X] - 2Z\right] \\
&+\frac{2\pi\alpha(A-B)}{\beta R^2}\sin[Y]\Big(\sin[X]h_{-1}[X] - \cos[X]h_0[X]\Big)\Bigg\}, \qquad (4.31)\\
-2Gm\frac{z}{\ell}P_R' &= \frac{RP_R - 2\Lambda P_\Lambda}{RW}\cos[Y]\mathcal{D} + \frac{2\pi\Lambda P_\Lambda}{RW}\sin[X]h_{-1}[X]\left(1+\frac{C}{R^2}\right) \\
&+\frac{2\pi\Lambda}{RW}h_0[X]\left\{\left(\frac{C}{\alpha\gamma G}\right)\sin[X] + P_\Lambda\cos[X]\left(1+\frac{C}{R^2}\right)\right\} \\
&+\frac{2\Lambda\sin[Y]}{RW}\Bigg\{\frac{\alpha\pi}{\beta}P_\Lambda h_{-1}[X]\left(1+\frac{A}{R^2}\right) + \frac{A}{\beta\gamma G}\pi h_0[X] + \frac{2B}{\beta\gamma G}\sin[X] \\
&+\frac{2\alpha}{\beta}P_\Lambda\cos[X]\left(1+\frac{B}{R^2}\right)\Bigg\} - \frac{4\gamma\Lambda}{GW}\left\{\sin\left(\frac{\alpha}{R}\right) - \sin\left(\frac{2\alpha}{R}\right)\right\}, \\
& \qquad (4.32)
\end{aligned}
$$

where

$$
\mathcal{D}(X) \equiv \left(1+\frac{A}{R^2}\right)\pi h_0[X] + 2\left(1+\frac{B}{R^2}\right)\sin[X], \qquad (4.33)
$$

and a prime denotes the ordinary derivative with respect to z, with $z \equiv \exp(-\tau/\ell)$, where ℓ is a constant and has the length dimension. The function $h_{-1}[X]$ ($\equiv dh_0[X]/dX$) denotes the Struve function of order -1. In Appendix A, we present some basic properties of these functions, and for other properties of them, we refer readers to [45].

4.4 Some Known Loop Quantum Black Holes as Particular Limits of the ABP Model

To understand the quantum reduced loop black hole (QRLBH) spacetimes with both of the holonomy and inverse volume corrections, in this section let us first consider some limits of the parameters involved, and derive several well-known spacetimes. In doing so, we can gain a better understanding of the QRLBH spacetimes and their relation with other models.

4.4.1 Classical Limit

The classical limit is obtained by taking $\hbar \to 0$, that is, by setting $\ell_p = 0$, which leads to

$$
\begin{aligned}
& A = B = C = 0, \\
& \mathcal{D} \simeq W \simeq 4X, \quad Z \simeq \frac{2\gamma^2\alpha^2}{R^2}.
\end{aligned} \tag{4.34}
$$

Then, Eqs.(4.29) - (4.32) reduce respectively to

$$
-2Gm\frac{z}{\ell}R' = R, \tag{4.35}
$$

$$
-2Gm\frac{z}{\ell}P'_\Lambda = \frac{RP_R}{\Lambda}, \tag{4.36}
$$

$$
-2Gm\frac{z}{\ell}\frac{\Lambda'}{\Lambda} = -\frac{G^2P_\Lambda^2 + R^2}{2G^2P_\Lambda^2}, \tag{4.37}
$$

$$
-2Gm\frac{z}{\ell}P'_R = 3P_R - \frac{2\Lambda P_\Lambda}{R} + \frac{\Lambda R}{G^2P_\Lambda}, \tag{4.38}
$$

while the effective Hamiltonian (4.10) reduces to (4.7) with $L_0 = 2\mathcal{L}_0$. Then, from the Hamiltonian constraint $\mathcal{H}_c = 0$, we find the following two useful expressions

$$
\frac{RP_R}{\Lambda} = \frac{G^2P_\Lambda^2 - R^2}{2G^2P_\Lambda}, \tag{4.39}
$$

$$
\frac{\Lambda P_\Lambda}{R} = 2P_R + \frac{R\Lambda}{G^2P_\Lambda}. \tag{4.40}
$$

Inserting them into Eqs.(4.36) and (4.38), respectively, we obtain two new equations for P'_Λ and P'_R, and together with the other two, they can be cast in the forms

$$
\begin{aligned}
-2Gm\frac{z}{\ell}R' &= R, && (4.41)\\
-2Gm\frac{z}{\ell}P'_\Lambda &= \frac{G^2P_\Lambda^2 - R^2}{2G^2P_\Lambda}, && (4.42)\\
-2Gm\frac{z}{\ell}\frac{\Lambda'}{\Lambda} &= -\frac{G^2P_\Lambda^2 + R^2}{2G^2P_\Lambda^2}, && (4.43)\\
-2Gm\frac{z}{\ell}P'_R &= -\frac{G^2P_\Lambda P_R + \Lambda R}{G^2P_\Lambda}. && (4.44)
\end{aligned}
$$

Now, the above equations can be solved in sequence, that is, we first solve Eq.(4.41) to find $R(z)$, and then substituting it into Eq.(4.42), we can find $P_\Lambda(z)$. Once $R(z)$ and $P_\Lambda(z)$ are given, we can substitute them into Eq.(4.43) to find $\Lambda(z)$. Then, we can find $P_R(z)$ either by integrating Eq.(4.44) explicitly or by using the Hamiltonian constraint $\mathcal{H}_c = 0$. In the first approach, we shall have four integration constants, but only three of them are independent, as the Hamiltonian constraint $\mathcal{H}_c = 0$ must be satisfied, which will relate one of the four constants to the other three. Therefore, a simpler way is to solve $\mathcal{H}_c = 0$ directly to find P_R, once R, P_Λ and Λ are found from Eqs.(4.41)-(4.43). However, to illustrate what we mentioned above, let us first integrate the above four equations directly to get

$$
\begin{aligned}
R &= c_0 e^{\frac{\tau}{2Gm}}, && (4.45)\\
P_\Lambda &= \mp\frac{\sqrt{c_1G^2e^{\frac{\tau}{2Gm}} - {c_0}^2e^{\frac{\tau}{Gm}}}}{G}, &&\\
\Lambda &= c_2e^{-\frac{\tau}{4Gm}}\sqrt{c_1G^2 - c_0^2e^{\frac{\tau}{2Gm}}}, && (4.46)\\
P_R &= c_3e^{-\frac{\tau}{2Gm}} \pm \frac{c_0c_2}{G}, && (4.47)
\end{aligned}
$$

where c_n's are the four integration constants. As noticed above, only three of them are independent. In fact, substituting the above expressions into the Hamiltonian constraint $\mathcal{H}_c = 0$ we find that

$$c_1 c_2 G = \mp 2 c_0 c_3. \tag{4.48}$$

On the other hand, from Eq.(4.24), we find

$$\begin{aligned} N &= -\frac{R^2}{2mG^2 P_\Lambda} \\ &= \pm \frac{c_0^2 e^{\frac{\tau}{Gm}}}{2Gm\sqrt{c_1 G^2 e^{\frac{\tau}{2Gm}} - c_0^2 e^{\frac{\tau}{Gm}}}}. \end{aligned} \tag{4.49}$$

Thus, we finally obtain

$$\begin{aligned} ds_c^2 &= -N^2 d\tau^2 + \Lambda^2 dx^2 + R^2 d\Omega^2 \\ &= -\frac{dR^2}{\frac{G^2 c_1}{c_0 R} - 1} + c_0^2 c_2^2 \left(\frac{G^2 c_1}{c_0 R} - 1\right) dx^2 + R^2 d\Omega^2. \end{aligned} \tag{4.50}$$

Clearly, using the gauge residual (4.2), we can always absorb the factor $c_0^2 c_2^2$ into x by setting $a_0 \equiv (c_0 c_2)^{-1}$. Then, the metric essentially depends only on one independent combination, $G^2 c_1 / c_0$, of the parameters, which is related to the mass of the black hole via the relation

$$m \equiv \frac{c_1 G}{2 c_0}. \tag{4.51}$$

It should be noted that the integration constants c_n's can be also determined by the boundary conditions

$$R = 2Gm, \quad \Lambda = 0, \quad P_\Lambda = 0, \ (\tau = 0), \tag{4.52}$$

and the Hamiltonian constraint at the horizon $\tau = 0$, which will be elaborated in more detail below, when we try to solve the field equations (4.29) - (4.32) numerically for the general case. In the current case, it can be shown that the above conditions together with the Hamiltonian constraint lead to

$$c_0 = 2Gm, \quad c_1 = \frac{c_0^2}{G^2}, \quad c_2 = \frac{1}{c_0}, \quad c_3 = \mp\frac{1}{2G}, \tag{4.53}$$

so the classical metric finally takes its standard form

$$\begin{aligned} ds_c^2 &= \left(1 - \frac{2Gm}{R}\right)^{-1} dR^2 - \left(1 - \frac{2Gm}{R}\right) dx^2 \\ &\quad + R^2 d\Omega^2. \end{aligned} \tag{4.54}$$

4.4.2 Böhmer-Vandersloot Limit

Following the so-called $\bar{\mu}$ scheme in LQC [14], Böhmer-Vandersloot (BV) [15] considered the case in which the physical area of the closed loop is equal to the minimum area gap predicted by LQG

$$\Delta = 2\sqrt{3}\pi\gamma\ell_{\mathrm{p}}^2. \tag{4.55}$$

For example, the holonomy loop in the (x,θ)-plane leads to

$$A_{x\theta} = \delta_b\delta_c p_b, \tag{4.56}$$

while the one in the (θ,ϕ)-plane leads to

$$A_{\theta\phi} = \delta_b^2 p_c, \tag{4.57}$$

where the new variable b, c and their moment conjugates p_b, p_c are related to the ABP variables through Eq.(4.3), which can be written in the form

$$\begin{aligned} p_b &= L_0\Lambda R, \quad b = -\alpha^{-1}RX, \\ p_c &= R^2, \quad c = -\beta^{-1}L_0\Lambda Y, \end{aligned} \tag{4.58}$$

where X and Y are defined in Eq.(4.9). Then, setting

$$A_{x\theta} = \Delta = A_{\theta\phi}, \tag{4.59}$$

will lead to

$$\delta_b = \sqrt{\frac{\Delta}{p_c}}, \quad \delta_c = \frac{\sqrt{\Delta p_c}}{p_b}. \tag{4.60}$$

Making the replacements

$$b \to \frac{\sin(\delta_b b)}{\delta_b}, \quad c \to \frac{\sin(\delta_c c)}{\delta_c}, \tag{4.61}$$

in the classical lapse function $N_{\rm cl}$ (4.4) and Hamiltonian $H_{\rm cl}$ (4.7), we obtain

$$N_{\rm BV} = \frac{\gamma \delta_b \sqrt{p_c}}{\sin(\delta_b b)}, \tag{4.62}$$

$$\begin{aligned} H^{\rm eff}_{\rm BV}[N] &= -\frac{1}{2\gamma G}\left[2\frac{\sin(\delta_c c)}{\delta_c} p_c \right. \\ &\quad \left. + \left(\frac{\sin(\delta_b b)}{\delta_b} + \frac{\gamma^2 \delta_b}{\sin(\delta_b b)}\right) p_b\right]. \end{aligned} \tag{4.63}$$

It is remarkable to note that the above effective Hamiltonian can be obtained from the ABP Hamiltonian without the inverse volume corrections presented in the last subsection. In fact, making the following approximation

$$h_0[X] \to \frac{2}{\pi}\sin[X], \quad \cos[\epsilon]\sin^2\left[\frac{\epsilon}{2}\right] \to \frac{\epsilon^2}{4}, \tag{4.64}$$

where ϵ is defined in Eq.(4.20), we find that [4]

$$\begin{aligned} A &= B = C = 0, \\ W &\simeq 4\sin[X], \quad \mathcal{D} \simeq 4\sin[X], \\ \frac{\mathcal{D}}{W} &\simeq 1, \quad Z \simeq 2\gamma^2 \left(\frac{\alpha}{R}\right)^2, \\ h_{-1} &\simeq \frac{2}{\pi}\cos[X]. \end{aligned} \tag{4.65}$$

[4] It should be noted that Eq.(4.8) tells that physically the conditions $A = B = C = 0$ imply that: (a) the parameters α and β defined in terms of the spin numbers j and j_x [cf. Eq.(4.13)] must satisfy the condition $\alpha,\ \beta \gg \ell_p$; and (b) the spread dimensionless parameters δ_x and δ appearing in the quantum reduced coherent states [42] must satisfy the condition $\delta,\ \delta_x \gg \gamma^2$. Both conditions are consistent with the semi-classical approximation of the effective Hamiltonian [42]. Further considerations of these conditions are presented in Section 4.5 given below.

Then, substituting the above into the effective Hamiltonian (4.10), we shall obtain precisely the BV Hamiltonian (4.63) with

$$\delta_b = \frac{\alpha}{R} = \frac{\alpha}{\sqrt{p_c}}, \quad \delta_c = \frac{\beta}{\Lambda L_0} = \frac{\beta\sqrt{p_c}}{p_b}. \tag{4.66}$$

Comparing them with those given by Eq.(4.60), we find that

$$\alpha^{(\mathrm{BV})} = \beta^{(\mathrm{BV})} = \sqrt{\Delta}, \tag{4.67}$$

which immediately leads to

$$\begin{aligned} j^{(\mathrm{BV})} &= \sqrt{\frac{3}{128\pi}} \simeq 0.0864 \simeq 0.313 j_x^{(\mathrm{BV})} > \gamma j_x^{(\mathrm{BV})}, \\ j_x^{(\mathrm{BV})} &= \frac{\sqrt{3}}{2\pi} \simeq 0.275. \end{aligned} \tag{4.68}$$

Therefore, the BV Hamiltonian is precisely the limit of the effective ABP Hamiltonian,[5] provided that:

- the inverse volume corrections vanish, $A = B = C = 0$;
- the Struve functions $h_0[X]$ and $h_{-1}[X]$ are replaced respectively by $(2/\pi)\sin[X]$ and $(2/\pi)\cos[X]$; and
- the spin parameters j_x and j are chosen as those given by Eq.(4.68).

It is clear that the last condition is in sharp conflict with the semi-classical limit requirement of Eq.(4.14).

In addition, as $T \to -\infty$, BV found the following asymptotic behaviors

$$\begin{aligned} b &\simeq \bar{b}, \quad p_b \simeq \bar{p}_b e^{-\bar{\alpha}T}, \\ c &\simeq \bar{c}e^{-\bar{\alpha}T}, \quad p_c \simeq \bar{p}_c, \end{aligned} \tag{4.69}$$

[5] In the BV limit, $N(\tau) \to \frac{N_{\mathrm{BV}}}{2Gm}$ because $d\tau = 2GmdT$. Thus, we have $H_{int}^{IV+CS}[N] \to \frac{H^{\mathrm{eff}}_{\mathrm{BV}}[N]}{2Gm}$.

where $\bar{b}, \bar{p}_b, \bar{c}, \bar{p}_c$ and $\bar{\alpha} > 0$ are constants, given by [cf. Eqs.(64) - (69) in [15]]

$$2\sin(\bar{\delta}_b\bar{b}) - \sin(\bar{\delta}_b\bar{b})^2 = \frac{\Delta\gamma^2}{\bar{p}_c}, \tag{4.70}$$

$$\bar{\alpha} = -\cos(\bar{\delta}_b\bar{b}) + \cot(\bar{\delta}_b\bar{b}), \tag{4.71}$$

$$\sin(\bar{\delta}_b\bar{b}) - \left(\bar{\delta}_b\bar{b} + \frac{\pi}{2}\right)\left[\cos(\bar{\delta}_b\bar{b}) - \cot(\bar{\delta}_b\bar{b})\right] - 2 = 0, \tag{4.72}$$

with

$$\bar{\delta}_b = \frac{\sqrt{\Delta}}{\sqrt{\bar{p}_c}}, \quad \bar{\delta}_c = \frac{\sqrt{\Delta\,\bar{p}_c}}{\bar{p}_b}, \quad \bar{\delta}_c\bar{c} = -\frac{\pi}{2}. \tag{4.73}$$

Then, from Eqs.(4.60) and (4.62) we find that asymptotically

$$N_{\rm BV} \simeq \bar{N} \equiv \frac{\gamma\sqrt{\Delta}}{\sin(\bar{\delta}_b\bar{b})}. \tag{4.74}$$

Hence, the spacetime is asymptotically described by the metric

$$\begin{aligned} ds^2 &= -N_{\rm BV}^2 dT^2 + \frac{p_b^2}{L_0^2 p_c}dx^2 + p_c d\Omega^2 \\ &\simeq \left(\frac{\bar{t}_0}{\bar{t}}\right)^2\left(-d\bar{t}^2 + d\bar{x}^2\right) + \bar{p}_c d\Omega^2, \end{aligned} \tag{4.75}$$

where

$$d\bar{t} = e^{\bar{\alpha}T}dT, \quad \bar{x} = \frac{\bar{p}_b}{\bar{N}L_0\sqrt{\bar{p}_c}}x, \quad \bar{t}_0 \equiv \frac{\bar{N}}{\bar{\alpha}}. \tag{4.76}$$

Loop quantum black holes do not satisfy the classical Einstein's equations. However, in order to study the loop quantum gravitational effects (with respect to GR), we introduce the effective energy-momentum tensor $T_{\mu\nu}^{\rm eff}$ by $T_{\mu\nu}^{\rm eff} \equiv G_{\mu\nu}$ [6], which takes the form

$$T_{\mu\nu}^{\rm eff} \simeq \rho u_\mu u_\nu + p_{\bar{x}}\bar{x}_\mu\bar{x}_\nu + p_\perp\left(\theta_\mu\theta_\nu + \phi_\mu\phi_\nu\right), \tag{4.77}$$

[6] It should be noted that the Einstein field equations usually read as $G_{\mu\nu} = (8\pi G/c^4)T_{\mu\nu}$, while in this chapter we drop the factor $8\pi G/c^4$, as this will not affect our analysis and conclusions.

in the current case, where $u_\mu = (\bar{t}_0/\bar{t})\delta^{\bar{t}}_\mu$, $\bar{x}_\mu = (\bar{t}_0/\bar{t})\delta^{\bar{x}}_\mu$, $\theta_\mu = \sqrt{p_c}\delta^\theta_\mu$, $\phi_\mu = \sqrt{p_c}\sin\theta\delta^\phi_\mu$, and

$$\rho \simeq \frac{1}{\bar{p}_c}, \quad p_{\bar{x}} \simeq -\frac{1}{\bar{p}_c}, \quad p_\perp \simeq -\frac{1}{\bar{t}_0^2}. \tag{4.78}$$

From the above it is clear that the spacetime corresponds to a spacetime with a homogeneous and isotropic perfect fluid only when $\bar{t}_0 = \sqrt{\bar{p}_c}$. When $\bar{t}_0 \neq \sqrt{\bar{p}_c}$, the radial pressure is different from the tangential one, despite the fact that they are all constants. The latter (with $\bar{t}_0 \neq \sqrt{\bar{p}_c}$) can be interpreted as the charged Nariai solution [46]. In addition, we also have

$$\begin{aligned}
\mathcal{R} &\simeq 2\left(\frac{1}{\bar{p}_c} + \frac{1}{\bar{t}_0^2}\right), \\
R_{\mu\nu}R^{\mu\nu} &\simeq 2\left(\frac{1}{\bar{p}_c^2} + \frac{1}{\bar{t}_0^4}\right), \\
R_{\mu\nu\alpha\beta}R^{\mu\nu\alpha\beta} &\simeq 4\left(\frac{1}{\bar{p}_c^2} + \frac{1}{\bar{t}_0^4}\right), \\
C_{\mu\nu\alpha\beta}C^{\mu\nu\alpha\beta} &\simeq \frac{4\left(\bar{p}_c + \bar{t}_0^2\right)^2}{3\bar{t}_0^4\bar{p}_c^2}.
\end{aligned} \tag{4.79}$$

It is remarkable to note that, even when $\bar{t}_0 = \sqrt{\bar{p}_c}$, the spacetime is still not conformally flat. So, it must not be the de Sitter space. In fact, as noticed by BV [15], it is the Nariai space [47, 48].

On the other hand, from Eqs.(4.70)-(4.72), BV found the following solutions

$$\begin{aligned}
&\bar{b} \simeq 0.156, \quad \bar{p}_c \simeq 0.182\ell_p^2, \quad \bar{\alpha} \simeq 0.670, \\
&\frac{\bar{c}}{\bar{p}_b} \simeq -2.290 m_p^2, \quad \bar{N} \simeq 0.689\ell_p,
\end{aligned} \tag{4.80}$$

from which we find that

$$\bar{t}_0 = \frac{\bar{N}}{\bar{\alpha}} \approx 1.029\ell_p \neq \sqrt{\bar{p}_c}\,(\approx 0.427\ell_p)\,. \tag{4.81}$$

Therefore, the solution is asymptotically approaching to the charged Nariai solution [46], instead of the Nariai solution [47].

It should be noted that in the above calculations, BV took $\gamma \approx 0.2375$ in the expression $\Delta = 2\sqrt{3}\pi\gamma\ell_p^2$. Instead, if we take $\gamma \approx 0.274$ [42] we find

$$\begin{aligned} \bar{N} &\approx 0.854\ell_p, \quad \bar{p}_c \approx 0.279\ell_p^2, \ (\gamma \approx 0.274), \\ \bar{t}_0 &\equiv \frac{\bar{N}}{\alpha} \approx 1.275\ell_p \neq \sqrt{\bar{p}_c}\,(\approx 0.529\ell_p)\,, \end{aligned} \tag{4.82}$$

that is, even in this case the spacetime is still not asymptotically Nariai, but the charged Nariai [46].

4.4.3 *Ashtekar-Olmedo-Singh Limit*

From the analysis of the BV limit, it becomes clear that from the general ABP model, the AOS limit [9, 23] can be obtained by the replacements

$$\begin{aligned} & h_0[X] \to \frac{2}{\pi}\sin[X], \quad h_{-1}[x] \to \frac{2}{\pi}\cos[X], \\ & \cos[\epsilon]\sin^2\left[\frac{\epsilon}{2}\right] \to \frac{\epsilon^2}{4}, \end{aligned} \tag{4.83}$$

so that

$$\begin{aligned} W &\simeq 4\sin[X], \quad \mathcal{D} \simeq 4\sin[X], \\ \frac{\mathcal{D}}{W} &\simeq 1, \quad Z \simeq 2\gamma^2\left(\frac{\alpha}{R}\right)^2. \end{aligned} \tag{4.84}$$

In addition, we must also set

$$\begin{aligned} & A = B = C = 0, \\ & \delta_b,\ \delta_c = \text{Constant}. \end{aligned} \tag{4.85}$$

Then, the resultant lapse function and effective Hamiltonian will be precisely given by the same form as Eqs.(4.62) and (4.63) but with different $\delta_b,\ \delta_c$. With the above in mind, AOS found the following solutions [9]

$$\begin{aligned}
\sin(\delta_c c) &= \frac{2a_0 e^{2T}}{a_0^2 + e^{4T}},\\
\cos(\delta_b b) &= b_0 \frac{b_+ e^{b_0 T} - b_-}{b_+ e^{b_0 T} + b_-},\\
p_b &= -\frac{GmL_0 e^{-b_0 T}}{2b_0^2}\left(b_+ e^{b_0 T} + b_-\right)\mathcal{A},\\
p_c &= 4(Gm)^2\left(a_0^2 + e^{4T}\right)e^{-2T},
\end{aligned} \tag{4.86}$$

where m is an integration constant, related to the mass parameter as noticed previously, and

$$\begin{aligned}
\mathcal{A} &\equiv \left[2\left(b_0^2+1\right)e^{b_0 T} - b_-^2 - b_+^2 e^{2b_0 T}\right]^{1/2},\\
a_0 &\equiv \frac{\gamma\delta_c L_0}{8Gm}, \quad b_0 \equiv \left(1+\gamma^2\delta_b^2\right)^{1/2},\\
b_\pm &\equiv b_0 \pm 1,
\end{aligned} \tag{4.87}$$

with

$$\begin{aligned}
&\delta_b b \in (0,\pi), \quad \delta_c c \in (0,\pi),\\
&p_b \leq 0, \quad p_c \geq 0, \quad -\infty < T < 0.
\end{aligned} \tag{4.88}$$

In terms of p_b and p_c, the metric takes the form

$$ds^2 = -N_{\text{AOS}}^2 dT^2 + \frac{p_b^2}{|p_c| L_0^2}dx^2 + |p_c| d\Omega^2, \tag{4.89}$$

where [7]

$$\begin{aligned}
N_{\text{AOS}} &= \frac{\gamma\delta_b \operatorname{sgn}(p_c)|p_c|^{1/2}}{\sin(\delta_b b)}\\
&= \frac{2Gm}{\mathcal{A}}e^{-T}\left(b_+ e^{b_0 T} + b_-\right)\left(a_0^2 + e^{4T}\right)^{1/2}.
\end{aligned} \tag{4.90}$$

[7] In the AOS limit, $N(\tau) \to \frac{N_{\text{AOS}}}{2Gm}$ because $d\tau = 2GmdT$. Thus, we have $H_{int}^{IV+CS}[N] \to \frac{H_{\text{AOS}}^{\text{eff}}[N]}{2Gm}$.

From Eq.(4.86), it can be seen that the transition surface is located at $\partial p_c(\mathcal{T})/\partial T = 0$, which yields

$$\mathcal{T} = \frac{1}{2}\ln\left(\frac{\gamma\delta_c L_0}{8Gm}\right) < 0. \tag{4.91}$$

There exist two horizons, located respectively at

$$T_{\rm BH} = 0, \quad T_{\rm WH} = -\frac{2}{b_0}\ln\left(\frac{b_0+1}{b_0-1}\right), \tag{4.92}$$

at which we have $\mathcal{A}(T) = 0$, where $T = T_{\rm BH}$ is the location of the black hole horizon, while $T = T_{\rm WH}$ is the location of the white hole horizon. In the region $\mathcal{T} < T < 0$, the 2-spheres are all trapped, while in the one $T_{\rm WH} < T < \mathcal{T}$, they are all anti-trapped. Therefore, the region $\mathcal{T} < T < 0$ behaves like the internal of a black hole, while the one $T_{\rm WH} < T < \mathcal{T}$ behaves like the internal of a white hole.

The extension across the black hole horizon can be obtained by the following replacements [9, 23]

$$\begin{aligned} &b \to ib, \quad p_b \to ip_b,\\ &c \to c, \quad p_c \to p_c. \end{aligned} \tag{4.93}$$

Then, AOS found that the corresponding Penrose diagram consists of infinite diamonds along the vertical direction, alternating between black holes and white holes, but the spacetime singularity used appearing at $p_c = 0$ now is replaced by a non-zero minimal surface with

$$p_c^{\rm min} = p_c(\mathcal{T}) > 0, \tag{4.94}$$

where $\mathcal{T}$ is given by Eq.(4.91).

To completely fix the values of δ_b and δ_c, AOS required that on the transition surface $\mathcal{T}$, the physical areas of $A_{x\theta}$ and $A_{\theta\phi}$ be equal to the area gap Δ [9, 23]

$$2\pi\delta_c\delta_b\,|p_b(\mathcal{T})| = \Delta, \tag{4.95}$$

$$4\pi\delta_b^2 p_c(\mathcal{T}) = \Delta. \tag{4.96}$$

It is interesting to note that, substituting Eq.(4.66) into the above equations, we find that

$$2\pi\alpha\beta = \Delta, \quad 4\pi\alpha^2 = \Delta, \tag{4.97}$$

which are all independent of p_b and p_c and given by

$$\alpha = \frac{1}{2}\beta = \sqrt{\frac{\Delta}{4\pi}} = \sqrt{2\sqrt{2}\,\gamma}\,\ell_p. \tag{4.98}$$

Comparing it with Eq.(4.13) we find that

$$\begin{aligned} j^{(\mathrm{AOS})} &= \frac{1}{4\pi^{3/2}} < \frac{1}{2}, \quad j_x^{(\mathrm{AOS})} = \frac{1}{\sqrt{2}\,\pi^2} < \frac{1}{2}, \\ j^{(\mathrm{AOS})} &= \sqrt{\frac{\pi}{8}}\, j_x^{(\mathrm{AOS})} \simeq 0.6265 j_x^{(\mathrm{AOS})} > \gamma j_x^{(\mathrm{AOS})}, \end{aligned} \tag{4.99}$$

from which we find that such given j and j_x do not satisfy the semi-classical limit conditions (4.14) either. Therefore, the AOS model cannot be realized in the framework of QRLG either, although it can be obtained formally by the approximations (4.84) and (4.85) from the ABP model.

4.5 Quantum Reduced Loop Black Holes without Inverse Volume Correction Terms

Setting the three constants A, B and C to zero, the effective Hamiltonian (4.10) reduces to the one given in [41], but with the replacement of the constants α and β by

$$\alpha \equiv \sqrt{8\pi\gamma}\,\ell_p\,\sqrt{\hat{j}_0}, \quad \beta = \frac{\sqrt{8\pi\gamma}\,\ell_p\,\hat{j}}{\sqrt{\hat{j}_0}}, \tag{4.100}$$

where now $\hat{j}_0$ and $\hat{j}$ denote the quantum numbers associated respectively with the longitudinal and angular links of the coherent states, as mentioned in Section II. The relations between (j, j_x) and $(\hat{j}, \hat{j}_0)$ are given explicitly by Eq.(4.23). Without causing any confusion, in the rest of this section we shall drop the hats from $(\hat{j}, \hat{j}_0)$:

$$(\hat{j}, \hat{j}_0) \quad \rightarrow \quad (j, j_0),$$

unless some specific statements are given.

It is interesting to note that dropping the terms that are proportional to the constants $A,\ B$ and C defined in Eq.(4.8) is physically equivalent to assuming that

$$\frac{A}{R^2},\ \frac{B}{R^2},\ \frac{C}{R^2} \ll 1, \tag{4.101}$$

as can be seen from the effective Hamiltonian given by Eq.(4.10). Before proceeding further, let us first pause here for a while and consider the above limits. In particular, from Eqs.(4.13) and (4.21), we find $\alpha \sim \beta \sim \sqrt{j}\ell_p$, where "$\sim$" means "being the same order". On the other hand, introducing the spread parameters δ_i via the relations [42]

$$\begin{aligned}
\delta_r &= \frac{\pi^2 \ell_p^2 R^2}{\alpha^4 (\sin\theta)^2}\delta_x\,, \quad \delta_\theta = \frac{\pi^2 \ell_p^2 R^2}{\alpha^2\beta^2 (\sin\theta)^2}\delta\,, \\
\delta_\varphi &= \frac{\pi^2 \ell_p^2 R^2}{\alpha^2 \beta^2}\frac{\delta}{\nu},
\end{aligned} \tag{4.102}$$

we find that the terms appearing in the expressions of $A,\ B$ and C behave, respectively, as

$$\begin{aligned}
&\ell_p^2 \left(\frac{\ell_p^2\gamma^2}{\beta^2}\right) \sim \frac{\ell_p^2\gamma^2}{j}, \quad \ell_p^2 \left(\frac{\gamma^2}{\delta_x}\right) \sim \frac{\gamma^2\pi^2 R^2}{j^2 \sin^2(\theta)\delta_r}, \\
&\ell_p^2 \left(\frac{(3-\nu)\gamma^2}{\delta}\right) \sim \frac{\pi^2\gamma^2 R^2}{j^2 \sin^2(\theta)\delta_\theta} - \frac{\pi^2\gamma^2 R^2}{j^2\delta_\varphi}.
\end{aligned} \tag{4.103}$$

Thus, the conditions (4.101) imply

$$(i)\ \ \frac{\ell_p}{R} \ll 1, \quad (ii)\ \ j\delta_i \gg 1, \quad (i = r, \theta, \varphi). \tag{4.104}$$

Condition (ii) is required by the effective Hamiltonian approach [42], while condition (i) tells us that the effects of the inverse volume corrections are negligible when the geometric radius of the two-spheres (with $\tau, x =$ Constant) is much large than the Planck length.

With the above in mind, let us now turn to consider the effective Hamiltonian given by Eq.(4.10) with

$$A = B = C = 0. \tag{4.105}$$

It was shown [41] that the classical singularity of the Schwarzschild black hole now is replaced by a quantum bounce at $R = R_{\text{min}} > 0$, at which all the physical quantities, such as the Ricci scalar $\mathcal{R}$, Ricci squared $R_{\mu\nu}R^{\mu\nu}$, Kretschmann scalar $R_{\mu\nu\alpha\beta}R^{\mu\nu\alpha\beta}$, and Weyl squared $C_{\mu\nu\alpha\beta}C^{\mu\nu\alpha\beta}$, remain finite. In addition, at the black hole horizons, the quantum effects become negligible for macroscopic black holes.

A remarkable feature of this class of spacetimes is that the spacetime on the other side of the bounce is not asymptotically a white hole, as normally expected from the minisuperspace considerations [26]. Instead, depending on the values of η, defined by

$$\eta \equiv \frac{\alpha}{\beta} = \frac{j_0}{j}, \tag{4.106}$$

the spacetime has three different asymptotical limits, as $\tau \to -\infty$.

In this section, we shall provide a more detailed study over the whole parameter space. To this goal, let us consider the three cases $\eta = 1$, $\eta < 1$ and $\eta > 1$, separately.

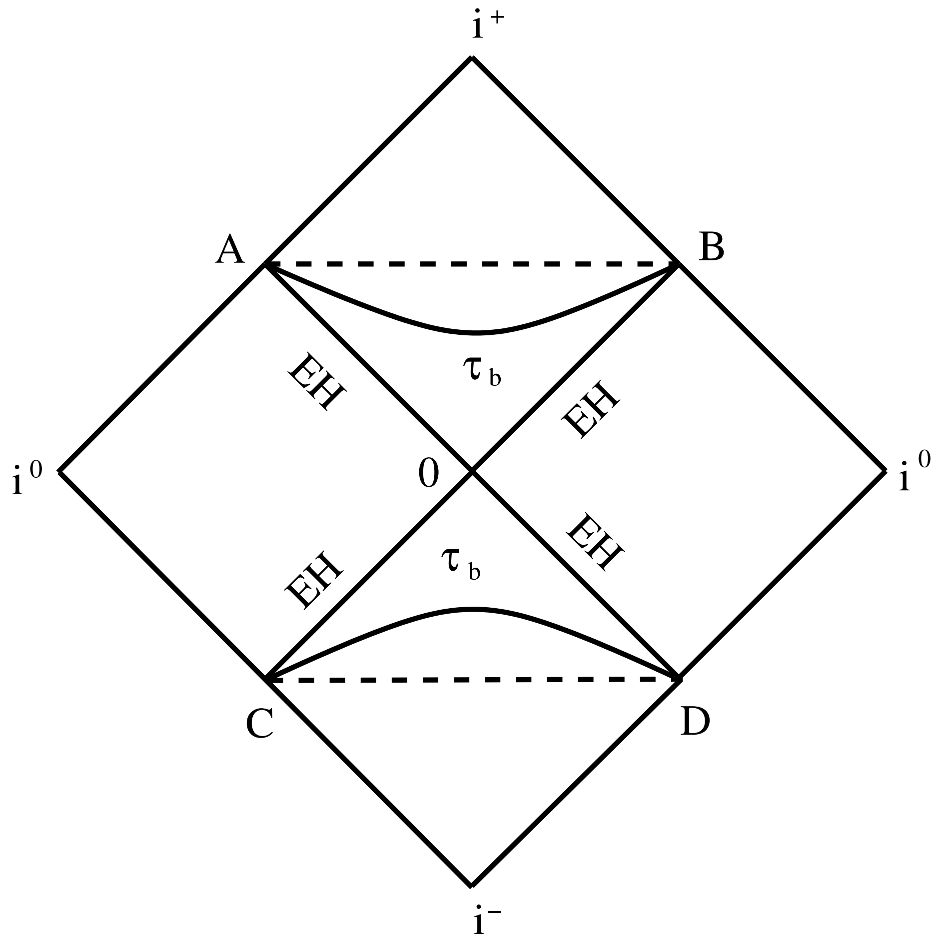

Figure 4.2: The Penrose diagram for the loop quantum spacetimes without the inverse volume corrections in the case $\eta = 1$. The curved lines denoted by τ_b are the transition surfaces (throats), and the straight lines AD and CB are the locations of the black hole horizons. The dashed lines AB and CD are the locations of the classical singularities of the Schwarzschild black and white holes, which now are all free of singularities.

4.5.1 $\eta = 1$

In this case from Eq.(4.106) we find that $j = j_0$. Then, as $\tau \to -\infty$, we have

$$\begin{aligned} X &\simeq -\pi, \quad Y \simeq -\pi, \quad W \simeq -\pi h_0[\pi], \\ \frac{P_\Lambda}{R^2} &\simeq -\frac{\pi}{\alpha\gamma G}, \quad \frac{P_R}{R\Lambda} \simeq -\frac{2\pi}{\alpha\gamma G}. \end{aligned} \tag{4.107}$$

Hence, the metric coefficients have the following asymptotical behavior [41] [8]

$$
\begin{aligned}
N(\tau) &\simeq -\frac{2\gamma\sqrt{8\pi\gamma}\ \ell_p\ \sqrt{j_0}}{mG\left(-\pi h_0[\pi]\right)} \simeq 0.886\frac{\sqrt{j}\ \ell_p}{mG},\\
\Lambda(\tau) &\simeq 31.49\left(\frac{mG}{\sqrt{j}\ \ell_p}\right)^{1/3},\\
R(\tau) &\simeq 0.0504\left(\frac{j^2\ell_p^4}{mG}\right)^{1/3}\exp\left(-\frac{\tau}{2mG}\right).
\end{aligned}
\tag{4.108}
$$

Thus, the metric takes the following asymptotical form

$$
ds^2 \simeq -d\bar{\tau}^2 + d\bar{x}^2 + R^2 d\Omega^2, \tag{4.109}
$$

which has a topology $R^2 \times S^2$, and the $(\bar{\tau}, \bar{x})$-plane is flat, where $\bar{\tau} \equiv -N(\tau \to -\infty)\tau$ and $\bar{x} \equiv \Lambda(\tau \to -\infty)x$. Then, the low half plane $-\infty < \tau < 0$ and $-\infty < x < \infty$ is mapped to the upper half plane $0 < \bar{\tau} < \infty$ and $-\infty < \bar{x} < \infty$, and the corresponding Penrose diagram is given by Fig. 4.2.

It should be noted that the spacetime is not vacuum as $\tau \to -\infty$, despite the fact that the $(\bar{\tau}, \bar{x})$-plane is asymptotically flat. This can be seen clearly by writing the metric (4.109) in terms of the timelike coordinate R

$$
ds^2 \simeq -\left(\frac{R_0}{R}\right)^2 dR^2 + d\bar{x}^2 + R^2 d\Omega^2, \tag{4.110}
$$

where $R_0 \equiv 2\sqrt{j}\ \ell_p$. For the metric (4.110), we find that the corresponding effective energy-momentum tensor can still be cast in the form of Eq.(4.77), but with $u_\mu =$

[8] We found that the numerical factor, 31.49, of Λ weakly depends on the mass parameter m. For example, it is respectively $31.55, 31.77, 32.63$ for $m/m_p = 10^6, 10^5, 10^4$. On the other hand, the numerical factors of $N(\tau)$ and $R(\tau)$ are very insensitive to m. In particular, they are the same up to the third digital for $m/m_p = 10^{12}, 10^6, 10^5, 10^4$.

$(R_0/R)\delta^R_\mu$, $\bar{x}_\mu = \delta^{\bar{x}}_\mu$, $\theta_\mu = R\delta^\theta_\mu$, $\phi_\mu = R\sin\theta\delta^\phi_\mu$, and

$$\begin{aligned} \rho &\simeq \frac{1}{R^2} + \frac{1}{R_0^2}, \\ p_{\bar{x}} &\simeq -\frac{1}{R^2} - \frac{3}{R_0^2}, \\ p_\perp &\simeq -\frac{1}{R_0^2}. \end{aligned} \tag{4.111}$$

The commonly used three energy conditions are *the weak, dominant and strong energy conditions* [20]. For $T^{\text{eff}}_{\mu\nu}$ given by Eq.(4.77), they can be expressed respectively as

- the weak energy condition (WEC):

$$\rho \geq 0, \quad \rho + p_{\bar{x}} \geq 0, \quad \rho + p_\perp \geq 0, \tag{4.112}$$

- the dominant energy condition (DEC):

$$\rho \geq 0, \quad -\rho \leq p_{\bar{x}} \leq \rho, \quad -\rho \leq p_\perp \leq \rho, \tag{4.113}$$

- the strong energy condition (SEC):

$$\rho + p_{\bar{x}} \geq 0, \;\; \rho + p_\perp \geq 0, \;\; \rho + p_{\bar{x}} + 2p_\perp \geq 0. \tag{4.114}$$

Clearly, Eq.(4.111) does not satisfy any of these conditions, but the energy density and the two principal pressures do approach constant values that are inversely proportional to $R_0^2 \propto \ell_p^2$, that is, the spacetime curvature approaches to the Planck scale. On the other hand, we also find

$$\begin{aligned} &\mathcal{R} \simeq \frac{2}{R^2} + \frac{6}{R_0^2}, \\ &R_{\mu\nu}R^{\mu\nu} \simeq 2\left(\frac{1}{R^4} + \frac{4}{R^2R_0^2} + \frac{6}{R_0^4}\right), \\ &R_{\mu\nu\alpha\beta}R^{\mu\nu\alpha\beta} \simeq 4\left(\frac{1}{R^4} + \frac{2}{R^2R_0^2} + \frac{3}{R_0^4}\right), \\ &C_{\mu\nu\alpha\beta}C^{\mu\nu\alpha\beta} \simeq \frac{4}{3R^4}. \end{aligned} \tag{4.115}$$

Table 4.1: The initial values $P_R(\tau_i)$ obtained from the effective Hamiltonian constraint (4.117) and the choice of the initial values of the other three variables given by Eq.(4.116), and its corresponding relativistic values $P_{R_c}(\tau_i)$, for different choices of τ_i. Results are calculated with $m = 10^{12} m_p,\ j = j_0 = 10$.

τ_i/τ_p	-0.01	-0.02	-0.05	-0.1	-1	-10	-100	-10^3	-10^4
P_{R_c}	0.500	0.500	0.500	0.500	0.500	0.500	0.500	0.500	0.500
P_R	0.506	0.500	0.501	0.500	0.500	0.500	0.500	0.500	0.500

Table 4.2: The initial values $P_R(\tau_i)$ obtained from the effective Hamiltonian constraint (4.117) and the choice of the initial values of the other three variables given by Eq.(4.116), and its corresponding relativistic values $P_{R_c}(\tau_i)$, for different choices of j with $j_0 = j$ (or $\eta = 1$). Results are calculated with $m = 10^{12} m_p,\ \tau_i = -10\ \tau_p$.

j	10	10^3	10^5	10^7	10^8	10^9	10^{10}	10^{11}	10^{12}
P_{R_c}	0.500	0.500	0.500	0.500	0.500	0.500	0.500	0.500	0.500
P_R	0.500	0.500	0.500	0.500	0.500	0.500	0.500	0.500	0.501

It is interesting to note that the last expression of the above equation shows that asymptotically the spacetime is conformally flat, while the Ricci, Ricci squared and Kretschmann scalars are approaching to their Planck values.

To study this class of solutions in more details, we need first to specify the initial conditions, which are often imposed near the black hole horizons [9, 15, 23, 41], as normally it is expected that the quantum effects for macroscopic black holes should be negligible [26], and the spacetime can be well-described by the Schwarzschild black hole spacetime. So, near the horizon, say, $\tau = \tau_i \simeq \tau_H$, we can take the initial values of

Table 4.3: The initial values $P_R(\tau_i)$ obtained from the effective Hamiltonian constraint (4.117) and the choice of the initial values of the other three variables given by Eq.(4.116), and its corresponding relativistic values $P_{R_c}(\tau_i)$, for different choices of m. Results are calculated with $j = 10,\ \tau_i = -10\ \tau_p$.

m/m_p	10	10^2	10^3	10^5	10^{10}	10^{12}	10^{14}
P_{R_c}	0.176	0.474	0.497	0.500	0.500	0.500	0.500
P_R	0.051	0.474	0.497	0.500	0.500	0.500	0.500

(Λ, P_Λ) and (R, P_R) as their corresponding relativistic values, $(\Lambda_c, P_{\Lambda_c})$ and (R_c, P_{R_c}). However, there is a caveat with the above prescription of the initial conditions, that is, before carrying out the integrations of the effective Hamiltonian equations, we do not know if the corresponding model indeed has negligible quantum gravitational effects near the black hole horizons even for macroscopic black holes. Therefore, a consistent way to choose the initial conditions should be: *First choose the initial conditions for any three of the four variables,* $(R, \Lambda, P_R, P_\Lambda)$*, and then obtain the initial condition for the fourth variable through the Hamiltonian constraint* $\mathcal{H}_{int}^{IV+CS} = 0$. The choice of the initial conditions for the first three variables clearly are arbitrary, which form the complete phase space $\mathcal{D}$ of the initial conditions of the theory. However, in order to study quantum effects, one can choose them as their corresponding relativistic values.

For the ABP model, we shall choose these three variables as (R, Λ, P_Λ), so that

$$\begin{aligned}
\Lambda(\tau_i) &= \Lambda_c(\tau_i), \quad P_\Lambda(\tau_i) = P_{\Lambda_c}(\tau_i), \\
R(\tau_i) &= R_c(\tau_i),
\end{aligned} \tag{4.116}$$

while $P_R(\tau_i)$ is obtained from the effective Hamiltonian constraint

$$\mathcal{H}_{\text{int}}^{\text{IV+CS}}(\tau_i) = 0, \quad \text{or} \quad \mathcal{C}(\tau_i) = 0, \tag{4.117}$$

where $\mathcal{C}(\tau)$ is defined by Eq.(4.11). This reduced parameter space will be referred to as $\hat{\mathcal{D}}$. It is clear that this reduced space is much smaller than the whole phase space $\mathcal{D}$. However, for our current purpose, this is enough. With such chosen initial conditions, the Hamiltonian equations will uniquely determine the evolutions of the four variables (Λ, P_Λ) and (R, P_R) at any other time τ. Once these four variables are known, from Eq.(4.24) we can find the lapse function $N(\tau)$.

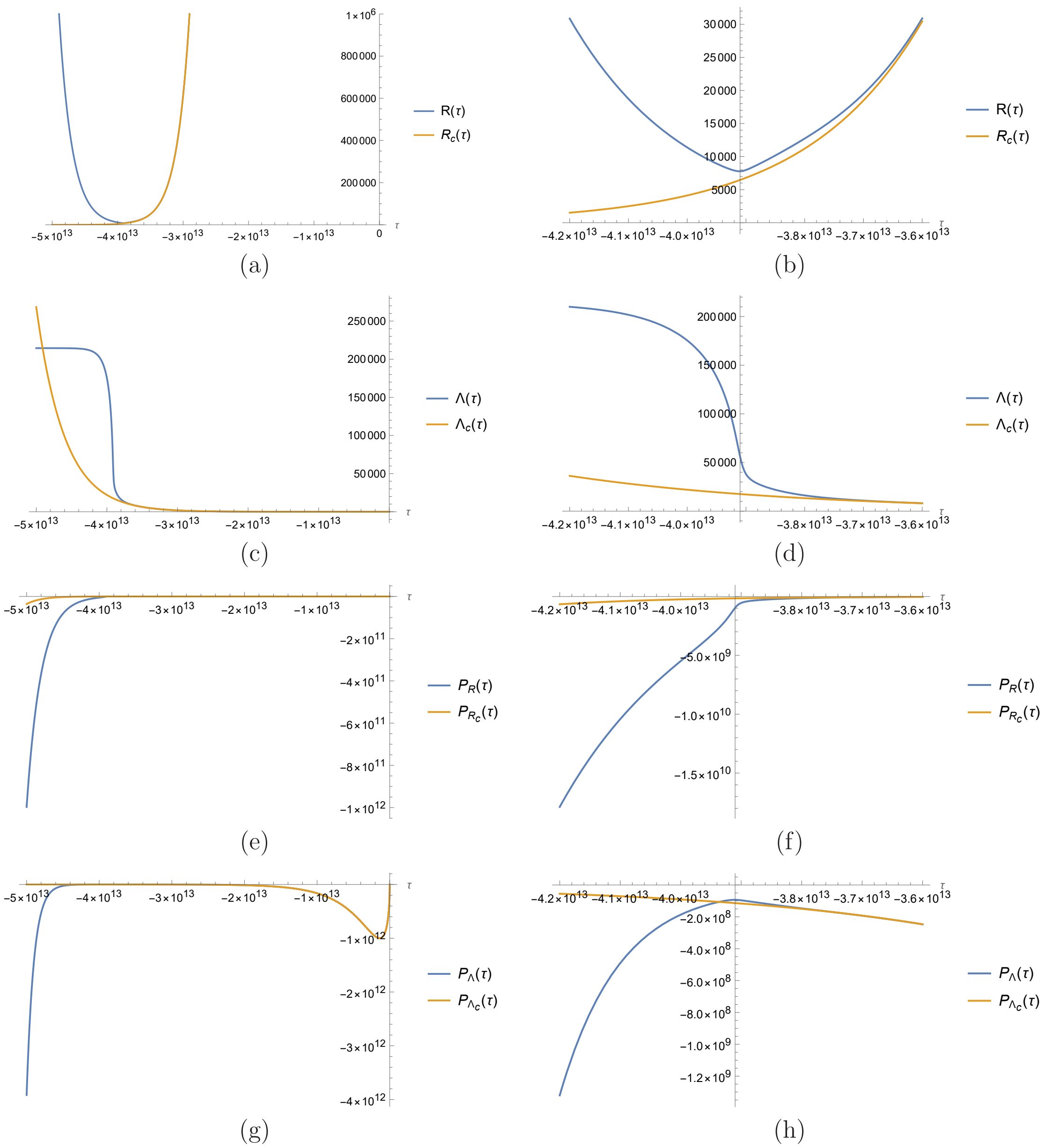

Figure 4.3: Plots of the physical variables $(R, \Lambda, P_R, P_\Lambda)$ and their classical correspondences $(R_c, \Lambda_c, P_{R_c}, P_{\Lambda_c})$. Particular attention are paid to the region near the throat $\tau = -3.91 \times 10^{13}$. Graphs are plotted with $m = 10^{12} m_p,\ j = j_0 = 10$.

With the above prescription, we can see that the initial values of the four variables will depend not only on the choice of the initial moment τ_i but also on the values of $j_0,\ j$ and m. In particular, if the quantum effects are not negligible at the

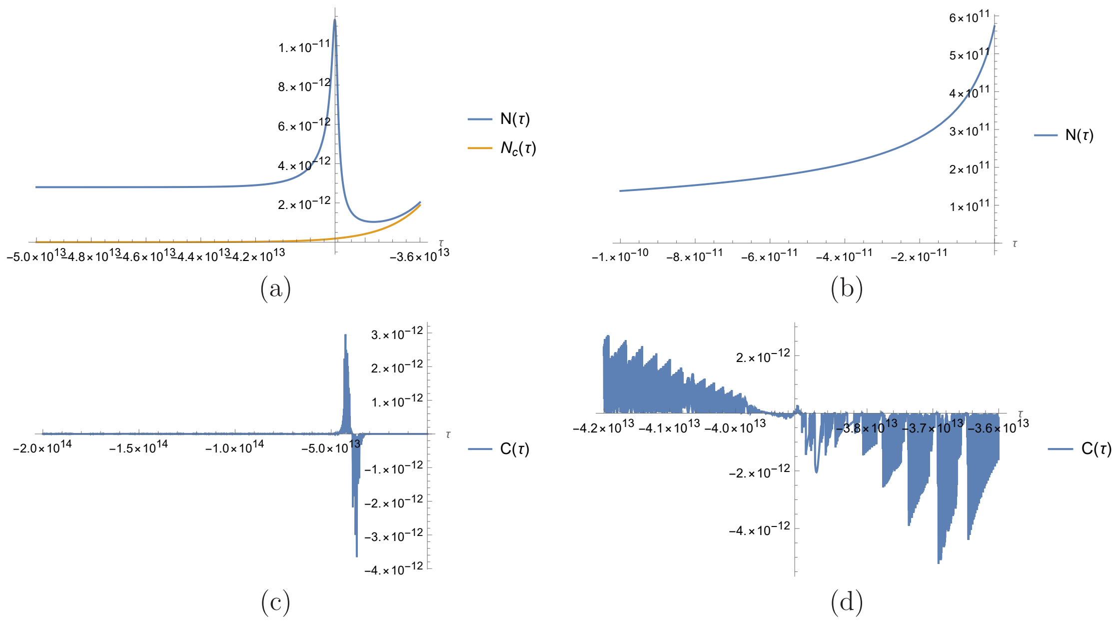

Figure 4.4: Plots of $\mathcal{C}(\tau)$ and the lapse function $N(\tau)$ for $m = 10^{12} m_p,\ j = j_0 = 10$.

moment τ_i, it is expected that such obtained $P_R(\tau_i)$ should be significantly different from its corresponding relativistic value $P_{R_c}(\tau_i)$.

To see this clearly, in Tables 4.1 - 4.3 we show such differences. In particular, in Table 4.1 we show the dependence of $P_R(\tau_i)$ on the choice of the initial time τ_i for $m = 10^{12} m_p,\ j = j_0 = 10$. From this table we can see that $\Delta P_R(\tau_i) \equiv P_R(\tau_i) - P_{R_c}(\tau_i) \simeq 0$ for $\tau_i/\tau_p \lesssim -0.1$. As $\tau_i \to 0$, the difference becomes larger.

In Table 4.2, we show the dependence of $P_R(\tau_i)$ on the choices of j with $m = 10^{12} m_p$ and $\tau_i = -10.0\ \tau_p$. Physically, the lager the parameter j is, the closer to the relativistic value of P_R should be. However, due to the accuracy of the numerical computations, it is difficult to obtain precisely the values of P_R from the effective Hamiltonian constraint (4.117). So, in Table 4.2 we only consider the initial values of $P_R(\tau_i)$ for $j \lesssim 10^{12}$.

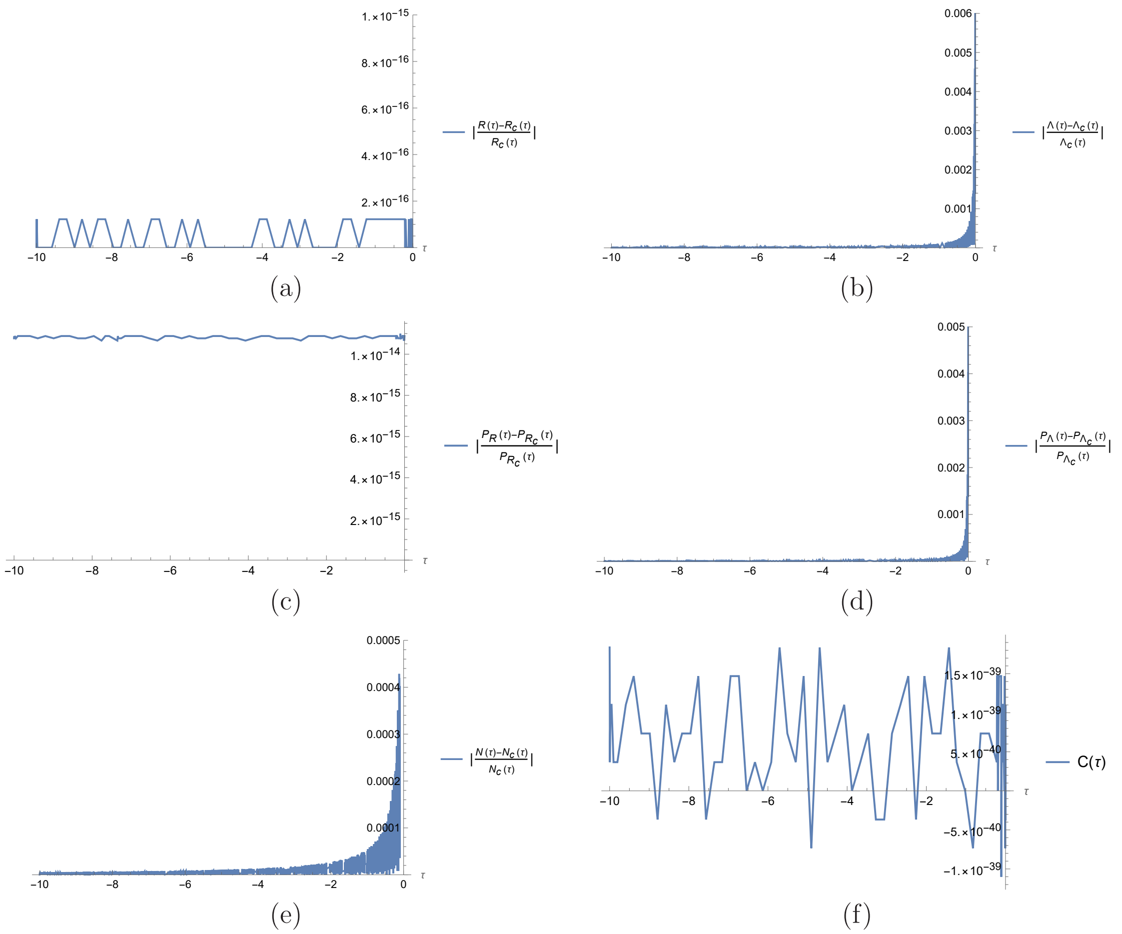

Figure 4.5: Plots of the relative differences of the functions $(R, \Lambda, P_R, P_\Lambda, N)$ and $\mathcal{C}(\tau)$ near the black hole horizon with the same choice of the parameters m and j, as those specified in Figs. 4.3 and 4.4, that is, $m = 10^{12} m_p,\ j = j_0 = 10$.

In Table 4.3, we show the dependence of $P_R(\tau_i)$ on the choices of m with $j = 10$ and $\tau_i = -10.0\ \tau_p$, from which it can be seen that the deviations becomes larger for $m \lesssim 10^3\ m_p$. It should be also noted that for very large masses, the initial time τ_i must be chosen very negative. Otherwise, the term $e^{\tau/(Gm)}$, appearing in the effective Hamiltonian constraint [cf. Eqs.(4.45) - 4.47)], becomes extremely small, and numerical errors can be introduced. So, in Table 4.3 for the choice of $\tau_i = -10\tau_p$, we only consider the cases where m is up to $10^{14}\ m_p$, although physically the larger m is, the closer $P_R(\tau_i)$ is to its relativistic values.

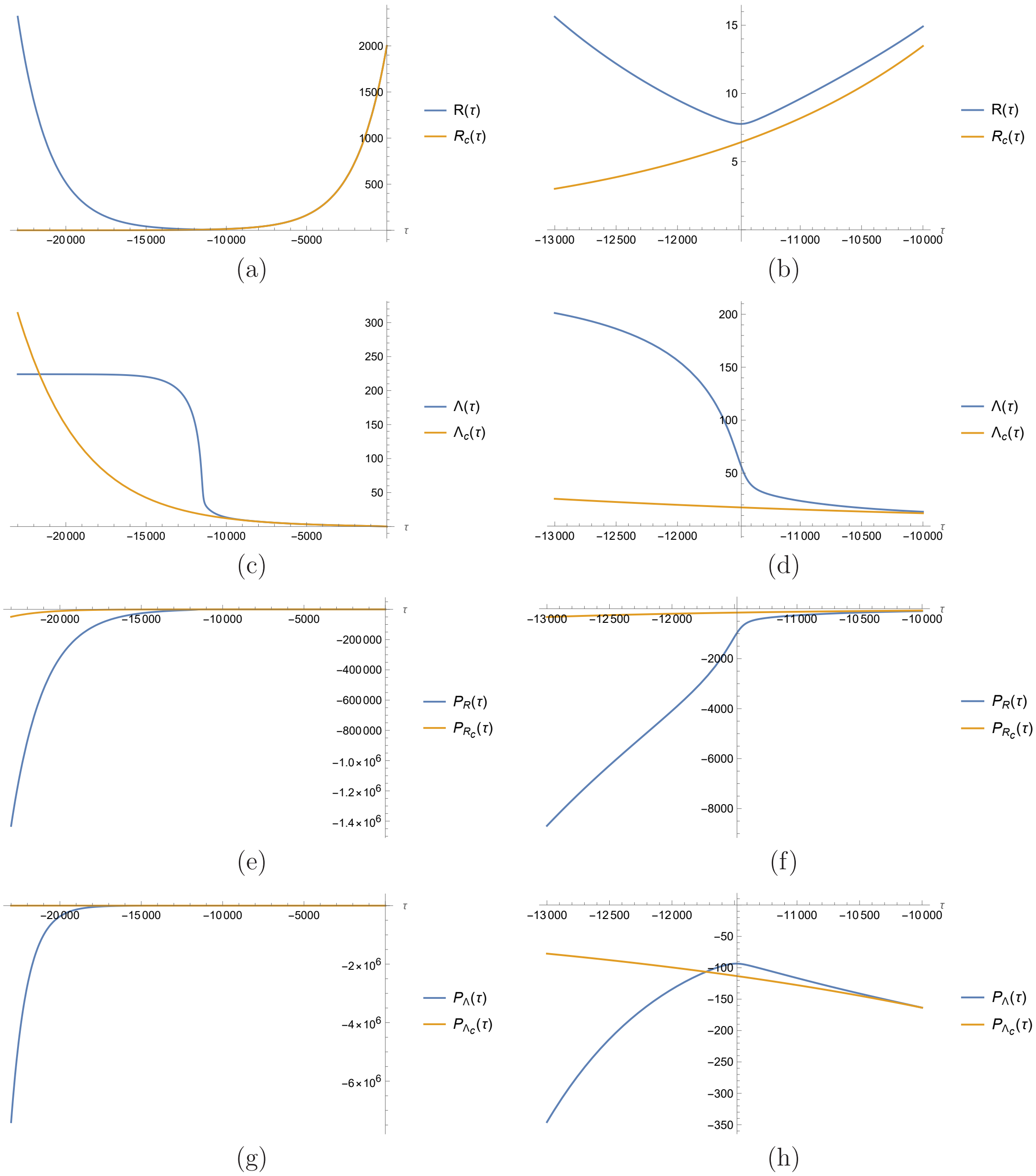

Figure 4.6: Plots of the physical variables $(R, \Lambda, P_R, P_\Lambda)$ and their classical correspondences $(R_c, \Lambda_c, P_{R_c}, P_{\Lambda_c})$. Particular attention is paid to the region near the throat $\tau_{\text{min}} = -1.148 \times 10^4$. Graphs are plotted with $m = 10^3 m_p,\ j = j_0 = 10$.

In Fig. 4.3, we plot the four functions $(R, \Lambda, P_R, P_\Lambda)$, and their classical correspondences for $m = 10^{12} m_p,\ j = j_0 = 10,\ \tau_i = -10\ \tau_p$. With such initial conditions, we find that the location of throat (transition surface) is around

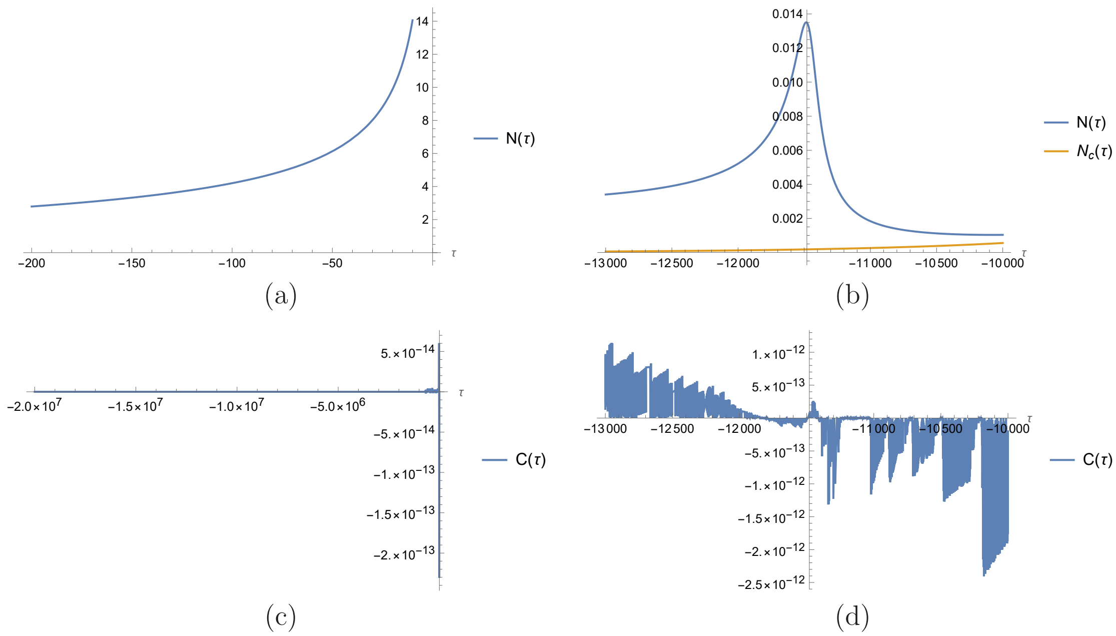

Figure 4.7: Plots of the lapse function $N(\tau)$ and $\mathcal{C}(\tau)$ for $m = 10^3 m_p$ and $j = j_0 = 10$.

$\tau_{\rm min} \simeq -3.9108 \times 10^{13} \tau_p$, at which $R(\tau)$ reaches its minimum value, $R_{\rm min} \simeq 7779.35\ \ell_p$. It is interesting to note that near the throat the four functions all change dramatically, especially $\Lambda(\tau)$, which behaves like a step function. In addition, even at the transition surface, we find that the conditions of Eq.(4.16) are well satisfied.

To closely monitor the numerical errors, we also plot out the effective Hamiltonian ($\mathcal{C}(\tau) \simeq 0$) in Fig. 4.4 together with the lapse function $N(\tau)$, from which we can see that in the region near the throat the numerical errors indeed become large. But out of this region, the numerical errors soon become negligible. From Fig. 4.3 and 4.4 we also find that our numerical solutions match well with their asymptotic behaviors given by Eq.(4.108), as $\tau \to -\infty$.

To consider the quantum effects near the horizons, in Fig. 4.5 we plot out the relative differences between functions $(R, \Lambda, P_R, P_\Lambda, N)$ and their classical value. To monitor the numerical errors, we also plot out the effective Hamiltonian constraint

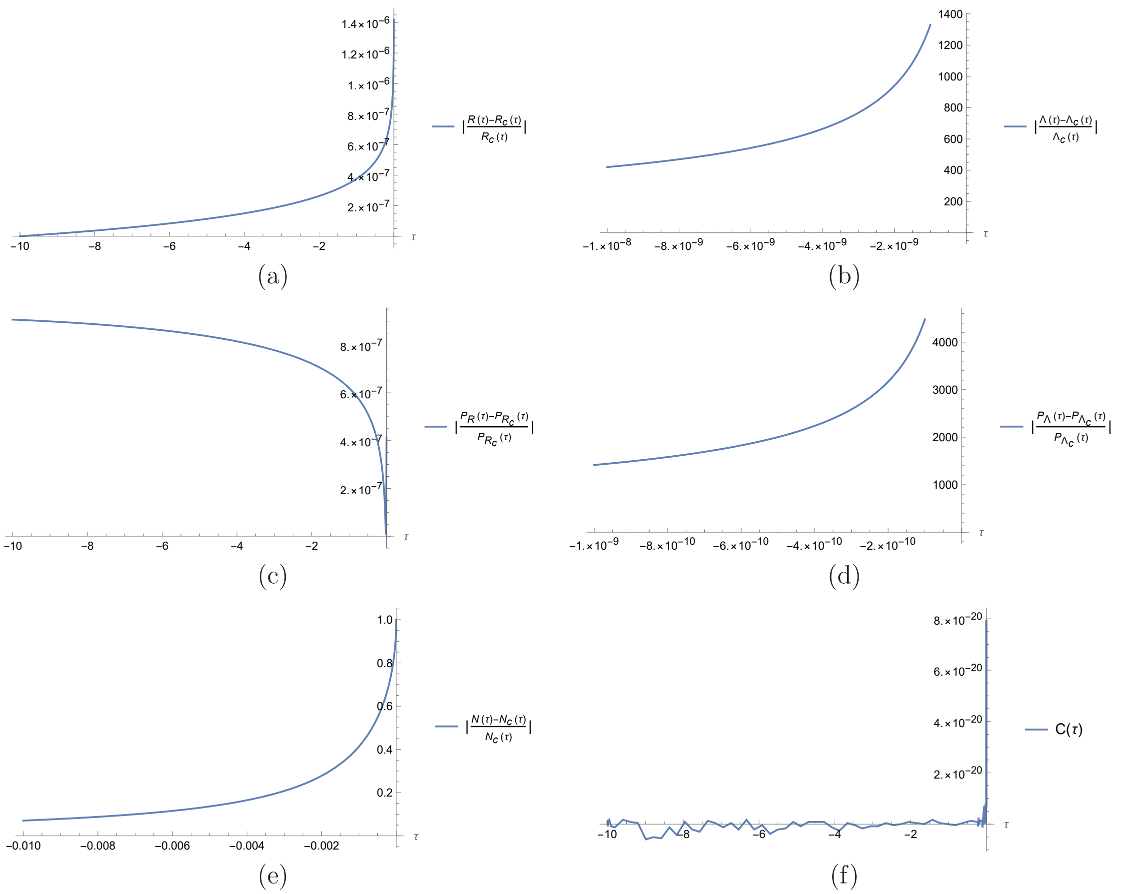

Figure 4.8: Plots of the relative differences of the functions $(R, \Lambda, P_R, P_\Lambda)$, the lapse function $N(\tau)$ and $\mathcal{C}(\tau)$ near the black hole horizon ($\tau = 0$) with $m = 10^3 m_p$ and $j = j_0 = 10$, the same choice as those specified in Figs. 4.6 and 4.7.

$\mathcal{C}(\tau) \simeq 0$. From these plots, we can see clearly that the quantum effects indeed become negligible near the horizons [9].

On the other hand, when the mass of the black hole is near the Planck scale, such effects are not negligible even near the horizon. To show this, in Figs. 4.6 - 4.8 we plot various physical variables for $m = 10^3\ m_p$, $j = j_0 = 10$, for which we find that the location of throat is around $\tau_{\min} \simeq -1.148 \times 10^4 \tau_p$, at which $R(\tau)$ reaches its

[9] Note that at the horizon $N(\tau)$ diverges. So, in the region very near the horizon $N(\tau)$ becomes extremely large, and the accurate numerical calculations become difficult, so it is unclear whether the sudden growth of $\Delta N/N_c$, as shown in Fig. 4.5 is due to numerical errors or not. In fact, similar growths can be also noticed from the plots of $\Delta\Lambda/\Lambda_c$ and $\Delta P_\Lambda/P_{\Lambda_c}$. Such sudden growths happen also in the cases $\eta > 1$ and $\eta < 1$, as to be seen below.

minimum value, $R_{\rm min} \simeq 7.76\ \ell_p$. From these figures it is clear that now the quantum effects become large near the horizons, and cannot be negligible. It should be noted that for such small black hole, the semi-classical limit conditions (4.108) are not well satisfied at the throat, and as a result, the corresponding effective Hamiltonian may no longer describe the real quantum dynamics well. For more details, we refer readers to [41, 42].

4.5.2 $\eta \gtrsim 1$

In this case, we find

$$\begin{aligned} X &\simeq \eta_0, \quad Y \simeq \frac{\eta_0}{\eta}, \\ W &\simeq \pi h_0[\eta_0] + 2\sin[\eta_0], \\ \frac{P_\Lambda}{R^2} &\simeq \frac{\eta_0}{\alpha\gamma G}, \quad \frac{P_R}{R\Lambda} \simeq \frac{2\eta_0}{\alpha\gamma G}, \end{aligned} \tag{4.118}$$

as $\tau \to -\infty$. Then, the metric coefficients have the following asymptotical behavior,

$$\begin{aligned} N(\tau) &\simeq N_0 = -\frac{2\gamma\sqrt{8\pi\gamma}\ \ell_p\ \sqrt{j_0},}{mG\left(\pi h_0[\eta_0] + 2\sin[\eta_0]\right)}, \\ \Lambda(\tau) &\simeq \Lambda_0 \exp\left\{\frac{\mathcal{F}(\eta)}{2mG}\tau\right\}, \\ R(\tau) &\simeq R_0 \exp\left\{\frac{\cos\left(\frac{\eta_0}{\eta}\right)}{2mG}\tau\right\}, \end{aligned} \tag{4.119}$$

where Λ_0 and R_0 are constants, and

$$\begin{aligned} \mathcal{F}(\eta) = & \frac{1}{\mathcal{D}(\eta_0)^2}\left[2\pi h_{-1}(\eta_0)\sin^2(\eta_0) + \pi^2\cos(\eta_0)h_0^2(\eta_0)\right] \\ & - \cos\left(\frac{\eta_0}{\eta}\right), \end{aligned} \tag{4.120}$$

where $\mathcal{D}(\eta_0)$ is defined by Eq.(4.33) but now with $A = B = 0$, and the constant η_0 is implicitly determined by

$$\eta \sin\left(\frac{\eta_0}{\eta}\right) + \frac{\pi}{\mathcal{D}(\eta_0)} \sin(\eta_0) h_0(\eta_0) = 0. \tag{4.121}$$

In [41], it was shown that $\mathcal{F}(\eta) < 0$ and $\eta_0 < -\pi$ when $\eta > 1$, so that both R and Λ grow exponentially as $\tau \to -\infty$. Setting

$$a \equiv \frac{|\mathcal{F}(\eta)|}{2mG} > 0, \quad d \equiv \frac{\left|\cos\left(\frac{\eta_0}{\eta}\right)\right|}{2mG} > 0, \tag{4.122}$$

we find that

$$\Lambda = \Lambda_0 e^{-a\tau}, \quad R = R_0 e^{-d\tau}. \tag{4.123}$$

Then, the metric takes the following asymptotical form

$$ds^2 \simeq -\left(\frac{\hat{N}_0}{R}\right)^2 dR^2 + R^{\frac{2a}{d}} d\bar{x}^2 + R^2 d\Omega^2, \tag{4.124}$$

where $\hat{N}_0 \equiv N_0/d$, but now with $\bar{x} \equiv \left(\Lambda_0/R_0^{a/d}\right) x$. Similar to the last case, the corresponding spacetime is not vacuum, and the effective energy-momentum tensor takes the same form as that given by Eq.(4.77), but now with $u_\mu = (\hat{N}_0/R)\delta^R_\mu$, $\bar{x}_\mu = R^{a/d}\delta^{\bar{x}}_\mu$, and

$$\begin{aligned} \rho &\simeq \frac{2a+d}{d\hat{N}_0^2} + \frac{1}{R^2}, \\ p_{\bar{x}} &\simeq -\frac{3}{\hat{N}_0^2} - \frac{1}{R^2}, \\ p_\perp &\simeq -\frac{a^2+ad+d^2}{d^2\hat{N}_0^2}, \end{aligned} \tag{4.125}$$

from which we find that

$$\begin{aligned} \rho + p_{\bar{x}} &\simeq \frac{2(a-d)}{d\hat{N}_0^2} + \mathcal{O}\left(\frac{1}{R^2}\right), \\ \rho + p_\perp &\simeq -\frac{a(a-d)}{d^2\hat{N}_0^2} + \mathcal{O}\left(\frac{1}{R^2}\right). \end{aligned} \tag{4.126}$$

Therefore, in this case none of the three energy conditions is satisfied either, provided that $a \neq d$. When $a = d$, the spacetime is asymptotically de Sitter, as shown below. In particular, we find that

$$
\begin{aligned}
\mathcal{R} &\simeq 2\left(\frac{a^2 + 2ad + 3d^2}{d^2 \hat{N}_0^2} + \frac{1}{R^2}\right), \\
R_{\mu\nu}R^{\mu\nu} &\simeq 2\frac{a^4 + 2a^3 d + 5a^2 d^2 + 4ad^3 + 6d^4}{d^4 \hat{N}_0^4} \\
&\quad + \frac{4(a+2d)}{d\hat{N}_0^2 R^2} + \frac{2}{R^4}, \\
R_{\mu\nu\alpha\beta}R^{\mu\nu\alpha\beta} &\simeq 4\frac{a^4 + 2a^2 d^2 + 3d^4}{d^4 \hat{N}_0^4} + \frac{8}{\hat{N}_0^2 R^2} + \frac{4}{R^4}, \\
C_{\mu\nu\alpha\beta}C^{\mu\nu\alpha\beta} &\simeq \frac{4\left(aR^2(a-d) + d^2 \hat{N}_0^2\right)^2}{3d^4 \hat{N}_0^4 R^4}.
\end{aligned}
\tag{4.127}
$$

Therefore, different from the last case, asymptotically the spacetime is conformally flat only when $a = d$. Otherwise, we have $C_{\mu\nu\alpha\beta}C^{\mu\nu\alpha\beta} \simeq 4a^2(a-d)^2/(3d^4\hat{N}_0^4) + \mathcal{O}\left(1/R^2\right)$.

On the other hand, introducing the quantity $\bar{t}$ via the relation

$$
\bar{t} = -\frac{d\hat{N}_0}{aR_0^{a/d}}\left(\frac{R_0}{R}\right)^{a/d} \equiv -\bar{t}_0\left(\frac{R_0}{R}\right)^{a/d}, \tag{4.128}
$$

we find that the metric (4.124) takes the form

$$
ds^2 \simeq R_0^{2a/d}\left(\frac{\bar{t}_0}{\bar{t}}\right)^2\left(-d\bar{t}^2 + d\bar{x}^2\right) + R^2 d\Omega^2. \tag{4.129}
$$

When $a = d$, Eq.(4.129) reduces to

$$
ds^2 \simeq R_0^2\left(\frac{\bar{t}_0}{\bar{t}}\right)^2\left(-d\bar{t}^2 + d\bar{x}^2 + d\Omega^2\right), \ (a = d), \tag{4.130}
$$

which is the same as the de Sitter spacetime for $R \gg R_\Lambda$, where R_Λ is the de Sitter radius. In fact, when $R \gg R_\Lambda$ we have that the de Sitter spacetime is given by

$$\begin{aligned} ds^2_\Lambda &= -\left(1-\left(\frac{R}{R_\Lambda}\right)^2\right)d\bar{x}^2 + \left(1-\left(\frac{R}{R_\Lambda}\right)^2\right)^{-1} dR^2 \\ &\quad + R^2 d\Omega^2 \\ &\simeq \left(\frac{R_\Lambda}{\bar{t}}\right)^2\Big(-d\bar{t}^2 + d\bar{x}^2 + d\Omega^2\Big), \end{aligned} \tag{4.131}$$

but now with the rescaling $\bar{x} \to \bar{x}/R_\Lambda$ and

$$\bar{t} \equiv -\frac{R_\Lambda}{R}. \tag{4.132}$$

Note that the angular sectors of the two metrics (4.129) and (4.131) are different in terms of $\bar{t}$. In particular, in the metric (4.129) we have $R^2 \propto (-\bar{t})^{-2d/a}$, while in the de Sitter spacetime we have $R^2 \propto (-\bar{t})^{-2}$. Therefore, they are equal only when $a = d$. However, the sectors of the $(\bar{t}, \bar{x})$-planes are quite similar even when $a \neq d$. As a result, in both cases the surfaces $\bar{t} = 0$ represent spacelike hypersurfaces and form the boundaries of the spacetimes. Then, the corresponding Penrose diagram in the current case is given by Fig. 4.9.

When $a = d$, since $\mathcal{F}(\eta) < 0$ and $\cos\left(\frac{\eta_0}{\eta}\right) < 0$, from Eq.(4.122) we find

$$\mathcal{F}(\eta) = \cos\left(\frac{\eta_0}{\eta}\right). \tag{4.133}$$

On the other hand, η and η_0 must satisfy Eq.(4.121), too. So, these two equations uniquely determine η and η_0. For $\eta_0 \lesssim -\pi$, we find that Eqs.(4.121) and (4.133) have the solution,

$$(\eta, \eta_0) \approx (1.142, -3.329)\,, \tag{4.134}$$

for which, from Eqs.(4.13) and (4.22) we find that

$$\gamma = \frac{\sqrt{2\pi}}{8\eta} \simeq 0.274. \tag{4.135}$$

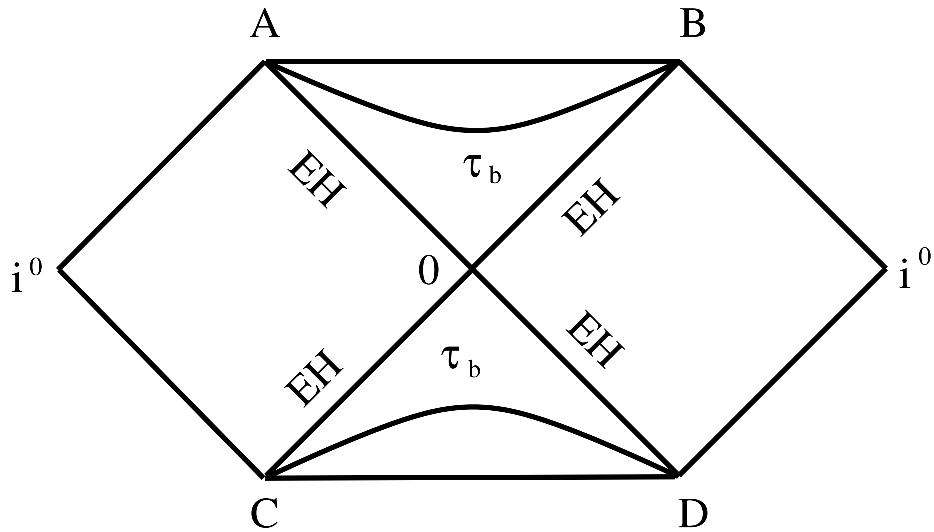

Figure 4.9: The Penrose diagram for the loop quantum spacetimes without the inverse volume corrections in the case $\eta > 1$ (As to be shown below, the corresponding Penrose diagram for the case $\eta < 1$ is also given by this figure). The curved lines denoted by τ_b are the transition surfaces (throats), and the straight lines AD and BC are the locations of the black hole horizons, while the straight lines AB and CD are the spacelike infinities, which correspond to $\bar{t} = 0$ and form the future/past boundaries. The whole spacetime is free of singularities.

It is remarkable to note that this value is precisely the one found from the analysis of black hole entropy [43]. It should be also noted that Eqs.(4.121) and (4.133) have multi-valued solutions, as these two equations are involved with periodic functions. In this chapter, we consider only the case $\eta_0 \lesssim -\pi$ [41].

In Figs. 4.10 - 4.12, we plot various physical quantities for $m = 10^{12}m_p,\ j_0 = 11.42,\ j = 10$, so that $\eta \equiv j_0/j = 1.142$. This corresponds to the case studied in [42], which will be analyzed in more detail in the next section with $ABC \neq 0$. Then, we find that the transition surface is located at $\tau_{\min}/\tau_p \simeq -3.896\times10^{13}$, at which we have $R(\tau_{\min}) \simeq 8059.95$. Note that with these choices of $m,\ j$ and j_x, the semiclassical limit conditions (4.14) and (4.16) are well satisfied. Then, from Figs. 4.10 and 4.11 we find that the asymptotical behavior of the metric coefficients given by Eq.(4.116) is well justified, while Fig. 4.12 shows that the quantum effects near the black hole

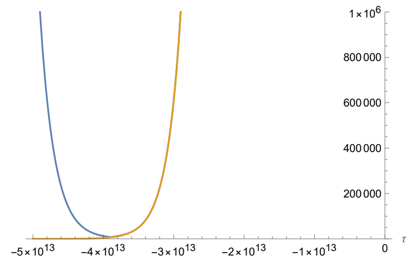

(a)

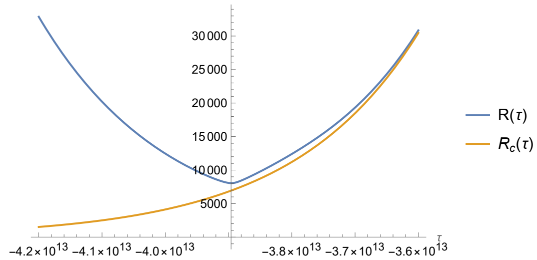

(b)

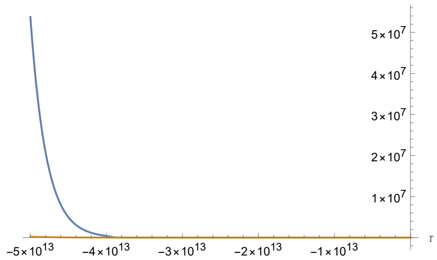

(c)

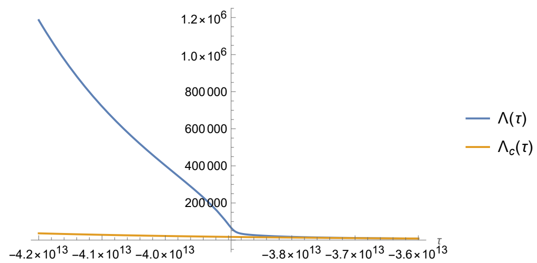

(d)

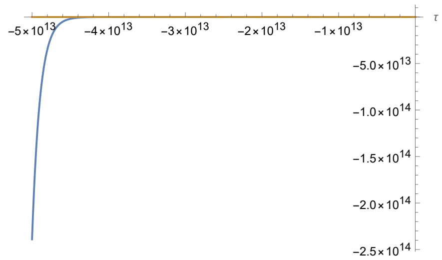

(e)

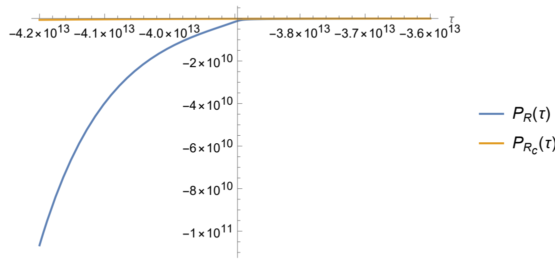

(f)

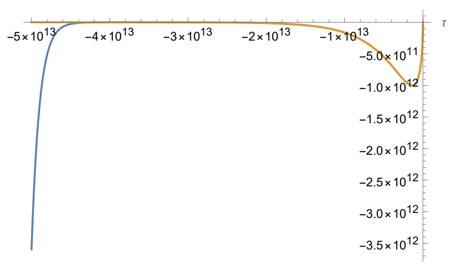

(g)

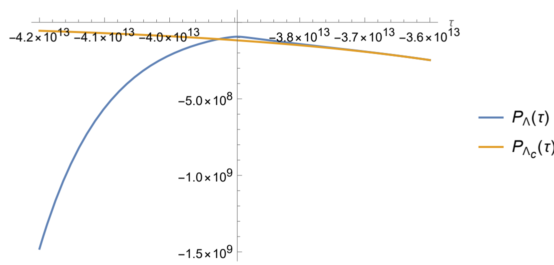

(h)

Figure 4.10: Plots of the physical variables $(R, \Lambda, P_R, P_\Lambda)$ and their classical correspondences $(R_c, \Lambda_c, P_{R_c}, P_{\Lambda_c})$. Particular attention is paid to the region near the throat $\tau_{\min} = -3.896 \times 10^{13}$, at which $R(\tau) = 8059.95$. Graphs are plotted with $m = 10^{12} m_p,\ j_0 = 11.42,\ j = 10,\ \eta = 1.142$.

horizon ($\tau \simeq 0$) are negligible even for $m/m_p = 10^{12}$. For the cases with solar mass $m/m_p \gtrsim 10^{38}$, it is expected that such effects are even smaller.

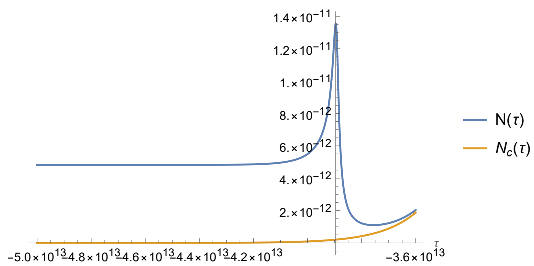

(a)

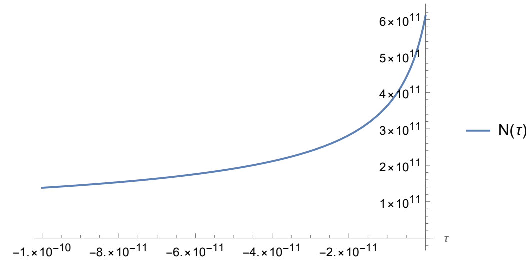

(b)

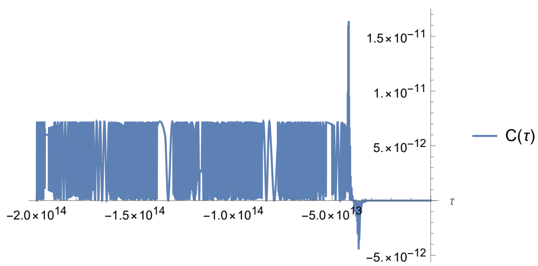

(c)

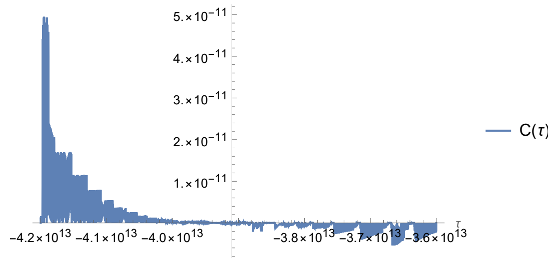

(d)

Figure 4.11: Plots of $\mathcal{C}(\tau)$ and the lapse function $N(\tau)$ for $m = 10^{12}m_p,\ j_0 = 11.42,\ j = 10,\ \eta = 1.142$.

Table 4.4: The dependence of the constants N_0, R_0, Λ_0 of Eq.(4.116) on m with $\eta \approx 1.142,\ \gamma \approx 0.274,\ j_x = 10^5$. The corresponding transition times $\tau_{\min}$ and radii $R_{\min}$ are also given.

$\frac{m}{m_p}$	$\frac{\tau_{\min}}{\tau_p}$	$\frac{R_{\min}}{\ell_p}$	N_0	R_0	Λ_0
10^{12}	-3.260×10^{13}	193114	5.706×10^{-10}	0.0226	0.00725
10^{10}	-2.646×10^{11}	41605.1	5.706×10^{-8}	0.0968	0.0311
10^{6}	-1.418×10^{7}	1929.73	5.706×10^{-4}	1.787	0.631

It should be noted that the specific values of the factors N_0, R_0 and Λ_0 appearing in Eq.(4.116) depend on the choice of m, although the asymptotic behavior of N, R and Λ all take the form of Eq.(4.116). As a result, the corresponding Penrose diagram is the same and given by Fig. 4.9 for any given $\eta > 1$. In Table 4.4 we present their values for several choices of m.

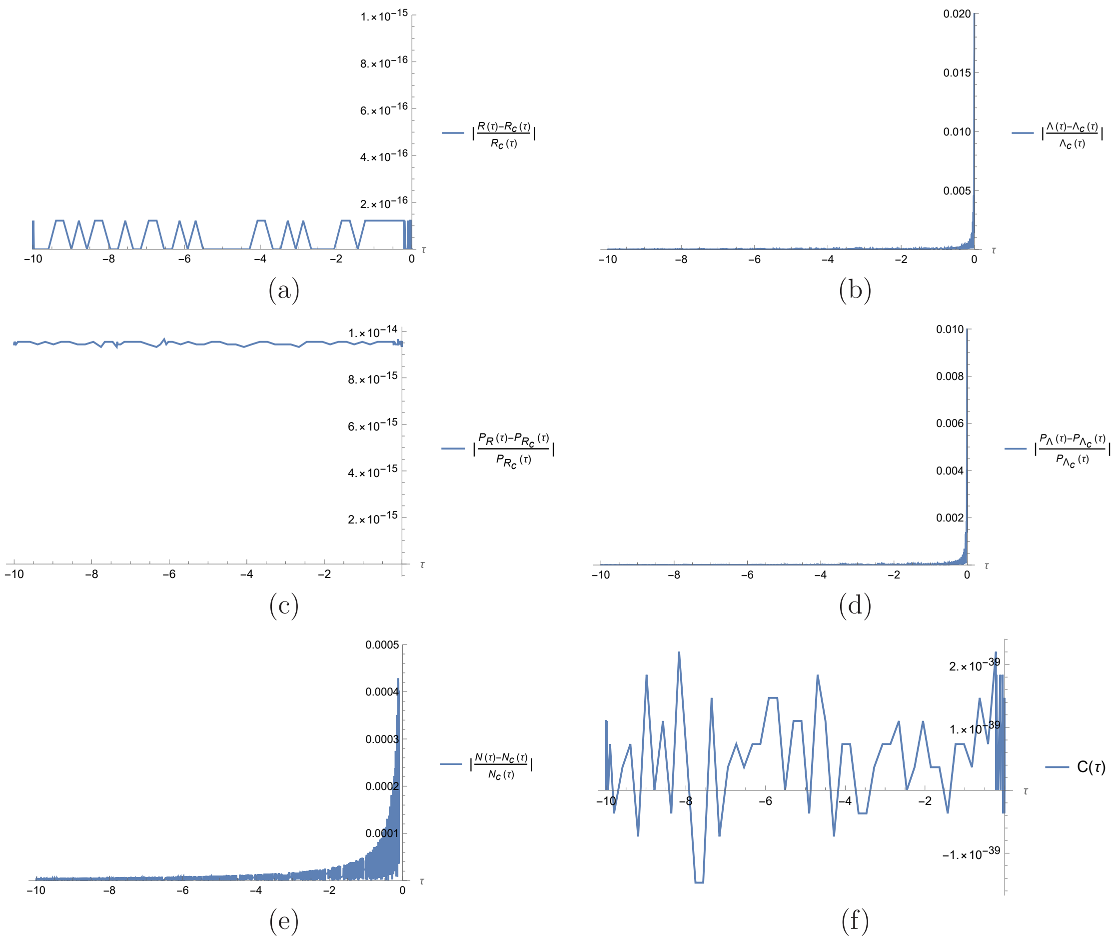

Figure 4.12: Plots of the relative differences of the functions $(R, \Lambda, P_R, P_\Lambda, N(\tau))$ and $\mathcal{C}(\tau)$ near the black hole horizon with the same choice of the parameters m and j, as those specified in Figs. 4.10 and 4.11, that is, $m = 10^{12} m_p,\ j_0 = 11.42,\ j = 10,\ \eta = 1.142$.

We also study the effects of η, and find that the quality behaviors of the spacetimes are quite similar to the above even when $\eta = 2$, as long as the semiclassical limit conditions (4.14) and (4.16) are satisfied and m is not too small ($m/m_p \gtrsim 10^6$).

4.5.3 $\eta \lesssim 1$

When $\eta \lesssim 1$, the metric coefficients take the same asymptotical forms as those given by Eqs.(4.116) - (4.121), but now with $\mathcal{F}(\eta) > 0$ and $\eta_0 > -\pi$ [41]. Therefore, now Λ decreases exponentially as $\tau \to -\infty$, while R still keeps increasing

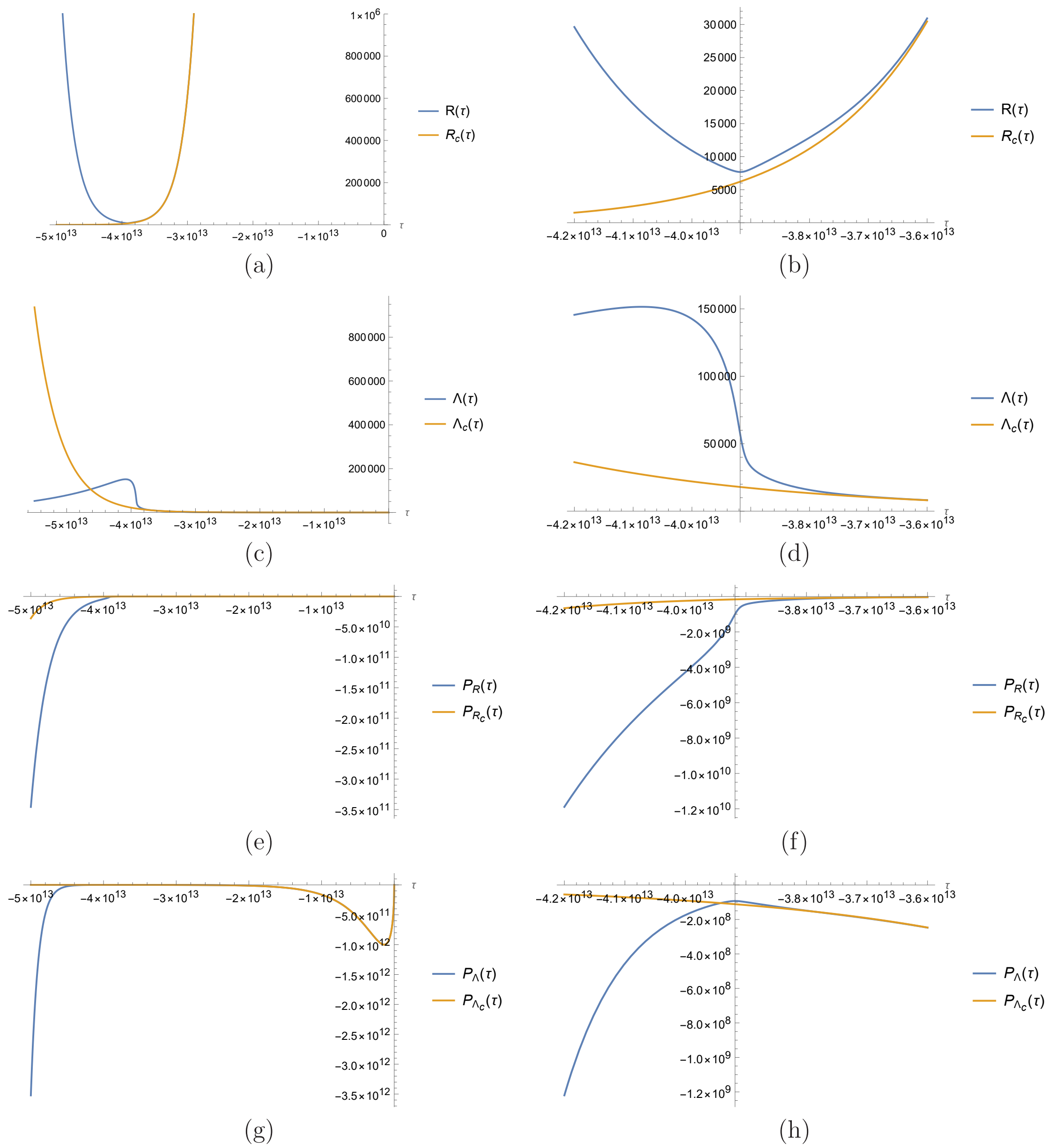

Figure 4.13: Plots of the physical variables $(R, \Lambda, P_R, P_\Lambda)$ and their classical correspondences $(R_c, \Lambda_c, P_{R_c}, P_{\Lambda_c})$. Particular attention is paid to the region near the throat $\tau_{\rm min} = -3.918 \times 10^{13}$, at which $R(\tau_{\rm min}) = 7676.1$. Graphs are plotted with $m = 10^{12} m_p,\ j_0 = 9.5,\ j = 10,\ \eta = 0.95$.

exponentially, i.e.

$$
\begin{aligned}
N &\simeq -\frac{2\gamma\sqrt{8\pi\gamma}\ \ell_p\ \sqrt{j_0},}{mG\left(\pi h_0[\eta_0] + 2\sin[\eta_0]\right)}, \\
\Lambda &= \Lambda_0 e^{a\tau}, \quad R = R_0 e^{-d\tau}.
\end{aligned} \tag{4.136}
$$

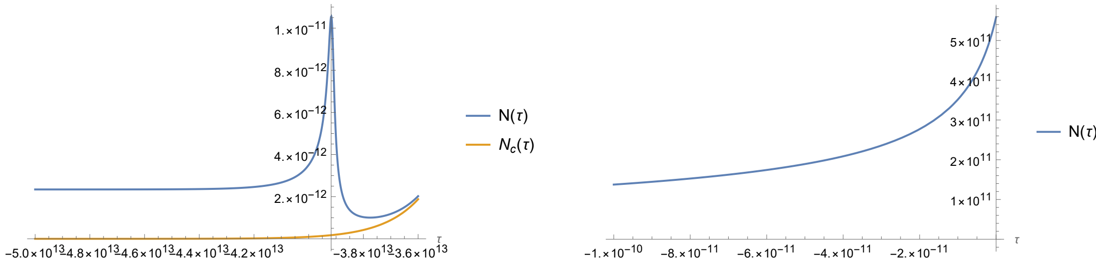

(a) (b)

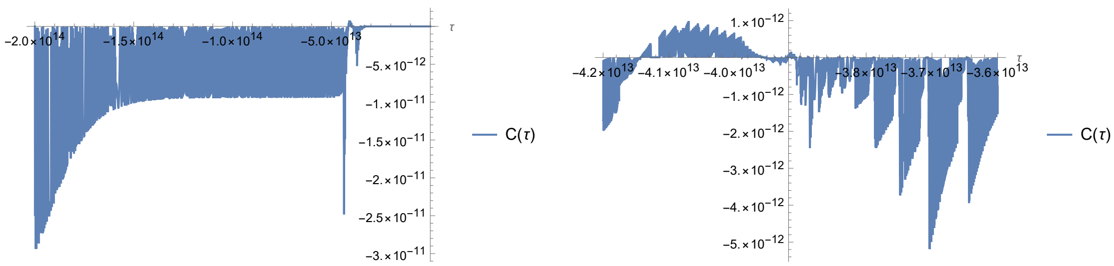

(c) (d)

Figure 4.14: Plots of $\mathcal{C}(\tau)$ and the lapse function $N(\tau)$ for $m = 10^{12}m_p,\ j_0 = 9.5,\ j = 10,\ \eta = 0.95$.

Then, the metric takes the following asymptotical form

$$ds^2 \simeq -\left(\frac{\hat{N}_0}{R}\right)^2 dR^2 + \frac{d\bar{x}^2}{R^{2a/d}} + R^2 d\Omega^2. \tag{4.137}$$

The corresponding effective energy-momentum tensor also takes the same form as that given by Eq.(4.77), but now with $u_\mu = (\hat{N}_0/R)\delta^R_\mu$, $\bar{x}_\mu = R^{-a/b}\delta^{\bar{x}}_\mu$, and

$$\begin{aligned}
\rho &\simeq \frac{d-2a}{d\hat{N}_0^2} - \frac{1}{R^2},\\
p_{\bar{x}} &\simeq -\frac{3}{\hat{N}_0^2} - \frac{1}{R^2},\\
p_\perp &\simeq -\frac{a^2 - ad + d^2}{d^2\hat{N}_0^2},
\end{aligned} \tag{4.138}$$

from which we can see that none of the three energy conditions are satisfied for any given a and d. In particular, when $a = d$ we have $\rho \simeq p_{\bar{x}}/3 \simeq p_\perp < 0$. In addition,

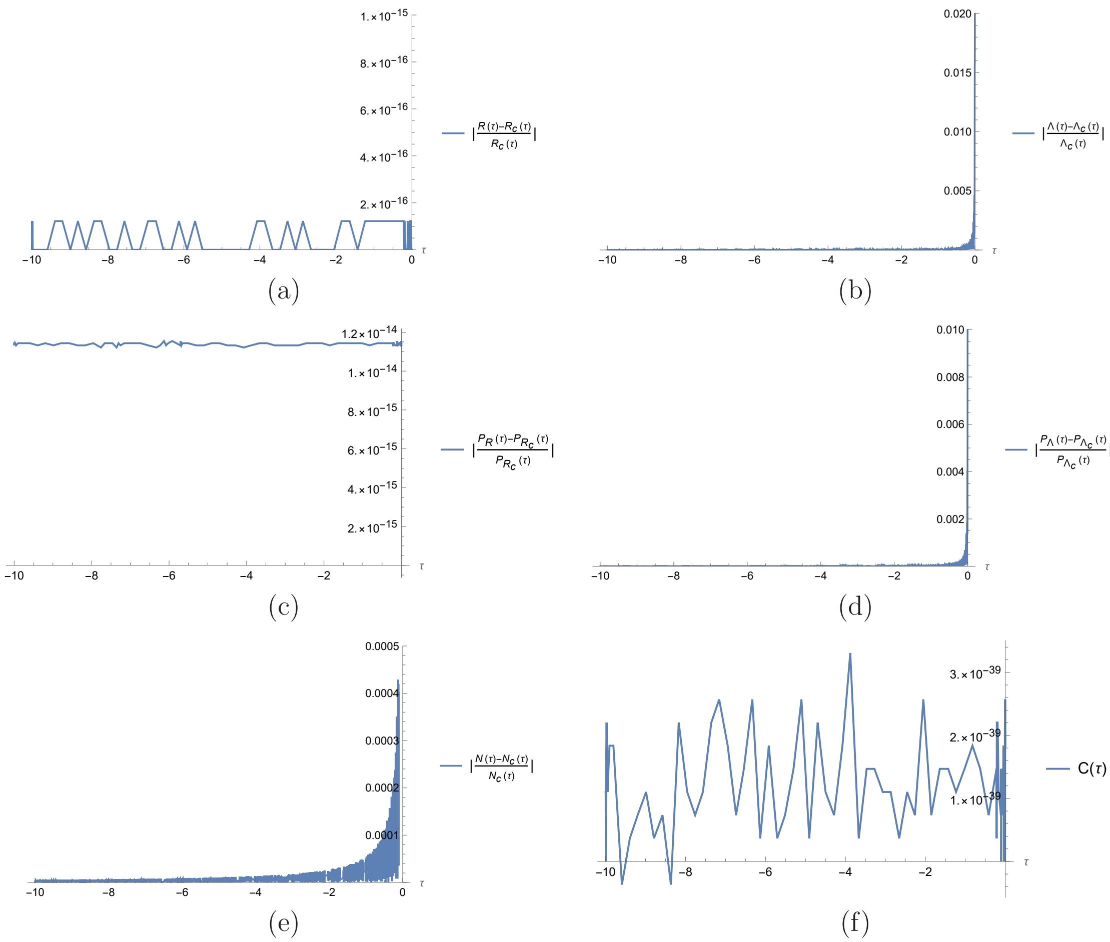

Figure 4.15: Plots of the relative differences of the functions $(R, \Lambda, P_R, P_\Lambda, N(\tau))$ and $\mathcal{C}(\tau)$ near the black hole horizon with the same choice of the parameters m and j, as those specified in Figs. 4.13 and 4.14, that is, $m = 10^{12} m_p$, $j_0 = 9.5$, $j = 10$, $\eta = 0.95$.

we also have

$$
\begin{aligned}
\mathcal{R} &\simeq 2\left(\frac{a^2 - 2ad + 3d^2}{d^2 \hat{N}_0^2} + \frac{1}{R^2}\right), \\
R_{\mu\nu}R^{\mu\nu} &\simeq 2\frac{a^4 - 2a^3 d + 5a^2 d^2 - 4ad^3 + 6d^4}{d^4 \hat{N}_0^4} - \frac{4(a-2d)}{d\hat{N}_0^2 R^2} + \frac{2}{R^4}, \\
R_{\mu\nu\alpha\beta}R^{\mu\nu\alpha\beta} &\simeq 4\left(\frac{a^4 + 2a^2 d^2 + 3d^4}{d^4 \hat{N}_0^4} + \frac{2}{\hat{N}_0^2 R^2} + \frac{1}{R^4}\right), \\
C_{\mu\nu\alpha\beta}C^{\mu\nu\alpha\beta} &\simeq \frac{4\left(aR^2(a+d) + d^2 \hat{N}_0^2\right)^2}{3d^4 \hat{N}_0^4 R^4},
\end{aligned}
\tag{4.139}
$$

which can be obtained from Eq.(4.115) by the replacement $a \to -a$, as expected.

To consider the corresponding Penrose diagram, we first write the metric (4.137) in the form

$$ds^2 \simeq -R_0^{-2a/d}\left(\frac{\bar{t}_0}{\bar{t}}\right)^2\left(-d\bar{t}^2 + d\bar{x}^2\right) + R^2 d\Omega^2, \tag{4.140}$$

where

$$\begin{aligned} \bar{t} &= \bar{t}_0\left(\frac{R}{R_0}\right)^{a/d}, \quad \bar{x} \equiv \left(\Lambda_0 R_0^{a/d}\right) x, \\ R &= R_0\left(\frac{\bar{t}}{\bar{t}_0}\right)^{d/a}, \quad \bar{t}_0 \equiv \frac{d\hat{N}_0 R_0^{a/d}}{a}. \end{aligned} \tag{4.141}$$

Comparing Eq.(4.140) with Eq.(4.129), we find that the $(\bar{t}, \bar{x})$-planes in both spacetimes have the same structure, and the only difference is to replace a by $-a$. Thus, the corresponding Penrose diagram is also given by Fig. 4.9. It is interesting to note that now the spacetime is not asymptotically de Sitter, even when $a = d$. In fact, now it is even not asymptotically conformally flat as can be seen from Eq.(4.139). In addition, in the current case none of the three energy conditions are satisfied.

In Figs. 4.13 - 4.15, we plot various physical quantities for $m/m_p = 10^{12}$, $j_0 = 9.5$, $j = 10$ so that $\eta \equiv j_0/j = 0.95 < 1$. In this case, the transition surface is located at $\tau_{\min} = -3.918 \times 10^{13}$, at which we find $R(\tau_{\min}) = 7676.1$. Then, it can be shown that both of the conditions (4.14) and (4.16) are satisfied. Therefore, the corresponding semiclassical description of the quantum black holes is well justified. In particular, from Figs. 4.13 and 4.14 we find that the asymptotic behavior of the metric coefficients are well approximated by Eq.(4.136), while Fig. 4.15 shows that near the horizon ($\tau \simeq 0$) the quantum geometric effects become negligible, possibly except the region very near to the horizon [cf. Fig. 4.15].

It is interesting to note that the asymptotic behavior in the current case is very sensitive to the choice of η. In particular, we find that when $\eta = 0.5$ the asymptotic behavior of the spacetime is already quite different from the one described by Eq.(4.136), although the semiclassical conditions (4.14) and (4.16) are still well justified.

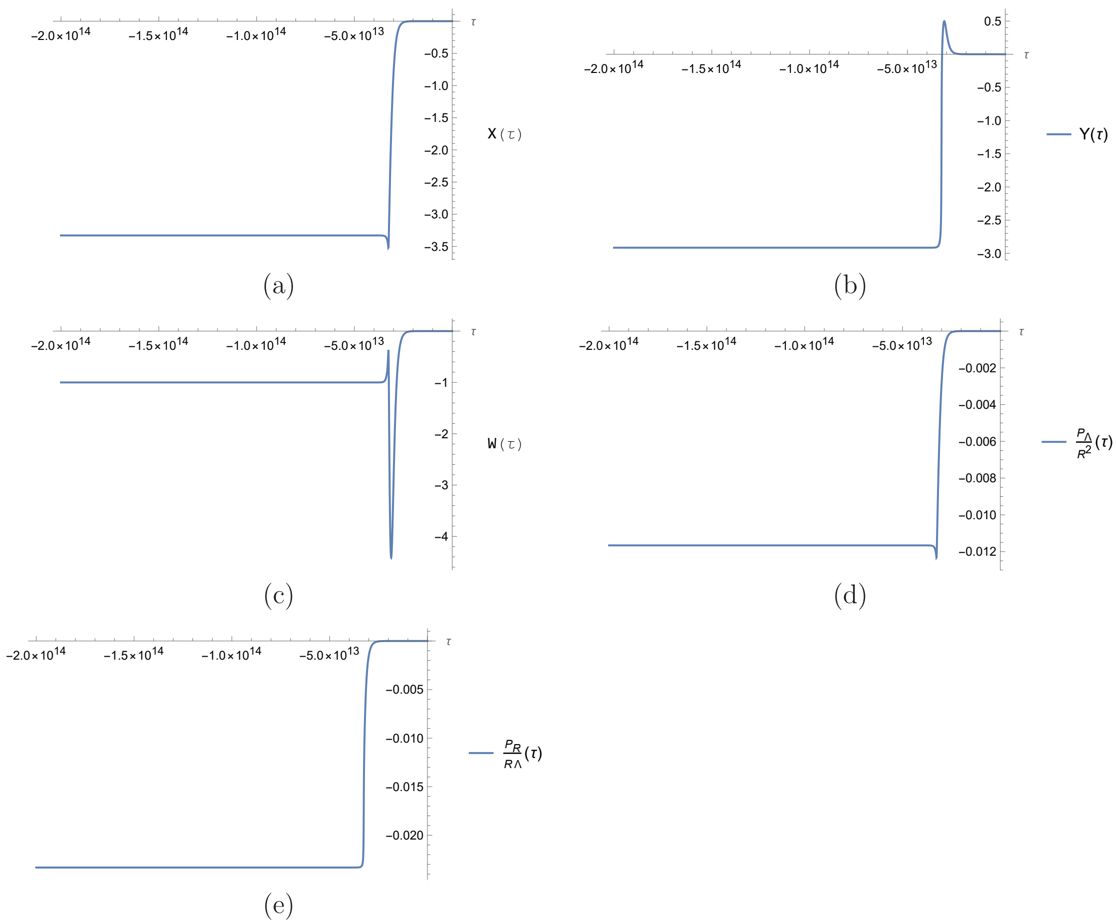

Figure 4.16: Plots of the functions $\left(X, Y, W, \frac{P_\Lambda}{R^2}, \frac{P_R}{R\Lambda}\right)$. The throat is lcated at $\tau_{\text{min}} = -3.260 \times 10^{13}$, at which $R(\tau_{\text{min}}) = 193115$. Curves are plotted with $\gamma \approx 0.274$, $m = 10^{12} m_p$, $j_x = 10^5$, $\eta \approx 1.142$.

4.6 Main Properties of the quantum reduced loop Black Holes with the Inverse Volume Corrections

As shown in [42], the inverse volume corrections, represented by terms proportional to the constants A, B and C in the effective Hamiltonian given by Eqs.(4.10)

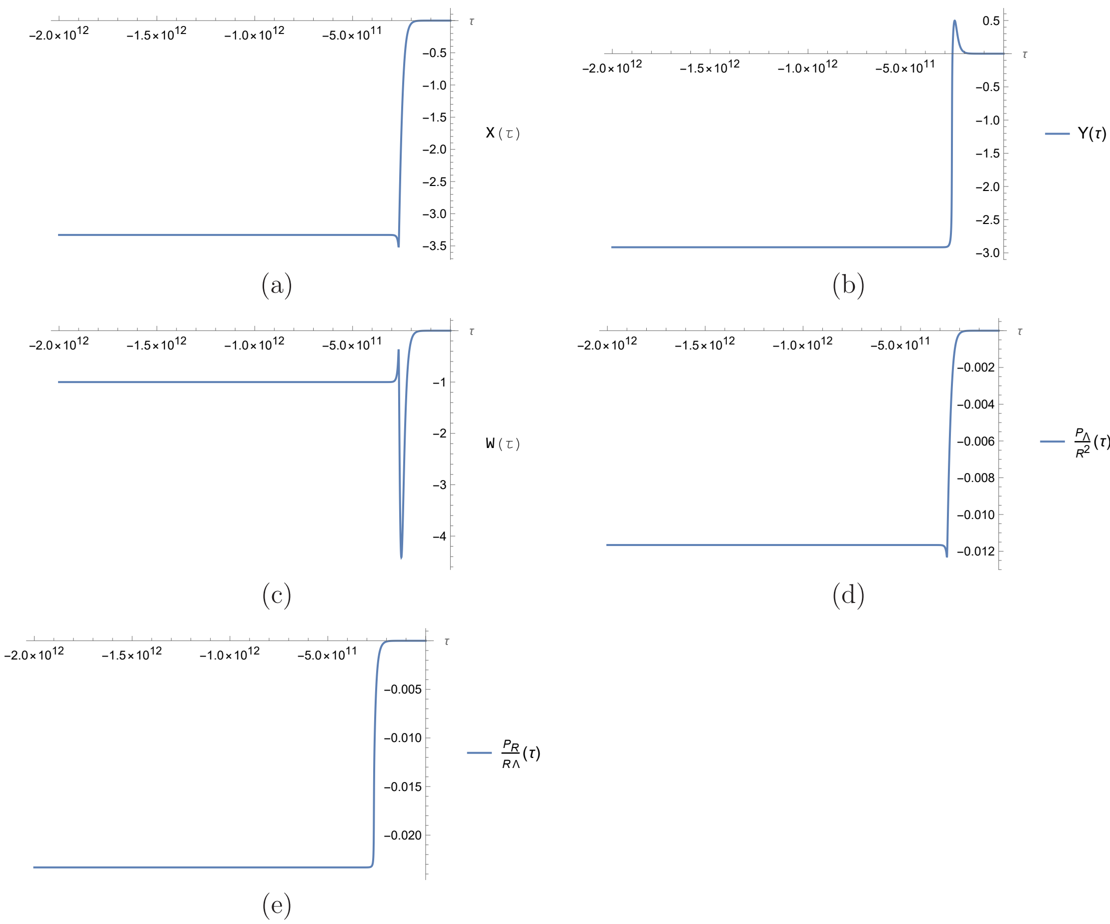

Figure 4.17: Plots of the functions $\left(X, Y, W, \frac{P_\Lambda}{R^2}, \frac{P_R}{R\Lambda}\right)$. The throat is at $\tau_{\text{min}} = -2.646 \times 10^{11}$, at which $R(\tau_{\text{min}}) = 41609.4$. Graphs are plotted with $\gamma \approx 0.274,\ m = 10^{10} m_p,\ j_x = 10^5,\ \eta \approx 1.142$.

and (4.11), are sub-leading. This can be also seen clearly from the analysis given in the beginning of the last section. Therefore, the inverse volume corrections should not change the main properties of the solutions with $\eta = 1,\ \eta > 1,\ \eta < 1$, respectively. However, demanding that the spatial manifold triangulation remain consistent on both sides of the black hole horizons, ABP found [42]

$$j = \gamma j_x, \tag{4.142}$$

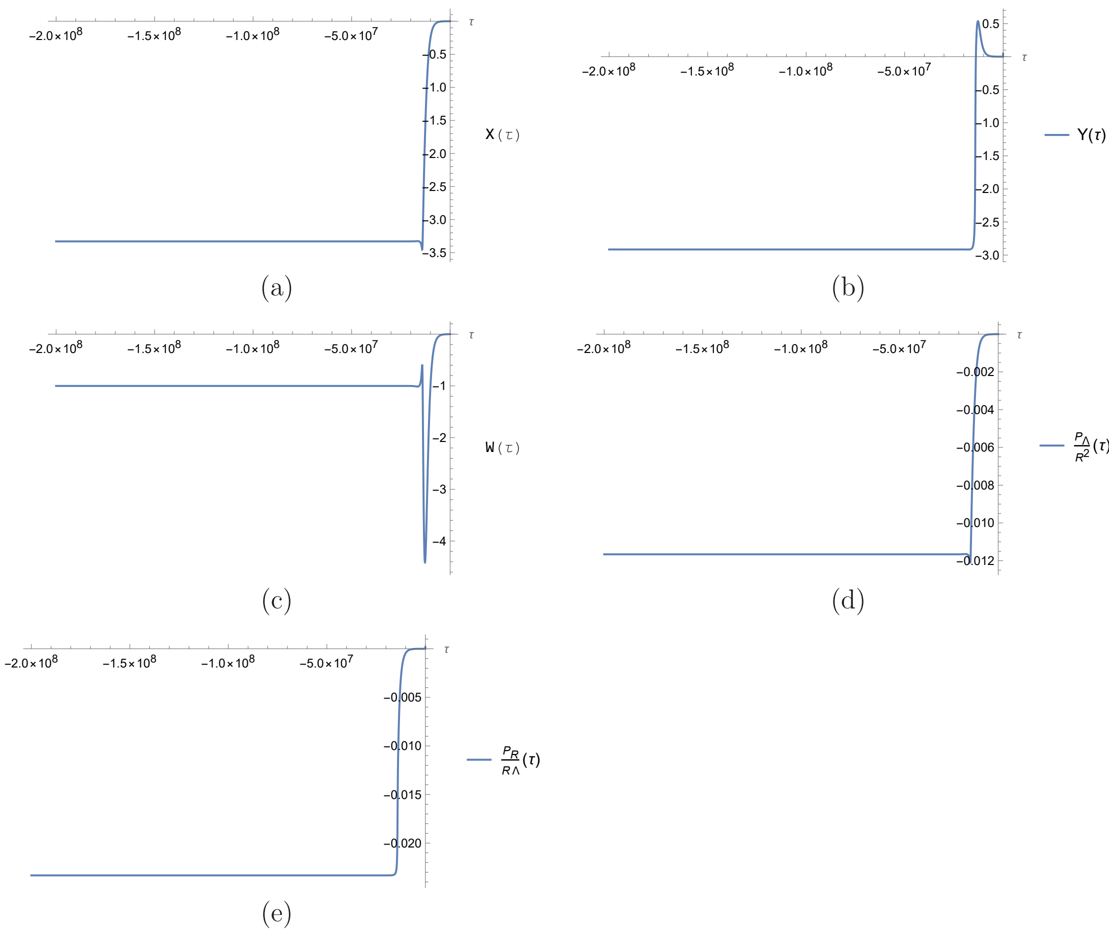

Figure 4.18: Plots of the functions $\left(X, Y, W, \frac{P_\Lambda}{R^2}, \frac{P_R}{R\Lambda}\right)$. The throat is at $\tau_{\min} = -1.416 \times 10^7$, at which $R(\tau_{\min}) = 2012.19$. Graphs are plotted with $\gamma \approx 0.274,\ m = 10^6 m_p,\ j_x = 10^5,\ \eta \approx 1.142$.

which immediately leads to

$$\eta \equiv \frac{\alpha}{\beta} = \frac{\sqrt{2\pi}}{8\gamma}, \tag{4.143}$$

as can be seen from Eq.(4.13). On the other hand, the considerations of black hole entropy in LQG showed that [43]

$$\gamma \simeq 0.274, \tag{4.144}$$

which is precisely the solution obtained by requiring $a = d$ in Section 4.5.2 for the case $\eta > 1$, in order to have the spacetime on the other side of the transition surface to be de Sitter, where a and b are the constants defined in Eq.(4.122). This "surprising coincidence" was first noted in [42] with a different approach, but in this chapter we obtained it simply by requiring that the transition surface connect two regions, one is asymptotically the Schwarzschild and the other is de Sitter. Therefore, following [42] in this section we consider only the case $\gamma \simeq 0.274$ [10], for which we have $\eta \simeq 1.142$.

Once γ and η are fixed, the five-parameter solutions of ABP are uniquely determined, after the inverse value correction parameters ν, δ and δ_x are given. In the following, we adopt the values given by ABP [42],

$$\begin{aligned} \nu &= 1.802, \quad \delta = \frac{1.458}{\beta^2} + \mathcal{O}\left(\beta^{-6}\right), \\ \delta_x &= \frac{0.729}{\beta^2} + \mathcal{O}\left(\beta^{-6}\right). \end{aligned} \tag{4.145}$$

In Figs. 4.16 - 4.18, we plot out the functions $\left(X,\ Y,\ W,\ \frac{P_\Lambda}{R^2},\ \frac{P_R}{R\Lambda}\right)$, for different m. From these figures we find

$$\begin{aligned} X &\simeq -\iota \approx -3.329, \quad Y \simeq -\frac{\iota}{\eta} \approx -2.915, \\ W &\simeq -(\pi h_0[\iota] + 2\sin[\iota]) \approx -1.001, \\ \frac{P_\Lambda}{R^2} &\simeq -\frac{\iota}{\alpha\gamma G} \approx -0.012, \\ \frac{P_R}{R\Lambda} &\simeq -\frac{2\iota}{\alpha\gamma G} \approx -0.023, \end{aligned} \tag{4.146}$$

as $\tau \to -\infty$, where $\iota \equiv -\eta_0 \simeq 3.329$ [42]. With the above expressions, we find that the asymptotical behavior of $N(\tau), R(\tau)$ and $\Lambda(\tau)$ is precisely given by Eq.(4.119), with the dependence of the three constants $N_0,\ R_0$ and Λ_0 being given by Table 4.4.

As shown in Sec. 4.5.2 for the case $\eta > 1$, the inverse volume corrections become important only when the geometric radius R is in the order of the Planck scale,

[10] It should be noted that a second solution in [42] was also found with $\gamma \simeq 0.227$. However, we find that this solution does not satisfy the Hamiltonian constraint $\mathcal{H}^{\rm IV+CS}_{\rm int} \simeq 0$, so it must be discarded.

$R \simeq \ell_p$. However, for macroscopic black holes, the radius of the transition surface $R_{\min}$ is always much larger than ℓ_p. For example, when $m/m_p = 10^{12}$, $R_{\min}/\ell_p \simeq 8059.95 \gg 1$ [cf. Fig. 4.10]. Therefore, for macroscopic black holes the inverse volume corrections can be safely neglected. This is true not only for the case $\eta = 1.142$, but also true for all the cases considered in Sec. 4.5 for macroscopic black holes. Therefore, in this section we shall not repeat our analyses carried out in that section.

4.7 Concluding Remarks

In this chapter, we systematically study quantum black holes in the framework of QRLG, proposed recently by ABP [40–42]. Starting from the full theory of LQG, ABP derived the effective Hamiltonian with respect to coherent states peaked around spherically symmetric geometry, by including both the holonomy and inverse volume corrections. Then, they showed that the classical singularity used to appear inside the Schwarzschild black hole is replaced by a regular transition surface with a finite and non-zero radius.

To understand such obtained effective Hamiltonian well and shed light on the relations to models obtained by the bottom-up approach, in Sec. 4.4.1 we first consider its classical limit, and obtained the desired Schwarzschild black hole solution, whereby the physical and geometric interpretation of the quantities used in the effective Hamiltonian are made clear. Then, in Sec. 4.4.2 and Sec. 4.4.3 by taking proper limits we re-derive respectively the BV [15] and AOS [9, 23, 25] solutions, all obtained by the bottom-up approach. In doing so, we can see clearly the relation between models obtained by the two different approaches, top-down and bottom-up.

In particular, the BV effective Hamiltonian was originally obtained from the classical Hamiltonian (4.7) with the polymerization,

$$b \to \frac{\sin(\delta_b b)}{\delta_b}, \quad c \to \frac{\sin(\delta_c c)}{\delta_c}. \tag{4.147}$$

However, instead of taking the parameters δ_b and δ_c as constants, following the $\bar{\mu}$-scheme first proposed in LQC [14] [11], BV took them as

$$\delta_b^{(\mathrm{BV})} = \sqrt{\frac{\Delta}{p_c}}, \quad \delta_c^{(\mathrm{BV})} = \frac{\sqrt{\Delta p_c}}{p_b}. \tag{4.148}$$

In Sec. 4.4.2, we show explicitly that the BV effective Hamiltonian can be obtained from the ABP Hamiltonian by taking the following replacement and limit,

$$(i)\ h_0[X] \to \frac{2}{\pi}\sin[X], \quad h_{-1}[X] \to \frac{2}{\pi}\cos[X], \tag{4.149}$$

$$(ii)\ \frac{A}{R^2}, \frac{B}{R^2}, \frac{C}{R^2} \ll 1. \tag{4.150}$$

It should be noted that with the choice of Eq.(4.148), the corresponding values of j_x and j are given by Eq.(4.68), from which we can see that they all violate the semi-classical limit (4.14), with which the ABP effective Hamiltonian (4.10) was derived. As a result, the BV model cannot be physically realized in the framework of QRLG, although formally they can be obtained from the ABP effective Hamiltonian by the above replacement and limit.

On the other hand, in addition to the replacement and limit given respectively by Eqs.(4.149) and (4.150), if we further assume that

$$\delta_b^{(\mathrm{AOS})}, \quad \delta_c^{(\mathrm{AOS})} = \text{Constants}, \tag{4.151}$$

[11] This is known to be the only possible choice in LQC, and results in physics that is independent from underlying fiducial structures used during quantization, and meanwhile yields a consistent infrared behavior for all matter obeying the weak energy condition [49].

and are determined by Eqs.(4.95) and (4.96), the ABP effective Hamiltonian (4.10) reduces precisely to the AOS one [9,23,25]. However, as shown explicitly by Eq.(4.99), such choices are also out of the semi-classical limit (4.68). Therefore, the AOS model cannot be realized in the framework of QRLG either.

It must be noted that the above conclusions do not imply that the BV and AOS models are unphysical, but rather than the fact that they must be realized in a different top-down approach.

With the above in mind, in Sec. 4.5 we study the ABP effective Hamiltonian without the inverse volume corrections, represented by the A, B, C terms in Eq.(4.10) in detail, by first confirming the main conclusions obtained in [41] and then clarifying some silent points. In particular, we find that the spacetime on the other side of the transition surface (throat) indeed sensitively depends on the ratio $\eta \equiv \alpha/\beta$, where α and β are defined by Eq.(4.13) in terms of $(j_x,\ j)$, or Eq.(4.100) in terms of $(\hat{j}_0,\ \hat{j})$, where the parameters $(j_x,\ j)$ were introduced in [42], while $(\hat{j}_0,\ \hat{j})$ were used in [41], and related one to the other through Eq.(4.23). As noticed previously, in Sec. 4.5 we drop the hats from $(\hat{j}_0,\ \hat{j}) \rightarrow (j_0,\ j)$, for the sake of simplicity.

When $\eta = 1$, the spacetime on the other side of the transition surface is conformally flat, and the non-vanishing curvatures are all of the order of the Planck scale, as can be seen from Eq.(4.115). Then, the corresponding Penrose diagram is given by Fig. 4.2. At this point, we find that it is very helpful to make a closer comparison of the ABP model with the BV one, as for the BV choice of Eq.(4.67), we have $\eta^{(\mathrm{BV})} = 1$. In particular, we find the following:

- In both models, the spacetime singularity used to appear at the center is replaced by a transition surface with a finite non-zero radius.

- In both models, the spacetime on one side of the transition surface is quite similar to the internal region of a Schwarzschild black hole with a black hole like horizon located at a finite distance from the transition surface (but with the removal of the black hole singularity used to occur at the center).
- In both models, the spacetime is asymmetric with respect to the transition surface, and model-dependent. In particular, in the BV model, the spacetime on the other side of the black hole like internal region approaches asymptotically to a charged Nariai space [46–48], of which the radius of the two-sphere S^2 approaches to a Planck scale constant, $R \to R_0 \simeq \mathcal{O}(\ell_p)$. In contrast, in the ABP model the radius grows exponentially without limits, $R \to \exp\left(-\frac{\tau}{2mG}\right)$ as $\tau \to -\infty$, and a macroscopic universe is obtained. The corresponding global structure can be seen clearly from its Penrose diagram given by Fig. 4.2.
- In the BV model, there exists multiple transition surfaces at which we have $dp_c/d\tau = 0$. When passing each transition surface, p_c decreases. As a result, p_c will soon decreases to a value at which the two-spheres S^2 have areas smaller than Δ, whereby the effective Hamiltonian is no longer valid. On the other hand, in the ABP model, only one such transition surface exists, and the above mentioned problem is absent. As a matter of fact, the two-planes spanned by τ and x are asymptotically flat, as shown explicitly by Eq.(4.109), although the four-dimensional spacetime is not [cf. Eq.(4.115)].

When $\eta \gtrsim 1$, the spacetime in general does not become conformally flat, as can seen from Eq.(4.127), unless $a = d$, where a and d are two constants defined by

Eq.(4.122). Then, the corresponding Penrose diagram is given by Fig. 4.9. When

$$a = d, \tag{4.152}$$

the spacetime is conformally flat and asymptotically de Sitter. It is remarkable that the condition (4.152) together with the one (4.21) leads to

$$\gamma = \frac{\sqrt{2\pi}}{8\eta} \simeq 0.274, \tag{4.153}$$

which is precisely the value obtained from the consideration of loop quantum black hole entropy obtained in [43]. As emphasized in [42], this coincidence should not be underestimated, and may provide some profound physics. In particular, the above picture is also consistent with the recently emerging picture in modified LQC models [50], in which the quantum bounce, which corresponds to the current transition surface, connects two regions, one is asymptotically de Sitter, and the other is asymptotically relativistic, after considering the expectation values of the Hamiltonian operator in LQG [51–53], by using complexifier coherent states [54–56], as shown explicitly in [57–59]. In addition, a similar structure of the spacetime of a spherical black hole also emerges in the framework of string [60], but now the transition surface is replaced by an S-Brane.

When $\eta \lesssim 1$, the spacetime cannot be conformally flat for any given values of a and d, as it can be seen from Eq.(4.139). However, the corresponding Penrose diagram is the same as that of the case with $\eta \gtrsim 1$, and given precisely by Fig. 4.9.

In review of all the above three cases, it is clear that the spacetime on the other side of the transition surface is no longer a white hole structure without spacetime singularities, as obtained from most of the bottom-up models [26, 61, 62], so that the corresponding Penrose diagram is extended repeatedly along the vertical line to include infinite identical universes of black holes and white holes (without spacetime singularities). Instead, the white hole region is replaced by either a conformally flat spacetime or a non-conformally flat one, given respectively by Figs. 4.2 and 4.9. But, in any case the spacetime is already geodesically complete, and no extensions are needed beyond their boundaries, so that in this framework multiple identical universes do not exist.

In addition, the undesirable feature in the BV model that multiple horizons exist on the other side of the transition surface disappears in the ABP model. In this model, the large quantum gravitational effects near the black hole horizons seemingly do not exist either, despite the fact that our numerical computations show that deviations may exist when very near to the black hole horizons, as shown explicitly in Figs. 4.5, 4.12, and 4.15. However, more careful analysis is required, as the metric becomes singular when crossing the horizons, and our numerical simulations may become unreliable. We wish to come back to this important question in another occasion.

When inverse volume corrections, represented by terms proportional to the constants A, B, C in the effective Hamiltonian (4.10), are taken into account, the effects are always sub-leading, as these terms become important only when the radius of the two-sphere $\tau, x =$ Constant is of the order of the Planck scale. For macroscopic black holes, we find that the corresponding radii of the transition surfaces are always much larger than the Planck scale, so their effects will be always sub-leading even when across the transition surface. Such analysis was carried out in Sec. 4.6, in which we mainly focus on the case in which the conditions (4.152) and (4.153) hold. In [42] it was shown that these sub-leading terms precisely make up all the requirement for a spacetime to be asymptotically de Sitter, defined in [63], even to the sub-leading order.

CHAPTER FIVE

Non-existence of quantum black hole horizons in the improved dynamics approach

This chapter has been submitted as [3]: W. C. Gan, X. M. Kuang, Z. H. Yang, Y. Gong, A. Wang and B. Wang, Non-existence of quantum black hole horizons in the improved dynamics approach, [arXiv:2212.14535 [gr-qc]].

5.1 Abstract

In this chapter, we study the quantum geometric effects near the locations that black hole horizons used to appear in Einstein's classical theory within the framework of the improved dynamic approach, in which the two polymerization parameters of the Kantowski-Sachs spacetime are functions of the phase space variables. Our detailed analysis shows that the effects are so strong that black hole horizons of the effective quantum theory do not exist any longer, and the corresponding Kantowski-Sachs model now describes the entire spacetime of the trapped region, instead of being only the internal region of a black hole, as it is usually expected in loop quantum gravity.

5.2 Introduction

In LQC, there exist two different quantization schemes, the so-called μ_o and $\bar{\mu}$ schemes, which give different representations of quantum Hamiltonian constraints and lead to different effective dynamics [64]. The fundamental difference of these two approaches rises in the implementation of the minimal area gap mentioned above. In the μ_o scheme, each holonomy $h_k^{(\mu)}$ is considered as an eigenstate of the area operator, associated with the face of the elementary cell orthogonal to the k-th direction. The parameter μ is fixed by requiring the corresponding eigenvalue be the minimal area gap. As a result, μ is a constant in this approach [65]. However, it has been shown [66] that this quantization does not have a proper semiclassical limit, and suffers from the dependence on the length of the fiducial cell. It also lacks of consistent identified curvature scales. On the other hand, in the $\bar{\mu}$ scheme [14], the quantization of areas is referred to the physical geometries, and when shrinking a loop until the minimal area enclosed by it, one should use the physical geometry. Since the latter depends on the phase space variables, now when calculating the holonomy $h_k^{(\mu)}$, one finds that the parameter μ depends on the phase space variables, too. In the literature, this improved dynamical approach is often referred to as the $\bar{\mu}$ scheme, and has been shown to be the only scheme discovered so far that overcomes the limitations of the μ_o scheme and is consistent with observations [64].

In parallel to the studies of LQC, loop quantum black holes (LQBHs) have been also intensively studied in the past decade or so (See, for example, [9, 26, 67–69] and references therein). In particular, since the Schwarzschild black hole interior can be treated as the Kantowski-Sachs cosmological model, in which the spacetime is homogeneous and the metric is only time-dependent, some of the LQC techniques can be borrowed to study the black hole interiors directly. Along this line of thinking, LQBHs were initially studied within the μ_o scheme [10, 13, 70]. However, this LQBH model also suffers from similar limitations as the μ_o scheme in LQC [8, 9, 71]. Soon the $\bar{\mu}$ scheme was applied to the Schwarzschild black hole interior by Böhmer and Vandersloot (BV) [15] (See also [72, 73] for a similar prescription in the Kantowski-Sachs universe, and [62, 74–78] in the Painlevé-Gullstrand-like coordinates that cover both of the internal and external regions of the classical Schwarzschild black hole.[1]). Later, the $\bar{\mu}$ quantization scheme was shown to be the unique quantization scheme that is free from the dependence on the fiducial length and has consistent ultraviolet and infrared behavior [84]. It was also shown that it has universally bounded curvature scales and energy density, and that the expansion and shear scalars are all finite, in addition to the geodesic completeness and generic resolution of strong singularities [85].

Despite of these attractive features, the BV model suffers a severe drawback: *there are large departures from the classical theory very near the classical black hole horizon even for massive black holes, for which the curvatures at the horizon become very low* [8, 9, 15, 71]. In addition, when the curvature reaches the Planck scale, the geometric radius of the round 2-spheres researches a minimum and then bounces, giving rise to a transition surface $\mathcal{T}$, whereby the original singularity is replaced by a quantum bounce. The transition surface $\mathcal{T}$ naturally divides the spacetime into two regions. To the past of $\mathcal{T}$ we have a trapped region, and to its future an anti-trapped region appears, in which the geometric radius of the 2-spheres increases. However, in contrast to other LQBH models, this anti-trapped region is not bounded by a white-hole-like horizon, instead it is followed by another bounce, across which the region becomes trapped again, and the radius of the 2-spheres starts to decrease [15, 72, 73]. This process will be repeating indefinitely, and after each bounce the geometric radius of the 2-spheres will get smaller. So, soon the area of the 2-spheres will become smaller than the minimal area gap, whereby the model becomes self-inconsistent [9].

[1] For rigorous mathematical development of Ashtekar's formalism for spherically symmetric general minisperspaces and its loop quantization, see, for example, [76, 79–83] and references therein.

In this chapter, we shall mainly focus our attention to the past of $\mathcal{T}$, as the spacetimes in the pre-transition phase were already studied in detail first in the vacuum case [15, 72, 73] and then in the case filled with matter [84] or a cosmological constant [86]. In all the cases, the spacetimes approach to the classical "charged" Nariai solutions, in which the radii of the two-spheres become constants asymptotically, but with values smaller than the Planck scale. So, the validity of this asymptotic behavior is questionable [9]. In this chapter, we shall put this question aside, and study in detail the spacetimes to the past of $\mathcal{T}$ by focusing ourselves onto the quantum geometric effects near the location that the classical black horizon used to appear, especially the possible development of black hole horizons [9, 87–90]. To our surprising, we find that such a horizon is never developed within a finite time. Thus, in the BV model the quantum geometric effects are so strong that the black hole horizon used to appear classically at $T_H \equiv \ln(2m)$ now disappears, and the resultant Kantowski-Sachs model covers already the entire spacetime to the past of the transition surface $\mathcal{T}$ [85]. As a result, the external region of a quantum black hole in this model does not exist.

Specifically, this chapter is organized as follows: In Sec. 5.3, we consider the BV model by first introducing the BV prescription of the two polymerization parameters δ_b and δ_c given by Eq.(2.61), and then write down the corresponding dynamical equations, given explicitly by Eqs.(2.64) - (2.67). To estimate the region where the quantum effects near the classical black hole horizon become important, we first introduce a parameter ϵ via the relation $T_\epsilon = T_H(1-\epsilon)$ at which $|\delta_c c|_{T_\epsilon} \simeq \mathcal{O}(1)$, from which we find that such effects become important only very closed to T_H for massive black holes. To study such effects explicitly, the choice of initial time and conditions are crucial. In this chapter we choose the initial time T_i that is far from both the transition surface and the classical black horizon, $T_{\mathcal{T}} \ll T_i \ll T_H$, so that the initial conditions are as closed to those of classical theory as possible [cf. Table 5.1]. With these initial conditions we study the evolution of the dynamical equations, and find that the metric coefficients remain finite and non-singular within any given finite time. These results are strongly supported by the analytical studies carried out in [85]. In particular, it was shown explicitly that $0 < p_b(\tau), p_c(\tau) < \infty$ at any given finite time τ, where p_b and p_c are the metric coefficients defined in Eq.(2.10), and τ denotes the proper time, obtained by setting the lapse function to be unity. Then, we turn to study the existence of marginally trapped surfaces by analyzing the expansions of the in-going and out-going radially-moving light rays, as well as the normal vector to the two-spheres, and find that such surfaces indeed exist. However, they represent neither black hole horizons nor white hole ones, as they always separate trapped regions from anti-trapped ones, or vice versa, instead of separating trapped (anti-trapped) regions from untrapped ones, as a black (white) hole horizon usually does [9, 87–90]. Finally, in Sec. 5.4, we present our main conclusions.

Before proceeding to the next section, we note the following: In this chapter the Planck length ℓ_{pl} and mass M_{pl} are defined, respectively, by $\ell_{pl} \equiv \sqrt{G\hbar/c^3}$ and $M_{pl} \equiv \sqrt{\hbar c/G}$, where G denotes the Newtonian constant, $\hbar$ is the Planck constant divided by 2π, and c is the speed of light (Note that in the main text, c will be used to denote a phase space variable, and only in this paragraph we use it to denote the speed of light, without causing any confusion.). Thus, in terms of the fundamental units, M, L and T, the units of $\hbar$ and c are $[\hbar] = ML^2T^{-1}$, $[c] = LT^{-1}$, where M, L and T denote the units of mass, length and time, respectively. In this chapter we shall adopt the natural units, so that $\hbar = c = 1$. Then, we find $L = T,\ M = L^{-1}$, $[G] = L^3 M^{-1} T^{-2} = L^2$. In addition, all the figures will be plotted in the units of ℓ_{pl} and M_{pl}, whenever the length and mass parameters are involved.

5.3 Böhmer-Vandersloot Model

5.3.1 Quantum Effects Near the Classical Black Hole Horizon

Table 5.1: Initial values of $c(T_i)$ calculated from Eq.(5.7) at different times T_i and the corresponding classical values $c^{\rm GR}(T_i)$ for $m = M/G = \ell_{pl}$, for which we have $T_{\mathcal{T}} \simeq -1.49$ and $T_H \simeq 0.693$.

T_i	-1.45	0.3	0.643	0.685
$c(T_i)$	2.68044 - 2.09266 I	-0.13272	-0.0682837	-0.0883704 + 0.0213373 I
$c^{\rm GR}(T_i)$	-4.31636	-0.130343	-0.0656195	-0.0603504

The classical black hole horizon is located at

$$T_H = \ln(2m), \tag{5.1}$$

as can be seen clearly from Eq.(2.30), at which we have $p_b^{\rm GR} = 0$. Before solving the EoMs, let us first estimate the quantum effects near $T = T_H$. Substituting the classical Schwarzschild black hole solution given by Eqs.(2.20)-(2.23) into Eq.(2.61), we find

$$|\delta_b b| = \frac{\sqrt{\Delta}}{e^T}\gamma\sqrt{2me^{-T} - 1} \to 0, \quad T \to T_H, \tag{5.2}$$

but

$$|\delta_c c| = \frac{\sqrt{\Delta}\gamma m e^{-2T}}{\sqrt{2me^{-T} - 1}} \to \infty, \quad T \to T_H. \tag{5.3}$$

Eq.(5.3) indicates that the BV solution has large quantum effects near $T \simeq T_H$. To characterize these effects, in the vicinity of T_H let us introduce ϵ through $T = T_\epsilon \equiv$

$T_H(1-\epsilon)$ with $\epsilon \ll 1$. Then, assuming that at T_ϵ we have $|\delta_c c\,(T_\epsilon)\,| \simeq \mathcal{O}(1)$, so that

$$
\begin{aligned}
\left.|\delta_c c|\right|_{T=T_\epsilon} &= \frac{\sqrt{\Delta}\gamma m e^{-2T_\epsilon}}{\sqrt{2me^{-T_\epsilon}-1}} \approx \frac{\sqrt{\Delta}\gamma m e^{-2T_H}}{\sqrt{2me^{-T_\epsilon}-1}} \\
&\approx \frac{\sqrt{\Delta}\gamma}{4m\sqrt{(2m)^\epsilon - 1}} \sim \mathcal{O}(1),
\end{aligned} \tag{5.4}
$$

which leads to

$$
\epsilon \simeq \frac{\ln(\frac{\Delta\gamma^2}{16m^2}+1)}{\ln(2m)}. \tag{5.5}
$$

From this expression we can see that as m increases, ϵ decreases sharply, that is, we need to get very close to T_H in order to see the quantum effects for massive black holes. In fact, in the following we shall show that such quantum effects are so large that the horizon is never formed within a finite time T. Recall that the geometric radius r of the two spheres $T,\ x =$ constant now is given by $r = e^T$. This in turn implies that in the BV approach quantum black hole horizons do not exist in the whole trapped region, $T > \mathcal{T}$, with the only exception: it might be possible to exist at $r = \infty$ (or $T = \infty$).

5.3.2 Initial Conditions

To show our above claim, let us first consider the initial conditions. Since Eqs.(2.64) - (2.67) are four first-order ordinary differential equations, four initial conditions in general are needed. However, these initial conditions must also satisfy the Hamiltonian constraint $H^{\text{eff}} = 0$, so only three of them are independent. As a result, the phase space of the initial conditions is three-dimensional (3D). Without loss of the generality, we can first choose the initial conditions for $p_b(T_i)$, $p_c(T_i)$ and $b(T_i)$ at the initial time $T = T_i$, and then solve the effective Hamiltonian constraint to find $c(T_i)$. It is clear that such obtained 3D phase space includes all the possible real values of

$p_b(T_i)$, $p_c(T_i)$ and $b(T_i)$. However, to compare the resultant BV spacetimes with the Schwarzschild one, we choose them as their corresponding values of GR, that is

$$\begin{aligned} & p_b(T_i) = p_b^{\rm GR}(T_i), \quad p_c(T_i) = p_c^{\rm GR}(T_i), \\ & b(T_i) = b^{\rm GR}(T_i), \end{aligned} \tag{5.6}$$

and

$$H^{\rm eff}(T_i) = 0 \quad \Rightarrow \quad c(T_i) = c^{\rm eff}(T_i). \tag{5.7}$$

Once the initial conditions are chosen at a chosen initial time T_i, the EoMs Eqs.(2.64)-(2.67) will uniquely determine the four physical variables $(p_b, b; p_c, c)$ at any given later time T.

Due to the large quantum effects near T_H as estimated in the last subsection, normally we choose T_i far from T_H, that is, $T_i \ll T_H$ [2]. On the other hand, near the throat $T = T_{\mathcal{T}}$ it is expected that the spacetime geometry will be dramatically different from that of GR, so the conditions given by Eq.(5.6) near $T_{\mathcal{T}}$ might not hold. Therefore, in general we choose T_i so that

$$T_{\mathcal{T}} \ll T_i \ll T_H. \tag{5.8}$$

To understand the above arguments further, we consider the initial conditions at different times T_i's. We compare the effective value of $c(T_i) = c^{\rm eff}(T_i)$ obtained from Eq.(5.7) with its corresponding classical value $c^{\rm GR}(T_i)$ at different times T_i's in Table 5.1 for $m = \ell_{pl}$, for which we have $T_{\mathcal{T}} \simeq -1.49$, and $T_H \simeq 0.693$. From the Table

[2] It should be noted that $c(T_i) = c^{\rm eff}(T_i)$ obtained from $H^{\rm eff}(T_i) = 0$ can still be significantly different from $c^{\rm GR}(T_i)$, even $T_i \simeq T_H$ and $p_b(T_i)$, $p_c(T_i)$ and $b(T_i)$ are chosen as their corresponding values of GR, as given by Eq.(5.6), because now $H^{\rm eff}(T_i) \neq H^{\rm GR}(T_i)$. In fact, from Eq.(5.3) we find that $|\delta_c c|$ is still very large near T_H, precisely because the fact that now $c(T_i)$ still deviates from its classical value significantly. Then, the solution cannot be approximated by the classical Schwarzschild black hole at T_H.

we can see that Eq.(5.7) has no real-value solutions for $c(T_i)$ when T_i is very closed to either the transition surface $T_{\mathcal{T}}$ or to the classical horizon T_H, which means that the quantum effects are so large near these points, so that the effective Hamiltonian constraint Eq.(5.7) has no physical solutions for such chosen $p_b(T_i)$, $p_c(T_i)$ and $b(T_i)$. On the other hand, when far away from these points, the difference between $c(T_i)$ and $c^{\rm GR}(T_i)$ is small. Therefore, in the following, we shall choose T_i so that the condition (5.8) is always satisfied.

5.3.3 Numerical Results

Once the initial time and conditions are specified, we are ready to solve EoMs (2.64) - (2.67) numerically. To monitor the numerical errors, we shall closely pay attention to the effective Hamiltonian given by Eq.(2.71), which is required to vanish identically

$$H^{\rm eff} \simeq 0, \tag{5.9}$$

along any of physical trajectories. However, numerically this is true only up to certain accuracy. To make sure that such numerical calculations are reliable, and our physical conclusions will not depend on these numerical errors, we run our *Mathematica* code in supercomputers with high precisions. In particular, in all calculations we require that the Working Precision and Precision Goal be respectively 250 and 245, where Working Precision specifies how many digits of precisions should be maintained in internal computations of *Mathematica*, and Precision Goal specifies how many effective digits of precisions should be sought in the final result.

5.3.3.1 Asymptotic Behavior of the Spacetimes as $T \gg T_{\mathcal{T}}$

With the above in mind, let first consider the case $m = \ell_{pl}$. In this case, we have $T_{\mathcal{T}} \simeq -1.49$ and $T_H \simeq 0.693$. The initial point is chosen at $T_i = 0.3$, which satisfies Eq.(5.8). From Table 5.1 we can also see that at this point $c(T_i)$ is very closed to its corresponding classical value $c^{\mathrm{GR}}(T_i)$. In Fig. 5.1 we plot all the four variables $b,\ c,\ p_b$ and p_c, together with H^{eff}, the corresponding Kretchmann scalar K and the metric components N^2 and g_{xx}, where the Kretchmann scalar K is defined as $K(T) \equiv R_{\alpha\beta\mu\nu}R^{\alpha\beta\mu\nu}$. From Fig. 5.1 (h) we can see that the maximal errors happen near $T \simeq 10$ at which $\left|H^{\mathrm{eff}}\right| \le 2.0 \times 10^{-8}$. Before or after it, we have $\left|H^{\mathrm{eff}}\right| \ll 10^{-8}$. Therefore, our numerical computations are reliable.

On the other hand, from Fig. 5.1 (d) we can see that the geometric radius $r = \sqrt{p_c}$ is exponentially increasing. As a result, the metric coefficient g_{xx} decreases exponentially, but never be zero precisely for any given finite time T, as shown by Fig. 5.1 (f). In addition, the lapse function square N^2 is also oscillating with a similar period as that of p_b, but after each circle of oscillations it is getting larger and larger [cf. Fig. 5.1 (e)]. However, it always remains finite. Moreover, in Fig. 5.1 (g) we plot out the Kretchmann scalar $K(T)$ together with its classical counterpart $K^{\mathrm{GR}}(T) \equiv 48m^2/p_c^3$, from which we can see clearly that the quantum geometric effects indeed become very large near the location of the classical black hole horizon $T \simeq \ln(2m)$. This deviation lasts for a quite while [$T \in (T_H, 160)$ for $m = \ell_{pl}$], but finally $K(T)$ will be decreasing as p_c^{-3}, the same as $K^{\mathrm{GR}}(T)$, that is,

$$K(T) \simeq \frac{K_0}{p_c^3}, \quad K_0 > 48m^2, \tag{5.10}$$

as $T \to \infty$. But, we always have $K_0 > 48m^2$.

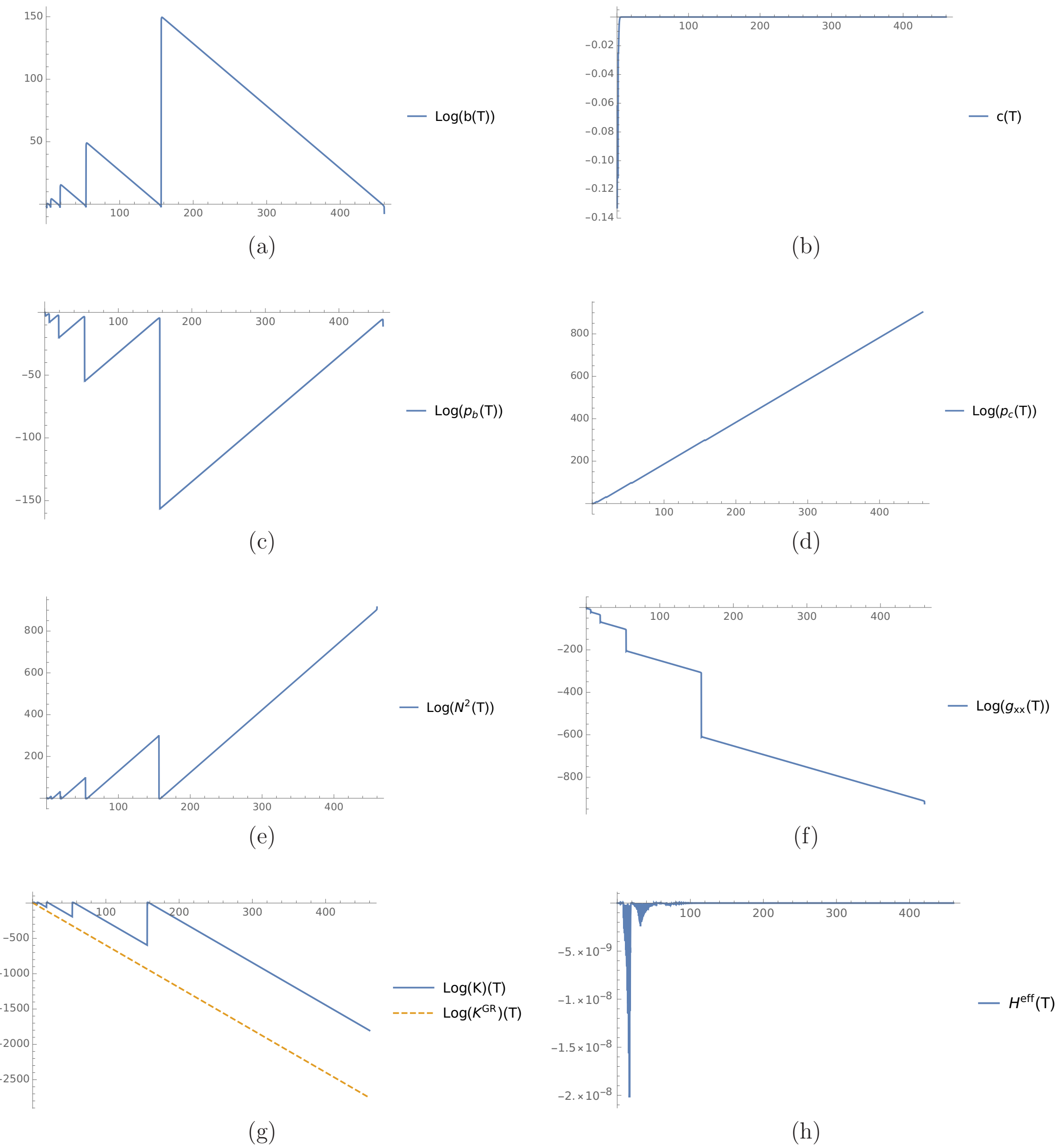

Figure 5.1: Plots of the four physical variables (b, c, p_b, p_c) and the effective Hamiltonian defined by Eq.(2.71), together with the metric components N^2, g_{xx} and the Kretchmann scalar K, as well as the classical counterpart $K^{\mathrm{GR}}(T) \equiv 48m^2/p_c^3$ of $K(T)$. The mass parameter m is chosen as $m/\ell_{pl} = 1$, for which we have $T_{\mathcal{T}} \simeq -1.49$ and $T_H \approx 0.693$. The initial time is chosen at $T_i = 0.3$.

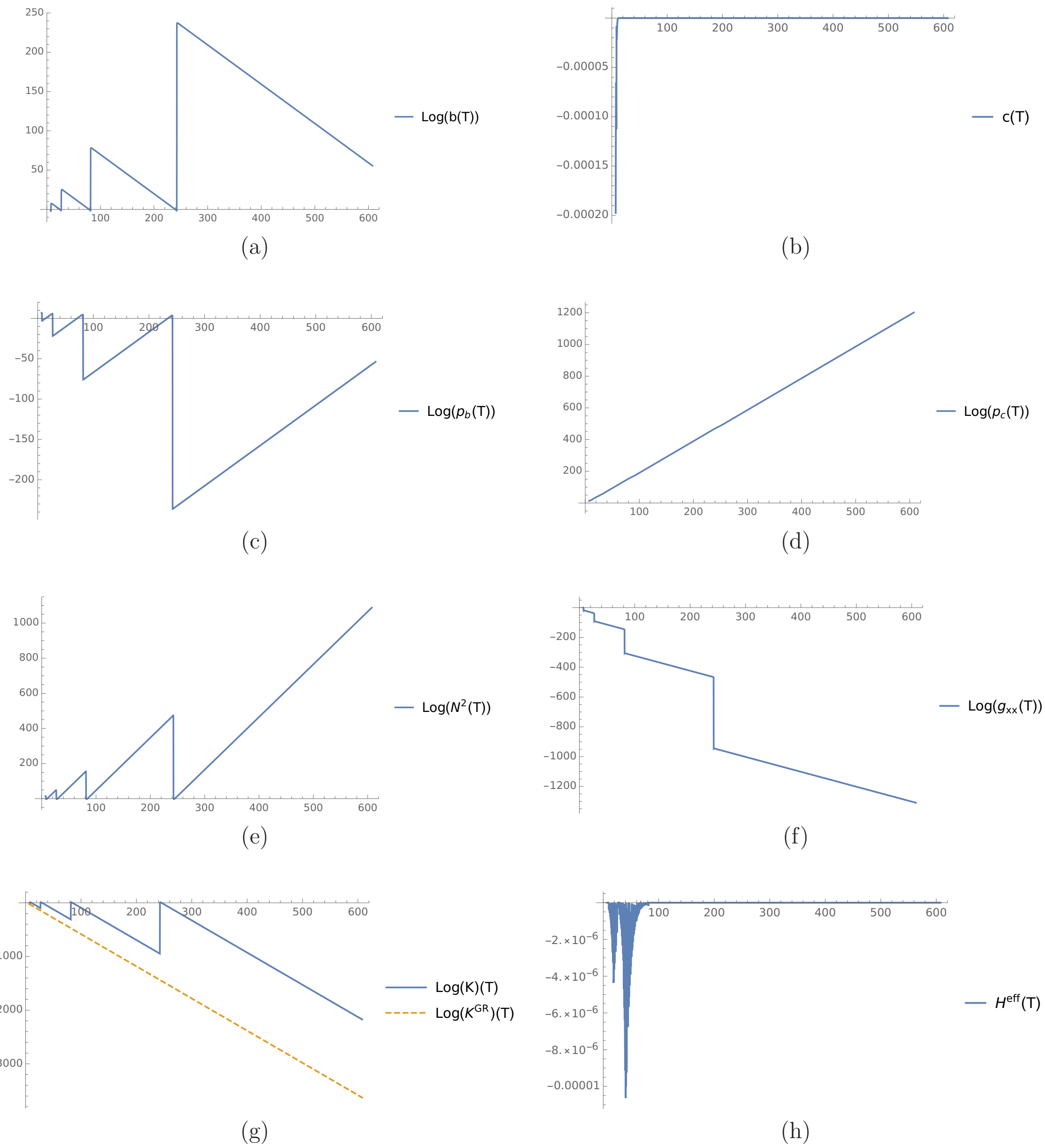

Figure 5.2: Plots of the four physical variables (b, c, p_b, p_c) and H^{eff}, together with the metric components N^2, g_{xx}, the Kretchmann scalar K, and the classical counterpart $K^{\text{GR}}(T) \equiv 48m^2/p_c^3$ with $m/\ell_{pl} = 10^3$, for which we have $T_{\mathcal{T}} \simeq 0.8327$ and $T_H \approx 7.6009$. The initial time is chosen at $T_i = 7.0$.

The above results are sharply in contrast to the classical case, in which $N^2|_{\rm GR} = e^{2T}/(2me^{-T}-1) \to \infty$ at the black hole horizon, $T_H = \ln 2 \simeq 0.693$, while $p_b^{\rm GR}$ becomes zero precisely at T_H, so is $g_{xx}^{\rm GR}$, as can be seen from Eqs.(2.23) and (2.24).

It should be also noted that similar results can be obtained when the initial time is chosen to be at $T_i = \ln(2m) - 0.05 \simeq 0.643$, which is also a point at which the difference between $c(T_i)$ and $c^{\rm GR}(T_i)$ is negligible, as shown in Table 5.1. In addition, we also consider the case $m = 10^3\ell_{pl}$. The corresponding physical quantities are plotted out in Fig. 5.2. From these figures we can see that the metric coefficients, $(N^2,\ g_{xx},\ p_c)$ are all finite and non-zero for any given finite time T.

It is remarkable to note that our above conclusions that *the metric coefficients* $g_{\mu\nu}$ *and* $g^{\mu\nu}$ *are not singular at any given finite time* T are strongly supported by the analytical results obtained in [85], in which it was shown explicitly that

$$0 < p_b(\tau),\ p_c(\tau) < \infty, \tag{5.11}$$

for any given finite time τ, where τ denotes the proper time obtained by choosing the lapse function to be unity, $N(\tau) = 1$. Note that in [85] the authors considered spacetimes filled with matter. However, their results for $p_b(\tau)$ and $p_c(\tau)$ equally hold in the vacuum case. The above results can be understood as follows: From the condition (2.59), we find

$$\delta_c p_b = \sqrt{\Delta p_c}. \tag{5.12}$$

Thus, for any given finite time T, the right-hand side is always finite and non-zero. Then, if $p_b = 0$ at a time, say, T_H, we must have $\delta_c(T_H) = \infty$, which in turn implies that the quantum geometric effects become numerous. As a result, in the reality p_b

will be never zero within a finite time. The above arguments are valid not only for the choice $N(\tau) = 1$ adopted in [85], but also for the current choice of the lapse function.

To study further the asymptotic behaviors of the spacetimes, let us first notice that $\log(N^2)$ and $\log(g_{xx})$ change periodically, but during each period $\log(N^2)$ increases almost linearly, while $\log(g_{xx})$ decreases almost linearly. In contrast, $\log(p_c)$ increases almost linearly all the time [See the analysis to be given below]. So, during each period we can approximate each of them as $F = F_0 T^\alpha$, where we find that

$$N^2 \simeq A_0 e^{3T}, \quad g_{xx} \simeq B_0 e^{-T}, \quad p_c = p_c^{(0)} e^{2T}, \tag{5.13}$$

where A_0, B_0 and $p_c^{(0)}$ are constants, usually depending on which period we consider, but the slopes remain almost constant. Then, we find that the effective energy-momentum tensor calculated from $\kappa^2 T_{\mu\nu} \equiv G_{\mu\nu}$ can be written in the form

$$\kappa^2 T_{\mu\nu} = \rho u_\mu u_\nu + p_x x_\mu x_\nu + p_\perp \left(\theta_\mu \theta_\nu + \phi_\mu \phi_\nu\right), \tag{5.14}$$

with

$$\rho \simeq p_x \simeq \frac{1}{p_c} + \mathcal{O}\left(e^{-3T}\right), \quad p_\perp \simeq \mathcal{O}\left(e^{-3T}\right), \tag{5.15}$$

where $(u_\mu,\ x_\mu,\ \theta_\mu,\ \phi_\mu)$ are the unit vectors along, respectively, the $(dT, dx, d\theta, d\phi)$-directions. In addition, we also have

$$R \simeq \frac{2}{p_c}, \quad K \simeq \frac{4}{p_c^2}, \quad C^{\alpha\beta\mu\nu} C_{\alpha\beta\mu\nu} \simeq \frac{4}{3p_c^2}, \tag{5.16}$$

where $C_{\alpha\beta\mu\nu}$ denotes the Weyl tensor. Thus, the spacetime becomes asymptotically flat, but with the Kretchmann scalar decreasing as p_c^{-2}, quite similar to the case studied in [9, 91], instead of p_c^{-3} as in the classical case.

5.3.3.2 Non-existence of Black/White Hole Like Horizons

To see if a black or white hole like horizon exists, let us first consider if *a marginally trapped surface* will be developed in the BV model as T (or p_c) increases. To this goal, we can calculate the expansions of the in-going and out-going radially moving light rays [9,87–89]. Introducing the unit vectors, $u_\mu \equiv N\delta^T_\mu$ and $s_\mu \equiv \sqrt{g_{xx}}\delta^x_\mu$, we construct two null vectors $\ell^{\pm}_\mu = (u_\mu \pm s_\mu)/\sqrt{2}$, which define, respectively, the in-going and out-going radially-moving light rays. Then, the expansions of these light rays are given by

$$\Theta_\pm \equiv m^{\mu\nu}\nabla_\mu \ell^{\pm}_\nu = -\frac{p_{c,T}}{\sqrt{2}Np_c}, \tag{5.17}$$

where $m_{\mu\nu} \equiv g_{\mu\nu} + u_\mu u_\nu - s_\mu s_\nu$.

Note that the existence of a marginally trapped surface can be equally characterized by the vanishing of the norm of the normal vector to the two-spheres, T, $x =$ Constant [90]. In fact, introducing the normal vector to the surface $\sqrt{p_c} = r_0$

$$N_\mu \equiv \frac{\partial(\sqrt{p_c} - r_0)}{\partial x^\mu} = \frac{p_{c,T}}{2\sqrt{p_c}}\delta^T_\mu, \tag{5.18}$$

where r_0 is a constant, we find

$$N_\lambda N^\lambda = -\frac{p^2_{c,T}}{4N^2 p_c}. \tag{5.19}$$

A marginally trapped surface will be developed when $N_\lambda N^\lambda = 0$, or equivalently $\Theta_\pm = 0$ [9, 87–90]. However, as shown above, the lapse function N always remains finite within a finite time (Recall that classically we have $N^{\mathrm{GR}}(T_H) = \infty$]. Thus, a marginally trapped surface can exist only if $p_{c,T} = 0$. From the dynamical equation (2.66), we can see that this is possible only when

$$\delta_c(T)c(T)|_{T=T_{\mathrm{tr}}} = \frac{\pi}{2}. \tag{5.20}$$

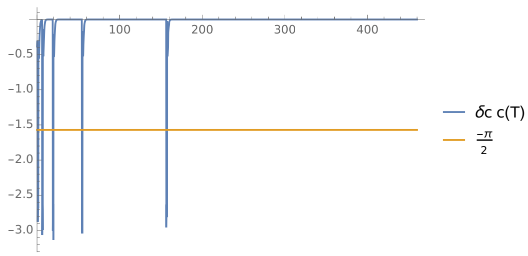

(a)

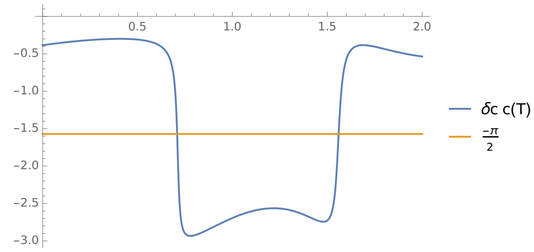

(b)

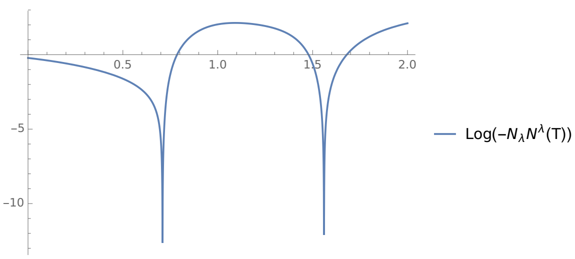

(c)

Figure 5.3: Plots of $\ln(-N_\lambda N^\lambda)$ defined by Eq.(5.19) and $\delta_c c(T)$. The mass parameter m is chosen as $m/\ell_{pl} = 1$, for which we have $T_{\mathcal{T}} \simeq -1.49$ and $T_H \approx 0.693$. The initial time is chosen at $T_i = 0.3$. (c) shows clearly that there exist two points at which N^μ becomes a null vector, $N_\lambda N^\lambda = 0$ in the interval $T \in (0, 2)$.

In Fig. 5.3 we plot out this quantity together with the norm, $N^\lambda N_\lambda$, from which we can see clearly that there indeed exist various points at which the above condition is satisfied, so that $p_c(T_{\text{tr}}) = 0$ at these points. In particular, in Figs. 5.3 (b) and (c) we zoom in to the interval $T \in (0, 2)$, which show clearly that two such points exist in this interval, at which $\log\left(-N^\lambda N_\lambda\right)$ becomes infinitely large, as N^λ becomes null.

On the other hand, in Fig. 5.4 we plot several physical quantities for $T \in (0, 2)$ including H^{eff}, which shows $\left|H^{\text{eff}}\right| \leq 2.0 \times 10^{-15}$. Therefore, our numerical results are quite reliable in this interval. From this figure, we can see clearly that across these marginally trapped surfaces the metric coefficients all remain finite and non-zero. As a result, these surfaces represent neither black nor white hole horizons, but transition surfaces that separate trapped regions from anti-trapped ones. In fact, across each of these points, $p_{c,T}$ changes its signs. Then, from Eq.(5.17) we can see that both Θ_+

and Θ_- change their signs simultaneously. Therefore, these surfaces always separate trapped regions from anti-trapped ones, while a black (white) hole horizon always separates a trapped region from an untrapped one [87–90]. Therefore, we conclude that *in the BV model, no black/white hole structure exists.*

It should be noted that simply looking at Figs. 5.1 and 5.2, one cannot tell the existence of these transition surfaces. This is because in these figures the quantities are plotted out in such a large range, $T \in (0, 600)$, in which the detailed changes of p_c were washed out, due to the fact that it has quite different values at different times. In particular, the moment $T = 600$ corresponds to $\sqrt{p_c}\big|_{T=600} \simeq 10^{265}$ m, which is much larger than the size of our current observational universe, $L_{\text{ob.}} \simeq 8.8 \times 10^{26}$ m.

5.3.3.3 Asymptotic Behavior of the Spacetimes as $T \ll T_{\mathcal{T}}$

To see the connection of our current studies to the ones carried out in [15,72,73,84,86], let us briefly consider the asymptotic behaviors of the spacetimes for $T \ll T_{\mathcal{T}}$, that is, the asymptotic behaviors of the spacetimes in the pre-transition surface. This can be shown by simply considering the case $m = \ell_{pl}$. With the same initial time and conditions as those chosen for Fig. 5.1, we plot the four variables $(p_b, b; c, p_c)$ in Fig. 5.5, from which we can see that they behave very much like the ones obtained in [2, 15, 72, 73, 84, 86]. In particular, as T decreases, p_c approaches to a constant $\bar{p}_c$, which is smaller than the Planck area. Such a spacetime with a constant radius of the two-spheres was first discussed by Nariai [92,93], and latter generalized to the charged case by Bousso [46]. As shown in detail in [2], in the current case the corresponding

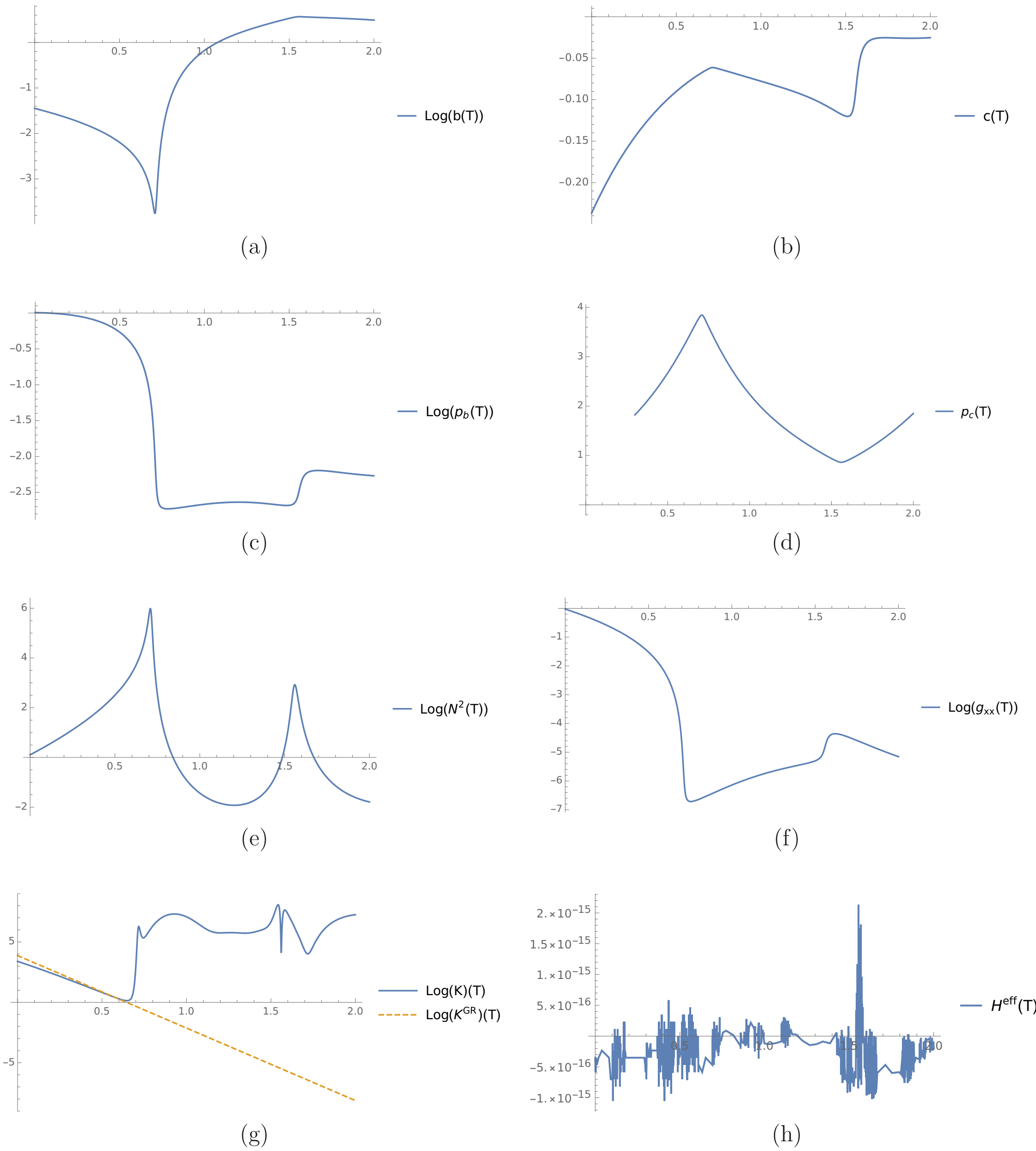

Figure 5.4: Plots of the four physical variables (b, c, p_b, p_c), together with the metric components N^2, g_{xx} the Kretchmann scalar K, as well as the classical counterpart $K^{\rm GR}(T) \equiv 48m^2/p_c^3$ of $K(T)$ and $H^{\rm eff}$ in the region $T \in (0, 2)$. The mass parameter m is chosen as $m/\ell_{pl} = 1$, for which we have $T_{\mathcal{T}} \simeq -1.49$ and $T_H \approx 0.693$. The same initial time and conditions are chosen as those of Fig. 5.1.

solutions are the charged Nariai solutions

$$
\begin{aligned}
ds^2 &\simeq \left(\frac{\bar{t}_0}{\bar{t}}\right)^2 \left(-d\bar{t}^2 + d\bar{x}^2\right) + \bar{p}_c d^2\Omega \\
&= -d\hat{t}^2 + e^{2\hat{t}/\bar{t}_0} d\hat{x}^2 + \bar{p}_c d^2\Omega,
\end{aligned} \tag{5.21}
$$

where $d\bar{t} = e^{\bar{\alpha}T}dT$, $\bar{x} = \bar{\beta}x$, and $\bar{\alpha}, \bar{\beta}$ and $\bar{t}_0$ are all positive constants [2], and $\hat{t} \equiv -\bar{t}_0 \log \bar{t}$, $\hat{x} \equiv \bar{t}_o \bar{x}$. From the above asymptotic behavior of the metric, we can see that it has a topology of $dS_2 \times S^2_{(0)}$, where $S^2_{(0)}$ denotes a two-spheres with a finite radius. As shown explicitly in [87], the coordinates $(\hat{t}, \hat{x})$ cover only part of the whole spacetime. After the extension, the corresponding Penrose diagram is that given explicitly in [94].

On the other hand, the Kantowski-Sachs spacetime (2.10) is usually singular in the classical theory, when filled with matter that satisfies certain energy conditions [87]. Then, the corresponding Penrose diagram is given by Fig. 5.6 (a), in which each point represents a two-sphere with the radius $p_c(T)$ that is a function of T, as shown in Figs. 5.1 and 5.2. Note that the horizontal line AB in Fig. 5.6 (a) represents the spaceitme singularity. In the vacuum case, classically it corresponds to $p_c^{\mathrm{GR}}(T = -\infty) = 0$. However, after quantum geometric effects are taken into account, this singularity is replaced by the transition surface $\mathcal{T}$ denoted by the curve APB, and the Penrose diagram for the whole spacetime now is given by Fig. 5.6 (b). In the past of $\mathcal{T}$, where $T > T_{\mathcal{T}}$, there actually exist infinite number of such transition surfaces, each of which separates a trapped region from an anti-trapped one. At each transition surface the geometric radius $\sqrt{p_c}(T)$ is different. As T increases, $\sqrt{p_c}(T)$ is getting larger and larger as shown in Figs. 5.1 and 5.2. However, in the future of $\mathcal{T}$, that is, when $T < T_{\mathcal{T}}$, the geometric radius $\sqrt{p_c}(T)$ first gets larger and then gets smaller and smaller, and asymptotically approaches a non-zero constant $\bar{p}_c$, as shown in Fig. 5.4 (b).

It must be emphasized that each point in the diagram of Fig. 5.6 (b) represents two-spheres with different radii. In particular, for $T \ll T_{\mathcal{T}}$, all the two-spheres have the same radius $\bar{p}_c$, while for $T > T_{\mathcal{T}}$, the radius $p_c(T)$ is time-dependent.

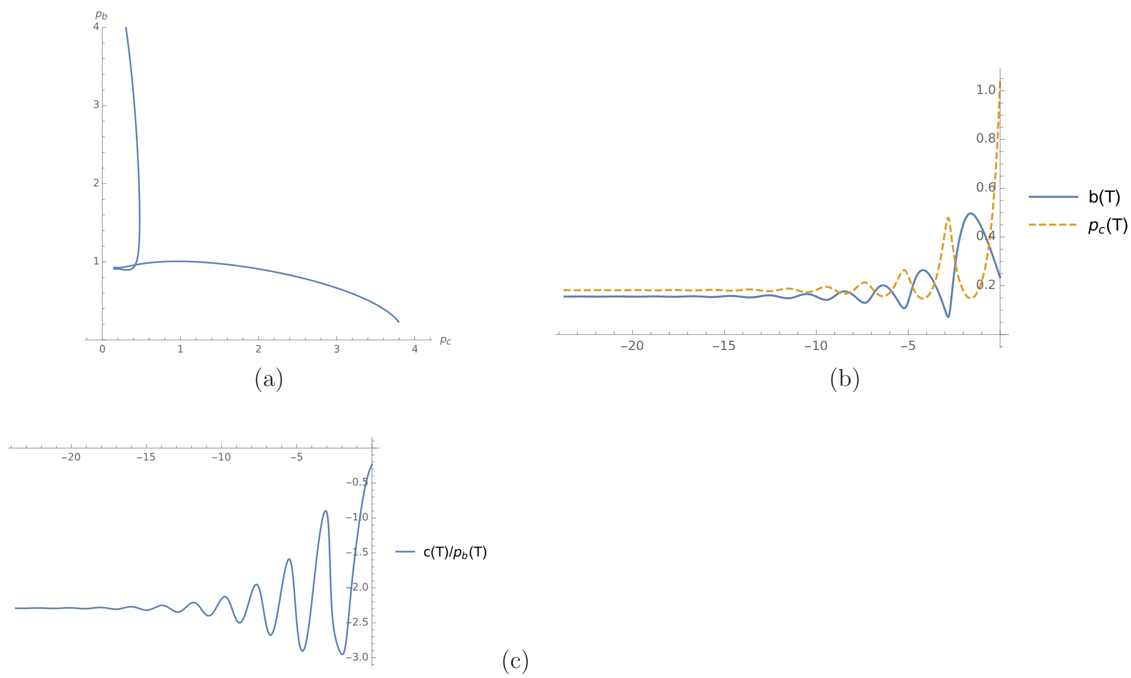

Figure 5.5: Plots of the four physical variables (b, c, p_b, p_c) for $T < T_{\mathcal{T}}$ and $m/\ell_{pl} = 1$, for which we have $T_{\mathcal{T}} \simeq -1.49$ and $T_H \approx 0.693$. The same initial time and conditions are chosen as those of Fig. 5.1.

5.4 Conclusions

In this chapter, we have studied the quantum effects near the location $T = T_H = \ln(2m)$ at which the classical black hole horizon used to appear within the framework of the improved dynamics approach, first considered by Böhmer and Vandersloot [15], in which the two polymerization parameters δ_b and δ_c are given by

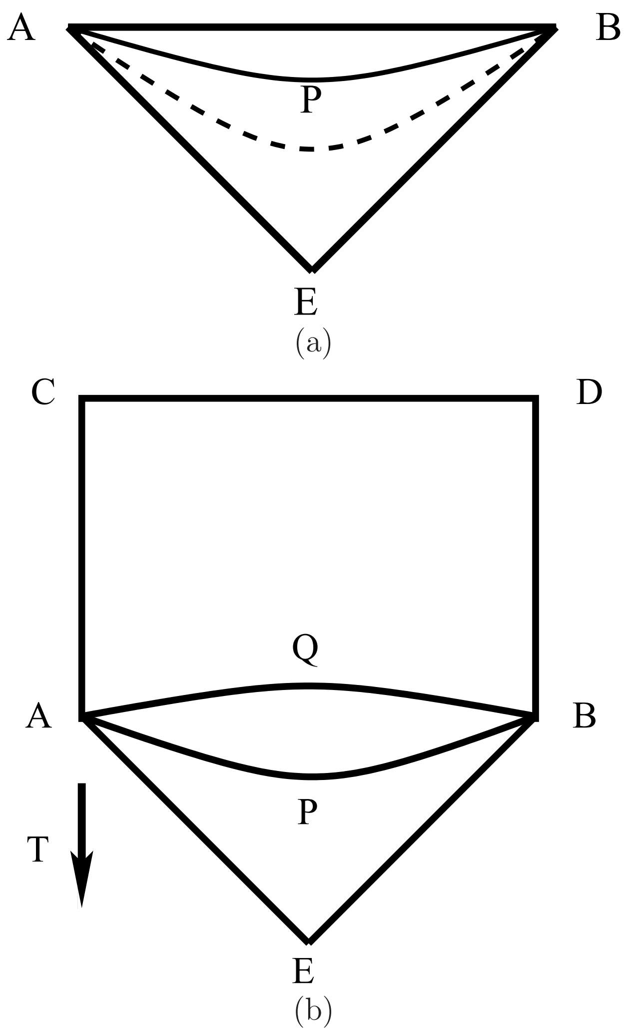

Figure 5.6: (a) The Penrose diagram for the Kantowski-Sachs spacetime in classical Einstein's gravity. The horizontal line AB represents the spacetime singularity. In the Schwarzschild case, it corresponds to $p_c^{\mathrm{GR}}(T = -\infty) = 0$. The curve APB corresponds to a $T =$ Constant surface with a non-zero radius. (b) The Penrose diagram for the BV model. Due to the quantum geometric effects, the classical singularity used to appear at $T = -\infty$ now is replaced by the transition surface $\mathcal{T}$ denoted by the curve APB, at which we have $p_c(T_{\mathcal{T}}) > 0$. The quantum geometric effects are large in the region between the two curves AQB and APB. The 2D plane with $\theta,\ \phi =$ Constant is asymptotically approaching to a 2D de Sitter spacetime with a fixed radius $\sqrt{\bar{p}_c}$ as $T \to -\infty$. In the region $T > T_{\mathcal{T}}$ the spaceitme is geodesically complete, and a black (or white) hole like horizon is never developed.

Eq.(2.61), where m is the classical black hole mass. To study such effects, we have chosen the initial conditions as closed to the corresponding classical ones as possible. We have found that this is always possible at a moment T_i, where T_i satisfies the condition $T_{\mathcal{T}} \ll T_i \ll T_H$ [cf. Eqs.(5.6) - (5.8) and Table 5.1], where $T = T_{\mathcal{T}}$ is the location of the (first) transition surface.

To our surprising, we have found that a black hole (or white hole) horizon is never developed within a finite time T to the past of the (first) transition surface $T > T_{\mathcal{T}}$. Instead, only subsequent transition surfaces exist, which always separate trapped regions from anti-trapped ones. The metric coefficients (N^2, g_{xx}, p_c) and their inverses (N^{-2}, g^{xx}, p_c^{-1}) are always finite and non-singular at any given finite time T. As a matter of fact, the quantum geometric effects near the classically black hole horizon $T = \ln(2m)$ (at which we have $p_b^{\mathrm{GR}}(T_H) = 0$) are so strong so that $\delta_c(T)|_{T \to T_H} \gg 1$, as can be seen from Eq.(5.12). Then, in reality p_b never becomes zero within a finite time [85].

These properties are sharply in contrast to those obtained in other models of LQBHs studied so far in LQG [9, 26, 67–69], and put the BV model as a physically viable one of LQBHs questionable.

CHAPTER SIX

Conclusion

In chapter one, we briefly reviewed basic concepts in LQG. LQG is based on canonical quantization of the Hamiltonian formalism of general relativity. In Hamiltonian formalism, spacetime is decomposed into $1D$ time + $3D$ space. The spatial metric and extrinsic curvature are then introduced as basic variables. The spatial metric can be equivalently described by orthonormal triads $e_i^a(x)$. Ashtekar introduced Ashtekar's variable which has simple Poisson brackets with densitized triads $E_i^a = \sqrt{q}e_i^a$. The Ashtekar connection is smeared as the holonomy which is defined as the path-ordered exponential of integral of the Ashtekar connection. The fluxes of densitized triads are defined by their surface integral. LQG is the canonical quantization of holonomy and flux of densitized triads. Hilbert spaces are composed of wave functions which are functions of all holonomies on the graph.

In chapter two, we briefly reviewed some basic concepts on LQBH. The interior of the Schwarzschild black hole is isometric to the KS cosmological model with symmetry group $\mathbb{R} \times SO(3)$. Thus loop quantization techniques of LQC can be used in loop quantization of black holes. The key point is that holonomies have exponential terms like $\exp(i\delta_b b)$, where δ_b corresponds to the edge length of holonomy. The leading order loop quantum effects are to replace classical b by $\sin(\delta_b b)/\delta_b$. This procedure is called polymerization. EoMs can then be derived from the effective Hamiltonian. The solution describes the LQBH with leading order quantum corrections. Different choices of δ_b and δ_c will lead to different quantization schemes and have different solutions. In this dissertation, we mainly focus on effective LQBH solutions with different quantization schemes.

In chapter three, we have studied in detail the main properties of spherically symmetric black/white hole solutions, found recently by Bodendorfer, Mele, and Münch [17]. This originates from polymerization of new phase space variables which are canonical transformation of (b, c).

The BMM model has three physically independent free parameters $(\mathcal{C},\ \mathcal{D},\ x_0)$. $\mathcal{D}$ is related to its ADM mass, while $\mathcal{C},\ x_0$ are related to its quantum effects. We investigate its local and global properties by calculating its effective energy-momentum tensor, which can be used to calculate the energy condition. We find that when $\mathcal{C} = 0,\ x_0 = 0$, the solution reduces to a classical Schwarzschild black hole with mass $M_{BH} = \mathcal{D}$. Different choices of parameters $(\mathcal{C},\ \mathcal{D},\ x_0)$ will lead to different properties of the solution, which have been summarized in Tables 3.1 - 3.3.

In chapter four, we systematically study the ABP model which originates from QRLG. QRLG is a top-down model of loop quantum gravity and the effective Hamiltonian is derived with respect to coherent states peaked around spherically symmetric geometry, by including both the holonomy and inverse volume corrections. This is in contrast with BV model and AOS model which are based on polymerization in mini-superspace. We find that the classical Schwarzschild black hole solution, BV model and AOS model can be obtained by taking proper limit of ABP model. Moreover, different choices of parameter $\eta = \alpha/\beta$ will lead to different asymptotic behavior of ABP model. Specifically, when $\eta \gtrsim 1$, and $a = d$, the spacetime is conformally flat and asymptotically de Sitter. In this case $\gamma = \frac{\sqrt{2\pi}}{8\eta} \simeq 0.274$, which is precisely the value obtained from the consideration of loop quantum black hole entropy obtained in [43].

In chapter five, we come back to investigate the properties of the BV model in detail. The BV model is an important model as it utilizes the $\bar{\mu}$-scheme, which is the unique quantization scheme that has proper semiclassical behavior in LQC. However, it has large quantum effects near the location $T = T_H = \ln(2m)$ at which the classical black hole horizon used to appear. We find that the quantum effects are so large that a BH/WH horizon never exits. These properties are sharply in contrast to those obtained in other models of LQBHs studied so far in LQG [9, 26, 67–69], and make the BV model as a physically viable solution of LQBHs questionable.

In the future, we will work on a) quantization of the exterior of the Schwarzschild black hole in the $\bar{\mu}$-scheme, b) a new scheme that has no large quantum effects near the horizon, and c) the covariant $\bar{\mu}$-scheme [78].

APPENDICES

APPENDIX A

THE GENERAL EXPRESSIONS OF THE ENERGY DENSITY AND PRESSURES

Inserting the solutions given by Eq.(3.11) into Eq.(3.18), we find that

$$\begin{aligned}
\rho(x) \;=\; & \frac{Y^3}{X^2 Z^8}\Bigg[\Big(10\mathcal{D}x_0^{10}x + 160\mathcal{D}x_0^8x^3 - 20x_0^6\mathcal{C}^6 + 672\mathcal{D}x_0^6x^5 + 1024\mathcal{D}x_0^4x^7 \\
& -260x_0^4\mathcal{C}^6x^2 + 110\mathcal{D}x_0^4\mathcal{C}^6x + 512\mathcal{D}x_0^2x^9 - 560x_0^2\mathcal{C}^6x^4 + 440\mathcal{D}x_0^2\mathcal{C}^6x^3 \\
& -320\mathcal{C}^6x^6 + 352\mathcal{D}\mathcal{C}^6x^5\Big)X + \mathcal{D}\mathcal{C}^{12} + \mathcal{D}x_0^{12} + 50\mathcal{D}x_0^{10}x^2 + 400\mathcal{D}x_0^8x^4 \\
& +22\mathcal{D}x_0^6\mathcal{C}^6 + 1120\mathcal{D}x_0^6x^6 - 100x_0^6\mathcal{C}^6x + 1280\mathcal{D}x_0^4x^8 - 500x_0^4\mathcal{C}^6x^3 \\
& +286\mathcal{D}x_0^4\mathcal{C}^6x^2 + 512\mathcal{D}x_0^2x^{10} - 720x_0^2\mathcal{C}^6x^5 + 616\mathcal{D}x_0^2\mathcal{C}^6x^4 - 320\mathcal{C}^6x^7 \\
& +352\mathcal{D}\mathcal{C}^6x^6\Bigg],
\end{aligned} \tag{A.1}$$

$$\begin{aligned}
p_r(x) \;=\; & -\frac{Y^3}{X^2 Z^8}\Bigg[\Big(2x_0^{12} + 100x_0^{10}x^2 - 10\mathcal{D}x_0^{10}x + 800x_0^8x^4 - 160\mathcal{D}x_0^8x^3 \\
& +2240x_0^6x^6 - 672\mathcal{D}x_0^6x^5 + 2560x_0^4x^8 - 1024\mathcal{D}x_0^4x^7 + 10\mathcal{D}x_0^4\mathcal{C}^6x \\
& +1024x_0^2x^{10} - 512\mathcal{D}x_0^2x^9 + 40\mathcal{D}x_0^2\mathcal{C}^6x^3 + 2\mathcal{C}^{12} + 32\mathcal{D}\mathcal{C}^6x^5\Big)X \\
& -\mathcal{D}\mathcal{C}^{12} - \mathcal{D}x_0^{12} + 20x_0^{12}x + 340x_0^{10}x^3 - 50\mathcal{D}x_0^{10}x^2 + 1664x_0^8x^5 \\
& -400\mathcal{D}x_0^8x^4 + 2\mathcal{D}x_0^6\mathcal{C}^6 + 3392x_0^6x^7 - 1120\mathcal{D}x_0^6x^6 + 3072x_0^4x^9 \\
& -1280\mathcal{D}x_0^4x^8 + 26\mathcal{D}x_0^4\mathcal{C}^6x^2 + 1024x_0^2x^{11} - 512\mathcal{D}x_0^2x^{10} \\
& +56\mathcal{D}x_0^2\mathcal{C}^6x^4 + 32\mathcal{D}\mathcal{C}^6x^6\Bigg],
\end{aligned} \tag{A.2}$$

and

$$
\begin{aligned}
p_\theta(x) \;=\; & \frac{Y^2}{2X^3Z^8}\Bigg[\Big(4x_0^{14}+244x_0^{12}x^2-34\mathcal{D}x_0^{12}x+2480x_0^{10}x^4-720\mathcal{D}x_0^{10}x^3 \\
& +9408x_0^8x^6-4256\mathcal{D}x_0^8x^5+16384x_0^6x^8-10240\mathcal{D}x_0^6x^7+12\mathcal{D}x_0^6\mathcal{C}^6x \\
& +13312x_0^4x^{10}-10752\mathcal{D}x_0^4x^9+88\mathcal{D}x_0^4\mathcal{C}^6x^3+4x_0^2\mathcal{C}^{12}+4096x_0^2x^{12} \\
& -4096\mathcal{D}x_0^2x^{11}+192\mathcal{D}x_0^2\mathcal{C}^6x^5+128\mathcal{D}\mathcal{C}^6x^7+4\mathcal{C}^{12}x^2-2\mathcal{D}\mathcal{C}^{12}x\Big)X \\
& -3\mathcal{D}x_0^{14}+44x_0^{14}x+924x_0^{12}x^3-194\mathcal{D}x_0^{12}x^2+5808x_0^{10}x^5-2080\mathcal{D}x_0^{10}x^4 \\
& +2\mathcal{D}x_0^8\mathcal{C}^6+16192x_0^8x^7-8288\mathcal{D}x_0^8x^6+22528x_0^6x^9-15104\mathcal{D}x_0^6x^8 \\
& +40\mathcal{D}x_0^6\mathcal{C}^6x^2+15360x_0^4x^{11}-12800\mathcal{D}x_0^4x^{10}+168\mathcal{D}x_0^4\mathcal{C}^6x^4-3\mathcal{D}x_0^2\mathcal{C}^{12} \\
& +4096x_0^2x^{13}-4096\mathcal{D}x_0^2x^{12}+256\mathcal{D}x_0^2\mathcal{C}^6x^6+4x_0^2\mathcal{C}^{12}x+128\mathcal{D}\mathcal{C}^6x^8 \\
& +4\mathcal{C}^{12}x^3-2\mathcal{D}\mathcal{C}^{12}x^2\Bigg]. \qquad \text{(A.3)}
\end{aligned}
$$

APPENDIX B

SOME PROPERTIES OF THE STRUVE FUNCTIONS

In general, the ν-th order Struve function $h_\nu[X]$ is defined as [45],

$$h_\nu[z] \equiv \left(\frac{1}{2}z\right)^{\nu+1} \sum_{k=0}^{\infty} \frac{(-1)^k \left(\frac{1}{2}z\right)^{2k}}{\Gamma\left(k+\frac{3}{2}\right)\Gamma\left(k+\nu\frac{3}{2}\right)}, \tag{B.1}$$

which satisfies the differential equation,

$$z^2\frac{d^2w}{dz^2} + z\frac{dw}{dz} + \left(z^2-\nu^2\right)w = \frac{4\left(\frac{1}{2}z\right)^{\nu+1}}{\sqrt{\pi}\,\Gamma\left(\nu+\frac{1}{2}\right)}. \tag{B.2}$$

The general solution of the above equation is

$$w = aJ_\nu(z) + bY_\nu(z) + h_\nu(z), \tag{B.3}$$

where a and b are two integration constants, $J_\nu(z)$ and $Y_\nu(z)$ are the Bessel functions of the first and second kind, respectively, and satisfy the associated homogeneous differential equation.

Some useful properties of $h_\nu(z)$ are,

$$\begin{aligned} \frac{d\left(z^\nu h_\nu\right)}{dz} &= z^\nu h_{\nu-1}, \\ \frac{d\left(z^{-\nu} h_\nu\right)}{dz} &= \frac{1}{\sqrt{\pi}\,2^\nu\,\Gamma\left(\nu+\frac{3}{2}\right)} - z^{-\nu}h_{\nu+1}, \end{aligned} \tag{B.4}$$

while their asymptotic behaviors are given by

$$h_0[X] \simeq \begin{cases} \frac{2}{\pi X} + \frac{1}{\sqrt{\pi X}}\left(\sin X - \cos X\right) + \mathcal{O}\left(X^{-3/2}\right), & X \to \infty, \\ \frac{2X}{\pi} - \frac{2X^3}{9\pi} + \mathcal{O}\left(X^4\right), & X \to 0, \end{cases} \tag{B.5}$$

and

$$h_{-1}[X] \simeq \begin{cases} \frac{2}{\pi X} + \frac{1}{\sqrt{\pi X}}\left(\sin X + \cos X\right) + \mathcal{O}\left(X^{-3/2}\right), & X \to \infty, \\ \frac{2}{\pi} - \frac{2X^2}{3\pi} + \mathcal{O}\left(X^4\right), & X \to 0. \end{cases} \tag{B.6}$$

In Fig. 4.1, we plot out the Struve function h_0 together with h_{-1}. For other properties of the Struve functions, we refer readers to [45].

[1] W.-C. Gan, N. O. Santos, F.-W. Shu, and A. Wang, Properties of the spherically symmetric polymer black holes, Phys. Rev. D **102**, 124030 (2020).

[2] W.-C. Gan et al., Understanding quantum black holes from quantum reduced loop gravity, Phys. Rev. D **106**, 126013 (2022).

[3] W.-C. Gan et al., Non-existence of quantum black hole horizons in the improved dynamics approach, (2022).

[4] T. Thiemann, *Modern Canonical Quantum General Relativity*, Cambridge Monographs on Mathematical Physics, Cambridge University Press, 2007.

[5] A. Ashtekar and J. Lewandowski, Background independent quantum gravity: A Status report, Class. Quant. Grav. **21**, R53 (2004).

[6] I. Mäkinen, *Dynamics in canonical models of loop quantum gravity*, PhD thesis, Warsaw U., 2019.

[7] S. M. Carroll, *Spacetime and Geometry*, Cambridge University Press, 2019.

[8] A. Corichi and P. Singh, Loop quantization of the Schwarzschild interior revisited, Class. Quant. Grav. **33**, 055006 (2016).

[9] A. Ashtekar, J. Olmedo, and P. Singh, Quantum extension of the Kruskal spacetime, Phys. Rev. D **98**, 126003 (2018).

[10] A. Ashtekar and M. Bojowald, Quantum geometry and the Schwarzschild singularity, Class. Quant. Grav. **23**, 391 (2006).

[11] K. A. Meissner, Black hole entropy in loop quantum gravity, Class. Quant. Grav. **21**, 5245 (2004).

[12] L. Modesto, Black hole interior from loop quantum gravity, Adv. High Energy Phys. **2008**, 459290 (2008).

[13] L. Modesto, Loop quantum black hole, Class. Quant. Grav. **23**, 5587 (2006).

[14] A. Ashtekar, T. Pawlowski, and P. Singh, Quantum Nature of the Big Bang: Improved dynamics, Phys. Rev. D **74**, 084003 (2006).

[15] C. G. Boehmer and K. Vandersloot, Loop Quantum Dynamics of the Schwarzschild Interior, Phys. Rev. D **76**, 104030 (2007).

[16] H. Goldstein, C. Poole, and J. Safko, *Classical Mechanics*, Third Edition, Addison Wesley, New York, 2002.

[17] N. Bodendorfer, F. M. Mele, and J. Münch, Effective Quantum Extended Spacetime of Polymer Schwarzschild Black Hole, Class. Quant. Grav. **36**, 195015 (2019).

[18] N. Bodendorfer, F. M. Mele, and J. Münch, Mass and Horizon Dirac Observables in Effective Models of Quantum Black-to-White Hole Transition, Class. Quant. Grav. **38**, 095002 (2021).

[19] A. Ashtekar, T. Pawlowski, P. Singh, and K. Vandersloot, Loop quantum cosmology of k=1 FRW models, Phys. Rev. D **75**, 024035 (2007).

[20] S. Hawking and G. Ellis, *The Large Scale Structure of Spacetime*, Cambridge University Press, Cambridge, 1973.

[21] A. Komar, Covariant conservation laws in general relativity, Phys. Rev. **113**, 934 (1959).

[22] G. D. Birkhoff, *Relativity and Modern Physics*, Cambridge, Massachusetts, Harvard University Press, 1923.

[23] A. Ashtekar, J. Olmedo, and P. Singh, Quantum Transfiguration of Kruskal Black Holes, Phys. Rev. Lett. **121**, 241301 (2018).

[24] M. Bouhmadi-López, S. Brahma, C.-Y. Chen, P. Chen, and D.-h. Yeom, A consistent model of non-singular Schwarzschild black hole in loop quantum gravity and its quasinormal modes, JCAP **07**, 066 (2020).

[25] A. Ashtekar and J. Olmedo, Properties of a recent quantum extension of the Kruskal geometry, Int. J. Mod. Phys. D **29**, 2050076 (2020).

[26] A. Ashtekar, Black Hole evaporation: A Perspective from Loop Quantum Gravity, Universe **6**, 21 (2020).

[27] M. Bojowald, R. Goswami, R. Maartens, and P. Singh, A Black hole mass threshold from non-singular quantum gravitational collapse, Phys. Rev. Lett. **95**, 091302 (2005).

[28] L. Modesto, Gravitational collapse in loop quantum gravity, Int. J. Theor. Phys. **47**, 357 (2008).

[29] Y. Zhang, Y. Zhu, L. Modesto, and C. Bambi, Can static regular black holes form from gravitational collapse?, Eur. Phys. J. C **75**, 96 (2015).

[30] Y. Liu, D. Malafarina, L. Modesto, and C. Bambi, Singularity avoidance in quantum-inspired inhomogeneous dust collapse, Phys. Rev. D **90**, 044040 (2014).

[31] J. Ben Achour, S. Brahma, and J.-P. Uzan, Bouncing compact objects. Part I. Quantum extension of the Oppenheimer-Snyder collapse, JCAP **03**, 041 (2020).

[32] J. Ben Achour and J.-P. Uzan, Bouncing compact objects. II. Effective theory of a pulsating Planck star, Phys. Rev. D **102**, 124041 (2020).

[33] J. G. Kelly, R. Santacruz, and E. Wilson-Ewing, Black hole collapse and bounce in effective loop quantum gravity, Class. Quant. Grav. **38**, 04LT01 (2021).

[34] J. Ben Achour, S. Brahma, S. Mukohyama, and J. P. Uzan, Towards consistent black-to-white hole bounces from matter collapse, JCAP **09**, 020 (2020).

[35] B.-F. Li and P. Singh, Loop quantum cosmology and its gauge-covariant avatar: A weak curvature relationship, Phys. Rev. D **106**, 026009 (2022).

[36] E. Alesci and F. Cianfrani, Quantum-Reduced Loop Gravity: Cosmology, Phys. Rev. D **87**, 083521 (2013).

[37] E. Alesci and F. Cianfrani, Quantum Reduced Loop Gravity and the foundation of Loop Quantum Cosmology, Int. J. Mod. Phys. D **25**, 1642005 (2016).

[38] A. Ashtekar, T. Pawlowski, and P. Singh, Quantum nature of the big bang, Phys. Rev. Lett. **96**, 141301 (2006).

[39] E. Alesci, G. Botta, F. Cianfrani, and S. Liberati, Cosmological singularity resolution from quantum gravity: the emergent-bouncing universe, Phys. Rev. D **96**, 046008 (2017).

[40] E. Alesci, S. Bahrami, and D. Pranzetti, Quantum evolution of black hole initial data sets: Foundations, Phys. Rev. D **98**, 046014 (2018).

[41] E. Alesci, S. Bahrami, and D. Pranzetti, Quantum gravity predictions for black hole interior geometry, Phys. Lett. B **797**, 134908 (2019).

[42] E. Alesci, S. Bahrami, and D. Pranzetti, Asymptotically de Sitter universe inside a Schwarzschild black hole, Phys. Rev. D **102**, 066010 (2020).

[43] I. Agullo, J. Fernando Barbero, E. F. Borja, J. Diaz-Polo, and E. J. S. Villasenor, Detailed black hole state counting in loop quantum gravity, Phys. Rev. D **82**, 084029 (2010).

[44] J. Engle, K. Noui, A. Perez, and D. Pranzetti, Black hole entropy from an SU(2)-invariant formulation of Type I isolated horizons, Phys. Rev. D **82**, 044050 (2010).

[45] M. Abramowitz and I. Stegun, *Handbook of Mathematical Functions with Formulas, Graphs, and Mathematical Tables*, Dover Publications, Inc., New York, 1972.

[46] R. Bousso, Charged Nariai black holes with a dilaton, Phys. Rev. D **55**, 3614 (1997).

[47] H. Nariai, On a New Cosmological Solution of Einstein's Field Equations of Gravitation, Gen. Relativ. Gravit. **31**, 963 (1999).

[48] R. Bousso, Adventures in de Sitter space, in *Workshop on Conference on the Future of Theoretical Physics and Cosmology in Honor of Steven Hawking's 60th Birthday*, pages 539–569, 2002.

[49] A. Corichi and P. Singh, Is loop quantization in cosmology unique?, Phys. Rev. D **78**, 024034 (2008).

[50] B.-F. Li, P. Singh, and A. Wang, Phenomenological implications of modified loop cosmologies: an overview, Front. Astron. Space Sci. **8**, 701417 (2021).

[51] A. Dapor and K. Liegener, Cosmological Effective Hamiltonian from full Loop Quantum Gravity Dynamics, Phys. Lett. B **785**, 506 (2018).

[52] A. Dapor and K. Liegener, Cosmological coherent state expectation values in loop quantum gravity I. Isotropic kinematics, Class. Quant. Grav. **35**, 135011 (2018).

[53] M. Assanioussi, A. Dapor, K. Liegener, and T. Pawłowski, Emergent de Sitter Epoch of the Quantum Cosmos from Loop Quantum Cosmology, Phys. Rev. Lett. **121**, 081303 (2018).

[54] T. Thiemann, Gauge field theory coherent states (GCS): 1. General properties, Class. Quant. Grav. **18**, 2025 (2001).

[55] T. Thiemann and O. Winkler, Gauge field theory coherent states (GCS). 2. Peakedness properties, Class. Quant. Grav. **18**, 2561 (2001).

[56] T. Thiemann, Complexifier coherent states for quantum general relativity, Class. Quant. Grav. **23**, 2063 (2006).

[57] B.-F. Li, P. Singh, and A. Wang, Towards Cosmological Dynamics from Loop Quantum Gravity, Phys. Rev. D **97**, 084029 (2018).

[58] B.-F. Li, P. Singh, and A. Wang, Qualitative dynamics and inflationary attractors in loop cosmology, Phys. Rev. D **98**, 066016 (2018).

[59] B.-F. Li, P. Singh, and A. Wang, Genericness of pre-inflationary dynamics and probability of the desired slow-roll inflation in modified loop quantum cosmologies, Phys. Rev. D **100**, 063513 (2019).

[60] R. Brandenberger, L. Heisenberg, and J. Robnik, Through a black hole into a new universe, Int. J. Mod. Phys. D **30**, 2142001 (2021).

[61] N. Bodendorfer, F. M. Mele, and J. Münch, (b,v)-type variables for black to white hole transitions in effective loop quantum gravity, Phys. Lett. B **819**, 136390 (2021).

[62] R. Gambini, J. Olmedo, and J. Pullin, Loop Quantum Black Hole Extensions Within the Improved Dynamics, Front. Astron. Space Sci. **8**, 74 (2021).

[63] A. Ashtekar, B. Bonga, and A. Kesavan, Asymptotics with a positive cosmological constant: I. Basic framework, Class. Quant. Grav. **32**, 025004 (2015).

[64] A. Ashtekar and P. Singh, Loop Quantum Cosmology: A Status Report, Class. Quant. Grav. **28**, 213001 (2011).

[65] A. Ashtekar, M. Bojowald, and J. Lewandowski, Mathematical structure of loop quantum cosmology, Adv. Theor. Math. Phys. **7**, 233 (2003).

[66] A. Corichi and P. Singh, A Geometric perspective on singularity resolution and uniqueness in loop quantum cosmology, Phys. Rev. D **80**, 044024 (2009).

[67] J. Olmedo, Brief review on black hole loop quantization, Universe **2**, 12 (2016).

[68] R. Gambini, J. Olmedo, and J. Pullin, Quantum geometry and black holes, (2022).

[69] A. Ashtekar, J. Olmedo, and P. Singh, Regular black holes from Loop Quantum Gravity, (2023).

[70] L. Modesto, The Kantowski-Sachs space-time in loop quantum gravity, Int. J. Theor. Phys. **45**, 2235 (2006).

[71] J. Olmedo, S. Saini, and P. Singh, From black holes to white holes: a quantum gravitational, symmetric bounce, Class. Quant. Grav. **34**, 225011 (2017).

[72] D.-W. Chiou, Phenomenological dynamics of loop quantum cosmology in Kantowski-Sachs spacetime, Phys. Rev. D **78**, 044019 (2008).

[73] D.-W. Chiou, Phenomenological loop quantum geometry of the Schwarzschild black hole, Phys. Rev. D **78**, 064040 (2008).

[74] R. Gambini and J. Pullin, Loop quantization of the Schwarzschild black hole, Phys. Rev. Lett. **110**, 211301 (2013).

[75] R. Gambini, J. Olmedo, and J. Pullin, Quantum black holes in Loop Quantum Gravity, Class. Quant. Grav. **31**, 095009 (2014).

[76] R. Gambini, J. Olmedo, and J. Pullin, Spherically symmetric loop quantum gravity: analysis of improved dynamics, Class. Quant. Grav. **37**, 205012 (2020).

[77] Y.-C. Liu, J.-X. Feng, F.-W. Shu, and A. Wang, Extended geometry of Gambini-Olmedo-Pullin polymer black hole and its quasinormal spectrum, Phys. Rev. D **104**, 106001 (2021).

[78] M. Han and H. Liu, Covariant $\bar{\mu}$-scheme effective dynamics, mimetic gravity, and non-singular black holes: Applications to spherical symmetric quantum gravity and CGHS model, (2022).

[79] M. Bojowald, Spherically symmetric quantum geometry: States and basic operators, Class. Quant. Grav. **21**, 3733 (2004).

[80] M. Bojowald and R. Swiderski, The Volume operator in spherically symmetric quantum geometry, Class. Quant. Grav. **21**, 4881 (2004).

[81] M. Bojowald and R. Swiderski, Spherically symmetric quantum geometry: Hamiltonian constraint, Class. Quant. Grav. **23**, 2129 (2006).

[82] M. Campiglia, R. Gambini, and J. Pullin, Loop quantization of spherically symmetric midi-superspaces, Class. Quant. Grav. **24**, 3649 (2007).

[83] D.-W. Chiou, W.-T. Ni, and A. Tang, Loop quantization of spherically symmetric midisuperspaces and loop quantum geometry of the maximally extended Schwarzschild spacetime, (2012).

[84] A. Joe and P. Singh, Kantowski-Sachs spacetime in loop quantum cosmology: bounds on expansion and shear scalars and the viability of quantization prescriptions, Class. Quant. Grav. **32**, 015009 (2015).

[85] S. Saini and P. Singh, Geodesic completeness and the lack of strong singularities in effective loop quantum Kantowski–Sachs spacetime, Class. Quant. Grav. **33**, 245019 (2016).

[86] N. Dadhich, A. Joe, and P. Singh, Emergence of the product of constant curvature spaces in loop quantum cosmology, Class. Quant. Grav. **32**, 185006 (2015).

[87] S. W. Hawking and G. F. R. Ellis, *The Large Scale Structure of Space-Time*, Cambridge Monographs on Mathematical Physics, Cambridge University Press, 2011.

[88] A. Wang, No-Go Theorem in Spacetimes with Two Commuting Spacelike Killing Vectors, Gen. Rel. Grav. **37**, 1919 (2005).

[89] A. Wang, Comment on 'Absence of trapped surfaces and singularities in cylindrical collapse', Phys. Rev. D **72**, 108501 (2005).

[90] Y. Gong and A. Wang, The Friedmann equations and thermodynamics of apparent horizons, Phys. Rev. Lett. **99**, 211301 (2007).

[91] G. Ongole, H. Zhang, T. Zhu, A. Wang, and B. Wang, Dirac Observables in the 4-Dimensional Phase Space of Ashtekar's Variables and Spherically Symmetric Loop Quantum Black Holes, Universe **8**, 543 (2022).

[92] H. Nariai, On Some Static Solutions of Einstein's Gravitational Field Equations in a Spherically Symmetric Case, General Relativity and Gravitation **31**, 945 (1999).

[93] N. Hidekazu, On a new cosmological solution of Einstein's field equations of gravitation, Sci. Rep. Tohoku Univ. Eighth Ser. **35**, 46 (1951).

[94] M. Casals, S. R. Dolan, A. C. Ottewill, and B. Wardell, Self-Force Calculations with Matched Expansions and Quasinormal Mode Sums, Phys. Rev. D **79**, 124043 (2009).